Gamma rhythm and its relationship with neuronal activity in early visual cortex

Xiaoxuan Jia

Candidate:	Thesis Advisor:
_____	_____
Signature	Signature
Xiaoxuan Jia	Adam Kohn Ph.D
Name	Name
	Associate Professor of Neuroscience
	Title

Submitted in partial fulfillment of the requirements for the degree of Doctor of Philosophy in the Graduate Division of Medical Sciences

Albert Einstein College of Medicine

Yeshiva University

New York

Jan, 2012

THESIS ABSTRACT

Gamma rhythm and its relationship with neuronal activity in early visual cortex

Xiaoxuan Jia

Local field potentials (LFPs) are low frequency (<200 Hz), extracellular voltage fluctuations, which are thought to reflect aggregated activity of a neural ensemble. The gamma components (30-50 Hz) of the LFP are correlated with numerous perceptual and cognitive phenomena, and have been proposed to have important functions in sensory processing. Abnormal gamma activity has been reported in patients suffering from a range of neurological disorders.

Despite its interesting response properties and the theories which these have spawned, the relationship between gamma and neuronal spiking activity—the activity that relays information between cortical areas—remains unclear. My thesis focuses on elucidating this relationship. To do so, I simultaneously recorded LFPs and spiking activity with multi-electrode arrays in the primary visual cortex and area V2 of anesthetized macaque monkeys.

The first data chapter of my thesis explores the stimulus selectivity of gamma, its relationship with the tuning of local spiking activity, and its spatial extent. Previous studies have provided widely disparate views about these properties. We provide evidence that this arises in part because gamma power arises from two sources that reflect different spatial scales of neural ensemble activity: a 'global' rhythm that is spatially coherent, and well-tuned tuned with shared stimulus preference across millimeters of

cortex; and a broadband increase in LFP power that reflects local spiking activity. The relative contribution of these two components depends on stimulus conditions, which can thus alter gamma tuning and spatial coherence. These results indicate that the tuning properties and spatial extent of gamma are flexible and the relationship between gamma rhythm and neuronal activity is dependent on stimulus conditions.

The second data chapter of my thesis explores the plasticity of the LFP and of its gamma components in particular. We compare the orientation tuning of spiking activity and of LFP power in a range of frequency bands, before and after prolonged adaptation to an oriented grating. We find that the shared preference of the 'global' component of gamma rhythm induced with large gratings is extremely sensitive to adaptation: its preference can shift by as much as 90 degrees after adaptation. This suggests that its preference magnifies a bias in the neuronal representation of visual stimuli. Higher frequency components of the LFP (70 Hz+), on the other hand, show more subtle effects, like those of spiking activity. Low frequency power is untuned both before and after adaptation.

The final data chapter explores the interaction between gamma and spiking timing, a poorly understood relationship that lies at the heart of many proposed gamma functions. To test how fluctuations in gamma power affect the coordination of spiking activity in V1, we compared pairwise and higher-order synchrony under a variety of stimulus conditions, inducing either the global gamma rhythm or more local one. We find that spiking activity is phase modulated and thus more coordinated when a global gamma rhythm is induced.

To test the consequence of this coordinated V1 activity on downstream networks, we paired our V1 recordings with recordings in the middle layers of V2. The coordination of V1 spiking activity results in an enhanced probability that each V1 spike that will be followed by a spike in downstream neurons in V2, in a retinotopically specific and gamma-phase dependent manner.

In the appendices, I measure the laminar dependence of gamma power and show that it peaks in the middle layers, a trend opposite to that of low frequency (<10 Hz) power. In addition, I provide preliminary evidence that feedback from higher cortical regions could enhance gamma power. These features are important to understand the underlying network mechanisms of gamma formation.

Together my thesis provides a more complete understanding of the properties of gamma rhythm in the LFP and its relationship with spiking activity, providing important constraints on its proposed function and on the mechanisms that generate it.

Acknowledgement

I am very grateful to my supervisor, Dr. Adam Kohn, for his constant support, guidance and patient instructions during my Ph.D. Particularly, I appreciate the inspiring scientific interactions and his demonstration of the important characteristics of a scientist. I owe my sincere thanks to my advisory committee members, Dr. Michael V L Bennett, Dr. Donald Faber and Dr. Odelia Schwartz, for their continuous guidance throughout my thesis work. I would like to thank my other thesis committee members, Dr. Charles Schroeder, Dr. Jose Luis Pena, and Dr. Alberto Pereda for their time and patience in reading this tremendously long thesis. I would like to express my sincere thanks to Dr. Pablo Castillo and Dr. Susanne R. Zukin for giving me the opportunities to rotate in their labs and learn about their research. I owe my sincere gratitude to the neuroscience department for a friendly and collaborative research atmosphere. I would also like to thank all the lab members, Carlyn Patterson, Stephanie Wissig, Amin Zandvakili and Seiji Tanabe, and members from our longtime collaborating lab, Dr. Odelia Schwartz, Ruben Coen Cagli, Michoel Snow and Florian Roehrbein, for their kindness, insightful and critical scientific comments and helpful advice during my years at Einstein. I wish to thank Dr. Dajun Xing, Dr. Steffen Katzner, Jeremy Freeman and Dr. Ulf Knoblich for their helpful comments and suggestions on my research projects. I thank my close friends at Einstein, who made my life outside the lab more enjoyable. I also want to thank all my friends in the US, in Singapore and in China, who have shared part of my life. Lastly, I want to give my special thanks to my parents and my husband, for their love and constant support, and also my grandma for her wisdom and positive attitude of life.

Table of Contents

List of Figures

Chapter 1: Introduction

We perceive the outside world through our sensory systems. Sensory stimuli are transduced by sensory receptors and converted into neural signals. These signals then travel through different neural pathways to sensory cortex, where they are processed to form our perception of the world. Sensory inputs form the building blocks of our knowledge, thoughts and memory. Deciphering how sensory information is processed in the brain is thus central to understanding brain function.

Information is relayed between neurons by action potentials, or spikes. Individual neurons in sensory cortex, although specialized in their functions, are densely interconnected, forming neural networks. The response properties of a single neuron are shaped by the synaptic inputs it receives from other neurons in the network. How single neuronal activity relates to activity in a larger neural population is critical for understanding information processing in cortical circuitry. Single or multi-electrode recordings of spiking activity allow us to monitor the responses of a limited number of neurons, only the tip of a neuronal network. Other recording methods allow us to evaluate brain activity at larger scales of organization. One of them is through measuring the extracellular fluctuations in the electric field – brain rhythms.

Brain rhythms are slow voltage fluctuations that are generated from the aggregate electrical activity of a neural population, discussed in more detail below. These signals provide information complementary to that of spiking activity, namely some measure of

neural ensemble activity (Buzsaki, 2006). Brain rhythms are typically categorized into different frequency bands. Because of its correlation with a variety of perceptual and cognitive functions in the brain, the changes in the gamma rhythm (30-80Hz) have attracted much attention recently. The gamma rhythm has been proposed to function as a temporal reference for spike timing in a neuronal population and to temporally "bind" spatially separated neurons into a functional neural ensemble (Engel et al., 1999; Fries, 2009).

While theories of gamma's role in cortical function have flourished, an understanding of its properties has lagged. First, the spatial extent of the gamma rhythm and the similarities of its stimulus selectivity to local spiking activity is still ambiguous (Berens et al., 2008). Second, the cellular mechanisms generating gamma have revealed a role for the activity of inhibitory neurons (Bartos et al., 2007), and suggested a mechanism for regulating spike timing. For gamma to function as an active signal, it needs to modulate spiking activity which ultimately carries signals between neurons. However, most of these studies have been conducted in vitro or in the hippocampus. How gamma rhythm relates to spike timing in a cortical neuronal population in vivo is still unclear. This thesis focuses on understanding the properties of gamma—including its stimulus selectivity and relationship to the tuning of nearby neurons, its spatial extent, its plasticity, and its ability to modulate spike timing and affect the transmission of signals between cortical areas. These issues will be studied in the visual cortex of macaque monkeys.

1.1 An overview of visual cortex

Humans and non-human primates rely on vision as the major contributor to our perception of the world. We experience the diversity and colorfulness of nature by eye. Correspondingly, a large percentage of cortex is involved in visual information processing, roughly 30-40% in macaque monkeys (Van Essen et al., 1992).

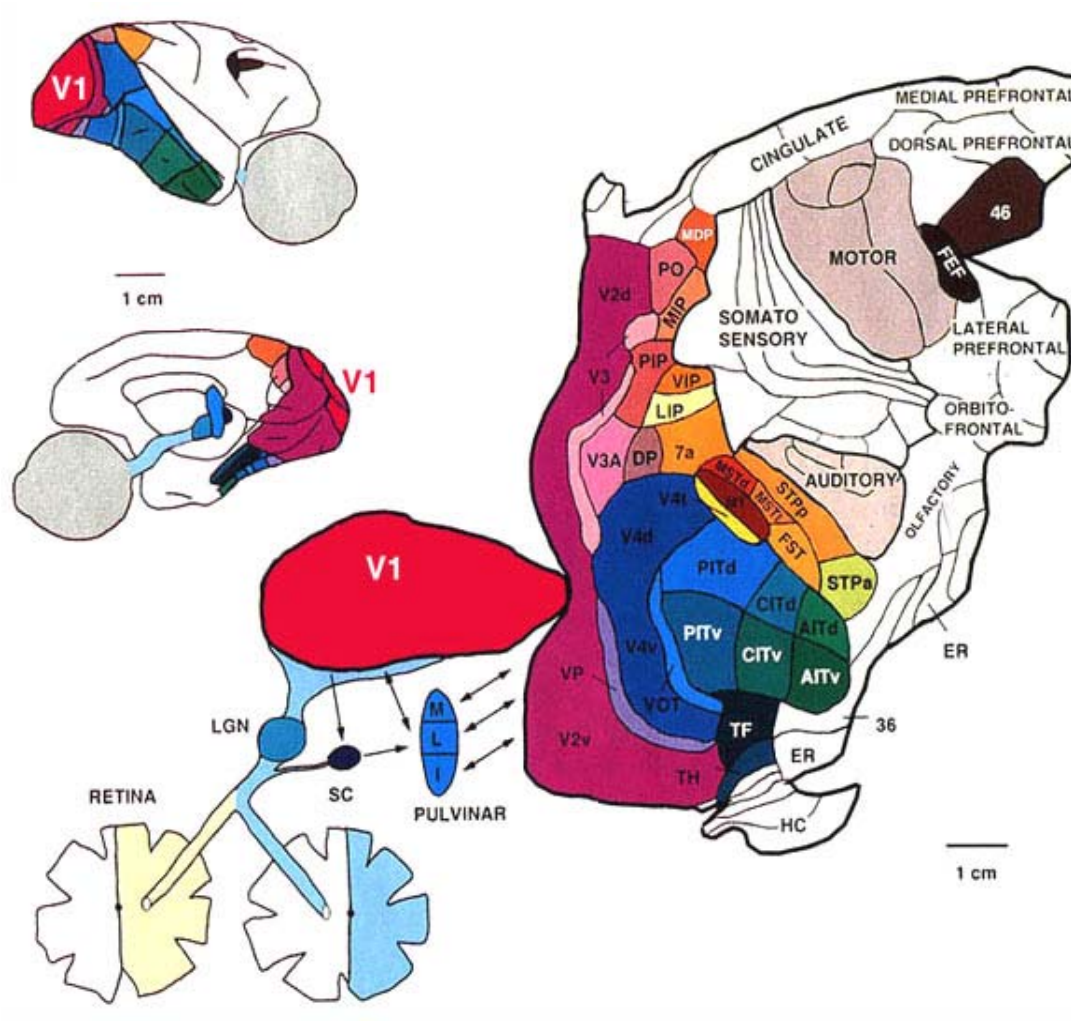

Figure 1.1 Illustration of anatomical and functional organization of the visual system in macaque monkey. From Van Essen et al. (1992) with permission.

Visual cortex is located in the occipital, parietal and temporal lobes. It consists of striate cortex, also called primary visual cortex or V1, and a number of extrastriate visual areas, including V2, V3, V4, V5 (middle temporal area; MT) and others (Figure 1). Visual information is first processed by the retina, which relays information through the optic nerves to the lateral geniculate nucleus (LGN) of the thalamus, and then V1. Neuronal circuitry in visual cortex consists of feedforward, horizontal and feedback connections, with extensive converging and diverging connections (Grossberg, 2001; Lamme and Roelfsema, 2000; Lamme et al., 1998a; Van Essen et al., 1992).

The visual system is thus a hierarchical structure (Felleman and Van Essen, 1991; Lamme et al., 1998a; Movshon and Newsome, 1996). Visual information is primarily relayed by feedforward connections from lower cortical areas to higher ones, with individual cells representing more complex visual features in higher areas and responding more slowly after stimulus onset. Visual features are processed in two parallel but interconnected pathways in extrastriate cortex (Nassi and Callaway, 2009). In very gross terms, the dorsal pathway travels to parietal cortex and mainly processes information about stimulus location, motion and disparity. The ventral stream terminates in the temporal lobe and processes information of object shape and identity (Brincat and Connor, 2004; Desimone et al., 1984; Logothetis and Sheinberg, 1996; Tanaka, 1996).

V1 is the most widely studied and well-understood cortical area. Each neuron in V1 responds to a specific location in the visual field, which is referred to as its spatial receptive field (RF). The concept of RF was first described by Stephen Kuffler in the

1950s who pointed out that retinal ganglion cells respond to contrast and movement in a specific location in the visual field (Kuffler, 1953). V1 has a retinotopic organization, so that neuron are arranged in an orderly map of locations in visual space (Daniel and Whitteridge, 1961; Dow et al., 1985; Guld and Bertulis, 1976; Tootell et al., 1988; Van Essen et al., 1984).

In addition to locations in the visual field, neurons in V1 are sensitive to a variety of visual features, including orientation, spatial frequency, temporal frequency, color, contrast and size (Foster et al., 1985; Hubel and Wiesel, 1962, 1968; Movshon et al., 1978; Tolhurst and Movshon, 1975). The selectivity of these features is thought to be generated from feedforward connections (Andersen et al., 1990; Felleman and Van Essen, 1991; Hubel and Wiesel, 1962, 1965), which are modulated by horizontal connections from nearby neurons and feedback connections from higher cortical areas (Hupe et al., 2001b; Hupe et al., 1998; Lamme and Roelfsema, 2000; Lamme et al., 1998a). Receptive field properties are similar across the cortical layers (Lund, 1988), with this vertical organization forming a basic structure of cortex termed the cortical column (Horton and Adams, 2005; Lund et al., 2003; Mountcastle et al., 1957). Cortical columns are arranged into orderly patterns or functional maps for some visual features (Figure 1.2), such as stimulus orientation (Blasdel and Salama, 1986; Bonhoeffer and Grinvald, 1991; Koulakov and Chklovskii, 2001; Paik and Ringach, 2011; Wiesel and Hubel, 1974), ocular dominance (Crair et al., 1997; LeVay et al., 1985; Wiesel et al., 1974), spatial frequency (Everson et al., 1998; Issa et al., 2000) and perhaps color (Landisman and Ts'o, 2002; Livingstone and Hubel, 1984;

Xiao et al., 2003) as well. Each of these functional maps has a different spatial pattern and column size.

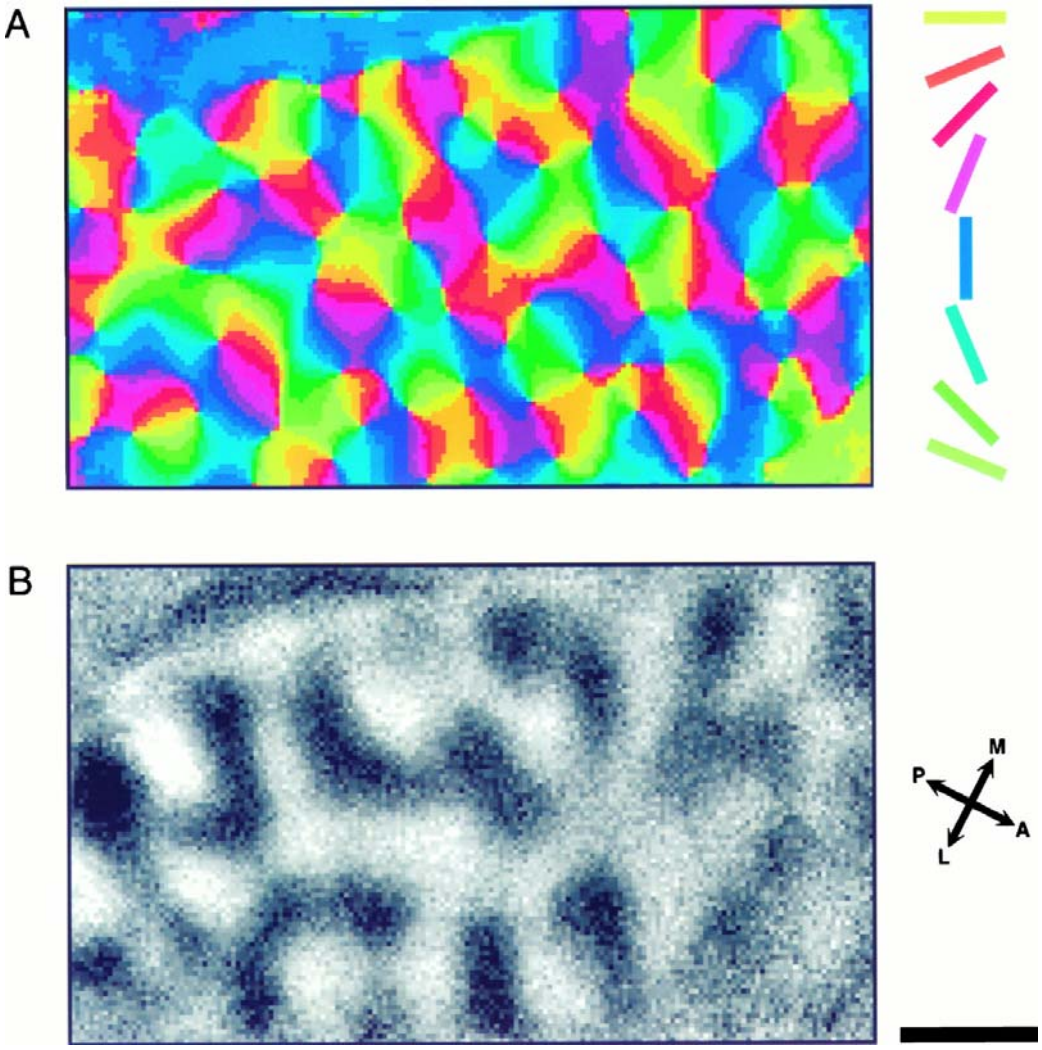

Figure 1.2 Illustration of orientation preference and ocular dominance map in primary visual cortex. *A*, Orientation map with angles of preferred orientation color-coded. *B*, Ocular dominance map with dark color representing contralateral and white color indicating ipsilateral eye dominants. Black scale bar indicates 1 mm. From Hubener et al. (1997) with permission pending.

Because of the detailed knowledge of V1 single neuron properties, circuitry and functional organization, this area is an attractive model system for understanding the relationship between brain rhythms--a collective signal that is poorly understood--and neuronal activity.

1.2 Brain rhythms

Hans Berger first successfully measured the brain waves of human subjects in 1924 using the electroencephalogram (EEG) (Haas, 2003). His goal was to demonstrate that the electromagnetic fields of the human brain could be used for telepathy. Although the signals he detected were unsuccessful for this purpose, the EEG was widely adopted by clinicians and scientists. This is because the recordings are easy to perform and the rhythms detected are informative of brain state. For example, when we are deep asleep, the EEG consists of low-frequency, large-amplitude rhythms (Clement et al., 2008; Hobson and Pace-Schott, 2002; McGinty and Drucker-Colin, 1982; Poe et al., 2010); when we are awake and attentive, it consists primarily of fast, small amplitude rhythms (Jensen et al., 2007; Muller et al., 1996; Tallon-Baudry and Bertrand, 1999; Tallon-Baudry et al., 1999).

Brain rhythms mostly reflect synchronized subthreshold activity in dendrites (Buzsaki, 2006; Logothetis, 2003; Logothetis et al., 2007; Mitzdorf, 1985), shaped by the geometry and alignment of the active neurons (Buzsaki, 2006). The resultant fluctuations can be measured on the scalp by EEG or magnetoencephalography (MEG), intracranially with subdural electrodes (electrocorticography) and with electrodes inserted into the brain—the local field potential. Generally, these rhythmic activity fluctuations can be

decomposed into different frequency components—delta (<4Hz), theta (4-8Hz), alpha (8-12Hz), beta (12-30Hz), gamma (30-80Hz) and high-gamma or high-frequency activity (>80Hz)—although the precise frequency ranges associated with these terms vary across studies.

1.2.1 Different rhythms correlate with different brain states

Different frequency components of brain rhythms reflect different brain states. The delta rhythm (<4Hz), which is dominated by large amplitude, slow fluctuations, occurs during deep sleep. The theta rhythm (4-8Hz) reflects a more alert state. It is normally correlated with exploration and spatial navigation and is suggested to reflect sensorimotor integration in rats (Bland, 2004; Bland et al., 2006; Bland and Oddie, 2001). The strength of theta rhythm also correlates with learning and memory and has been associated with long-term potentiation (LTP) in the hippocampus (Barr et al., 1995; Cantero et al., 2003; Jones and Wilson, 2005a, b; Siapas et al., 2005). Additionally, the phase of spiking within the theta rhythm can code for the animals spatial location (Ego-Stengel and Wilson, 2007; Foster and Wilson, 2007; Jones and Wilson, 2005b). The alpha rhythm (8-12Hz) has been linked with relaxed or reflective states, which is a mentally relaxed arousal state (Bash, 1968; Cantero et al., 1999). Alpha is also observed during rapid eye movement (REM) sleep (Cantero et al., 2000; Crespel et al., 2009; Gelisse and Crespel, 2008). Compared to the lower frequency rhythms, the beta rhythm (12-30Hz) has a wider frequency range, and is associated with active working state, for example during speaking and movement (Murthy and Fetz, 1992; Poenaru et al., 1992; Rubino et al., 2006). An even higher frequency band, known as gamma (30-80 Hz),

correlates with more active brain states involved in attention, learning and working memory (Fries et al., 2001; Jensen et al., 2007; Jutras et al., 2009; Pesaran et al., 2002; Popescu et al., 2009; Tallon-Baudry, 2009; Tallon-Baudry and Bertrand, 1999; Womelsdorf et al., 2006). Finally, frequency components between 80-150 Hz, referred to as high gamma, behave similarly to local spiking activity (Ray and Maunsell, 2011a) and can be coordinated to the low frequency theta rhythms (Canolty et al., 2006).

1.2.2 Changes in brain rhythms in mental diseases

Brain rhythms are thought to reflect coordinated activity among large groups of neurons, either within one cortical area or in a more distributed network (Engel et al., 1991a; Fries et al., 2007). Abnormal brain rhythms could indicate a disruption of this coordination, which might result in severe functional deficits (Uhlhaas and Singer, 2006). Recent studies using EEG, MEG and event related potentials (ERP) have tested for differences in brain rhythms under a variety of neurological diseases. Disrupted rhythms and impairments in behavioral performance and cognition are observed in schizophrenia (Krishnan et al., 2005; Kwon et al., 1999), autism (Grice et al., 2001), Alzheimer's disease (AD) (Babiloni et al., 2004a; Babiloni et al., 2004b), Parkinson's disease (Mochizuki et al., 1999; Nagasaki et al., 1978) and epilepsy (Rampp and Stefan, 2006). For example, patients with schizophrenia have an impaired ability to perform perceptual grouping, and also show reduced activity in the beta and gamma frequencies of the EEG. Enhanced gamma activity has been observed preceding seizures. Finally, the EEG in AD patients shows enhanced lower frequency activity but a reduction in the gamma band during resting state. These observations demonstrate that understanding the basic nature

and mechanisms of different brain rhythms might help with the diagnosis of neurological diseases.

1.3 The LFP

As mentioned previously, the local field potential (LFP) measures brain rhythms on a more local basis, with a high impedance electrode placed in the brain (Figure 1.3A). Typically, these electrodes are the same as those used to detect the spiking activity of individual neurons, but the voltage signal is low-pass filtered (<250Hz) to capture the slower fluctuations of brain rhythms (Figure 1.3B). The LFP was frequently used to study brain function, until it fell in popularity with the advent of single-cell electrophysiology in the late 1950's. Over the last decade, however, LFPs have attracted renewed interest, as a potentially useful signal for studying the behavior of ensembles of neurons.

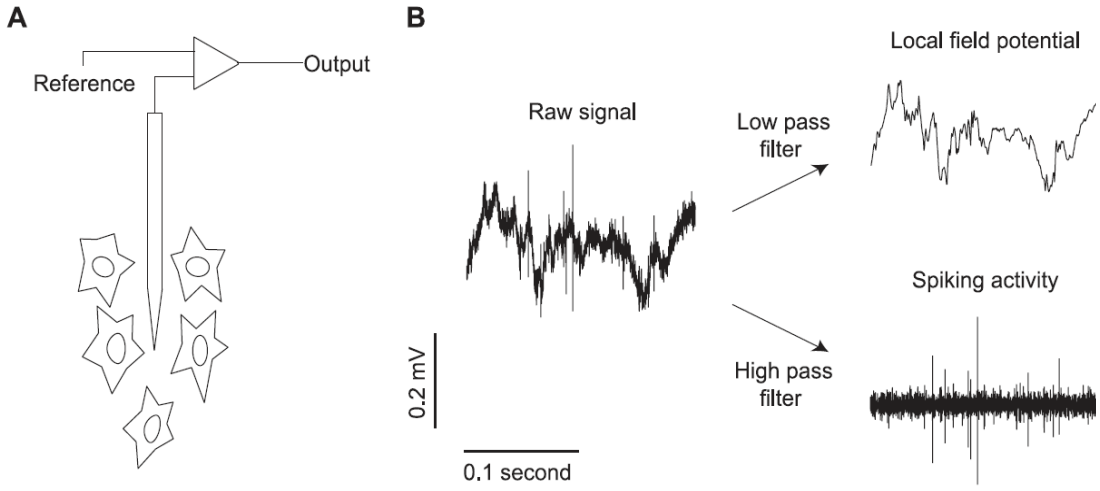

Figure 1.3 Illustration of LFP and spiking activity recordings. (A) A high impedance electrode detects extracellular electrical activity of nearby neurons. (B) This raw signal is low-pass filtered (e.g., <250 Hz) to provide the local field potential (LFP), and high-pass filtered (e.g., 0.5–10 kHz) to isolate spiking activity. From Jia and Kohn (2011) with permission.

The amplitude of the LFP is related to the geometry of the active neural tissue (Buzsaki, 2006; Logothetis, 2003). When a neuron has asymmetric dendrites distribution around the cell body, the current from apical dendrites to soma forms an electrical dipole. These fields are larger when neurons are aligned (e.g. as with pyramidal neurons in the hippocampus), so that the fields sum. Neurons that have irregular geometry or a distorted arrangement of soma and dendrite contribute less to the field potential. The electrical activity contributing to the field potential is thought to come primarily from synaptic and dendritic activity, including synaptic potentials, spike afterpotentials and intrinsic voltage-dependent membrane fluctuations (Haberly and Shepherd, 1973; Logothetis, 2002; Mitzdorf, 1985).

1.4 Relationship between the LFP and neuronal membrane potential

Although the LFP is generally believed to reflect aggregated neural activity, it is critical to understand how it relates to membrane potential fluctuations and spiking in single neurons. It has been proposed that one way to infer the relationship between membrane potential fluctuations in individual neurons and the LFP is to predict spike trains from the phase and amplitude of the simultaneously recorded LFP (Galindo-Leon and Liu, 2010; Rasch et al., 2009; Rasch et al., 2008). In general, these studies have revealed that broadband LFP fluctuations (4-100 Hz) predict reasonably well the slow fluctuations in neuronal firing rate. The phase of low frequency rhythms (<10Hz) can predict the occurrence of the temporally clustered spiking activity (Rasch et al., 2008), whereas higher frequency

rhythms including gamma make a worse prediction, with gamma amplitude being more informative than its phase (Galindo-Leon and Liu, 2010).

A more direct approach is to perform intracellular recordings and compare the membrane potential to simultaneously recorded LFPs. This has revealed a significant correlation, both in the gamma frequencies (Hasenstaub et al., 2005) and lower frequency components (Okun et al., 2010; Poulet and Petersen, 2008). Assuming that the LFP correlates with membrane potential fluctuations of neurons in the local population, it has been suggested that the functional connectivity could be assessed by evaluating the relationship between average membrane voltage of a neuronal population in one area and the firing of neurons at another location through measuring the temporal correlation between individual spikes and the averaged amplitude of field potential before and after each spike measured at different locations (Nauhaus et al., 2009; Ray and Maunsell, 2011b).

Together these studies suggest a strong link between low frequency fluctuations in the LFP and fluctuations in the membrane potential and spiking activity, and a weaker but measurable correlation in higher frequency bands.

1.5 Relationship between LFP and BOLD fMRI signal

In addition to its relationship with activity at the single neuron level, the LFP also has a potential link with the blood-oxygen level dependent (BOLD) functional magnetic resonance imaging (fMRI) signal. BOLD-fMRI is widely used to study human brain function (Buxton and Frank, 1997; Kwong et al., 1992; Ogawa and Lee, 1990; Ogawa et

al., 1990a; Ogawa et al., 1990b; Ogawa et al., 1998; Ogawa et al., 1992; Turner et al., 1991). The spatial resolution of the BOLD signal is on the order of 1 cubic millimeter, which contains on the order of two million neurons (Powell and Hendrickson, 1981), and its temporal resolution is on the order of seconds. In principle, changes in the BOLD indicate changes in the metabolic rate of the cells. Understanding more concretely the relationship between neural activity and the BOLD signal is necessary for the interpretation of BOLD measurements.

The BOLD signal has been compared with both spiking activity and the LFP. It has been demonstrated that the BOLD signal is positively correlated with neuronal firing rates (Rees et al., 2000), although its temporal dynamics are much slower. Several studies have compared the BOLD-fMRI signal and the LFP under identical stimulus conditions. The widespread coherent nature of low frequency and gamma frequency band-limited power (BLP) of the LFP make it a potentially good correlate of the BOLD signal (Leopold et al., 2003). Indeed, there is a better correspondence between LFPs and the BOLD signal than between spiking activity and the BOLD signal. Specifically, the broadband power of the LFP is better maintained than spiking activity after stimulus onset, and thus better predicts the temporal dynamics of the BOLD signal (Logothetis, 2003; Logothetis et al., 2001). Additionally, the correlation between band-limited gamma power of the LFP and the BOLD signal is significantly higher than that of spiking activity (Goense and Logothetis, 2008; Kayser et al., 2004; Leopold et al., 2003; Logothetis et al., 2001; Nir et al., 2007). Although whether the BOLD signal is more correlated with spiking activity or the LFP remains controversial, previous studies have shown that understanding the properties of

the LFP is likely to be helpful for understanding and interpreting changes in the BOLD signal.

1.6 The stimulus evoked and induced components of LFP

Before investigating the properties of LFP, it is important to note that there are two types of stimulus driven LFPs. One is an evoked potential, which is time-locked to the onset of a sensory stimulus; the other is a stimulus-induced potential, which does not have a strict timing or phase relationship with stimulus onset (Juergens et al., 1999; Katzner et al., 2009; Kruse and Eckhorn, 1996; Tallon-Baudry and Bertrand, 1999). Distinguishing between these two components of the LFP is important because of their different phase relationship to external stimuli and the potentially different cellular mechanisms underlying them.

The evoked potential is typically measured by averaging across multiple responses to the same stimulus. As a result, all phase-varying oscillations are averaged out and only stimulus phase-locked components remain. The evoked LFP is prominent in the first 100 ms after stimulus onset and is normally dominated by low frequency power. The visual evoked potential (VEP) (Bonds, 1982; Givre et al., 1994; Pang and Bonds, 1991; Schroeder et al., 1992; Schroeder et al., 1991) has been used to decode the relationship between a visual stimulus and aggregated neural activity of a population. The difference in amplitude of the evoked potentials for different visual stimuli indicates the selectivity of this signal (Katzner et al., 2009).

In contrast to the stimulus-evoked response, the stimulus-induced potential has relatively slow dynamics. It normally peaks 200 ms after stimulus onset (Burns et al., 2010a; Gruber and Muller, 2002; Tallon-Baudry and Bertrand, 1999). The induced LFP contains higher frequency rhythms than typically observed in the evoked potential. These rhythms can be elicited by sustained stimuli and any abrupt changes in visual input will interrupt them (Kruse and Eckhorn, 1996). Because the phases of the constituent rhythms vary across trials with respect to stimulus onset, the signal cancels out if averaged across trials. Therefore, this potential is often analyzed in the frequency domain for each trial.

According to these features, we can separate the evoked and induced potentials in two steps: (1) defining the stimulus-evoked potential by averaging across trials and (2) subtracting the evoked potential from the raw LFP to isolate the induced signal.

1.7 Gamma rhythm

One signature of the LFP, shared by both its evoked and induced components, is that its power spectrum declines with frequency, meaning that power is dominated by lower frequencies (Henrie and Shapley, 2005; Petermann et al., 2009; Touboul and Destexhe, 2010). This is still the case when networks are driven by external sensory drive or internal states, but less so: the power in higher frequencies increases whereas that in lower frequencies is suppressed. Among all the frequencies ranges, the change in gamma power in the driven state is particularly striking in visual cortex. Gamma is a higher frequency ongoing rhythm; the induced LFP thus contains much higher gamma power than the evoked potential, in which most of these fast oscillations are averaged out.

Gamma has been observed in visual cortex (Eckhorn et al., 1988; Engel et al., 1991a; Gail et al., 2000; Gray et al., 1989; Tallon-Baudry et al., 1996; Womelsdorf et al., 2006), auditory cortex (Brosch et al., 2002; Edwards et al., 2005), motor cortex (Schoffelen et al., 2005a), parietal cortex (Pesaran et al., 2002), and hippocampus (Bragin et al., 1995; Csicsvari et al., 2003), and also subcortical structures. It has been found in numerous species, from mammals (rat, monkey, cat, human) to insects (Stopfer et al., 1997). A prominent gamma rhythm can provide a signature of an engaged network. In sensory cortex, gamma power increases with sensory drive (Adrian, 1942; Henrie and Shapley, 2005), and a broad range of cognitive phenomena, including perceptual grouping (Tallon-Baudry and Bertrand, 1999), attention (Fries et al., 2001), working memory (Pesaran et al., 2002) and learning (Bauer et al., 2007). Irregular gamma activity has been associated with various neurological disorders, such as Alzheimer's disease, Parkinson's disease, schizophrenia, and epilepsy (Uhlhaas and Singer, 2006).

1.8 Response properties of gamma – a comparison with neurons in V1

As a signal that correlates with a variety of cognitive functions, it is important to understand the response properties of the gamma rhythm. Taking advantage of the widely studied neuronal response properties in V1, researchers have compared the basic tuning properties of gamma with that of neuronal spiking activity. Gray and colleagues found that the gamma components of the LFP are orientation selective (Gray and Singer, 1989), similar to individual neurons. The orientation tuning of gamma suggests that there might be a specific neural circuit that gives rise to its preference. Because they found the

orientation preference of gamma to be similar to that of local spiking activity, Gray and colleagues suggested that gamma reflects activity in an orientation column, roughly ~250 μm in extent (Horton and Adams, 2005).

In recent years, a number of studies have further investigated the stimulus selectivity of gamma and compared it to local neuronal activity. Gamma power is selective for a number of stimulus attributes. The orientation tuning of gamma in V1 has been confirmed in several studies (Berens et al., 2008; Frien and Eckhorn, 2000; Frien et al., 2000; Siegel and Konig, 2003), and gamma has been shown to be tuned for spatial and temporal frequencies (Kayser and Konig, 2004). In MT, gamma is tuned for speed and direction (Liu and Newsome, 2006). In all of these studies, selectivity is most prominent in the gamma and higher frequency ranges, but not in the lower frequency bands of the LFP.

Neurons in V1 are also sensitive to stimulus size. Responses are strongest when the size of a preferred stimulus matches the classical receptive field (CRF). Stimuli outside the CRF can modulate neuronal responses in the receptive field center (Hubel and Wiesel, 1965; Kapadia et al., 2000; Knierim and van Essen, 1992; Maffei and Fiorentini, 1976; Nelson and Frost, 1985; Yu et al., 2003). This modulation contributes to contextual effects (Levitt and Lund, 1997; Zipser et al., 1996) and perceptual grouping (Eckhorn, 2000; Schmidt et al., 1997) in lower visual cortex. In most cases, the response evoked by stimuli in the CRF are suppressed by stimuli outside (in the "surround"), an effect termed surround suppression (Angelucci et al., 2002a; Angelucci et al., 2002b; Cavanaugh et al., 2002a, b; Haider et al., 2010; Hubel and Wiesel, 1965; Sceniak et al., 2002; Xing et al., 2005). The

source of this suppression is unclear. It has been proposed to involve inhibition recruited by long-range horizontal connections (Angelucci and Bressloff, 2006; Angelucci et al., 2002a; Das and Gilbert, 1995) or feedback from higher cortical areas (Angelucci and Bressloff, 2006; Bair et al., 2003), or from reduced excitatory drive from LGN (Ozeki et al., 2004; Webb et al., 2005).

Gamma is modulated differently by stimulus size from neuronal responses. Gamma does not show surround suppression, instead it grows monotonically with increasing stimulus size (Bauer et al., 1995; Gieselmann and Thiele, 2008), and its peak frequency shifts lower (Gieselmann and Thiele, 2008; Kang et al., 2009; Ray and Maunsell, 2011a). In contrast to gamma, higher frequency components of the LFP show surround suppression similar to local spiking activity. If surround suppression involves some form of lateral and feedback inhibition, the monotonic increase in gamma power with enlarging size suggests that the strength of gamma might reflect the level of inhibition in the network.

Stimulus contrast can also modulate neuronal responses in V1. Lowering contrast reduces neuronal responses and leads to an apparent increase in the CRF (Cavanaugh et al., 2002a; Sceniak et al., 1999). The broadband power of the LFP is modulated similarly by stimulus contrast (Logothetis et al., 2001), with a particularly strong effect in gamma band power. Indeed, gamma power grows monotonically with stimulus contrast (Henrie and Shapley, 2005), whereas the responses of single neurons show saturation (Albrecht and Hamilton, 1982; Carandini et al., 1997). The peak frequency in the gamma range also depends on

contrast: with lower contrast, the peak frequency of gamma shifts lower (Ray and Maunsell, 2010).

The selectivity of gamma power in V1, which is comparable in its richness to single neurons, suggests that gamma could be used a useful neural signal to understand the response properties of a neural ensemble. However, given differences in the selectivity of neurons and gamma for stimulus size and contrast, it is not clear whether gamma reflects the activity of a local ensemble, a more distributed one, or the level of inhibitory activity in the network.

1.9 Spatial scale of gamma rhythm

To understand and interpret the gamma rhythm, it is important to know its spatial extent, which is governed both by passive volume conduction and the scale of neural ensemble that is involved in its generation.

1.9.1 Passive signal transmission in the brain

As an extracellular electrical signal, gamma could be passively transmitted by volume conduction. Volume conduction is defined as the transmission of the electrical field generated from the current source of the signal to the recording sensor through brain tissue, the skull and the scalp (Legatt et al., 1980). Within the brain, the passive conduction of visually evoked LFPs, is limited within 300 μm of the recording site (Katzner et al., 2009; Xing et al., 2009), which is similar as multi-unit activity (MUA) detected from the same recording electrode (Henze et al., 2000). These conclusions were drawn based on

comparisons between LFPs and the responses of local MUA. However, a direct measurement showed that the passive spread of the field potential can be more than 1 cm (Kajikawa and Schroeder, 2011). These different conclusions of passive propagation indicate that the estimation of volume conduction based on comparison with response properties of spiking activity could be very different from direct measurement. The contribution of field potentials that passively conducted from distant sites may not be large enough to affect the response properties of locally generated LFP.

Because neurons in the brain are buried in glia and other capacitive tissues, one would expect that the brain tissue could have both conductor and capacitor properties. The time constant of a capacitor could act as a signal filter which biases signal transduction towards signals with longer oscillating cycles. As a result, the spatial extent of the LFP, when passively transmitted, could be frequency dependent. This hypothesis proposes that the high frequency components of the LFP, whose oscillation is fast, may not get effectively transmitted with the filter property of the brain tissue compared to the low frequency components, which could give rise to different spatial extents from the current source. To test this hypothesis, Logothetis and colleges measured the cortical impedance in the grey matter as a function of frequency, and found surprisingly that the cortical impedance can be viewed as a pure-resistive conductor. These results suggest that the grey matter, even though contains massive fat and proteins, is dominated by its conductivity rather than a capacitor that filters higher frequency signals (Kruse and Eckhorn, 1996; Logothetis et al., 2007; Ranck, 1963). Therefore, based on the previous findings that the passive transmission of evoked LFP signal, which is dominated by low frequency fluctuations, is

reflecting neural activity within 300 μm of the electrode tip, the spatial extents of higher frequency components should be similar but not less.

However, since these conclusions are based on evoked potentials and the stimulus induced activity might have a different spatial extent of neural ensemble that actively generating the rhythms, the spatial resolution of the induced gamma rhythm is still unclear.

1.9.2 Discrepancy in the estimation of spatial spread of gamma

Leaving aside the issue of the volume conduction, numerous studies have tried to estimate the spatial extent of neural activity that gives rise to gamma. However, the spatial spread of gamma rhythm of LFP remains unclear, with different conclusions reached, depending on the approaches used and the stimulus paradigm.

Initially, the spatial spread of gamma was estimated from its spatial coherence (Juergens et al., 1999; Mitzdorf, 1985). Because gamma was found to be coherent between cortical sites separated by many millimeters, the signal was thought to reflect a broad summation of neural activity. This idea faded with the observation that gamma is orientation-tuned, which suggests a more local source (about 250 μm (Gray and Singer, 1989). This observation was confirmed by the findings that gamma and spiking activity recorded on the same electrode had similar stimulus preferences (Frien and Eckhorn, 2000; Frien et al., 2000; Katzner et al., 2009; Siegel and Konig, 2003) (Liu and Newsome, 2006).

However, other studies failed to find such similarity: a comparison of the object selectivity of the LFP with spiking activity in inferotemporal cortex (IT) showed that the LFP preference was dissociated from spikes for frequency components below 100 Hz, and better predicted by the weighted average of spiking activity within 3 mm of the recording electrode (Kreiman et al., 2006). Even in V1, the orientation preference of gamma components of the LFP have been found to be quite different from local spiking activity (Berens et al., 2008), leading to the suggestion that gamma reflects activity that extends for roughly 600 μm.

The existing literature thus paints a confusing and seemingly contradictory of the spatial extent of gamma and the size of the neural ensemble it reflects. Gamma is coherent over long distances but well-tuned, with a preference that sometimes matches local spiking activity but, in other studies, does not. Resolving this confusion is a prerequisite for understanding how gamma may contribute to cortical function. This issue will be addressed in Chapter 2 of the thesis.

1.10 Cellular mechanisms of gamma

To interpret changes in the gamma rhythm, we need to understand the neural activity that is involved in its generation, specifically, the neuronal substrates and circuitries.

1.10.1 Neuronal substrates involved in gamma generation

Numerous studies in the hippocampus and neocortex have shown that GABAergic interneurons are important for generating gamma, and that the recurrent connections

between excitatory and inhibitory neurons affect the strength and maintenance of the rhythm (Bartos et al., 2007; Buzsaki and Chrobak, 1995; Cardin et al., 2009; Traub et al., 2004; Wang and Buzsaki, 1996; Whittington et al., 2011; Whittington et al., 1995). The relevant inhibitory neurons can provide synchronized inhibitory postsynaptic potentials when activated (Hasenstaub et al., 2005; Traub et al., 2004; Whittington et al., 1995). Because they innervate the cell body or axon initial segment of pyramidal neurons, the rhythmic firing of fast-spiking GABAergic interneurons (Cardin et al., 2009), such as basket cells and chandelier cells, can rhythmically hyperpolarize or shunt the pyramidal cell, and thus modulate the timing of action potentials (Buzsaki et al., 1983; Csicsvari et al., 2003; Lytton and Sejnowski, 1991; Mann et al., 2005; Miles et al., 1996; Penttonen et al., 1998; Vida et al., 2006).

The frequency of the gamma rhythm is related to the discharge rate of interneurons and the conduction delay between neurons (Whittington et al., 1995). Gamma fluctuations can be induced in interneuron networks in hippocampal slices by tonic activation of metabotropic receptors (mGluRs) (Whittington et al., 1995), kainite receptors (Cunningham et al., 2003; Fisahn, 2005; Fisahn et al., 2004; Hajos et al., 2000) and muscarinic acetylcholine receptors (mAChRs) (Fellous and Sejnowski, 2000; Fisahn et al., 1998), and can be effectively blocked by antagonists of $GABA_A$ receptors (Traub et al., 2003; Traub et al., 1996a). Gamma can also be induced in vivo by directly activating fast-spiking interneurons, using optogenetic tools (Cardin et al., 2009).

In addition to interneurons, some studies find that a unique type of pyramidal-shaped neuron can contribute to generating gamma as well. Gray and McCormick have found that 'chattering cells', a distinctive subtype of pyramidal neurons located in the superficial layer of visual cortex, can intrinsically fire in the gamma frequency range with visual stimulation or simple intracellular current injection (Gray and McCormick, 1996). The nature of these chattering cells is still unclear, but they may contribute to the gamma rhythm induced by visual stimuli (Cardin et al., 2009; Cunningham et al., 2004b; Steriade et al., 1998).

1.10.2 Different circuitry models proposed for gamma generation

Building on the experimental data that revealed the neuron types involved in gamma generation, different network models have been proposed to account for the formation of gamma synchronization in local neuronal circuits. The simplest model is an interneuron network gamma (ING), which suggests that gamma is generated by activating fast-spiking interneurons with tonic excitation, driving a recurrently connected interneuron network. This network mechanism of gamma generation has been received experimental support in hippocampus slices (Csicsvari et al., 2003) and the cerebellum (Middleton et al., 2008). In the ING model, the frequency of gamma is determined by the strength of excitatory drive and the kinetics of postsynaptic potentials in the inhibitory network (Traub et al., 1996a; Whittington et al., 2011; Whittington et al., 1995). A signature of this model is that the generation of gamma is heavily dependent on the degree of synchrony in the tonic excitatory drive. When different interneurons in the network are depolarized asynchronously, the gamma rhythm is disrupted (Wang and Buzsaki, 1996).

One proposed mechanism to rescue this unsteady state is to have gap junctions between interneurons (Bartos et al., 2007; Buhl et al., 2003; Draguhn et al., 1998; Fukuda and Kosaka, 2000; Fukuda et al., 2006; Gibson et al., 1999; Hormuzdi et al., 2001; Nase et al., 2003; Traub et al., 2004; Traub et al., 2001). The fast equalization of membrane potential discharge through electrical-coupling makes the inhibitory interneuron network less sensitive to heterogeneity in its excitatory drive.

An alternative model of gamma generation is called pyramidal interneuron network gamma (PING). This model requires reciprocal connections between the inhibitory interneurons and excitatory neurons (Traub et al., 1997; Whittington et al., 2001; Whittington et al., 1997) and, thus, arguably more realistic in the cerebral cortex. This model proposes that the strong, phasic activation of inhibitory neurons by pyramidal neurons can generate bursts of spikes in the gamma frequency in the inhibitory neurons, which in turn regulates the firing pattern of the excitatory neurons and, as a consequence, the timing of spikes in the interneurons themselves. For the PING model to generate gamma, there are two prerequisites: first, strong activation of inhibitory neurons by excitatory neurons (Traub et al., 1997); second, the relative firing rate of excitatory and inhibitory neurons should be balanced, because high firing rates of the interneurons can reduce the firing probability of excitatory neurons and terminate the rhythm (Tiesinga and Sejnowski, 2009). The frequency of gamma rhythm generated by the PING network depends on the decay time constant of postsynaptic currents and the delay time of the reciprocal connections between excitatory and inhibitory neurons. The PING network is more tolerant of variability in excitatory inputs.

An additional mechanism of gamma generation is called persistent gamma (PG). Chemical activation of metabotropic glutamatergic, kainite and muscarinic acetylcholine receptors can induce long-lasting gamma rhythms. The mechanism of this form of gamma generation is intermingled with the ING and PING models, but has distinctive features. First, PG rhythms do not require a recurrently connected interneuron network (Buhl et al., 2003; Hormuzdi et al., 2001; Wulff et al., 2009). Second, in PG, the principal neurons have very low firing rates, notably different from the PING model (Cunningham et al., 2003; Cunningham et al., 2004a; Cunningham et al., 2004b; Gillies et al., 2002). The mechanisms of PG model are relatively unclear.

Gamma rhythm can be coherent over long distance (Frien and Eckhorn, 2000; Leopold et al., 2003; Murthy and Fetz, 1992). To form a coherent network requires a short delay time among the local generators. Large network models (Bartos et al., 2007; Buzsaki and Chrobak, 1995; Wang and Buzsaki, 1996) suggest that the local gamma-generating networks, discussed above, can be coupled by long-range horizontal connections (Traub et al., 1996b) or gap junctions among inhibitory interneurons (Gibson et al., 1999).

It is important to note that because the amplitude of the LFP is sensitive to the alignment of signal generators, the activity of aligned pyramidal neurons in cortex will be the primary contributor to the LFP, while the activity of interneurons with their star-shaped dendrites will contribute less. Therefore, the strength of gamma in the LFP is more likely to be directly dependent on input to pyramidal neurons from interneurons.

1.11 Gamma rhythm and spike timing

It is well-established that gamma correlates with engaged or driven neural networks, but it is less clear whether it is a simple by-product of activity or has an important functional role. This is not for lack of proposals: numerous functions have been attributed to this rhythm. Most of these hinge on a relationship between gamma and the timing of spiking activity in nearby neurons. Since spikes carry signals between neurons and networks, gamma can only play a role in information processing by influencing these events. Therefore, to understand the function of gamma, it is critical to analyze the temporal relationship between spikes and gamma.

Numerous studies have found phase modulation of spike timing in gamma frequencies (Csicsvari et al., 2003; Hasenstaub et al., 2005; Pesaran et al., 2002), suggesting a relationship between gamma and spike timing under certain circumstances. A phase-locking between gamma and spike timing of excitatory cells could arise because local inhibitory neurons fire action potentials preferentially at a particular phase of the gamma cycle, makes the spiking of excitatory neurons more likely to occur at an offset phase when inhibition is weaker. (Fries et al., 2007; Hasenstaub et al., 2005). Depending on the cellular mechanisms generating gamma, the spike timing of excitatory and inhibitory neurons could have different phase relationships with the gamma rhythm. If the gamma rhythm is generated solely based on a synchronized inhibitory interneuron network, the spike timing of the interneurons should occur at the trough of the gamma rhythm where network inhibition is the strongest, while the phases of excitatory neurons is ambiguous

(Tiesinga and Sejnowski, 2009). If gamma is generated by the PING model, the interneurons are depolarized by the pyramidal neurons, and thus the spike timing of inhibitory neurons tends to be delayed relative to that of the excitatory neurons (Csicsvari et al., 2003; Hasenstaub et al., 2005).

There are several standard ways to measure the timing relationship between gamma and spikes. One way is by calculating spike-field coherence (SFC), which is a correlation analysis between the amplitudes of oscillations in the LFP and the timing of spikes in a spike train in the frequency domain. When the SFC is high at certain frequency, this means spikes are phase-locked to the oscillation at that frequency. Another way to evaluate the timing relationship between gamma and spikes is by calculating spike-triggered averaging of the LFP. When spikes occur at a consistent phase on the gamma rhythm, averaging LFP epochs around each spike will remove the rhythms that have no phase relationship with spikes and leave only the rhythms that spikes are phase-locked to. An alternative way to check at which phase individual spikes occur on the gamma rhythm is by band-limited filtering of gamma rhythm and then deriving the phases where spikes occur accordingly. Combining these calculations provide a measure of the temporal or phase relationship between spike trains and the gamma rhythm.

Studies using these measures have revealed weak but measurable coupling between gamma and spikes, which increases when gamma power is elevated (Fries et al., 2001; Fries et al., 2008; Pesaran et al., 2002). This coupling is only meaningful, however, if the two signals are measured independently. LFPs and spikes are often recorded from a

single electrode. Because extracellular action potential waveforms have a broad frequency spectrum, including frequency components below 250Hz, this energy can leak into the LFP (David et al., 2010; Zanos et al., 2011). That is, the low-pass filtering of the extracellular voltage signal, which is used to isolate the LFP (Figure 1.3), may not remove entirely the action potential waveforms. The resultant contamination would introduce spurious correlations: the timing of spikes will appear to be related to fluctuations in LFP power for the simple reason that a remnant of the spike waveform remains in that signal. In our analysis, we focused on the low gamma rhythm, which is between 30-50Hz (Ray and Maunsell, 2011a), where this contamination is minimal. Further, when measuring the relationship between gamma and spiking activity, we used signals recorded by adjacent electrodes.

1.12 Proposed functional roles of gamma

Based on its regulation of spike timing, numerous theories have suggested that the gamma-coordination of spiking activity is central to cortical processing.

1.12.1 Temporal coding (phase of spike coding)

Information encoded in spike timing is referred to as 'temporal coding', in contrast to the rate coding theory, which proposes that the number of spikes in a time window encodes information. The phase-modulation of spike timing at gamma frequencies has also been suggested function as a temporal coding mechanism (Borgers et al., 2005; Buzsaki and Chrobak, 1995; Fries et al., 2007; Nikolic, 2007; Tiesinga et al., 2008; Vinck et al., 2010),

since the degree of phase-locking depends on stimulus properties and brain states (Fries et al., 2008; Gregoriou et al., 2009; Lepage et al., 2011; Pesaran et al., 2002; Wu et al., 2008).

The different gamma phases on which spikes occur has also been proposed as a coding mechanism for stimulus strength (Masquelier et al., 2009). Because different phases of the gamma cycle may reflect different strength of excitation and inhibition in the local network (Hasenstaub et al., 2005; Knoblich et al., 2010), strong and weak inputs may result in different timing of output spikes within the gamma cycle (Fries et al., 2007). A study using recordings from behaving monkeys has shown that neurons in visual cortex can encode stimulus orientation in 'phase-of-firing' relative to gamma cycle (Vinck et al., 2010). However, the detailed mechanism of how the brain could decode information carried in spike phase is still unclear.

1.12.2 Binding

Although the detailed information of an object is processed by different neurons, we always perceive the object as a whole. How we generate a coherent percept given the distributed processing in the brain is known as the binding problem (Treisman, 1996; Wolfe and Cave, 1999).

Because of its sensitivity to stimulus global structure, the synchronized gamma frequency activity has been proposed to bind together the information processed in different neuronal groups or brain regions to create a coherent percept (Csibra et al., 2000; Keil et al., 1999; Singer, 1999; Singer and Gray, 1995; Uhlhaas et al., 2009). Various manipulations that

disrupt stimulus structure have been shown to affect gamma activity. Gamma band synchronization of neuronal activity is stronger when two neurons are stimulated with a single bar at their preferred orientation (Gray et al., 1989), rather than two separate bars. Gamma activity is reduced when grating stimuli are masked with noise (Zhou et al., 2008) and suppressed on the border between a figure and background compared to a homogeneous background alone (Gail et al., 2000). Power is also suppressed by plaid stimuli compared with single drifting gratings (Lima et al., 2010). These observations that gamma depends on the global structure of a visual stimuli are the basis of suggesting that gamma contributes to binding.

This binding hypothesis suggests that gamma-band synchronization of neuronal responses can link the representation of a single sensory input (e.g. a visual object) (Engel et al., 2001; Engel et al., 1997; Singer, 1999; Singer and Gray, 1995). At the heart of this proposal is the concept that gamma can influence the spike timing of a neuronal group. When different neurons are phase-locked to the same gamma rhythm, the timing of spike are more coordinated (Tiesinga et al., 2008). These synchronized spikes can have a stronger impact on downstream neurons (Konig et al., 1996; Salinas and Sejnowski, 2000, 2001).

1.12.3 Communication through coherence (CTC)

Certain frequency bands of the LFP--including but not limited to gamma--can form coherent rhythms across cortical areas and thus potentially function as a communication channel. Propagating waves have been observed in motor cortex, auditory cortex and

hippocampus (Colgin et al., 2009; Lubenov and Siapas, 2009; Reimer et al., 2011; Rubino et al., 2006; Takahashi et al., 2011). Long-range coordination of rhythms has been observed between different cortical and sub-cortical regions (Buschman and Miller, 2007; Gregoriou et al., 2009; Montgomery and Buzsaki, 2007; Popescu et al., 2009; Schoffelen et al., 2005b) and between hemispheres.

Building on these observations, the 'communication through coherence' hypothesis proposes that a coherent gamma rhythm may influence or mediate signal communication and propagation between two neuronal populations (Fries, 2005, 2009; Womelsdorf et al., 2007). Specifically, this hypothesis states that 'neuronal communication between two neuronal groups mechanistically depends on coherence between them and the absence of neuronal coherence prevents communication' (Fries, 2005). Fries proposed that because gamma phase reflects neuronal excitability, only when the two neuronal groups are coherent in a good phase relationship which means the synaptic inputs from one group arrive at the most excitatory phase of the other, will 'maximum communication efficiency' be attained only (Womelsdorf et al., 2007). This hypothesis suggests that altering the relative phase between the two neuronal groups can be used as a mechanism to selectively route information. Modeling studies have confirmed that the relative phase between two neuronal groups can effectively gate information (Tiesinga and Sejnowski, 2010). Enhanced long-range coherence has been correlated with allocation of spatial attention (Gregoriou et al., 2009). However, there is limited physiological evidence supporting the idea of coherence directly mediating communication, except for the finding

of relative phase dependent correlation between pairs of neurons (Womelsdorf et al., 2007).

1.12.4 The other side of the coin - evidence anti-gamma functions

A number of recent studies have taken a more critical view of the role of gamma, testing whether it has the properties required for its purported functions. One study showed that the frequency of gamma can vary between nearby sets of neurons, limiting its ability to function as a global timing reference (Ray and Maunsell, 2010). Another has shown that, at a single site, the gamma rhythm is not 'auto-coherent', meaning that its absolute phase changes with time, a negative feature for a reference clock or integrative signal (Burns et al., 2010b). In this vein, it is also worth noting that gamma fluctuations are small, which are roughly 10-20 microvolts on average, and account for only 0.5-10% of the total power in the LFP. These observations raise the possibility that gamma could simply be a resonant frequency that has no special function, a by-product of a recurrently connected neuronal network (Burns et al., 2010b; Ray and Maunsell, 2010; Schroeder and Lakatos, 2009).

1.13 Brain rhythms and neuronal correlation

1.13.1 Neuronal correlation and population coding

Neuronal correlation describes the phenomenon of shared fluctuations of neuronal responses, and have been widely observed in the central and peripheral nervous systems (Alonso et al., 1996; Bair et al., 2001; Cohen and Kohn, 2011; Kohn and Smith, 2005; Mastronarde, 1983; Schneidman et al., 2006; Shlens et al., 2006; Stopfer et al., 1997;

Zohary et al., 1994). Shared fluctuations in neuronal responses occur in different time scales, from many seconds to very brief timescales, more commonly referred to as synchrony. Correlations can strongly affect the encoding of information in population responses (Pouget et al., 2000).

1.13.2 Brain rhythms and neuronal correlation: an implicit relationship with synchrony

Several recent studies have reported a link between brain states and neuronal correlation (Kohn et al., 2009). Because cortical rhythms also vary with brain state, this suggests a potential relationship with neuronal correlation and the rhythms of the LFP, which we will address in the discussion session.

In general, slow timescale correlations are more prominent in the resting state, and suppressed in the active state or with stimulus drive. Studies using whole-cell and extracellular recording in barrel cortex of awake mice have shown that during the quiet wakefulness state, membrane voltage fluctuations were dominated by low frequency activity (1-5Hz) and these fluctuations are correlated with the LFP and EEG (Poulet and Petersen, 2008). The cross-correlation of membrane potential between pairs of neurons during the resting state was significantly higher than that during whisker movement (Gentet et al., 2010; Poulet and Petersen, 2008). This suggests that arousal or engagement with the environment decorrelates neuronal activity. Similar observations in behaving monkeys revealed that spatial attention can reduce neuronal correlations (Cohen and Maunsell, 2009; Fries et al., 2008; Mitchell et al., 2009). Studies in the visual cortex have

also revealed that external stimulus drive can decorrelate slow neuronal fluctuations (Kohn and Smith, 2005; Lampl et al., 1999; Smith and Kohn, 2008).

Numerous studies have reported changes of gamma activity with brain states (Jensen et al., 2007; Tallon-Baudry, 2009) and several findings have shown that gamma-band synchronization of neuronal responses is correlated with elevated gamma power in the EEG or LFP (Fries et al., 2008; Herculano-Houzel et al., 1999). During active states or with the allocation of visual attention, gamma-band neuronal synchronization is enhanced along with gamma power. Thus, unlike long-time scale correlation, neuronal correlation at gamma frequencies is enhanced during active states or external stimulus drive.

While gamma-band synchronization has been linked to changes in brain state, the relationship between brief time-scale neuronal correlation (synchrony) and brain rhythms is less clear. Indeed, there is limited evidence for a relationship between synchrony and brain rhythms or states, except for some weak or negative observations (Fries et al., 2008; Roy et al., 2007; Samonds and Bonds, 2005). Since coordinating spike timing on a millisecond timescale in a group of neurons can permit the effective summation of synaptic currents and enhance signal transmission (Bruno and Sakmann, 2006; Tiesinga et al., 2008; Usrey et al., 1998), determining whether there is a link between brain state modulation of gamma and changes in ensemble spike timing is critical for understanding the function of gamma rhythm.

1.14 Questions to be address in the thesis

This thesis seeks to elucidate the contribution of gamma to relaying signals between early visual cortical areas. To do so, we must address several limitations in our current understanding. First, we need to determine the spatial extent of gamma and how it relates to the functional properties of local neurons. Second, we need detailed and quantitative assessment of the relationship between spike timing and gamma, and how this relationship affects the timing of events in a larger, distributed neuronal ensemble. Third, we need to test directly whether gamma-associated changes in ensemble spiking have an effect on transmitting signals between synaptically-coupled networks of neurons.

My thesis addresses each of these issues in turn. Chapter 2 compares the tuning of gamma with local spiking activity and evaluates its spatial coherence under different stimulus conditions in primary visual cortex. I find there are two signals with distinct origin and response properties contributing to the detected gamma power: one is a local signal that is predictable by higher frequencies; the other is an actively generated gamma rhythm which has the potential to form a spatially extensive global rhythm. This global gamma rhythm has highly selective tuning properties and the preference of this rhythm is shared across a large cortical region. The relative contribution of the two components is flexible and depends on visual input. Therefore, the tuning properties and the spatial extent of the gamma rhythm are not fixed. Chapter 3 tests a potential mechanistic basis for the shared preference of the global gamma rhythm, using an adaptation protocol. It also presents a full characterization of the effect of prolong adaptation on other frequency bands of the LFP, revealing that each frequency band shows a distinct form of plasticity. In Chapter 4, I examine the relationship between gamma and spike timing at the level of single neurons

and a large neuronal population, and determine the consequence of this interaction on signal propagation between areas V1 and V2.

Chapter 2: Stimulus selectivity and spatial coherence of gamma components of the local field potential

Xiaoxuan Jia[1], Matthew A. Smith[3], and Adam Kohn[1,2]

[1] Dominick Purpura Department of Neuroscience

[2]Department of Ophthalmology and Vision Sciences

Albert Einstein College of Medicine, Bronx NY 10461

[3] Center for the Neural Basis of Cognition and Department of Neuroscience

University of Pittsburgh, Pittsburgh PA 15213

Acknowledgements: This work was supported by grants from the National Institutes of Health to AK (EY016774) and MAS (EY015958 and EY018894). We thank Amin Zandvakili, Stephanie Wissig, and Carlyn Patterson for assistance with data collection; Ryan Kelly for technical assistance; and members of the lab, Ruben Coen Cagli, Franco Pestilli, Jason Samonds, and Robert Shapley for comments on an earlier version of this manuscript. We are grateful to Tai Sing Lee in whose lab we recorded data from an awake behaving macaque.

This chapter is published in *Journal of Neuroscience* 2011 31, 9390-9403.

X.Jia designed and performed the experiments, except for data collection from awake monkeys. X.Jia analyzed all the data in this section.

2.1 Abstract

The gamma frequencies of the local field potential (LFP) provide a physiological correlate for numerous perceptual and cognitive phenomena and have been proposed to play a role in cortical function. Understanding the spatial extent of gamma and its relationship to spiking activity is critical for interpreting this signal and elucidating its function, but previous studies have provided widely disparate views of these properties. We addressed these issues by simultaneously recording LFPs and spiking activity using microelectrode arrays implanted in the primary visual cortex of macaque monkeys. We find that the spatial extent of gamma and its relationship to local spiking activity is stimulus dependent. Small gratings, and those masked with noise, induce a broadband increase in spectral power. This signal is tuned similarly to spiking activity and has limited spatial coherence. Large gratings, on the other hand, induce a gamma rhythm characterized by a distinctive spectral "bump", which is coherent across widely separated sites. This signal is well tuned, but its stimulus preference is similar across millimeters of cortex. Gamma thus arises from two sources that reflect different spatial scales of neural ensemble activity. Our results show that there is not a single, fixed ensemble contributing to gamma and that the selectivity of gamma cannot be used to infer its spatial extent.

2.2 Introduction

LFPs reflect coordinated synaptic input and slow intrinsic conductances in neurons (Buzsaki, 2006; Mitzdorf, 1985) and thus provide a potentially useful view of neuronal ensemble activity. Gamma components of the LFP provide a physiological correlate of perceptual and cognitive phenomena (Fries et al., 2008; Gail et al., 2004; Pesaran et al., 2002; Wilke et al., 2006; Womelsdorf et al., 2006) and have been suggested to play an active role in cortical processing.

The spatial extent and functional specificity of gamma is a critical constraint on the role it may play in cortical processing. To function as a global reference signal (e.g. an internal clock;(Fries et al., 2007; Hopfield, 2004), gamma would need to form a widespread, coherent rhythm, potentially shared among neuronal ensembles with different response properties. To select specific subsets of neurons (e.g. those representing an attended location; (Fries, 2009)), gamma would need to be limited in extent. To link distributed neurons into an ensemble (e.g. binding or dynamically routing information; Gray, 1999; (Buzsaki, 2006; Colgin et al., 2009; Gray, 1999), gamma would need to target specific subsets of cells but also be coherent across locations.

The spatial extent and functional specificity of gamma are unclear. Recently, Katzner et al. (2009) showed that the evoked LFP, a stimulus-locked transient response, reflects neural activity within 250 microns of the recording site. Xing et al. (2009) showed that this "spatial footprint" reflects the volume conduction of extracellular fields (estimated to be 250 microns) and the extent of the neural ensemble generating the signal. However,

these measures of passive propagation and the evoked LFP do not directly address the extent of gamma. This is because gamma is an induced signal—an intrinsic rhythm generated by specific neurons and circuits (see Bartos et al., 2007 and Whittington et al., 2010 for review) that are modulated by, but not time locked to, stimulus drive (Brosch et al., 2002; Juergens et al., 1999; Kruse and Eckhorn, 1996; Siegel and Konig, 2003; Tallon-Baudry, 2003).

Previous studies have provided disparate views of the extent and functional specificity of gamma. In primary visual cortex (V1), gamma is stimulus selective (Berens et al., 2008; Frien et al., 2000; Gray and Singer, 1989; Henrie and Shapley, 2005; Liu and Newsome, 2006; Siegel and Konig, 2003), suggesting that the relevant circuits have a limited extent: a spatially distributed origin would involve averaging ensembles with different preferences and should thus produce a relatively unselective signal. However, gamma has sometimes (Katzner et al., 2009; Liu and Newsome, 2006) but not always (Berens et al., 2008; Kreiman et al., 2006) been found to have the same preference as spiking activity recorded at the same site. As a result, it has been suggested to reflect activity from a few hundred microns up to millimeters of the electrode. Another approach to estimating the extent of gamma is to measure it simultaneously at different locations. This has revealed a signal that is coherent across many millimeters of cortex (Frien and Eckhorn, 2000; Juergens et al., 1999; Leopold et al., 2003) and even across regions (Murthy and Fetz, 1992; Pesaran et al., 2002; Popescu et al., 2009; Schoffelen et al., 2005a). The presence of gamma in scalp recordings also suggests a widespread coherent signal (Tallon-Baudry, 2003).

To clarify the spatial extent of gamma and its relation to neuronal activity, we measured both signals simultaneously using multielectrode arrays implanted in the superficial layers of macaque V1. We compared the response properties of gamma across locations and, at each site, with local spiking activity, for a range of stimulus manipulations.

2.3 Materials and methods

Animal preparation and electrophysiology

We recorded data from 8 anesthetized, adult male macaque monkeys (*macaca fascicularis*). The techniques we use have been described in detail previously (Smith and Kohn, 2008). In brief, anesthesia was induced with ketamine (10 mg/kg) and maintained during preparatory surgery with isoflurane (1.5-2.5% in 95% O_2). Anesthesia during recordings was maintained with sufentanil citrate (6-18 μg/kg/hr, adjusted as needed for each animal). Vecuronium bromide (0.1 mg/kg/hr) was used to suppress eye movements. Drugs were administrated in normosol with dextrose (2.5%) to maintain physiological ion balance. Physiological signs (ECG, blood pressure, SpO_2, end-tidal $C0_2$, EEG, temperature, and urinary output and osmolarity) were monitored to ensure adequate anesthesia and animal well-being. Temperature was maintained at 36-37 C°.

Data were also obtained from an awake behaving male Rhesus macaque monkey (*macaca mulatta*). Detailed methods regarding our procedures for training and recording from awake behaving macaques can be found in a previous publication (Smith et al., 2007). All procedures were approved by the Institutional Animal Care and Use Committee of Carnegie Mellon University (awake recordings only) and the Albert Einstein College of Medicine at Yeshiva University (anesthetized recordings only) and were in compliance with the guidelines set forth in the United States Public Health Service Guide for the Care and Use of Laboratory Animals.

We implanted a 4×4 mm multielectrode array (0.4 mm spacing and 1 mm electrode length) with 100 electrodes into the upper layers of primary visual cortex (roughly 0.6-0.8 mm deep in anesthetized animals; 1 mm for awake recordings), ~10 mm lateral to the midline and ~8 mm posterior to the lunate sulcus. Two reference wires were placed between the brain surface and the dura. Events larger than a user-defined threshold were recorded (Cyberkinetics Neurotechnology Systems). We applied additional voltage thresholding offline (Plexon OfflineSorter) to remove any remaining noise. Units from the same electrode were then combined to form multi-unit activity (MUA). The peak firing rate of this signal was on average 20.7±0.5 ips, suggesting it arose from a handful of neurons at most. LFPs were obtained by band-pass filtering the same signal between 0.3 Hz and 250 Hz and sampling at 1 or 2 kHz.

In some experiments, a separate linearly arranged multielectrode device (Thomas Recording) was positioned between the lunate sulcus and the array, with each electrode referenced to the guide tubes. Raw signals recorded from this device were band-pass filtered between 0.5 Hz and 250 Hz, and digitized at 1 kHz. To remove 60 Hz noise, we applied a fourth order Butterworth band-stop filter to the raw data.

Visual stimulation

Visual stimuli were generated using custom software (EXPO or Matlab Psychtoolbox) and displayed on a monitor with a resolution of 1024 by 768 pixels, viewed at a distance of 110 cm (58 cm for awake recordings). We mapped the spatial receptive field of each channel by presenting small, drifting gratings (0.6 degrees; 250 ms duration) at a range of

spatial positions. We centered our stimuli on the aggregate receptive field of the recorded units. Stimuli were viewed binocularly and presented for 1 second at full contrast. We presented each stimulus 25 times (100 times for measurements of dynamics), in a pseudorandom sequence. In awake recordings, the animal was required to maintain fixation within a 1 degree window during the 1 s stimulus presentation and to make a saccade to a random target location at stimulus offset.

For our measurements of tuning at different sizes, stimuli were viewed monocularly. In these experiments, we included only those sites whose receptive field center was within 0.5 degrees of the stimulus center. This yielded typically about half of the recorded sites, with a maximal separation of 3.57±0.02 mm on average. In our noise masking experiments, spatial noise was created by selecting small patches (0.06×0.06 degree) randomly in the original image, computing the mean luminance of each patch, and then randomly permutating the patches (Zhou et al., 2008). The noise level (20, 50 and 80%) was defined by the proportion of total area replaced by noise. Noise was randomly distributed on each frame.

Data analysis

We isolated the induced components of the LFP by subtracting the evoked signal (the average response across trials, for each stimulus) from the raw signal on each trial (Figure 2.1A). We then analyzed responses 100-1000 ms after stimulus onset, when the magnitude of the evoked component was minimal. We did this to separate these two different components of the LFP (Katzner et al., 2009), but the power spectra of the raw

LFPs (i.e. not subtracting the evoked component) were in fact similar to the induced LFPs, except at low frequencies (<20 Hz) (Figure 2.1B). All of the findings reported here were thus similar when based on raw responses, even when we included the onset transient.

We calculated the power spectrum with a multi-taper method (Mitra and Pesaran, 1999), which uses a set of orthogonal Slepian tapers to provide a good estimate of power for a limited number of trials and small time windows. For a signal of duration T and a desired half-bandwidth of W (determining the smoothness of the spectrum), the taper number is given by $k = 2TW-1$. For most of our analysis, the duration of the analyzed epoch was 0.9 s, so we used 8 tapers to provide a half-bandwidth equal to 5 Hz. For the analysis of dynamics, we used a 129 ms sliding window (25 ms steps) and 3 tapers.

Tuning of the LFP was based on its average power within 4 Hz bins, spanning the range from 0 to 160 Hz. Orientation preference was determined by the vector sum of responses to 16 test directions (22.5° step). An orientation selectivity index (OSI) was calculated as the vector sum of the response vectors (combining responses to different drift directions of the same orientation), normalized by the sum of lengths of the vectors (Leventhal et al., 1995). For computing the OSI, we defined response strength with respect to that driven (MUA) or induced (LFP) by the least preferred orientation. Using spontaneous activity as a baseline was precluded because its power could be either greater or less than the stimulus-induced power, depending on the frequency band of interest.

Only sites with an OSI larger than 0.2 for both MUA and gamma were kept for tuning related analysis (i.e. for determining the orientation preference of the site or for the correlation between tuning curves). To determine the preference of individual sites, we used the best tuned frequency band (i.e. the 4 Hz band with highest selectivity;(Berens et al., 2008) in the gamma range (30-50Hz).

We quantified the variance of orientation preferences in the population, σ^2, as:

$$1 - \frac{\sqrt{(\sum_{i=1}^{n} \cos(2\theta_i))^2 + (\sum_{i=1}^{n} \sin(2\theta_i))^2}}{n},$$

where θ_i is the orientation preference for channel i and n is the number of sites.

To determine the tuning similarity between MUA and LFP from the same channel ($r_{MUA\text{-}LFP}$, or $r_{MUA\text{-}\gamma}$ when comparing only to the gamma components) or between two LFP sites ($r_{LFP\text{-}LFP}$ or $r_{\gamma\text{-}\gamma}$), we calculated the Pearson correlation between their tuning. We found that the peak gamma frequency was lower for large gratings (Gieselmann et al., 2008) and higher for stimuli masked by noise (similar to the effect of lowering stimulus contrast; Ray and Maunsell, 2010). To enable a meaningful comparison across conditions, we therefore computed tuning correlations (and all other measures, except orientation preferences) based on the average gamma power in 30-50 Hz. We obtained similar results if our analysis was based on any sub-band in this frequency range.

To measure the spatial coherence of the LFP, we calculated the coherency between signals measured at different sites (x and y) as:

$$C_{xy}(f) = \frac{S_{xy}(f)}{\sqrt{S_{xx}(f) S_{yy}(f)}},$$

where S_{xy} is the cross-spectrum calculated with the multitaper method (duration of 0.9 s, half-bandwidth of 5Hz, and taper number of 8), and S_{xx} and S_{yy} are the respective auto-spectra (Pesaran et al., 2002). C_{xy} is a complex number. Its modulus is the coherence (ranging from 0 to 1), a measure of the relationship between two signals as a function of frequency (f). The phase of C_{xy} is the relative phase difference between the two signals, as a function of frequency.

All indications of variation in the graphs and text are standard errors of the mean (s.e.m). The statistical significance of all results was evaluated with two-tailed t-tests, unless otherwise noted. Significance of correlation values was assessed after applying the Fisher Z-transform to the data.

2.4 Results

We implanted microelectrode arrays in the upper layers of V1 of 8 anesthetized macaque monkeys and recorded spiking activity and LFPs (0.3-250 Hz) simultaneously on each electrode. Each array covered roughly a 4×4 mm cortical region, corresponding to the representation of approximately 2-3 degrees of the lower visual field (2-5 degrees from the fovea).

Orientation tuning of gamma power

To compare the tuning of gamma power to local spiking activity, we measured responses to large gratings (7.4 or 10 degrees in diameter) drifting in 16 different directions. Gratings had a spatial frequency (1 cycle/deg) and drift rate (6.25 Hz) chosen to evoke robust activity in parafoveal V1 (Foster et al., 1985). Spiking activity was isolated from the filtered voltage signal (250 Hz-10 kHz) with a user-defined threshold, and sorted offline to yield multiunit activity (MUA). Tuning of the LFP was generated by computing the power spectrum of the induced signal on each trial and measuring how power in gamma and other frequency bands depended on stimulus orientation. Consistent with previous studies, we found that the LFP was stimulus selective. An example of its tuning at one site (for frequencies between 32 and 36 Hz) is shown in Figure 2.2A, together with that of the local MUA.

We quantified tuning quality using a selectivity index, for which a value of 0 indicates an equal response to all orientations and a value of 1 indicates an elevated response to a single orientation, relative to all others. The low frequency components of the LFP were

poorly tuned, but for frequencies in the gamma range and higher (above roughly 30 Hz) selectivity was relatively high (black line in Figure 2.2B; n=680 sites in 8 implants), albeit lower than that of MUA (0.47±0.01; indicated with black dot to the right).

To quantify the similarity of LFP orientation tuning to local MUA, we computed the correlation between their tuning at each site (termed $r_{MUA-LFP}$). A value of $r_{MUA-LFP}$ near 1 indicates very similar tuning; a value near -1 would indicate the opposite. For the tuning curves in Figure 2.2A, $r_{MUA-LFP}$ was 0.22. Consistent with previous V1 studies (Berens et al., 2008; Frien et al., 2000; Siegel and Konig, 2003), we found that high frequency components of the LFP were more similarly tuned to local spiking activity than low frequency components (Figure 2.2B, red trace). However, despite the tendency for $r_{MUA-LFP}$ to increase for higher frequencies, we observed a clear deviation in the range of 30 to 50 Hz (low gamma frequencies, hereafter 'gamma'; indicated by box): tuning of gamma was relatively distinct from that of MUA. A similar effect was observed at harmonics of these frequencies (70-90 Hz) in some, but not all, implants.

To explore this further, we compared the preferred orientation of gamma and MUA at each tuned site (selectivity index$\geq$ 0.2). The two signals had a similar preference at some sites but not at others (Figure 2.2C for data from an example implant). Strikingly, this occurred because the orientation preference of gamma was often similar across sites. This is evident in the marginal histograms (Figure 2.2C) which show a roughly uniform distribution of preferences for spikes (circular variance, σ^2, of 0.73) and a clearly biased distribution for gamma (σ^2 of 0.23), with a preference of about 110 degrees being the

most common. We found a similar pattern in other implants: the distribution of preferences was consistently uniform for spikes (σ^2 of 0.75±0.03, n=8) but strongly biased for gamma (0.23±0.06; $p<<0.001$ for the difference between the two signals; Wilcoxon Rank-Sum test). The orientation preferred by gamma, however, was different in each implant.

We considered that our results might be due to anesthesia, so we recorded responses using the same type of microelectrode arrays and visual stimuli in an awake monkey (see Methods). The data are consistent with, but more striking than, those observed in anesthetized animals (Figure 2.2D). In this data set, the orientation preference of gamma was always near 60 degrees (σ^2 of 0.07) whereas simultaneously recorded MUA showed a wide range of preferences (σ^2 of 0.80).

To evaluate the cortical distance over which orientation tuning is similar for gamma and other frequency components, we computed the correlation between its tuning ($r_{LFP\text{-}LFP}$) at all selective sites and sorted the data according to the distance between electrodes (Figure 2.3A; n=31,211 pairs of sites). The value of $r_{LFP\text{-}LFP}$ was well maintained across a distance of more than 4 mm for frequencies between approximately 35 and 90 Hz. In the 30-50 Hz band, it decayed only 10.2%, from 0.69±0.01 for nearby sites (0.4-0.8 mm; n=2,233) to 0.62±0.01 at distances of 4-5 mm (n=571). At lower frequencies (<30 Hz), $r_{LFP\text{-}LFP}$ decayed more rapidly (35% over the same distance). At higher frequencies (>100 Hz), $r_{LFP\text{-}LFP}$ was significantly smaller, even for nearby electrodes, as each site had a different preference.

Because gamma tuning was similar across the entire spatial extent of the array, we performed simultaneous recordings with a separate multielectrode device (Thomas Recording) positioned roughly 3 mm away (5 penetrations in 4 monkeys). These electrodes were arranged linearly and oriented orthogonally to the nearest edge of the array, providing neurons that were 3-9 mm from those sampled by the array. We used large gratings covering the receptive fields of all neurons to induce gamma activity. The tuning measured at these additional sites had a similar preference to those measured by the array (example shown in Figure 2.3B with each square representing the preference at one recording site and the respective distributions shown in Figure 2.3C), with a difference in mean preference of 4.5±1.0 degree. The orientation preference of gamma can thus be shared over many millimeters of cortex. Note that these recordings used independent multielectrode systems, with distinct electrical references (see Methods). As a result, these observations preclude the possibility that shared tuning involved an array-specific artifact (e.g. cross-talk between electrodes) or arose from a common referencing of array electrodes (see also Berens et al., 2008 for related findings and further discussion).

Our results show that when gamma is induced by large gratings, it is orientation selective but with a preference distinct from local spiking activity and similar across millimeters of cortex. Since its tuning is distinct, its power is thus not indicative of the strength of activity in local ensembles.

Dependence of gamma tuning on stimulus size

The similar tuning of gamma we observed across sites was based on responses to large gratings. Previous studies have shown that gamma power is weakened by reducing stimulus size (Bauer et al., 1995; Gieselmann and Thiele, 2008). We therefore tested how this manipulation affects the similar tuning of gamma across sites and the relationship between its tuning and that of local spiking activity.

To determine the influence of stimulus size, we measured orientation tuning with gratings ranging from 1 to 10 degrees in diameter. Stimuli were centered on the aggregate receptive field of the MUA, as determined by a separate mapping procedure (see Methods). We analyzed only those sites driven by our smallest stimulus so that the same locations would be compared across conditions. Consistent with previous observations (Bauer et al., 1995; Gieselmann and Thiele, 2008), gamma power increased with stimulus size (Figure 2.4A), nearly doubling over the range measured. In contrast, the spiking activity at these sites was suppressed by stimuli larger than 1 degree (Figure 2.4A), as expected given the prevalence of surround suppression in V1(Angelucci and Bressloff, 2006).

We found that the relationship between the orientation tuning of MUA and gamma depended strongly on stimulus size. When driven with small gratings (1 deg), gamma power had a similar preference to MUA at all sites, as shown in Figure 2.4B for a single implant. When stimulated with larger gratings (10 deg), the preference of gamma changed: it became more similarly tuned across sites, and its preference at many sites

became distinct from the local MUA (Figure 2.4C). Across our data set, we found $r_{\gamma\text{-}\gamma}$, the tuning similarity of gamma, increased strongly with stimulus size (Figure 2.4D), from 0.11±0.01 to 0.50±0.01 (n=2,961 pairs of sites in 3 implants). The similarity between the tuning of MUA and gamma ($r_{MUA\text{-}\gamma}$), on the other hand, decreased from 0.42±0.03 to 0.25±0.03 (n=129 sites), indicating these two signals became more distinct for large stimuli. Although the preference of gamma changed dramatically with stimulus size, its selectivity did not: the mean selectivity for small stimuli was 0.31±0.01 compared to 0.37±0.01 for large gratings, a small but statistically significant *increase* in tuning quality for the more global signal (p=0.007).

Our results show that gamma has a different preference for small stimuli (i.e. one matched to local spiking activity) and large ones (i.e. one shared across sites). This suggests that gamma does not reflect ensemble activity of a fixed extent. The shared preference we observed across millimeters of cortex, when gamma is induced by large stimuli, suggests a spatially-extensive mechanism underlying the signal. For small stimuli, the close match between the preference of spiking activity and gamma measured at the same site strongly suggests a local basis for the signal. Note that small gratings activated roughly 10 mm^2 of cortex, but the preference of gamma matched the spiking activity at each measured location. Thus, the close match between the preferences of these two signals is not a trivial consequence of small gratings only driving circuits near a particular electrode.

Two components of gamma power

The change in the tuning of gamma with stimulus size was paralleled by a change in the form of the LFP spectra. Small gratings induced a broadband (20-160 Hz) increase in power, which was stronger for some orientations than others (Figure 2.5A). The preference for gamma frequencies was similar to that of both higher (>50 Hz) and nearby lower (20-30 Hz) frequencies. Large gratings induced a notable increase in power at gamma frequencies, which strongly exceeded the power of both high and lower (20-30 Hz) frequencies (Figure 2.5B; Gieselmann et al., 2008; Ray and Maunsell, 2010). The tuning of this gamma "bump" was often distinct from neighboring frequencies, suggesting a distinct origin.

We estimated the strength of the broadband component of gamma using an exponential fit to the power measured between 20-26 and 80-160 Hz (outside the range of gamma; dashed lines in Figures 2.5A and 2.5B). For activity induced by small stimuli, this fit captured 92±2% of the variance in the spectra over the 20-160 Hz range. The gamma power estimated by this fit was 87±1% of that measured, and it was strongly correlated with the measured gamma across orientations ($r=0.64\pm0.02$). The remaining power—that exceeding this prediction—we refer to as the gamma bump. The broadband component of gamma decreased for larger stimuli (Figure 2.5C), much like spiking activity (Figure 2.4A); the gamma bump, on the other hand, grew with stimulus size (Figure 2.5C). The proportion of total gamma power attributable to the bump thus increased with stimulus size (Figure 2.5D).

To compare the tuning of these two components of gamma and their relationship to local

spiking activity, we calculated $r_{MUA-\gamma}$ and $r_{\gamma-\gamma}$ separately for each component (Figure 2.5E and F). We found that the gamma bump for large stimuli (for which it was most accurately measured) had a similar preference across sites ($r_{\gamma-\gamma}$ of 0.56±0.007) and thus a distinct preference from local spiking activity ($r_{MUA-\gamma}$ of -0.01±0.04). The broadband component of gamma, on the other hand, was always similarly tuned to local spiking activity ($r_{MUA-\gamma}$ ranging 0.50 to 0.62) and thus tuning across sites was only weakly correlated ($r_{\gamma-\gamma}$ ranging from 0.18 to 0.24).

We conclude that there is a component of gamma that arises from broadband changes in power. This component behaves similarly to local spiking activity. Large stimuli induce a second component, which has a shared preference across millimeters of cortex. The flexible relationship between the tuning of gamma and local spiking activity, revealed by changes in stimulus size, can be explained by the relative contribution of these two components to total gamma power.

Manipulations that do not alter stimulus size can also change the preference of gamma

Manipulating stimulus size shows that the preference of gamma and its relationship to local spiking activity are flexible, but leaves unclear when gamma is likely to display a shared preference across sites. It could be that shared tuning involves mechanisms that are recruited whenever an extensive region of cortex is visually driven, as with large gratings. Alternatively, shared tuning may occur because of the gamma bump induced by such stimuli. If so, manipulations that reduce the power of this component—without altering the extent of visually-driven cortex—would be expected to result in tuning

similar to that of local multiunit activity.

To distinguish between these possibilities, we manipulated gamma power by masking large gratings with noise (Zhou et al., 2008). This manipulation had a limited effect on V1 firing rate, with the response evoked by unmasked gratings and those masked with 80% noise being nearly indistinguishable in strength (dashed trace, Figure 2.6A): the mean firing rate across stimuli was 8.9±0.7 spikes/s for unperturbed grating compared to 8.4±0.7 for those masked with 80% noise (n=248 sites in 3 implants). With high levels of noise, however, gamma power was reduced more than two-fold (Figure 2.6A; from a normalized value of 0.99±3E-4 to 0.42±5E-3; n=248 sites; see (Lima et al., 2010) for related findings). This was due primarily to a loss of the gamma bump, as evident in the small proportion of the total power provided by this component with high masking noise (Figure 2.6B).

The relationship between the tuning of gamma and local spiking activity depended on the strength of masking noise. Figure 2.6C shows the orientation preference for one array at three noise levels. For unmasked gratings (0% noise; top panel), the preference of gamma was similar across sites (σ^2 of 0.12 and $r_{\gamma\text{-}\gamma}$ of 0.67) and distinct from local multiunit activity ($r_{MUA\text{-}\gamma}$ of 0.15). With high masking noise (80% noise; lower panel), the tuning of the two signals became more similar ($r_{MUA\text{-}\gamma}$ of 0.56) and, thus, the preference of gamma was no longer shared across sites (σ^2 of 0.59 and $r_{\gamma\text{-}\gamma}$ of 0.33). Across implants, as masking noise was increased, $r_{\gamma\text{-}\gamma}$ decreased from 0.74±3E-3 to 0.48±2E-3; $p<<0.001$; n=8,911 pairs of sites) and gamma became more similarly tuned to the local MUA ($r_{MUA\text{-}\gamma}$

increased from 0.14±0.02 to 0.46±0.02; $p<<0.001$; n=228 sites).

These results show that noise masking disrupts the gamma bump induced by large stimuli and results in gamma whose tuning is similar to local spiking activity. Compared to manipulations of stimulus size, masking required a larger decrease in gamma power to generate a signal with similar preference to local spiking activity: it is only at the highest level of masking noise, when the gamma bump is nearly entirely suppressed (Figure 2.6B), that the two signals become more similarly tuned. Thus, while the trends for size and noise masking manipulations are similar, the point at which gamma switches from a shared preference to a local one is different. This is presumably because of numerous differences in the drive provided by these two stimuli. Nevertheless, our masking results clearly show that the change in the tuning of gamma does not *require* reducing stimulus size or the spatial extent of activated cortex.

To test further the flexible relationship between the tuning of gamma and local spiking activity, we made use of the slow build-up of induced gamma after stimulus onset (Bauer et al., 1995; Ray and Maunsell, 2010). We analyzed responses to large gratings drifting in different directions, with interleaved blank stimuli, using a sliding window (129 ms epoch length with 25 ms steps). Gamma power increased soon after stimulus onset (Figure 2.7A, vertical dashed line) but reached its maximum roughly 250 ms later, on average (n=683 sites). The proportion of power attributable to the gamma bump reached its maximum at a similar time, but its onset was delayed, revealing that the initial enhancement of gamma reflects a broadband increase in power (Figure 2.7B).

During the initial epoch of the response (25-154 ms after stimulus onset; Figure 2.7C, top), gamma tuning was well matched to the local spiking activity ($r_{MUA-\gamma}$ of 0.47) and had a wide range of preferences (σ^2 of 0.87). In later epochs, gamma tuning changed to a common preference across sites (σ^2 of 0.25 for the epoch from 350-479ms). Across implants, we found that $r_{\gamma-\gamma}$ increased markedly over the first few hundred milliseconds of response (from 0.47±2E-3 to 0.71±2E-3; $p<<0.001$; Figure 2.7D, gray line). Over the same period, $r_{MUA-\gamma}$ fell more than two-fold (from 0.35±0.01 to 0.14±0.02; $p<<0.001$; Figure 2.7D, black line). The relationship between the tuning of gamma and local MUA is thus dynamic, and these dynamics mirror the relative contribution of the gamma bump to its total power.

In conclusion, there are two components to stimulus-induced increases in gamma power, and the relative weight of these determines the relationship between gamma tuning and that of local spiking activity. Stimuli that induce strong gamma bumps (large, unperturbed gratings) result in similar tuning across sites and a preference that is distinct from that of local MUA. Small gratings, or those masked with noise, induce gamma that arises from a broadband increase in power, resulting in a signal with similar tuning to the local spiking response. Similarly, the dynamic relationship between the tuning of gamma and local spiking activity reveals that as the contribution of the gamma bump to total gamma power increases, the preference of gamma switches from that of the local MUA to a common orientation across sites.

Spatial coherence of the gamma rhythm

When gamma power is high and the spectral bump prominent, tuning is similar across sites. This suggests that under these conditions the preference of locally measured signals arises from a shared rhythm. To test this directly, we measured the spatial coherence and phase difference of gamma across sites, for different stimulus conditions. A shared gamma rhythm would be indicated by higher coherence and smaller phase offsets.

We computed the coherence between signals induced by both large and small stimuli (n=2,961 pairs; averaging across different stimulus orientations), using the same set of driven sites. Small gratings (1 degree) induced a small increase in gamma coherence, relative to spontaneous conditions, with a limited spatial extent of roughly 2 mm (Figure 2.8A, left column, and 2.8B). Large gratings induced a more substantial increase in coherence and signals were also more phase aligned (Figure 2.8A; right column). This enhanced coherence extended across all measured distances (Figure 2.8B), and decayed more slowly for large gratings than small ones (exponential decay with a space constant of 1.6 mm, compared to 1.0 mm for small gratings). The enhanced coherence for activity induced by large gratings was strongest for the shared, preferred orientation (data not shown).

We also compared coherence for large, unperturbed gratings with those masked with noise. Gamma coherence was weaker and more localized for signals induced by masked gratings (Figures 2.8C, left column, and 2.8D; n=9,891 pairs). For 80% masking noise, coherence was nearly indistinguishable from that measured under spontaneous conditions

(without stimulus drive), although gamma and spiking responses were selective for such stimuli (as evidenced by the enhanced value of $r_{MUA-\gamma}$ in Figure 2.6).

Our coherence analysis suggests that large gratings induce a single, global gamma rhythm with little phase lag across sites. If so, gamma activity should be maintained after averaging the signals recorded at different sites on each trial—a signal we term the global LFP. Figure 2.9A shows single-trial examples of the global LFP induced by large (10 deg; top) and small (1 deg; bottom) gratings of the same orientation, averaged across the same sites. The large stimulus induced a prominent gamma rhythm; this was absent from the signal induced by the small stimulus. This result was not due to an undue influence of the signal recorded at a few electrodes, as Z-scoring the LFP before averaging yielded essentially identical results. We quantified the power in the global LFP for all frequencies and stimulus sizes we presented (n=3 implants; Figure 2.9B). For small gratings, gamma components of the global LFP had minimal power. For larger stimuli, however, power in the gamma band increased nearly six fold over the range measured. Other frequency bands did not show this behavior. The global LFP showed strong orientation selectivity for gamma power induced by large but not small stimuli (Figure 2.9C). Across implants (n=3), the selectivity of the gamma component of the global LFP was 0.32±0.08, comparable to the selectivity at each individual site (0.37±0.01), and its preferred orientation closely matched the mean preference of signals measured at individual sites (mean offset of 1.7±0.7 degrees; n=8 implants).

Together these results show that the gamma measured at each electrode reflects a

spatially extensive rhythm, when activity is induced by large but not small gratings. The power in this signal is stronger for some orientations than others, giving rise to a common preference across sites. A potential explanation for the extensive coherence of gamma induced by large stimuli is that it reflects volume conduction, which could in principle explain its similar tuning across sites as well (i.e. if the signal measured by each electrode reflects a spatial average of distantly-generated gamma signals). Several pieces of evidence argue against this. First, recent estimates of volume conduction suggest it is limited to 250 microns (Logothetis et al., 2007; Xing et al., 2009), roughly 20-fold smaller than the extent of spatially coherent gamma that we observe. Consistent with this, annular gratings induce no gamma power at sites where spiking activity is not elevated (Gieselmann and Thiele, 2008; Jia and Kohn, personal observations), showing that gamma from distant sites does not passively propagate over large distances. Second, because high-amplitude signals should conduct more effectively (i.e. remain measurable despite the attenuation associated with passive propagation through the extracellular space), one would expect low frequencies to be more coherent than gamma frequencies, as their power is substantially higher (Figure 2.1B). However, when induced by large gratings, gamma was slightly more coherent than low frequencies (Figure 2.8A; mean of 0.599±0.002 for gamma vs. 0.583±0.002 for frequencies <10 Hz), although gamma power was 26-fold lower. Note also that the change in the preference and coherence of gamma with stimulus conditions involved roughly two fold changes in power (Figures 2.4A and 2.6A). It seems unlikely that this would result in a signal whose tuning was different at sites separated by 400 microns, in one case, but shared up to 9 mm in another. Third, when a strong gamma rhythm is induced, spike-spike coherence in gamma

frequencies is elevated across the array (Jia et al., 2011). Since volume-conducted fields have little influence on membrane potential—compared to those locally generated—the enhanced coordination of neuronal activity argues strongly against an important contribution of volume conduction (Bauer et al., 2007). Fourth, if the gamma rhythm induced by large gratings involved simple volume conduction of distant signals, one would expect little or no selectivity, because each site would represent the average of locally-generated signals with different preferences. In fact, tuning was more selective for gamma induced by large gratings than small ones (as described above).

A neural representation bias underlies the preference of the global gamma rhythm

We have shown that large stimuli induce a spatially extensive gamma rhythm that is both well-tuned and has a common preference across millimeters of cortex. We wondered why some orientations would induce a stronger rhythm than others, over such a large region. One possibility is that this preferred orientation reflects or magnifies a small bias in the neuronal representation of orientation. An obvious source for this bias would be the purported systematic overrepresentation of cardinal orientations in primary visual cortex (Li et al., 2003). However, we observed a shared preference for non-cardinal orientations in a number of implants, such as those in Figures 2.2C and D. Alternatively, the shared preference could arise from an inhomogeneous representation within a more limited region, such as the bias seen in fMRI voxels which are orientation-tuned despite reflecting activity averaged over several (or even many) cubic millimeters (Haynes and Rees, 2006; Kamitani and Tong, 2005).

We attempted to detect this potential representational bias with our neuronal recordings, by comparing the preference of the gamma induced by large gratings to the most common preference of the spiking activity detected by our array. Figure 2.10A shows the range of MUA preferences from one array (σ^2=0.88; n=89 sites, arranged according to their position on the array), measured with large gratings. Figure 2.10B shows the orientation preference of gamma from the same array, with its characteristic narrow distribution of preferences (σ^2=0.26). In this implant, there is no obvious relationship between the preference distribution of gamma and that of the recorded spiking responses: the preferred orientation of gamma is near 0 degrees, but there is no bias for this orientation in the spiking responses. We quantified this relationship by computing the correlation between the population-averaged tuning of MUA and gamma, after normalizing the data for each site by the maximal response. For the example implant, this correlation was 0.28 (Figure 2.10C). Across implants the mean correlation was 0.27±0.24 (n=8), not significantly different from zero (p=0.72). We were thus unable to detect a bias in the spiking representation of orientation that could underlie the shared preference of gamma. However, this failure is perhaps not surprising given the limited sample of recording sites provided by the array.

Because we could not observe a relationship between the preferences of the sampled spiking activity and the shared orientation preference of gamma, we took advantage of the biased preference of V1 neurons in spatial and temporal frequency. We tested our explanation for the shared preference of gamma in an additional, independent manner: by measuring tuning for grating spatial and temporal frequency. Whereas the representation

of orientation would be expected to be at most weakly biased, neuronal preferences for spatial and temporal frequency are well known to be non-uniformly distributed (Foster et al., 1985; Hawken et al., 1996; O'Keefe et al., 1998). We reasoned that if a biased representation underlies the preference of gamma, its tuning for spatial and temporal frequency should be similar both across sites and implants.

We measured tuning using large gratings drifting at a fixed drift rate (6.25 cycles/s) and with spatial frequencies ranging from 0.1-8.6 cpd, or with a fixed spatial frequency (1 cpd) and a range of drift rates (0.3-25 cycles/s). Sites for which the minimal response was not at least 50% smaller than the peak response were deemed untuned (Foster et al., 1985; 6.3% of 567 MUA sites for spatial frequency and 9.6% of 732 MUA sites for temporal frequency). At selective sites, MUA often had high pass or low pass tuning (Figure 2.11C, D; 7.9% and 9.1%, respectively, for spatial frequency; and 10.3% and 36.0% for temporal frequency), defined as a response at the lowest or highest measured frequency that was larger than 75% of the peak response (Levitt et al., 1994; Movshon et al., 2005). At the remaining bandpass sites, we estimated the preference based on the fit of a difference-of-Gaussians function to the data. MUA had a wide range of spatial and temporal frequency preferences (Figures 2.11C, D).

Unlike the tuning of MUA, gamma power had bandpass tuning for both stimulus parameters at almost all sites (Figure 2.11A and B; 99.8% of sites for spatial frequency tuning and 97.8% for temporal frequency). There were no untuned gamma sites. Remarkably, gamma preferences for spatial and temporal frequency were similar across

sites and implants (Figure 2.11C and D). For instance, across 567 sites recorded in 7 implants, 86% of sites preferred a spatial frequency between 1 and 3 cpd; for MUA, these preferences were most common but they accounted for only 29% of sites. The similarity of spatial and temporal frequency tuning of gamma, across sites and implants, is consistent with its preference arising from the biased representation for these stimulus features.

2.5 Discussion

To determine the spatial extent of gamma and its relationship to spiking activity, we recorded LFPs and MUA simultaneously in the upper layers of macaque V1. We found that gamma could have similar tuning to local spiking activity, when it reflected a broadband increase in power. Under other conditions, gamma could form a coherent, spatially extensive rhythm with similar tuning across millimeters of cortex. This latter behavior was evident for stimuli that induced a distinct spectral bump, a signal that grew slowly after stimulus onset and that could be disrupted by reducing stimulus size, or using masking noise. Our results suggest two distinct components to gamma power, with very different relationships to neuronal activity. The relative weight of these two components is stimulus dependent, resulting in a flexible relationship between the tuning of gamma power and local spiking activity.

This flexible relationship offers an explanation for previous disparate findings. Some previous comparisons of the tuning of gamma and local MUA have found matched preferences, but others have not. This has lead to estimates that gamma reflects activity within 250 microns up to 3 mm of the electrode (Berens et al., 2008; Gray and Singer, 1989; Liu and Newsome, 2006); (Kreiman et al., 2006). Our findings show stimulus conditions under which each of these descriptions is accurate. Similarly, studies of the relationship between gamma and the BOLD fMRI signal have found both strong correlation ((Goense and Logothetis, 2008; Kayser et al., 2004) and a weak one (Maier et al., 2008, who used briefly flashed noise stimuli). These differences could be explained by the two components of gamma we observe, assuming the global gamma rhythm is

more directly related to the macroscopic measurement afforded by BOLD. More generally, our results emphasize that one must carefully consider stimulus properties—and the relative weight of broadband increases in power to the spectral bump—in understanding and interpreting the behavior of gamma.

When induced by large gratings, gamma is coherent over millimeters of cortex, consistent with previous studies (Frien and Eckhorn, 2000; Juergens et al., 1999; Leopold et al., 2003). Despite this spatial extent, it remains remarkably well tuned. Our observations thus reconcile previous work emphasizing the extent of gamma coherence with seemingly inconsistent claims that gamma is well tuned. Importantly, our results show that inferring the spatial extent of gamma rhythms from their selectivity is problematic: a well-tuned signal does not mean a local one. Only by measuring tuning and coherence across sites—a novel feature of our study—can one accurately determine the extent and functional specificity of gamma rhythms.

Our findings do not contradict recent reports that the evoked LFP reflects neural activity within 250 microns of recording site (Katzner et al., 2009) and that the passive propagation of extracellular fields has a similarly limited spatial extent (Xing et al., 2009). We focused on an induced signal whose extent is influenced by passive propagation but ultimately determined by the circuits generating it. Katzner et al. (2009) did compare the orientation tuning of the induced and evoked LFP and concluded they were similar. However, activity was driven by brief stimuli (32 ms) which do not induce a strong gamma rhythm (Figure 2.7; see also (Kruse and Eckhorn, 1996)). To be sure that our

different conclusions concerning induced gamma were not due to other factors, we recorded responses to similarly brief (40 ms) presentations and confirmed that the induced gamma power is weak, contains little evidence of a bump, and that both this signal and the evoked response are similarly tuned to local MUA (data not shown), entirely consistent with Katzner et al. (2009).

A previous study by Berens et al., 2008, conducted in awake macaque V1 using large gratings, reported findings similar to a subset of ours. Namely, they found that the orientation preference of gamma was similar across nearby sites (separated by 1 mm or less) and inferred that gamma reflects activity within 500-1000 microns of the electrode tip, due to a combination of extensive circuits generating the rhythm and the volume conduction of those signals. Our interpretation differs from theirs in part because we show that gamma power consists of two components. Shared tuning across sites is not a fixed property of gamma; it occurs only when a prominent bump is induced. Further, our data suggest that when tuning is similar across sites, this is not due to simple volume conduction of nearby signals (for reasons described in Results), but rather because of the formation of a spatially extensive, coherent rhythm. Our different interpretation arises because we considered a wider range of stimulus manipulations (size, noise masking, dynamics, and spatial and temporal frequency), sampled across a roughly 10-fold higher range of distances, and because we analyzed both coherence and tuning across sites.

Berens et al. (2008) also reported that the selectivity of gamma is positively correlated with its similarity to local spiking activity. They propose that this relationship reflects the

spatially extensive ensemble contributing to gamma and whether the recording site is situated in an iso-orientation domain (similar preference to MUA and high selectivity) or at a pinwheel center. We observe a similar relationship between selectivity and the match to local MUA (Jia and Kohn, unpublished observations), even when gamma was induced by large gratings and extends over many pinwheels. In this case, the correlation may arise because when gamma preference is matched to local spiking activity, the gamma bump and its broadband component will have a similar preference; at sites where gamma is different from local spiking activity, these two components will have different preferences, resulting in weaker selectivity.

Mechanisms

The mechanisms of gamma generation have been studied extensively, both in the hippocampus and neocortex. GABAergic interneurons have been shown to play a critical role in generating gamma (Atallah and Scanziani, 2009; Bartos et al., 2007; Cardin et al., 2009; Hasenstaub et al., 2005; Traub et al., 1996a; Whittington et al., 2010; Whittington et al., 1995), and this is perhaps enhanced by interactions with excitatory neurons (Buzsaki, 2006; Tiesinga and Sejnowski, 2009). In cortex, 'chattering cells' may also contribute (Cunningham et al., 2004b; Gray and McCormick, 1996).

These mechanisms do not appear to contribute strongly to the gamma induced by small stimuli and large, masked gratings, or at response onset. This is because gamma in these cases reflects a broadband increase in power, rather than a mechanism specific to gamma frequencies (see also Ray and Maunsell, 2010). Instead, the broadband increase in power

likely arises from a general elevation of synaptic and spiking activity in local circuits because this signal behaves similarly to local MUA (e.g. similar orientation tuning and suppression by large gratings). This component of gamma may also include direct spectral contamination of the LFP by spiking activity, although previous work suggests this is limited to frequency components above 50 Hz (David et al., 2010; Zanos et al., 2011).

The traditional inhibitory (or excitatory-inhibitory) mechanisms of gamma generation presumably do underlie the spectral bump we observe for activity induced by large stimuli. However, the global nature of this rhythm suggests additional spatially extensive mechanisms that coordinate or drive this inhibitory network. One possibility is that this involves feedback connections, which extend over long distances and are thought to contribute to the surround suppression recruited by large stimuli (Angelucci and Bressloff, 2006; Bair et al., 2003). Alternatively, the global gamma rhythm may be an emergent rhythm that involves the coordination of local generators through mechanisms such as long-range lateral connections or gap-junction coupling among inhibitory neurons (Buzsaki, 2006; Tiesinga and Sejnowski, 2009). Finally, the global gamma rhythm may arise from an altered balance between excitatory and inhibitory activity in cortex, because inhibitory cells may be only weakly surround suppressed (Brunel and Wang, 2003; Haider et al., 2010).

Whichever mechanisms contribute, they must be more effective for some stimuli than others, a property we suggest may be due to biased representations for these features (e.g.

stronger feedback or an enhanced local representation). An intriguing possibility is that this bias involves a recently described over-representation of orientations corresponding to the radial position of the spatial receptive fields (a radial bias; Freeman et al., 2011). The sites we recorded represented similar positions in the visual field across animals, so one might expect to observe similar preferences. However, the gratings we used were positioned slightly differently in each animal, and given the proximity of our recordings to the fovea. These small differences could alter the net bias in the recruited population. These explanations for our findings are, of course, speculative and additional work is needed to address the mechanisms underlying the novel properties of gamma we report.

Functional role of gamma rhythms

Through its suggested influence on spike timing, gamma has been proposed to provide a temporal window for communication (Fries, 2009), encode the amplitude of stimulus drive in response phase (Fries et al., 2007), bind distributed representations (Gray, 1999), or dynamically route information (Colgin et al., 2009; Fries, 2009; Pesaran et al., 2002). The spatially extensive, coherent gamma rhythm we observe seems better suited for an integrative function than one that requires targeting specific subsets of neurons. For instance, the gamma induced by a large vertical grating is similar at sites where neurons prefer vertical or horizontal structure. Thus, it could not be expected to emphasize or group specific subset of neurons. Only when gamma power is limited (reflecting a broadband increase in power), is it spatially and functionally selective. However, precisely because it is weak, it is unlikely to have a strong influence on spike timing under these conditions (Okun et al., 2010; Sohal et al., 2009).

As an integrative signal, the global gamma rhythm could, in principle, function as an internal reference. For instance, it seems well suited to modulate spike timing in a large region of cortex. However, this rhythm is much stronger for some stimuli than others, in a patch of cortex representing several degrees of visual field. Unless perceptual performance is similarly biased, this would suggest a limited functional role, at least for stimulus-induced gamma activity in V1. Under this interpretation, the global gamma rhythm may simply be a resonant frequency arising from the interaction between excitation and inhibition (Burns et al., 2010b; Ray and Maunsell, 2010), albeit one that can reflect a much more extensive ensemble than previously considered.

2.6 Figure legends

Figure 2.1 Evoked and induced components of the LFP. (**A**) Single epoch examples of the raw LFP (top) and the induced component (bottom). The induced component is calculated by subtracting the evoked component (middle) from the raw signal. (**B**) Example of the power spectrum of the induced LFP (red), compared to the raw LFP (black). Spontaneous activity was measured with a uniform luminance screen (gray dashed).

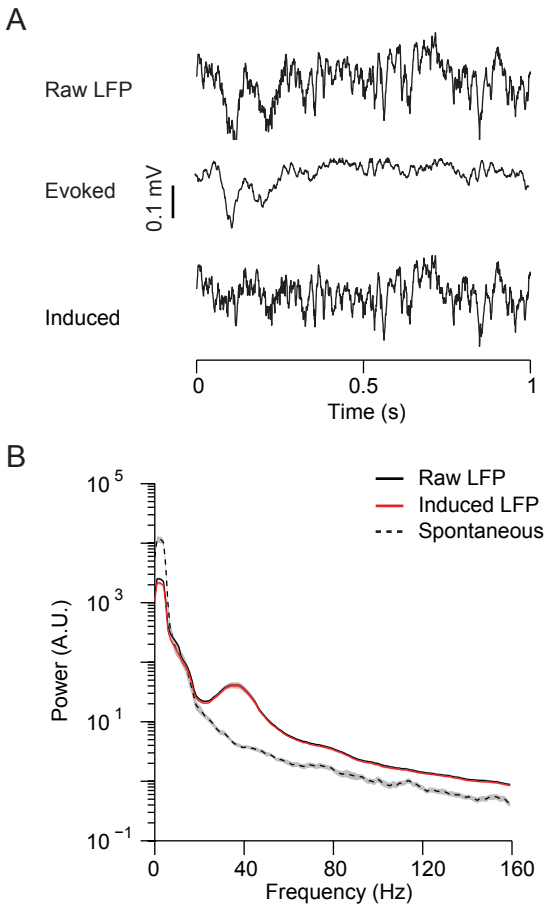
A
Raw LFP
Evoked
0.1 mV
Induced
0
0.5
1
Time (s)
B
Raw LFP
Induced LFP
Spontaneous
10 5
10 3
10 1
10 −1
Power (A.U.)
0
40
80
120
160
Frequency (Hz)

Figure 2.2 Comparison of the orientation tuning of the LFP with local spiking activity. (**A**) Example tuning curves for MUA (black) and gamma power (gray) at the same site (n=25 repeats). (**B**) Population average trends for LFP orientation selectivity (black) and correlation between the tuning of MUA and the LFP ($r_{MUA\text{-}LFP}$; red), as a function of frequency (n=680 sites). The mean orientation selectivity index for MUA is indicated to the right side (black dot). (**C**) Comparison of orientation preferences for gamma and MUA (n=71 sites from one implant). The circular variance (σ^2) of the distributions was 0.23 for gamma and 0.73 for MUA. (**D**) Similar example for data from an awake monkey (n=79 sites).

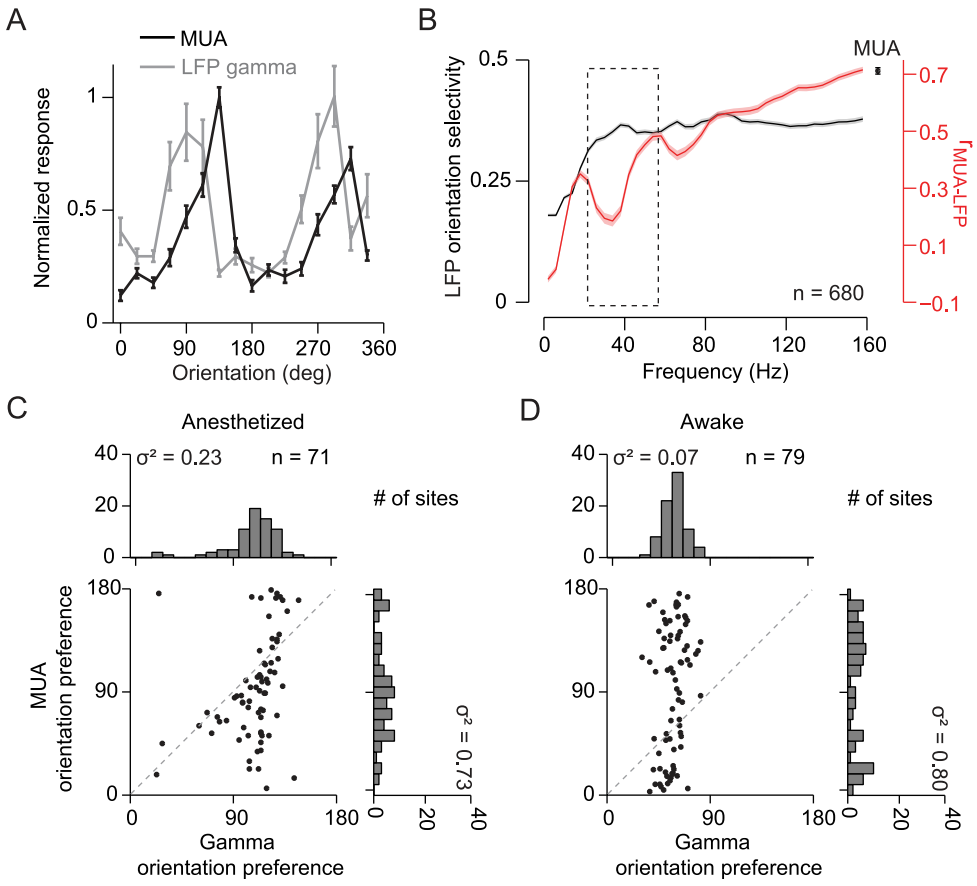
A
MUA
LFP gamma
Normalized response
1
0.5
0
0
90
180
270
360
Orientation (deg)
B
MUA
LFP orientation selectivity
0.5
0.25
0
0.7
0.5
0.3
0.1
−0.1
rMUA-LFP
n = 680
0
40
80
120
160
Frequency (Hz)
C
Anesthetized
σ² = 0.23
n = 71
# of sites
40
20
0
MUA
orientation preference
180
90
0
0
90
180
Gamma
orientation preference
σ² = 0.73
0
20
40
D
Awake
σ² = 0.07
n = 79
# of sites
40
20
0
180
90
0
0
90
180
Gamma
orientation preference
σ² = 0.80
0
20
40

Figure 2.3 Relationship between orientation tunings of the LFPs measured at different sites. (**A**) Population average of $r_{LFP\text{-}LFP}$ as a function of distance, for sites with orientation selectivity ≥ 0.2. Cross-sections of the color plot for distances of 0.4-0.8 mm (n=2,233 pairs) and 3.6-4.0 mm (n=1,347 pairs) are shown on the right. (**B**) An example of orientation preference in the gamma band, from simultaneously recording using two multielectrode systems. Each square represents the orientation preference of one recording site, plotted according to its position of the recording sites. (**C**) Distributions of orientation preference for the example in (**B**).

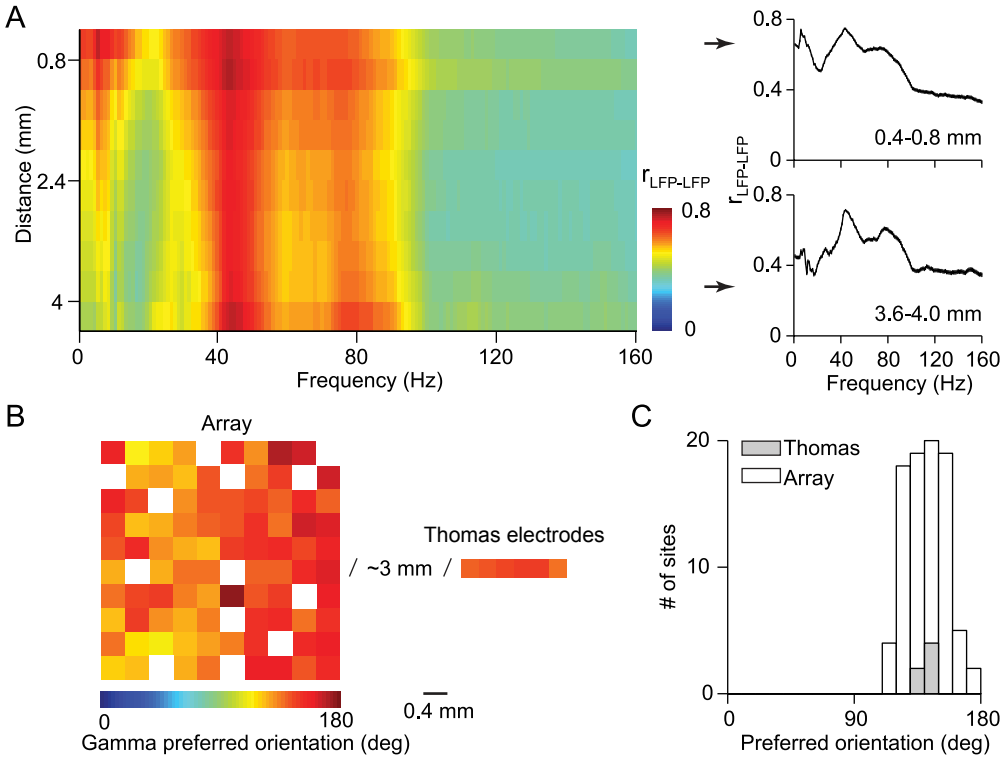
A
Distance (mm)
0.8
2.4
4
0
40
80
120
160
Frequency (Hz)
r LFP-LFP
0.8
0
0.8
0.4
0
0.4-0.8 mm
3.6-4.0 mm
Frequency (Hz)
B
Array
Thomas electrodes
~3 mm
0.4 mm
0
180
Gamma preferred orientation (deg)
C
20
10
0
# of sites
Thomas
Array
0
90
180
Preferred orientation (deg)

Figure 2.4 Effect of stimulus size on gamma power and its tuning. (**A**) Normalized firing rate (dashed trace) and gamma power (solid black trace) as a function of stimulus size. Data are shown only for sites driven by the smallest stimulus (n=129 sites; n=2,961 pairs). (**B**) Comparison of orientation preference for activity driven by a 1 deg grating (n=57 sites), for a single implant. The preference of gamma was similar to the MUA at all sites, and the distribution of preferences had a similar variance (0.85 and 0.74, respectively). (**C**) Orientation preferences for the same sites as (B) but when stimulated with a large grating (10 deg). Gamma preferences dissociated from MUA and became more uniformly tuned, with circular variance equal to 0.32. (**D**) Dependence of $r_{MUA\text{-}\gamma}$ (solid trace; n=129 sites) and $r_{\gamma\text{-}\gamma}$ (dashed trace; n=2,961 pairs) on stimulus size.

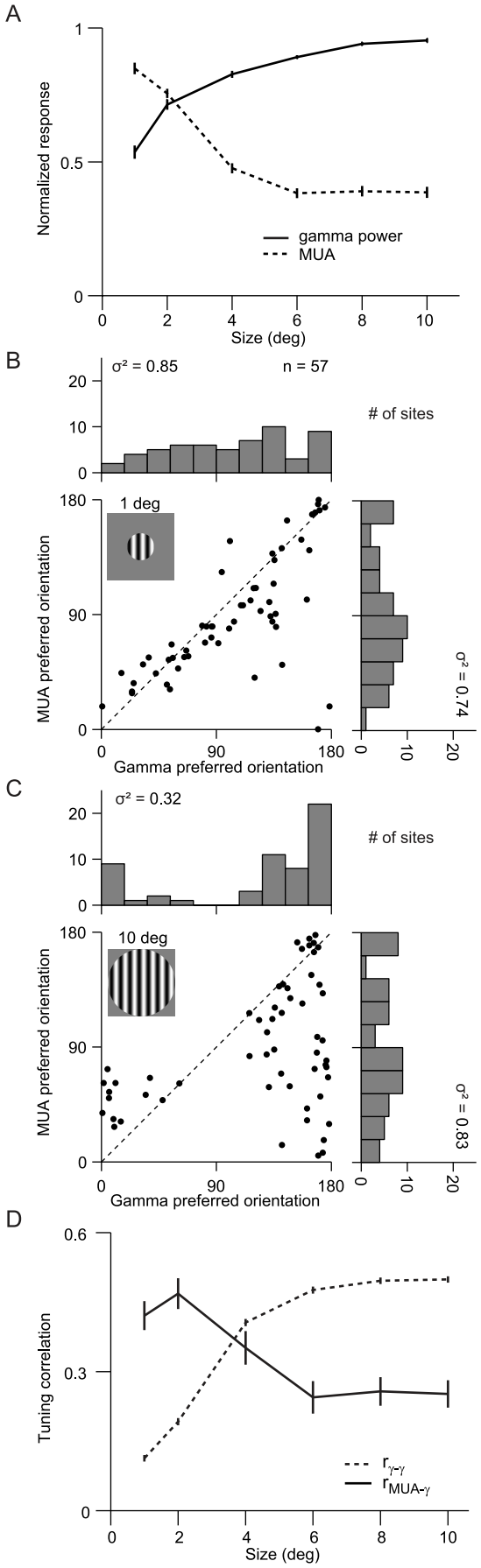
A
Normalized response
1
0.5
0
0
2
4
6
8
10
Size (deg)
gamma power
MUA
B
σ² = 0.85
n = 57
# of sites
20
10
0
1 deg
MUA preferred orientation
180
90
0
0
90
180
Gamma preferred orientation
σ² = 0.74
0
10
20
C
σ² = 0.32
# of sites
20
10
0
10 deg
MUA preferred orientation
180
90
0
0
90
180
Gamma preferred orientation
σ² = 0.83
0
10
20
D
Tuning correlation
0.6
0.3
0
0
2
4
6
8
10
Size (deg)
r γ-γ
r MUA-γ

Figure 2.5 Two components of gamma power and their dependence on stimulus size. (**A, B**) Power spectra of LFPs from one recording site, for large (10 deg; A) and small (1 deg; B) stimuli for two orientations (red and black lines) and spontaneous activity (gray lines). Estimate of broadband component of gamma power is provided by the exponential fit indicated with dashed lines. (**C**) Normalized power of the gamma bump and broadband component, as a function of stimulus size (n=129 sites). (**D**) Proportion of total power attributable to the gamma bump. (**E, F**) Dependence of $r_{MUA-\gamma}$ (solid trace; n=129 sites) and $r_{\gamma-\gamma}$ (dashed trace; n=2,961 pairs), for the gamma bump (E) and broadband component (F), on stimulus size.

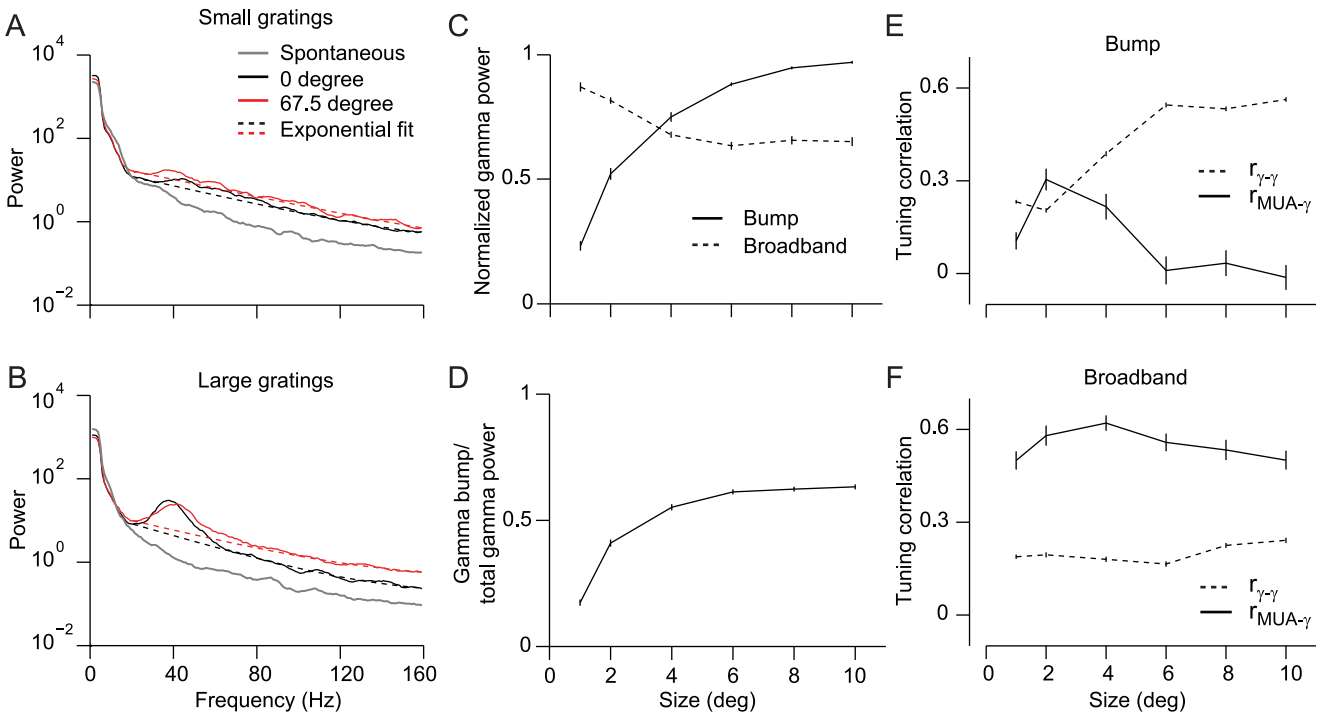
A
Small gratings
Spontaneous
0 degree
67.5 degree
Exponential fit
Power
B
Large gratings
Frequency (Hz)
C
Normalized gamma power
Bump
Broadband
D
Gamma bump/
total gamma power
Size (deg)
E
Bump
Tuning correlation
$r_{\gamma-\gamma}$
$r_{MUA-\gamma}$
F
Broadband

Figure 2.6 Masking noise modulates gamma power and its tuning. (**A**) Effect of masking noise on normalized gamma power (solid black trace; n=248 sites) and firing rate (dashed trace). (**B**) Proportion of total power attributable to the gamma bump. (**C**) Comparison of orientation preference of gamma and MUA for 3 noise levels (n=76 sites in one array). Gamma is more dissociated from local spiking activity when the gamma bump is more prominent. (**D**) Dependence of $r_{MUA\text{-}\gamma}$ (solid trace; n=228 sites) and $r_{\gamma\text{-}\gamma}$ (dashed trace; n=8,911 pairs; error bars are smaller than the line thickness) on the amount of masking noise. Stimuli size is 10 degrees. Representation of stimuli is shown at the bottom.

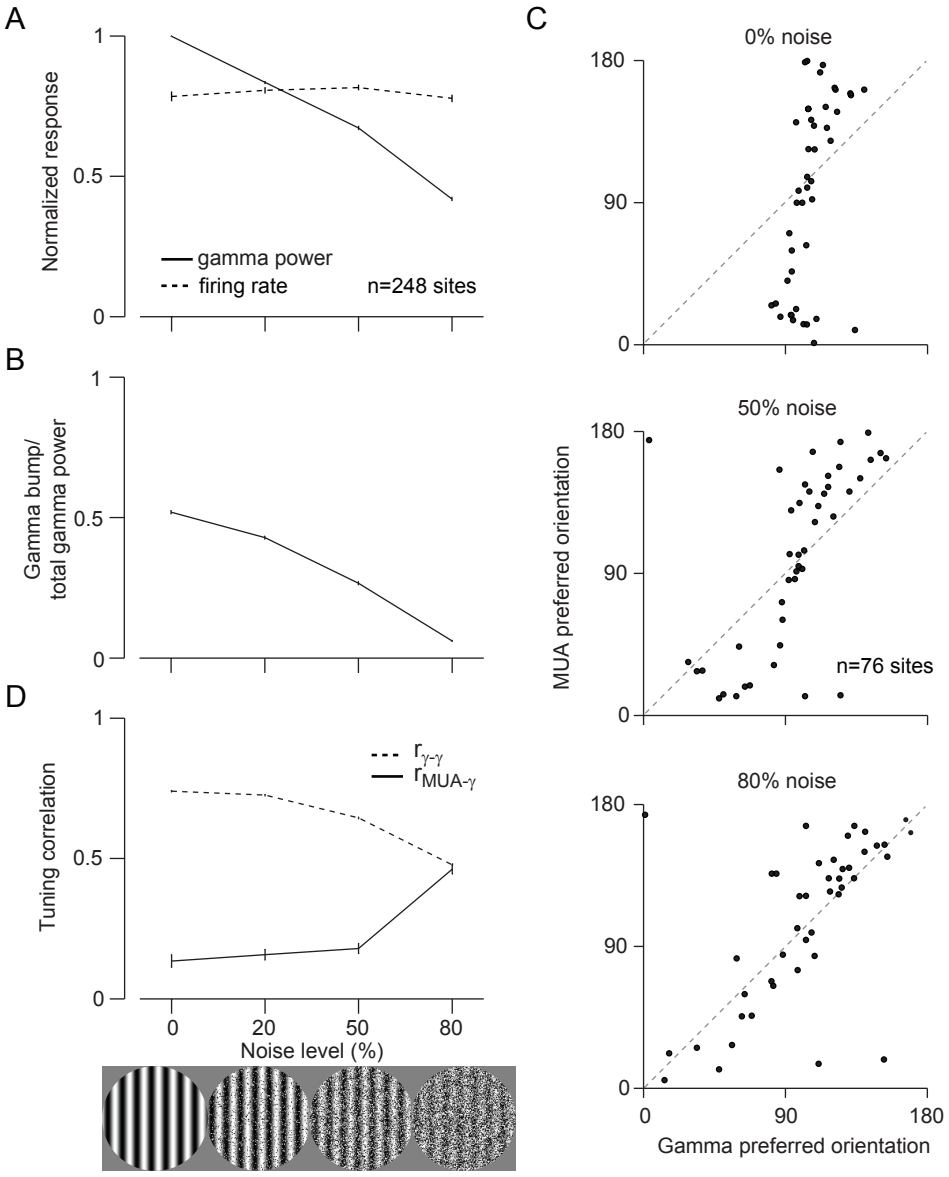
A
Normalized response
1
0.5
0
gamma power
firing rate
n=248 sites
B
Gamma bump/
total gamma power
1
0.5
0
D
Tuning correlation
1
0.5
0
$r_{\gamma-\gamma}$
$r_{MUA-\gamma}$
0
20
50
80
Noise level (%)
C
0% noise
180
90
0
50% noise
MUA preferred orientation
n=76 sites
80% noise
0
90
180
Gamma preferred orientation

Figure 2.7 Dynamics of gamma power and its tuning. (**A**) Population average of normalized gamma power, as a function of time relative to stimulus onset (n=683 sites; error bars are smaller than the line thickness). Power peaks around 250 ms after stimulus onset. Each point represents the center of one epoch (129 ms window). Dashed vertical line, to facilitate comparisons across plots, indicates time bin centered at 14.5 ms. (**B**) Dynamics of the proportion of total power attributable to the gamma bump. (**C**) Orientation preference of gamma and MUA for epochs 25-254ms, 225-354ms and 350-479ms after stimulus onset (n=86 sites). (**D**) Dynamics of $r_{MUA\text{-}\gamma}$ (black; n=683 sites) and $r_{\gamma\text{-}\gamma}$ (gray trace; n=29,870 pairs; error bars are smaller than the line thickness). Negative values indicate time before stimulus onset.

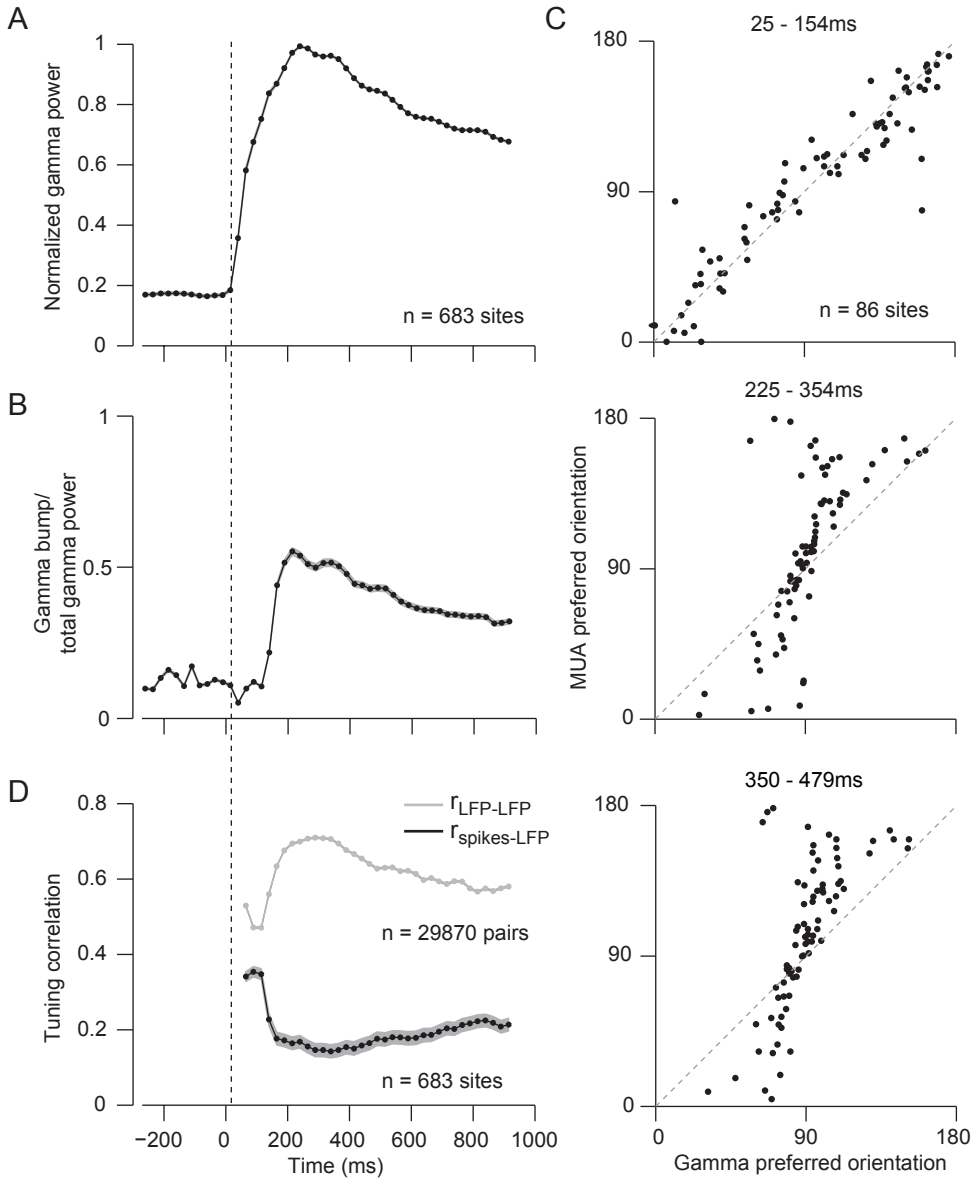
A
Normalized gamma power
1
0.8
0.6
0.4
0.2
0
n = 683 sites
B
Gamma bump/
total gamma power
1
0.5
0
D
Tuning correlation
0.8
0.6
0.4
0.2
0
r LFP-LFP
r spikes-LFP
n = 29870 pairs
n = 683 sites
−200
0
200
400
600
800
1000
Time (ms)
C
25 - 154ms
180
90
0
n = 86 sites
225 - 354ms
MUA preferred orientation
180
90
0
350 - 479ms
180
90
0
0
90
180
Gamma preferred orientation

Figure 2.8 Dependence of gamma coherence and phase alignment on distance. (**A**) Coherence (upper panels) and absolute phase difference (lower panels) of the LFP, as a function of the distance between recording sites (n=2,961 pairs). Results are shown for signals induced by small gratings (1 degree; left) and large gratings (10 degrees, averaged across stimulus orientations; right). Gamma coherence is weak and has a limited spatial extent when stimuli are small; gamma coherence increases markedly in both magnitude and spatial extent when stimuli are large, especially for the preferred orientation, and gamma activity shows a smaller phase difference across sites. (**B**) Coherence of gamma (averaged across orientations) induced by 1, 4 and 10 degree gratings as a function of distance between recording sites, as compared to that observed in the absence of visual stimulation (spontaneous; dashed line). Error bars, where not visible, are within the line thickness. (**C**) Coherence (upper panel) and absolute phase difference (lower panel) of LFPs induced by 80% noise masked large grating (n=9,891 pairs; left) and unperturbed large gratings (right). (**D**) Coherence of gamma induced by 50% and 80% noise masked and unperturbed gratings as a function of distance, compared to that observed for spontaneous activity.

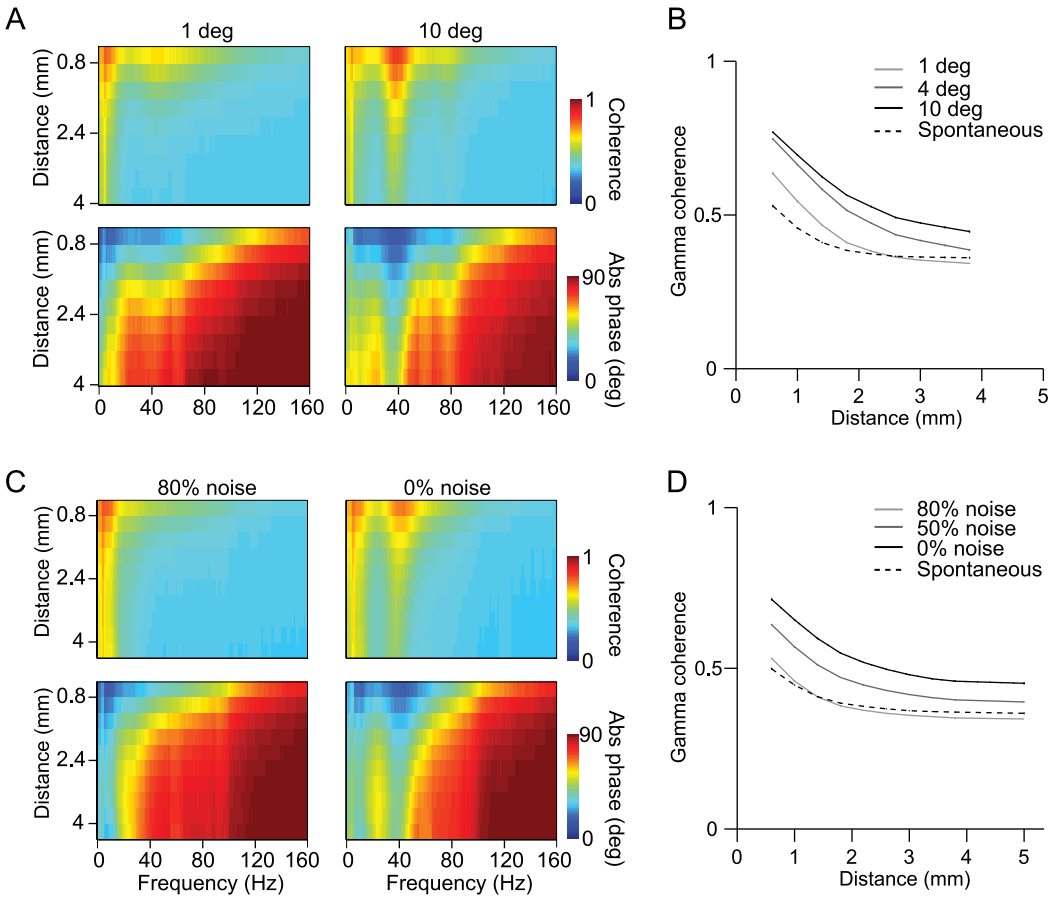
A
1 deg
10 deg
Distance (mm)
0.8
2.4
4
Coherence
1
0
Abs phase (deg)
90
0
0
40
80
120
160
B
1 deg
4 deg
10 deg
Spontaneous
Gamma coherence
0.5
Distance (mm)
C
80% noise
0% noise
Frequency (Hz)
D
80% noise
50% noise
0% noise
Spontaneous

Figure 2.9 The global LFP. (**A**) Single trial examples of the global LFP averaged across 31 sites of one implant, for activity induced by a large (upper) and small (lower) stimulus of the same orientation. Insets show the power spectrum of the signal. (**B**) Average of the global LFP power spectra for different sizes (n=3 implants). Value indicated is the average across orientations. (**C**) Orientation tuning of the gamma component of the global LFP, for 10 degree (upper) and 1 degree (lower) stimuli of an array implant.

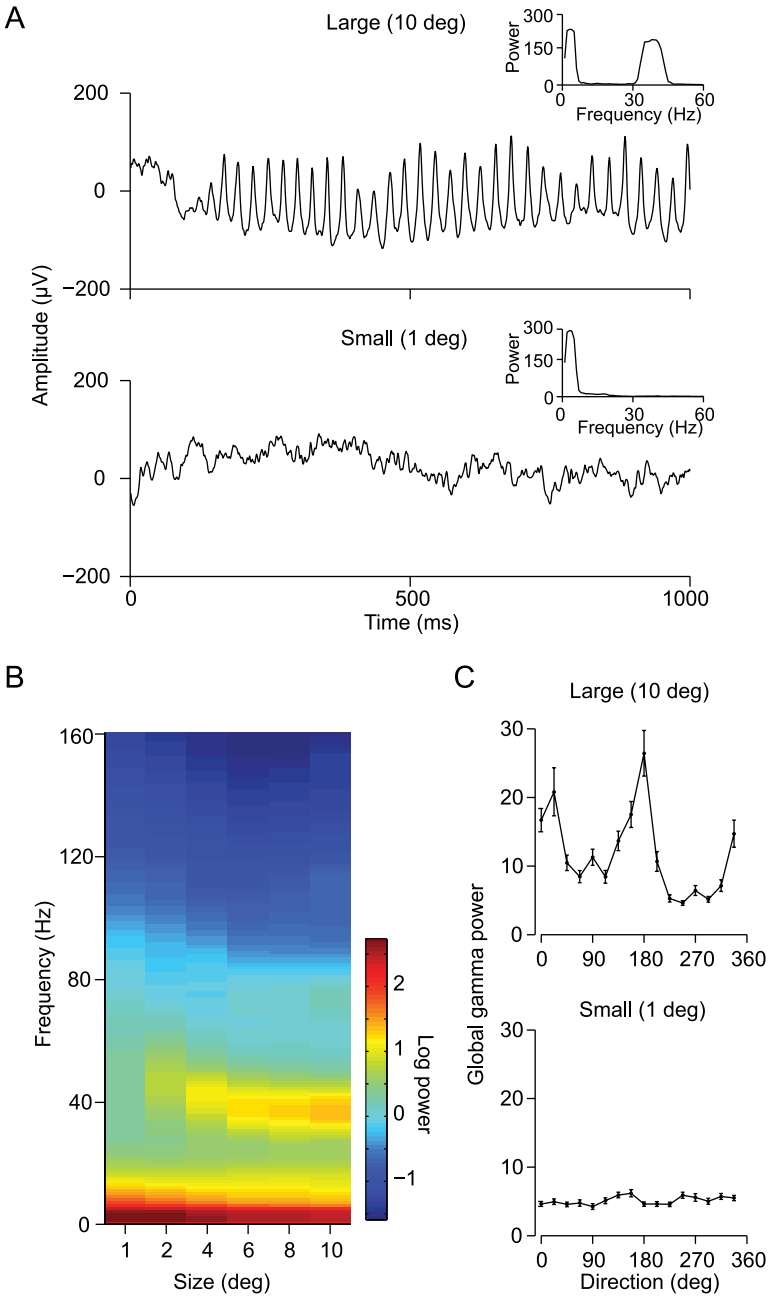
A
Large (10 deg)
Power
300
150
0
0
30
60
Frequency (Hz)
200
0
−200
Amplitude (μV)
Small (1 deg)
Power
300
150
0
0
30
60
Frequency (Hz)
200
0
−200
0
500
1000
Time (ms)
B
160
120
80
40
0
Frequency (Hz)
1
2
4
6
8
10
Size (deg)
2
1
0
−1
Log power
C
Large (10 deg)
30
20
10
0
0
90
180
270
360
Global gamma power
Small (1 deg)
30
20
10
0
0
90
180
270
360
Direction (deg)

Figure 2.10 Relationship between neuronal preferences sampled by the array and the preference of gamma. (**A**) MUA orientation preferences plotted according to electrode positions on the array (left) and corresponding distribution (right). (**B**) Gamma preferences from the same array as (**A**) and their distribution (n=86 sites). (**C**) Population tuning curve of MUA (dashed) and gamma (solid) calculated by averaging normalized tuning curves of all sites from the same array. The two tuning curves are only weakly related, with a correlation of 0.28.

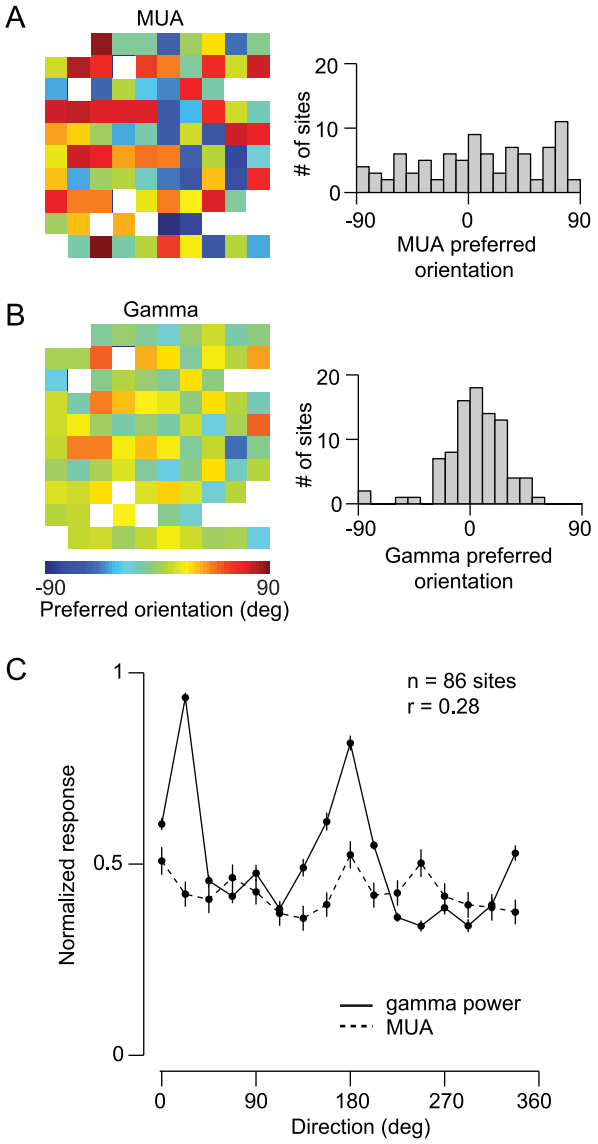
A
MUA
20
10
0
# of sites
-90
0
90
MUA preferred orientation
B
Gamma
20
10
0
# of sites
-90
0
90
Gamma preferred orientation
-90
90
Preferred orientation (deg)
C
n = 86 sites
r = 0.28
1
0.5
0
Normalized response
gamma power
MUA
0
90
180
270
360
Direction (deg)

Figure 2.11 MUA and gamma tuning for stimulus spatial and temporal frequency. (**A**) An example of gamma tuning for spatial frequency for a single site. (**B**) Same as (**A**) for temporal frequency tuning. (**C**) Distribution of spatial frequency preferences across all implants (567 sites from 7 implants), for tuned sites of MUA (top) and gamma (bottom). (**D**) Same as (**C**) for temporal frequency preferences (732 sites from 9 implants).

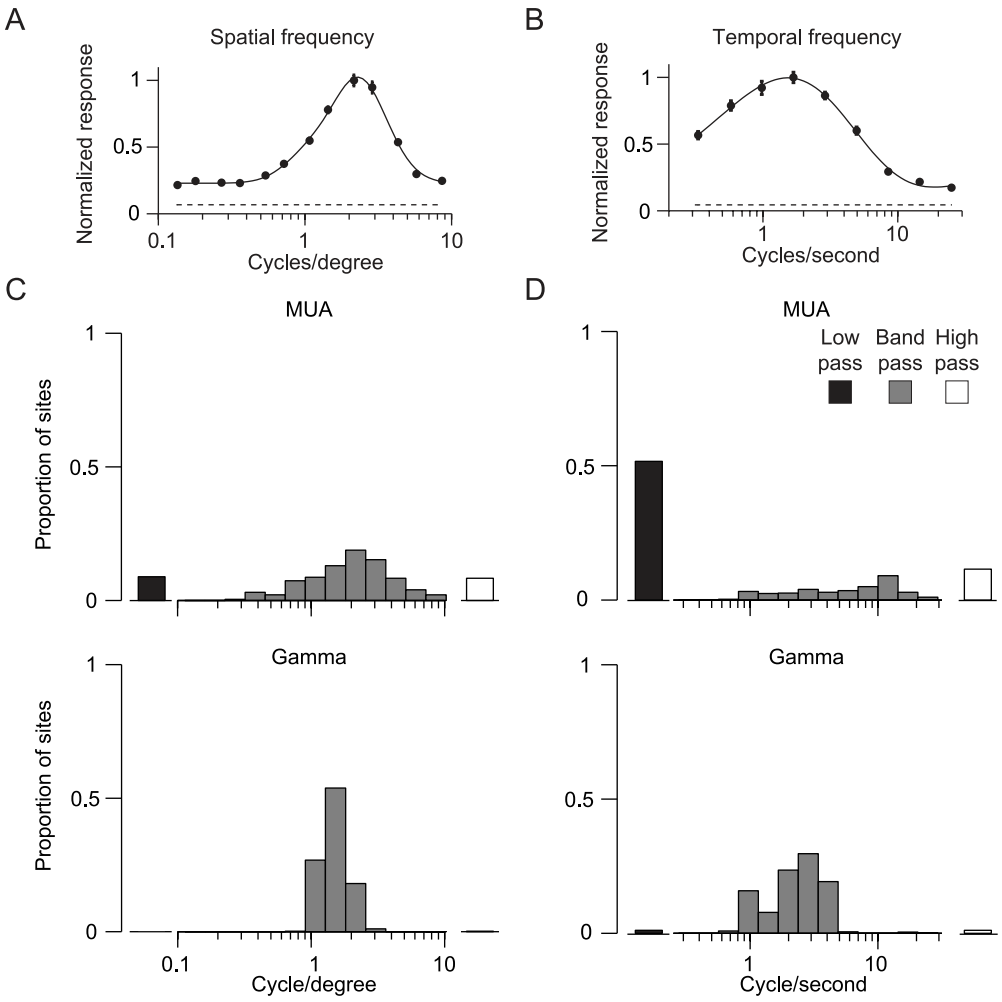
A
Spatial frequency
Normalized response
1
0.5
0
0.1
1
10
Cycles/degree
B
Temporal frequency
Normalized response
1
0.5
0
1
10
Cycles/second
C
MUA
Proportion of sites
1
0.5
0
Gamma
Proportion of sites
1
0.5
0
0.1
1
10
Cycle/degree
D
MUA
Low pass
Band pass
High pass
1
0.5
0
Gamma
1
0.5
0
1
10
Cycle/second

2.7 Appendix I – Peak frequency shifts in the gamma band

X.Jia designed and performed the experiments, analyzed data in this section.

2.7.1 Introduction

In Chapter 2, we have shown that when stimulus size increases, gamma power (especially power in the spectrum peak) increases monotonically. The signal that contributes to the spectral bump in the gamma frequency has the potential to form a spatially extensive global rhythm which is selective for stimulus orientation. This is accompanied by a peak frequency shift in the gamma range (30-50 Hz).

Previous studies have shown that with enlarging stimulus size the peak frequency in the gamma range of the power spectrum shifts lower while gamma power increases monotonically (Gieselmann and Thiele, 2008; Kang et al., 2009). Lowering stimulus contrast also makes the peak frequency in the gamma range shift lower (Ray and Maunsell, 2010), as well as causing a decrease in gamma power (Henrie and Shapley, 2005). Here, we would like to test whether there is a link between the changing gamma power and peak frequency with size and contrast manipulations that have been used previously and the noise masking stimulus, which we have shown decreasing gamma power with increasing noise level.

2.7.2 Materials and methods

Same as method section in Chapter 2.

2.7.3 Results

We found a decrease of peak frequency when gamma became more spatially extensive with enlarging gratings (Figure 2.12A). It has been proposed that the generation of gamma rhythm could include involve recurrent connection between excitation and inhibition and also feedback from higher cortical regions (Kang et al., 2009). This model predicts that as more feedback is recruited by enlarging a stimulus, the resonance frequency in gamma range will shift lower. Alternatively, with our finding of the spatial extent change in gamma rhythm, the peak frequency could reflect the average conduction delay time in the network generating gamma, with a larger network recruiting more long-range connections to generate a global rhythm.

Because the global rhythm can also be disrupted by adding masking-noise to the large gratings, I next checked the peak frequency change in the gamma band with different noise masking conditions. Noise masking affected peak frequency in a different way compared to stimulus size: as gamma power decreased, the peak frequency shifted to lower frequencies (Figure 2.12B), similar to the effect of lowering stimulus contrast (Figure 2.12C) (Ray and Maunsell, 2010).

These results suggest that the neural network that gives rise to the gamma rhythm changes similarly with noise-masking and lowing contrast. The opposite trend of gamma power and peak frequency shifts for size manipulation and the noise and contrast manipulations suggest that there is no fixed relationship between the gamma strength and its peak frequency. Modeling how oscillation strength and frequency change with these

manipulations could be a productive way to understand the properties of gamma rhythm and its relationship to excitation, inhibition and conduction delays.

2.7.3 Figure legends

Figure 2.12 Peak frequency shifts in the gamma range with different stimulus manipulations. (**A**) Power spectra of LFP for gratings of different sizes (n=236 sites). (**B**) Power spectra of LFP for different levels of noise-masking (n=248 sites). (**C**) Power spectra of LFP for different stimulus contrasts (n=91 sites).

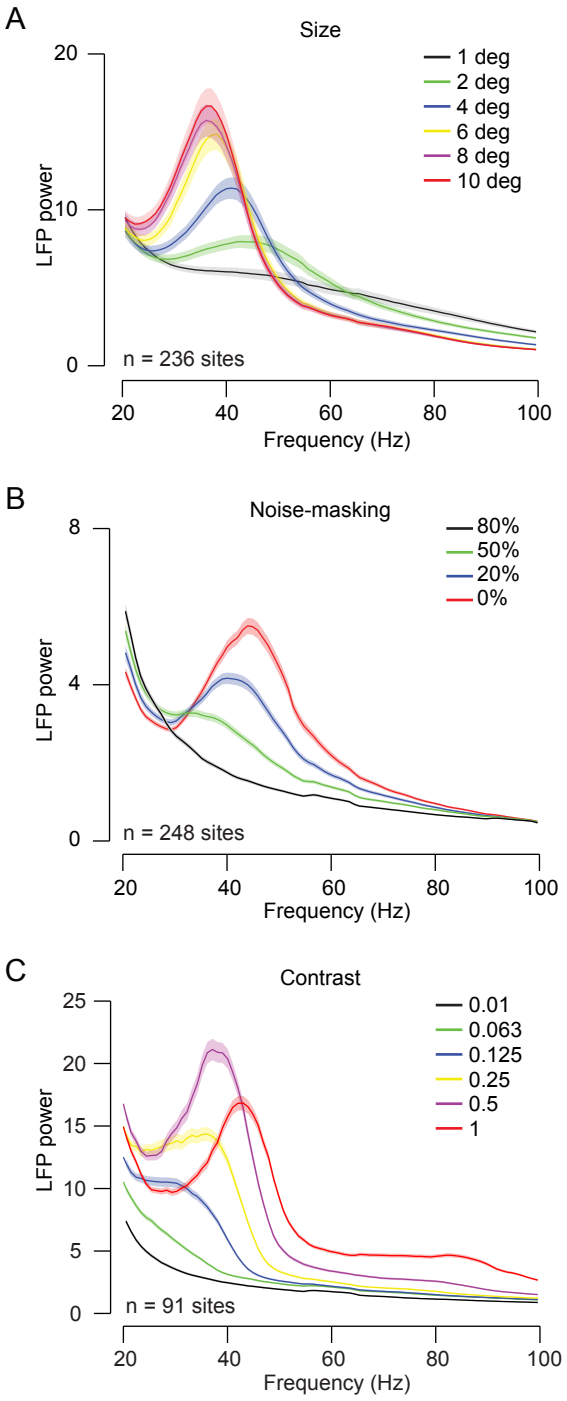
A
Size
1 deg
2 deg
4 deg
6 deg
8 deg
10 deg
LFP power
20
10
0
n = 236 sites
20
40
60
80
100
Frequency (Hz)
B
Noise-masking
80%
50%
20%
0%
LFP power
8
4
0
n = 248 sites
20
40
60
80
100
Frequency (Hz)
C
Contrast
0.01
0.063
0.125
0.25
0.5
1
LFP power
25
20
15
10
5
0
n = 91 sites
20
40
60
80
100
Frequency (Hz)

2.8 Appendix II – Effects of stimulus position on gamma tuning

X.Jia designed and performed the experiments, analyzed data in this section.

2.8.1 Introduction

In Chapter 2, we described a surprising orientation tuning phenomenon in the gamma band (30-50Hz) of the LFP which shows shared tuning across large cortical regions (~16 mm2) when stimulated with full contrast large gratings. The basis of the common preference is unclear. We propose that the preference of the global gamma rhythm reflects a neural representational bias based on the two following findings. First, the tuning of gamma for stimulus spatial and temporal frequency, across sites and implants in different animals, was nearly identical and had a preference consistent with that most common for neurons in early visual cortex (Foster et al., 1985), which is illustrated in Chapter 2, figure 2.12. Second, in Chapter 3, we show that the orientation tuning of gamma is extremely sensitive to the bias in the neuronal responses introduced by adaptation. Together, these results indicate that the preference of gamma may magnify a bias in the neural response and that this bias can be significantly and transiently altered by recent experience.

It has been suggested that V1 neurons over represent horizontal and vertical orientations , which could underlie the psychophysical phenomenon of 'oblique effect' (Li et al., 2003). However, we did not to observe a consistent preference for cardinal orientations in the global gamma rhythm. One possibility is that this inhomegeneity in preference across different implants could reflect an inhomogeneous representation of orientation within

the activated V1 region, which is not necessarily the cardinal orientation. Alternatively, the fact that gamma has a range of preference could be related to the proposal that the oblique effect in V1 neurons is an inadequate description of its coarse preference of a radial bias, that is neurons tend to prefer orientations specified by its angular-position relative to the fovea on the retinotopic map of V1 (Freeman et al., 2011).

2.8.2 Method and results

To test the alternative hypothesis, we recorded from neurons with receptive fields 2-5 degrees from the fovea, in the lower visual field (typically with an azimuth and elevation of 2,-2) with multielectrode arrays. We used large gratings (10 degree) to induce the global gamma rhythm. We then manipulated the position of the large grating with respect to the center of the aggregate receptive field of the array, which is about 2-3 degree, accordingly, while always covering receptive fields of the array, as illustrated in Figure 2.13A.

We found that altering the location of a large stimulus in the visual field caused orderly shifts in the common orientation preference of the global gamma rhythm (Figure 2.13B, C). More specifically, when the position of the large grating was moved rightward, the general preference of gamma shifted toward 90 degree, whereas when the position of the grating was moved leftward, the general preference of gamma shifted toward 180 degree.

The position of the visual field we recorded from relative to the fovea is illustrated in Figure 2.14A. When the array is implanted in the left hemisphere, the neurons we

recorded from the array are viewing (through a mirror) the right visual field indicated with a circle labeled RF. According to Freeman et al, the prediction made of the radial bias that RFs closer to the vertical meridian have an orientation bias towards 90 degree (e.g. prefer vertical gratings), whereas RFs closer to the horizontal meridian would have a tendency to prefer 180 degree on the left hemisphere and 0 degree on the right hemisphere. As a result, when activating different parts of the visual field with large gratings, the vector sum of the radial bias covered by the large grating shifts smoothly. With gratings shifting rightward, the radial bias shifts towards 90 degree and with gratings shift leftward, the radial bias shifts towards 180 degree (Figure 2.14B).

A radial bias could potentially explain our observation of the smooth shift of gamma preference accordingly with the position of large gratings (Figure 2.13B). A further test of the radial bias theory in generating the orientation selectivity of the global gamma is to compare the gamma preference from implants in the left and right hemispheres. For 22 implants, we observe a general tendency for the gamma orientation preference to concentrate in the 0-90 degree for right hemisphere implants and a tendency to concentrate in the 90-180 degree for left hemisphere implants (Figure 2.15). However, since our recording location is very close to the fovea, where the radial bias is noisier than in more peripheral regions (Freeman et al., 2011), our results can only demonstrate a possibility but cannot confirm the radial bias hypothesis in the generation of gamma preference.

In summary, our results of orientation preference in the global gamma could be related to the recent finding of Freeman et al that the representation of stimulus orientation has a radial bias. We were originally skeptical of this because, although we record at similar locations across animals, we find a range of preferred orientations for the global gamma rhythm. However, our experiments use large gratings, which always cover the RF of the recorded cells but which can be positioned slightly differently in different animals. Thus, the bias in the activated region of cortex can vary.

2.8.3 Figure legends

Figure 2.13: The orientation preference of global gamma depends on the spatial location of the visual stimulus. (**A**) To test further whether the common orientation preference of the gamma rhythm reflects a bias in the responding neural population, we presented large gratings (10 degrees in diameter) at different locations in the visual field (represented by black circle). The numbers to the left indicate the offset between the center of the stimulus and that of the aggregate neuronal receptive field of all recording sites from the same implant. The stimulus always covered all of the neuronal receptive fields (indicated by the red oval). We reasoned that since the population responding to the stimulus would differ across locations, with some overlap, the bias should change as well. (**B**) Distributions of orientation preference for gamma. Each row corresponds to the preference measured for a particular location. There is a clear shift in the most commonly preferred orientation, from roughly 135 degrees in the top histogram to 180 degrees in the bottom. (**C**) A similar phenomenon for a second implant.

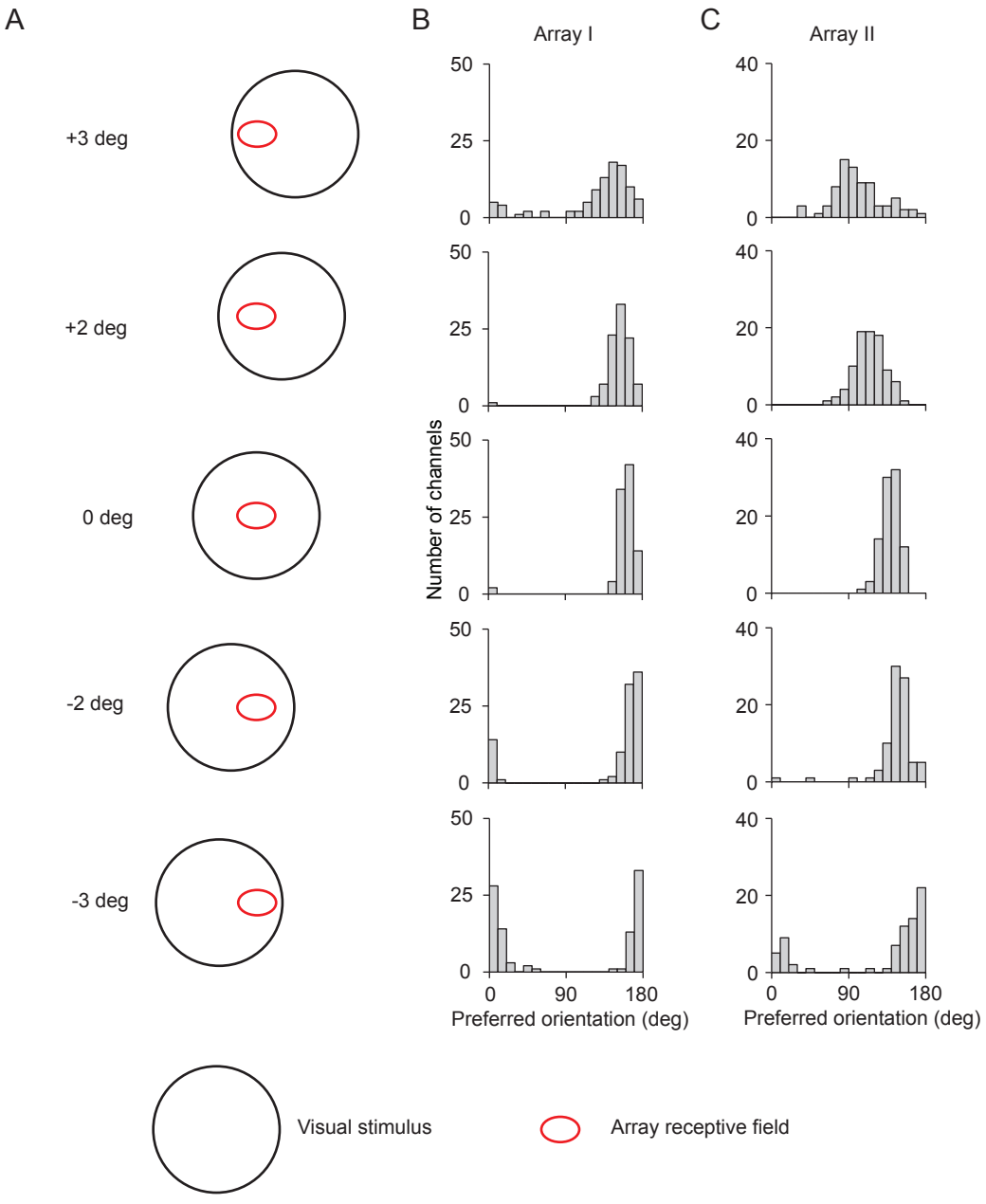
A
B
C
Array I
Array II
+3 deg
+2 deg
0 deg
-2 deg
-3 deg
Number of channels
Preferred orientation (deg)
Preferred orientation (deg)
Visual stimulus
Array receptive field

Figure 2.14: A schematic prediction of orientation bias based on retinotopic map in V1. (**A**) An illustration of visual field and the radial bias prediction with receptive field of the array implants indicated in black circle. (**B**) An illustration of the relative position of the aggregated receptive field of the array (red eclipse) and activated visual field region with large grating stimuli (black circle; solid and dashed).

A

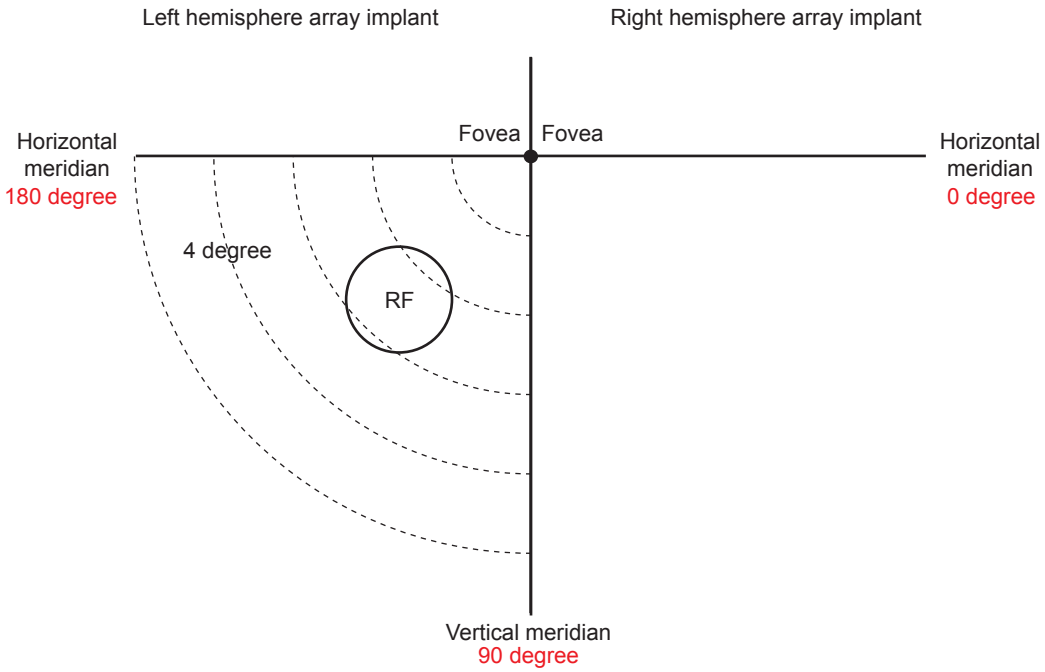

* Left hemisphere viewing right side visual field, but because of mirror the RF is on the left side of the monitor

B

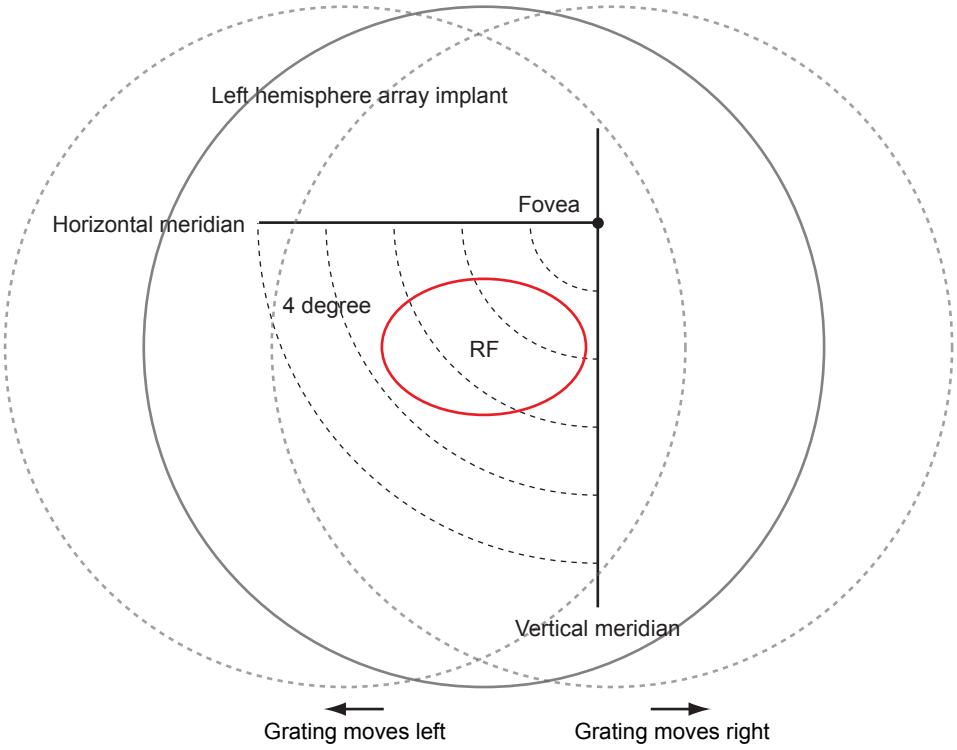

Figure 2.15: Preference distribution from different implants. The circular variance on the y axis indicates the degree of similar tuning on each implant, with value closer to 0 corresponding to a tighter cluster. Blue dots indicate left hemisphere implants (n = 14 implants) and red dots indicate right hemisphere implants (n = 8 implants).

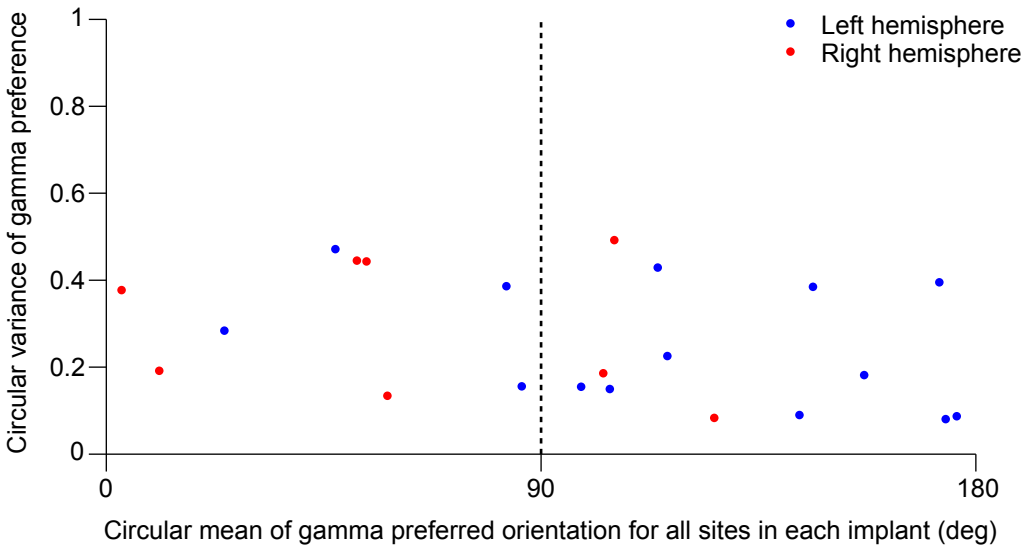
Left hemisphere
Right hemisphere
Circular variance of gamma preference
1
0.8
0.6
0.4
0.2
0
0
90
180
Circular mean of gamma preferred orientation for all sites in each implant (deg)

Chapter 3: The effects of adaptation on the local field potential

Xiaoxuan Jia[1], Carlyn Patterson[1], and Adam Kohn[1,2]

[1] Dominick Purpura Department of Neuroscience

[2]Department of Ophthalmology and Vision Sciences

Albert Einstein College of Medicine, Bronx NY 10461

Acknowledgements: This work was supported by grants from the National Institutes of Health to AK (EY016774) and MAS (EY015958 and EY018894). We thank Amin Zandvakili and Stephanie Wissig for assistance with data collection.

Figure 3.1A and Figure 3.2 C, D are published in *Journal of Neuroscience* 2011 31, 9390-9403.

X. Jia analyzed all the data in this section. Data from this section was collected in collaboration with C. Patterson.

3.1 Abstract

Adapting a sensory system with repetitive or prolonged exposure to the same stimulus reduces responsivity to that stimulus. Such adaptation-induced changes have been detected in single-unit recordings and with functional magnetic resonance imaging (fMRI). However, how adaptation affects the local field potential (LFP) is poorly understood. We undertook a study of this issue with three goals in mind. First, we aimed to provide a description of the plasticity of this signal. Since the LFP have been proposed as a useful signal for driving external devices with brain signals (brain-machine interface), it is important to know whether it is a stable signal or a particularly plastic one. Second, as a signal of intermediate scale between single neurons and more global signals like those measured in fMRI, understanding the LFP may help to bridge findings between these levels of study. Finally, we have found that the gamma frequency (30-50 Hz) components of the LFP share a common orientation preference across many millimeters of cortex. We hypothesize that this preference reflects a subtle bias in the underlying neuronal representation and use adaptation as a tool to explore this possibility. We measured the effects of adaptation on the LFP, and compared these with spiking activity recorded simultaneously. Low frequency power of the LFP was untuned both before and after adaptation. The gamma power induced with large grating stimuli showed significant suppression at the adapted orientation and facilitation at the orthogonal orientations, regardless of the original preference of the signal. High frequency components of the LFP showed similar adaptation effects as local spiking activity. Changes in LFP power were associated with changes in coherence with spiking activity at gamma but not low frequencies. Our results suggest that the preference of the global gamma rhythm is

sensitive to adaptation, in a manner consistent with it magnifying a bias in the neuronal representation of visual stimuli, and that this signal may be a neural correlate of fMRI adaptation effects. More generally, our results show the LFP is sensitive to the recent history of stimulation, and that the effects are different for distinct frequency components of the signal.

3.2 Introduction

The repeated or prolonged presentation of a sensory stimulus--adaptation--can strongly alter neuronal responses. This form of plasticity also alters our perception and has been used widely in psychophysics (Graham, 1989). In cortex, adaptation is well known to reduce the responsivity of cortical neurons whose preferences match the adapter and to have less effect on neurons with offset preferences (Grill-Spector et al., 2006; Kohn, 2007). Adaptation-induced plasticity can occur at different time scales, ranging from tens or hundreds of milliseconds (Dragoi et al., 2002; Felsen et al., 2002; Muller et al., 1999; Priebe and Lisberger, 2002) to many seconds or minutes (Giaschi et al., 1993; Hammond et al., 1988; Kohn and Movshon, 2003, 2004).

The local field potential (LFP) consists of low frequency extracellular voltage fluctuations (<200 Hz) measured in the brain and is thought to reflect aggregated electrical activity from a neural ensemble (Buzsaki, 2006; Mitzdorf, 1985). Changes in different frequency bands of the LFP have been correlated with numerous cognitive and perceptual phenomena (Fries et al., 2008; Pesaran et al., 2002; Scherberger et al., 2005; Wilke et al., 2006). Extensive studies have explored the basic response properties of the LFP signal (Berens et al., 2008; Gieselmann and Thiele, 2008; Henrie and Shapley, 2005; Liu and Newsome, 2006). However, there have been relatively few investigations of the effects of adaptation on the LFP (De Baene and Vogels, 2010; Hansen and Dragoi, 2011; Kaliukhovich and Vogels, 2011; Logothetis et al., 2001). Except for the null result (Logothetis et al., 2001), studies in monkey inferior temporal cortex showed that adaptation generally reduced power of the LFP in the frequency range of 60-100 Hz, but

not in lower frequencies (De Baene and Vogels, 2010; Kaliukhovich and Vogels, 2011). On the contrary, another study showed enhanced spike-field coherence in the gamma frequency (30-50Hz) with adaptation (Hansen and Dragoi, 2011). As a result, the adaptation effects on the LFP are still unclear.

Understanding the effects of adaptation on the LFP is important for the following reasons. First, as a basic neural signal that reflects neural population activity and is potentially useful for brain-machine interface (Heldman et al., 2006), it is important to understand the plasticity and sensitivity of LFP to sensory stimuli, in addition to its other basic response properties. Second, different frequency bands of the LFP have been suggested to have distinct origins (Berens et al., 2008; Liu and Newsome, 2006; Ray and Maunsell, 2011a). By comparing adaptation effects in different frequency bands of the LFP with effects on local spiking activity, we may gain more insight into the relationship between these two signals. Third, similar to cortical neuronal responses, the blood-oxygen level dependent functional magnetic resonance imaging (BOLD-fMRI) signal can adapt to the prolonged presentation of a visual stimulus (Boynton and Finney, 2003; Engel, 2005; Fang et al., 2005; Grill-Spector and Malach, 2001; Krekelberg et al., 2006; Tootell et al., 1998). However, the mechanisms underlying fMRI adaptation are still unclear and effects on the firing of single neurons may not be indicative of changes in the hemodynamic signal because of the significant differences in the two signals. As a signal with intermediate spatial resolution between spiking activity and BOLD-fMRI, understanding the adaptation effects of the LFP, especially its gamma frequencies (30-50 Hz) which have been suggested to be more closely related to the fMRI signal than spikes (Leopold

et al., 2003; Logothetis et al., 2001; Nir et al., 2007), may be helpful for interpreting adaptation-induced changes in the BOLD signal.

In addition to these general goals, we studied the adaptation properties of the LFP because of a peculiar property of its gamma frequency components. In Chapter 2 we showed that broadband gamma component and higher frequencies of the LFP behave similarly to local spiking activity (Jia et al., 2011; Ray and Maunsell, 2011a). The gamma spectral 'bump', on the other hand, is generated intrinsically from a neural network that extends for many millimeters, with shared response properties across that cortical region (Jia et al., 2011). We wondered why some orientations would induce more gamma power than others over such a large region. One hypothesis is that the shared tuning of the global gamma reflects a neural representation bias. With a limited sampling from a large network, detecting such a bias is difficult. Here we use adaptation to introduce a bias to the neural representation of orientation in V1. If the global gamma component magnifies a presumed bias in the neuronal representation of orientation, adaptation-induced changes in neuronal response should have a strong consequence for gamma tuning.

To address these issues, we measured the effect of prolonged adaptation on the orientation selectivity of the LFP from a 4×4 mm patch of cortex using multielectrode arrays implanted in superficial layers of primary visual cortex. We found that the effects of adaptation depended strongly on the frequency range of the LFP and that the global gamma rhythm is extremely sensitive to adaptation-induced changes in neuronal

representation, in a manner consistent with its preference magnifying a weak bias in that representation.

3.3 Materials and methods

Animal preparation and recording

We recorded from eight anesthetized, adult male macaque monkeys (Macaca fascicularis). Anesthesia was induced with ketamine (10 mg/kg) and maintained with isoflurane (1.5-2.5% in 95% O2) during venous cannulation. The animal was then placed in a stereotax and anesthesia was provided by intravenuous infusion of sufentanil citrate (6-18 μg/kg/hr, adjusted as needed for each animal), in normosol with dextrose (2.5%). Vecuronium bromide (0.1 mg/kg/hr) was administered to suppress eye movements. Temperature was maintained at 36-37 C°. Physiological signs were monitored (electrocardiogram, blood oxygen level, end-tidal CO2, electroencephalogram, temperature, and urinary output and osmolarity) to ensure adequate anesthesia and animal well-being. A broad-spectrum antibiotic (Baytril, 2.5 mg/kg) and an anti-inflamatory steroid (dexamethasome, 1 mg/kg) were administrated daily. All procedures were approved by the Institutional Animal Care and Use Committee of the Albert Einstein College of Medicine at YeshivaUniversity and were in compliance with the guidelines set forth in the United States Public Health Service Guide for the Care and Use of Laboratory Animals.

We implanted multielectrode arrays (10x10 grids with 0.4 mm spacing and 1 mm electrode length) into the upper layers (0.6-0.8 mm deep) of primary visual cortex (V1), ~10 mm lateral to the midline and ~8 mm posterior to the lunate sulcus. The electrical signal on each electrode was filtered between 250 Hz and 7.5 kHz to provide spiking activity. Events that exceeded a user-defined threshold were sampled at 30 kHz and saved for offline sorting. Raw signals were filtered between 0.3 Hz and 250Hz and sampled at 1

kHz to provide local field potentials (LFPs). Spiking activity were sorted using commercial software (Plexon Offline Sorter) and standard algorithms and criteria to further remove noise. The sorted spikes from the same recording site are grouped together and defined as multi-unit activity (MUA).

In some experiments, a separate linearly arranged multielectrode device (Thomas Recording) was positioned between the lunate sulcus and the array, with each electrode referenced to the guide tubes. Raw signals recorded from this device were band-pass filtered between 0.5 Hz and 250 Hz, and digitized at 1 kHz. To remove 60 Hz noise and its harmonics, we applied a fourth order Butterworth band-stop filter to the raw LFP data.

Visual stimuli

Visual stimuli were generated with EXPO and presented on a CRT monitor (resolution 1024 by 768 pixels; refresh rate 100 Hz) placed 110 cm from the animal. We mapped the receptive fields by briefly presenting small, full contrast drifting gratings (0.6 degree; 250 ms duration) of different orientations at a range of spatial positions. The spiking responses at each site were fitted with a 2D Gaussian to determine the receptive field location and extent.

We used these measurements to center full contrast gratings on the aggregate receptive field. Visual stimuli consisted of sinusoidal gratings with a fixed spatial (1 cycle/degree) and temporal frequency (6.25 cycle/second) drifting at 16 directions with 22.5 degree separation. We used an adaptation protocol similar to that used in previous neuronal and

fMRI studies (Figure 3.1A). The orientation tuning was measured with full contrast gratings drifting in 16 directions, which gives rise to two orientations that match the adapter but only one condition matching its direction. The stimuli were presented for 1 second followed by a 5 second inter-stimulus interval during which a blank, grey screen was shown. After 20 presentations of each test stimulus (in block randomized fashion), a single grating was presented continuously for 40 seconds and orientation tuning was measured again with the same test gratings, separated by top-up presentations (5 seconds) of the adapter to maintain the adaptation effects.

We used two stimulus sizes: 7.4 degrees and 1.28 degrees. The larger one is extensive enough to cover the spatial receptive fields of all recording sites. Since the small grating did not cover the receptive fields of all units, we only analyzed sites whose receptive field centers were covered by the smaller stimulus.

Data analysis

Tuning of the LFP was based on its average power in 4 Hz bins, sampled from low (0-20Hz), gamma (30-50Hz) and high frequencies (180-200Hz). An orientation selectivity index (OSI) was calculated as the vector sum of the response vectors (combining responses to different drift directions of the same orientation), normalized by the sum of lengths of the vectors (Leventhal et al., 1995). For computing the OSI, we defined response strength with respect to that driven (MUA) or induced (LFP) by the least preferred orientation.

We analyzed the power spectrum of the LFP (after discarding the first 100 ms of the response) and spiking activity with a multi-taper method. We applied 8 orthogonal Slepian tapers to the data (k=2TW-1), where T is 900 ms and W is determined to be 5 Hz. The LFP was treated as a continuous signal. The spike train was treated as a discrete signal, binned with 1 ms resolution into a sequence of event times (Pesaran et al., 2002). To evaluate how changes in LFP power affect their interaction with spiking activity, we compared the coherence between spikes and LFP (spike-field coherence; SFC) before and after adaptation for orientations similar and orthogonal to the adapter. Coherency was calculated by normalizing the cross-spectra between LFP and spike train by the geometric mean of their auto-spectra:

$$C_{xy}(f) = \frac{S_{xy}(f)}{\sqrt{S_{xx}(f)S_{yy}(f)}}.$$

Cxy is a complex number. The modulus of the complex number represents the value of coherence, which lies between 0 and 1.

Neuronal spike count correlation across stimulus repetitions was calculated with *Pearson* correlation:

$$r = \frac{\mathrm{E}[N_1 N_2] - \mathrm{E}N_1 EN_2}{\sigma_{N_1}\sigma_{N_2}}$$

where N_1 and N_2 are the spike counts of neuron 1 and 2 respectively for time epoch between 100 ms after stimulus onset to 1 second. E is the expected value, and σ is the standard deviation of the responses. (Kohn and Smith, 2005).

All error bars are presented as standard error of the mean (s.e.m.).

3.4 Results

In order to compare adaptation effects on the LFP and spiking activity, we recorded multi-unit activity (MUA) and LFPs simultaneously using multi-electrode arrays implanted in the primary visual cortex (V1) of 8 anesthetized macaque monkeys.

Effects of adaptation on the orientation tuning of the LFP

To evaluate how adaptation affects spiking activity and the LFP, we compared orientation tuning before (black) and after (red) adaptation to a single large drifting grating, for a range of frequency bands of the LFP and for spiking activity (Figure 3.1A; Method). Figure 3.1B shows the normalized orientation tuning for sites at which the adapter matched the preferred orientation before adaptation (within 22.5 degrees), with spiking activity shown on the left and effects for three frequency ranges of LFP power on the right. The population tuning curves were computed by averaging data from sites with similar pre-adaptation preferences (bins of 22.5 degrees) after normalizing the responses at each site by its maximum response before adaptation. Figure 3.1C shows data from sites at which tuning preference was orthogonal to the adapter (within 22.5 degrees). The tuning curves from individual sites are shifted so that the adapted orientation is always presented as 180 degree.

Consistent with previous reports (Dragoi et al., 2000), spiking responses were suppressed at preferred-adapted sites. Spontaneous activity—that measured in response to a gray screen—was also reduced after adaption, with the averaged firing decreasing from 6.0±0.3 to 5.1±0.4 spk/sec (ttest2 p=0.08). For preferred-adapted neurons, the stimulus

evoked response (i.e. the response relative to the spontaneous rate) at the preferred orientation decreased by 17.2±4.3%, but only decreased by 2.7±1.9% for the orthogonal orientations (n = 107 sites), indicating that the effects were strongest for stimuli matched to the adapter. For neurons whose preference was orthogonal to the adapter, opposite to the preferred adaptation condition, orthogonal adaptation increase spontaneous activity by 10.7±3.3%. The evoked response at the adapter decreased by 7.9±6.9%, and decreased by 1.7±4.7% at the orientations orthogonal to the adapter (n =126 sites). Thus, for spiking activity, adaptation caused a greater reduction in responsivity for cells whose preference was within 22.5 deg of the adapter (Fig. 1B left) than for those with the orthogonal preference (Fig. 1C left), confirming that adaptation alters the neuronal representation of orientation.

The low frequencies of the LFP are not well-tuned, whereas gamma and higher frequencies are more selective (Berens et al., 2008; Jia et al., 2011; Liu and Newsome, 2006). Therefore, we measured the effects of adaptation on the LFP for individual frequency bands. Consistent with previous findings, we found no orientation tuning in the low frequency power (0-4Hz) of the LFP before adaptation, or any clear orientation-dependent changes after adaptation (n = 110 sites). However, there was a consistent increase in low frequency power of spontaneous activity after adaptation, for both preferred-adapted and orthogonal adapted-conditions. Note that because sites were not well tuned, the labeling of a site as preferred- or orthogonal-adapted carried little meaning, and similar effects were seen in both portions of the data.

For gamma frequencies (36-40Hz), power was tuned for orientation before adaptation. Here we used large gratings to induce strong gamma 'bump' power, which can dissociate from local spiking activity and form a coherent rhythm. Adaptation caused a dramatic reduction in response to test stimuli matched to the adapter, and facilitation at orthogonal orientations. This was true at both preferred-adapted (n=110 sites) and orthogonally-adapted sites (n = 219 sites). For sites whose gamma preference was similar to the adapter, the response decreased by 48.1±1.7% (spontaneous activity subtracted) at the adapted orientation, but was enhanced by 51.8±2.7% for orthogonal orientations. For sites whose gamma preference was orthogonal to the adapter, power for stimuli matched to the adapter decreased by 29.5±1.0% and increased by 164.8±5.2% at orthogonal orientations. Thus, regardless of its preference, gamma power is extremely sensitive to adaptation with large gratings.

To quantify further the effects of adaptation on gamma, we compared its preferred orientation before and after adaptation. Figure 3.2A shows the orientation preferences of one example array. Each dot (black before adaptation, red after) compares the preferred orientation of gamma and MUA at the same site (n = 93 sites). For this example, the orientation preference of gamma shifted away from the adapter (0 degree) at all sites. The range of preferences was also reduced after adaptation, with the circular variance dropping from 0.27 to 0.08. However, there were no notable changes in the distribution of MUA preferences at those sites. Across implants (n=5), we found a significant reduction in the circular variance of gamma preference (0.29±0.07 to 0.09±0.03; p=0.03), so that there was a tighter clustering of preferences after adaptation. Figure 3.2B shows

the changes in preferred orientation after adaption (n = 536 sites), with values larger than 0 representing repulsive shifts and values less than 0 representing attractive shifts. We found that when the preferred orientation of gamma was more similar to the adapter (0 degree offset on the abscissa), the preferences shifted nearly to the orthogonal orientation. When the pre-adaptation preferred orientation was orthogonal to the adapter, there was little shift in preference.

Adaptation reduces the responsivity of neurons in a specific manner (Figure 3.1B,C; see Kohn, 2007 for a review). If the tuning of gamma reflects a bias in the neural response, it should thus shift strongly away from the adapter, since neurons responding to that stimulus will be most strongly suppressed. We found that the effect of adaptation on gamma was also evident when comparing the distributions of preferred orientation before and after adaptation in a single implant (Figure 3.2C). In this case, the adapter (indicated by the arrow) was well aligned with the most commonly preferred orientation, and adaptation caused a striking shift in preference to the orthogonal orientation (mean offset increasing from 20.7±1.9 deg to 65.4±2.5 deg; $p<<0.001$). After a period of several minutes without visual stimulation, the distribution of preferences nearly fully recovered to its pre-adaptation form. Across implants (n=8), there was a pronounced tendency for the preference to shift toward the orientation orthogonal to the adapter (Figure 3.2D). In those cases that the preference was nearly orthogonal to the adapter before adaptation, we observed smaller shifts. This is consistent with the behavior expected from a signal whose preference reflects the overall level of activity evoked by different stimuli in a large, distributed network.

In the higher frequencies of the LFP (196-200Hz), adaptation effects were more similar to spiking activity (Figure 3.1B, C). For sites whose preference was similar to the adapter, the response decreased by 23.0±2.6% at the adapted orientation, and reduced by 8.6±0.1% at orthogonal orientations. For sites whose preference was orthogonal to the adapter, power for stimuli matched to the adapter decreased by 11.3±1.8% from the pre-adaptation level and decreased by 11.3±0.1% at the orthogonal orientations.

To illustrate how adaptation alters LFP power across a wider range of frequencies, we calculated the ratio of the power spectra (after/before) adaptation for several orientations (Figure 3.3A; n = 480 sites). The adapted orientation (red line) was suppressed most strongly in the gamma band, an effect seen in higher frequencies as well. In addition, the suppression effect is direction specific, with less suppression at the orientation matched to the adapter but drifting in the opposite direction (black line). Interestingly, the facilitation for the orthogonal or near-orthogonal orientations was restricted to frequencies from 20 to 60 Hz; higher frequencies showed suppression for these stimulus conditions. Power of spontaneous activity was significantly enhanced in the low frequencies (<20 Hz) after adaptation, and suppressed for frequencies higher than 70 Hz. Figure 3.3B presents the adaptation-induced change in power for all orientations. The strongest suppression occurred at the adapted orientation (180 degrees), and response facilitation is strongest for orthogonal orientations in the gamma band.

In summary, spiking activity showed the strongest suppression at the preferred adapted

orientation, effectively reducing the representation of the adapted orientation. This change in the neuronal population spiking response was associated with a range of effects in the LFP. High-frequency LFP power adapted similarly to the spiking response, suggesting that these frequencies components may be tightly linked to local spiking activity. This would be consistent with the similarity in tuning between these two signals at individual sites (Gray and Singer, 1989; Katzner et al., 2009; Liu and Newsome, 2006). Low frequency power, on the other hand, showed no orientation specific changes, suggesting that it is strongly dissociated from local spiking activity, consistent with its poor tuning. Gamma power showed the most dramatic effects: it was strongly suppressed at the preferred adapted orientation and facilitated at the orthogonal orientation. This is consistent with proposal that the preference of gamma magnifies a weak bias in the neural representation: when adaptation suppresses the representation of a particular stimulus, the preference of gamma shifts dramatically.

Role of stimulus size

We have previously shown that large gratings induce a rhythm which can be coherent across millimeters of cortex. The power in the gamma band under these conditions is dominated by this rhythm, rather than the broadband change in power, which behave similarly to local MUA. The responses described above relied on responses driven by large gratings, so the adaptation effects observed reflected should have reflected changes in the coherent rhythm. To test this further, we studied adaptation effects on LFP power induced by small grating stimuli (1.28 degree), for which there is a stronger contribution of the broadband component to gamma power (Gieselmann and Thiele, 2008; Jia et al.,

2011; Ray and Maunsell, 2011a). We used the same adaptation protocol and a subset of sites recorded with large gratings, namely those that were driven by the small grating.

Figure 3.4A shows the ratio of the power spectra after and before adaptation, for signals induced by small gratings (n=238 sites). The effect of adaptation on gamma was significantly smaller than for large stimuli (Figure 3.3A). Whereas we observed a 3.1 fold increase in power at orthogonal orientations for gamma induced by large gratings, the corresponding effect was 1.9 fold for small gratings. Figure 3.4B shows the ratio of the power spectra as a function of orientation, with 180 degree representing the adapted orientation. This reveals more suppression for the orientation matched to the adapter and less enhancement in gamma power at the orientations orthogonal to the adapter, compared to data from large gratings (Figure 3.3B). In this data set, the proportion of gamma spectrum 'bump' in the total gamma power is 27.6±0.6% with large grating stimuli (predicted with same method as detailed in result section for Figure 2.5 of Chapter 2), while the proportion of gamma 'bump' power is 7.2±0.6% of the total gamma power with small grating stimuli. These results suggest that the enhancement in gamma power at orientations orthogonal to the adapter was related to the strength of the gamma 'bump'.

Interaction between spiking activity and the LFP

Comparing how the tuning of spikes and LFP are affected by adaptation provides one view of the relationship between these two signals. A more complete picture of this relationship can be provided by examining the correlation between fluctuations in spiking

activity with LFP. To this end, we examined whether adaptation-induced changes in the LFP would affect the interaction with spiking activity. We compared spike-field coherence (SFC; see Method), a measure of temporal correlation between spike times and the LFP for individual frequencies, before and after adaptation.

Figure 3.5A shows the effect of adaptation on SFC (after-before; n=480 sites) as a function of frequency, for orientations similar to the adapter (180 degree) and orientations orthogonal to the adapter. The change in SFC during spontaneous activity is indicated with a dashed line. The most significant changes in the SFC occur at low (<10Hz) and gamma (30-50Hz) frequencies. Figure 3.5B quantifies the gamma SFC for all orientations, before and after adaption, and for all sites. Effects on low frequency SFC under stimulus driven conditions were not orientation-specific, but showed a general enhancement, which is on average 8.7±1.0% of the value before adaption. Gamma SFC was enhanced for most test stimuli, with a decrease only observed at the adapted orientation. The average gamma band SFC was reduced by roughly 2.9±1.5% of the value before adaptation at the adapted orientation, and increased roughly 33.7±2.5% after adaptation at the orientations orthogonal to the adapter (Figure 3.5C), which is similar to the effects on gamma power (Figure 3.1B). These results suggest that although the firing rate at the orientations orthogonal to the adapter did not change on average, spike timing was more strongly modulated in the gamma frequencies after adaptation. Our results suggest that prolonged adaptation enhances synchronization of spikes in the gamma frequencies, for responses driven by stimuli different from the adapter.

In addition, opposite to the enhancement in low frequency power after adaptation during blank stimuli ('spontaneous'), we observed a significant reduction in the low frequency SFC (<10Hz; Figure 3.5A, dashed black line) during blank stimuli after adaptation, with a 23.7±2.0% reduction of the SFC value before adaptation. The opposite adaptation effects for low frequency power and the low frequency SFC suggests that the SFC measurement does not depend simply on power.

Adaptation effects on neuronal correlation

Spatial attention can suppress low frequency power of the LFP (Fries et al., 2008) as well as reduce neuronal correlation in V4 (Cohen and Maunsell, 2009; Mitchell et al., 2009). We have observed that prolonged adaptation suppressed low frequency power of the LFP during stimulus presentation, but increased the low frequency power during spontaneous activity. We next checked the effect of adaptation on neuronal correlation or noise correlation, a measure of how strongly trial-to-trial fluctuations in the response to a single stimulus are shared between pairs of neurons (Cohen and Kohn, 2011; Kohn and Smith, 2005; Smith and Kohn, 2008).

We compared pairwise neuronal correlation before and after prolonged adaptation with large gratings. Figure 3.6A presents the spike count correlations at the adapted orientation before (black) and after (red) adaptation. The mean spike count correlation (r_{sc}) increased from 0.178±0.002 to 0.246±0.002 (ttest2 $p<<0.001$; n=27208 pairs), roughly a 38% enhancement compared to pre-adaptation, with a distribution median increased from 0.182 to 0.250 (Mann-Whitney U-test $p<<0.001$). The spike count correlation showed a

general enhancement across orientations, from 0.166±0.001 to 0.181±0.001 (ttest2 $p<<0.001$; Figure 3.6B), a 9% change, with the median of distribution increased from 0.166 to 0.181 (Mann-Whitney U-test $p<<0.001$). Note that the increase in spike count correlation is larger for the adapted orientation than average. Correlation also increased for spontaneous activity after adaptation, from 0.306±0.002 to 0.320±0.002 (ttest2 $p<<0.001$). However, the median of the distribution decreased significantly from 0.328 to 0.322 (Mann-Whitney U-test p=9.4e-4) after adaptation. Consistent with previous work (Smith and Kohn, 2008), neuronal correlations were stronger during spontaneous activity than for visually driven activity.

We conclude that the effect of adaptation on neuronal correlation is more similar to the changes in low frequency SFC (<10Hz), which were enhanced for stimulus driven conditions after adaptation, rather than to low frequency power, which was reduced for stimulus driven condition after adaptation. The results for spontaneous activity are mixed. The median of the neuronal spike count correlation decreased after adaptation, similar to the low frequency SFC, but the mean spike count correlation increased. However, in general, neuronal correlation showed a positive relationship with the low frequency SFC (<10Hz).

3.5 Discussion

Prolonged adaptation has different effects on different frequency bands of the LFP. The low frequency band (<10Hz) had no orientation tuning before or after adaptation, and adaptation caused a general reduction of power for all stimuli. Higher frequencies of the LFP (> 100 Hz) adapted similarly to local spiking activity, with responses to the adapted orientation showing weak suppression. Gamma frequencies showed the strongest effects. For large gratings, which induce a distinct gamma spectral bump, power was significantly reduced at the adapted orientation and facilitated at offset orientations. This facilitation depends on the strength of the gamma 'bump': for small gratings, for which the gamma power reflects broadband LFP power, facilitation was much weaker. Adaptation-induced changes in LFP power had an effect on the interaction between spike timing and the LFP. The SFC in the low frequency (<10Hz) increased after adaptation for all orientations whereas the SFC in the gamma range was suppressed at the adapted orientation but enhanced at other orientations, with strongest increase at the orthogonal orientations. The enhancement in low frequency SFC is accompanied by an increase in neuronal spike count correlation.

Evidence for the representation bias hypothesis

We have shown that the gamma band of the LFP, when induced with large gratings, can form a spatially extensive coherent rhythm which is selective for different stimulus features (Chapter 2, Jia et al., 2011). Measured at individual recording sites, this selectivity is apparent as shared tuning. We previously proposed that the selectivity of this rhythm could reflect a bias in the neuronal representation that underlies the

generation of this rhythm. For instance, it could reflect the purported overrepresentation of cardinal orientations in V1 ("oblique effect", (Li et al., 2003)). However, we found no preponderance of these orientations in the tuning of gamma. Alternatively, the relevant spatial scale could be smaller, such as a bias in the representation within several millimeters of the electrode tip. This would be consistent with the finding that fMRI voxels of several cubic millimeters are orientation-tuned, thought to reflect that a finite, random sample of neurons will always result in a bias toward some orientation (Haynes and Rees, 2006).

Our results in the current chapter support this proposal. The orientation selectivity of the global gamma rhythm induced by large gratings was extremely sensitive to the neuronal representation bias introduced by adaptation, which is indicated by a 3 fold stronger reduction the gamma power compared to neuronal firing rate, at the adapted orientation. This was true regardless of the gamma preference before adaptation. This result supports the hypothesis that the changes in gamma power magnify small differences in population firing rate, which makes it possible for a small bias in the neuronal representation to be reflected in a highly selective signal. Under this interpretation, the facilitation arises because the gamma rhythm induced by large gratings magnifies the bias arising from stronger responses to stimuli that are different from the adapter. Using small stimuli, we found weaker facilitation at orientations further away from the adapter, suggesting this facilitation requires the presence of the gamma "bump".

Adaptation-induced changes in tuning were accompanied by a change in the relationship to the firing pattern of neurons, measured by SFC. Gamma SFC was strongly enhanced when gamma power was elevated. This suggests that in addition to its effects on neuronal firing rate, adaptation can strongly influence gamma coordinated spike timing (Hansen and Dragoi, 2011).

Comparison with previous studies

We are aware of several previous studies that evaluated the effects of adaptation on the LFP. The first compared the dynamics of averaged LFP power (40-130Hz, a combination of gamma and higher frequency components) and MUA (Logothetis et al., 2001). It found spiking activity was suppressed strongly and powerfully after stimulus onset, and that the LFP was better maintained throughout the stimulus presentation. The authors concluded that there is no adaptation effect on the LFP. In contrast, we observed more striking suppression for gamma power than spiking activity, inconsistent with this report. This difference may reflect, in part, that we calculated the average power and firing rate from 100 ms after stimulus onset till 1000 ms, and compared to activity before adaptation to evaluate the effect of adaptation. Logothetis et al. (2001), on the other hand, compared neuronal responses and broadband power to the baseline response before stimulus onset. The measurements are thus somewhat different. It bears mention, in addition, that the change in neuronal response reported by Logothetis et al (2001) involved a transient response that adapted quickly to the baseline (prestimulus level). Such drastic neuronal adaptation is inconsistent with a number of previous reports in the literature (Giaschi et al., 1993; Hammond et al., 1988; Kohn and Movshon, 2003; Movshon and Lennie, 1979).

Another study compared changes in SFC before and after adaptation in different cortical layers and found that adaptation induced stronger gamma band SFC in the superficial, but not in other layers (Hansen and Dragoi, 2011). This study did not report a suppression of SFC with adaptation in the gamma band, as we observed, but this likely reflects the fact that they averaged responses across orientations. A reduction in gamma SFC in our data was only apparent for the test stimulus whose orientation matched the adapter. In addition, the brief adaptation protocol (300 ms) used by Hansen and Dragoi (2001) may have affected SFC differently from the prolonged adaptation we studied.

Effects of adaptation on the LFP have also been observed in inferior temporal cortex (IT) (De Baene and Vogels, 2010; Kaliukhovich and Vogels, 2011). These two related studies found similar adaptation effects in spiking activity and high-gamma power (60-100Hz), but not for low gamma frequencies (30-50Hz). This is consistent with our findings that the activity of higher frequencies is more similar to spiking activity, especially when the spectrum is dominated by the broadband power. However, the stimuli in this study did not induce a gamma spectrum bump, which appears to be a necessary condition for observing the strong facilitation of gamma at orthogonal orientations.

Comparison with BOLD-fMRI signal

It has been proposed that the LFP is more closely related to the BOLD-fMRI signal than spikes are (Goense and Logothetis, 2008; Kayser et al., 2004; Leopold et al., 2003; Logothetis et al., 2001; Nir et al., 2007). Our characterization of adaptation effects for

different frequency bands of the LFP provides an opportunity to revisit this question, as adaptation has been used widely to study both spiking activity and the BOLD signal. The effects of adaptation on the BOLD signal, in particular, have been used extensively to infer the functional representation in different parts of cortex (Grill-Spector and Malach, 2001; Krekelberg et al., 2006).

Similar to neuronal spiking activity, we found that adaptation caused the strongest reduction in responsivity at the adapted orientation in the higher frequencies of the LFP, consistent with the idea that these reflect local spiking activity. Gamma power was also suppressed at the adapted orientation but, in addition, was strongly enhanced at orthogonal orientations (on average two fold). Using a similar prolonged adaptation protocol, it has been found that the BOLD signal is suppressed at the adapted orientation after adaptation, but strongly facilitated at orthogonal orientations relative to baseline (Fang et al., 2005). Since visual stimuli used in fMRI studies are typically large and thus would be expected to generate a global gamma rhythm, this is consistent with previous proposals that gamma is more strongly correlated with the BOLD signal (Leopold et al., 2003; Logothetis et al., 2001; Nir et al., 2007). Local spiking activity did not show a similar enhancement for orthogonal test stimuli, and thus had a behavior different from the BOLD signal.

Adaptation effects on slow fluctuations

Unlike the stimulus-specific adaptation effect in the gamma frequencies, the low frequency components of the LFP showed no orientation tuning before or after adaptation.

Instead, we observed a non-specific decrease in low frequency power. Therefore, this frequency range is unlikely to be correlated with the BOLD signal. However, low frequency power of spontaneous activity was significantly enhanced after adaptation with either small or large gratings. It has been suggested that the low frequency power of the LFP is correlated with less active brain states (Kohn et al., 2009). If the strength of low frequency power indicates a less excitable state, this suggests that the prolonged presentation of a stimulus could reduce excitability of the neuronal network, which is consistent with the reduction of the spontaneous spiking activity after adaptation.

We observed a strong, non-specific enhancement in the low frequency SFC (<10Hz) after adaptation. This finding indicates that the spiking activity is more correlated with low frequency fluctuations after adaptation. This was also reflected in neuronal correlations. These results suggest that adaptation enhances the slow timescale neuronal correlation in the brain.

Conclusions

Our findings show that the global gamma rhythm is extremely sensitive to prolonged adaptation, which introduces a bias to the neural responses, consistent with the hypothesis that the tuning of the global gamma could represent a neural representational bias. The effect of adaptation on gamma power is more similar to the effects on the BOLD-fMRI signal, compared to spiking activity or other frequency bands of the LFP. When using LFP to interpret neural activity of a large ensemble in the brain (e.g. in BMI), it is important to understand its instability and note the different representations and dynamics

of different frequency components. Therefore, the sensitivity of the gamma rhythm along with its slow dynamics (Jia et al., 2011) might make it less suitable to decode fast changes in the brain.

3.6 Figure Legends

Figure 3.1 Effect of adaptation on the tuning of MUA and LFP for large grating stimuli. (A) Illustration of the adaptation protocol. (B) Population average orientation tuning curves before (black) and after (red) adaptation for spiking activity (n=107 sites) and different frequency bands of the LFP. The orientation preferences were within 22.5 degree range of the adapter. All tuning curves were aligned so that 180 degree always represents the adapted orientation (indicated by arrow). The LFP tuning curves are based on the average power in 4Hz bins for low frequencies (0-4Hz; n=110 sites), gamma frequencies (36-40Hz; n=110 sites), and high frequencies (196-200Hz; n=115 sites). (C) Similar to (B), population average tuning curves before (black) and after (red) adaptation for spiking activity (n=126 sites) and different frequencies of the LFP. The preferences were within 22.5 degrees of the orientation orthogonal to the adapter. The LFP tuning curves are based on the power in low frequencies (0-4Hz; n=219 sites), gamma frequencies (36-40Hz; n=219 sites), and high frequencies (196-200Hz; n=132 sites). The spontaneous activity before and after adaptation are shown with dashed lines.

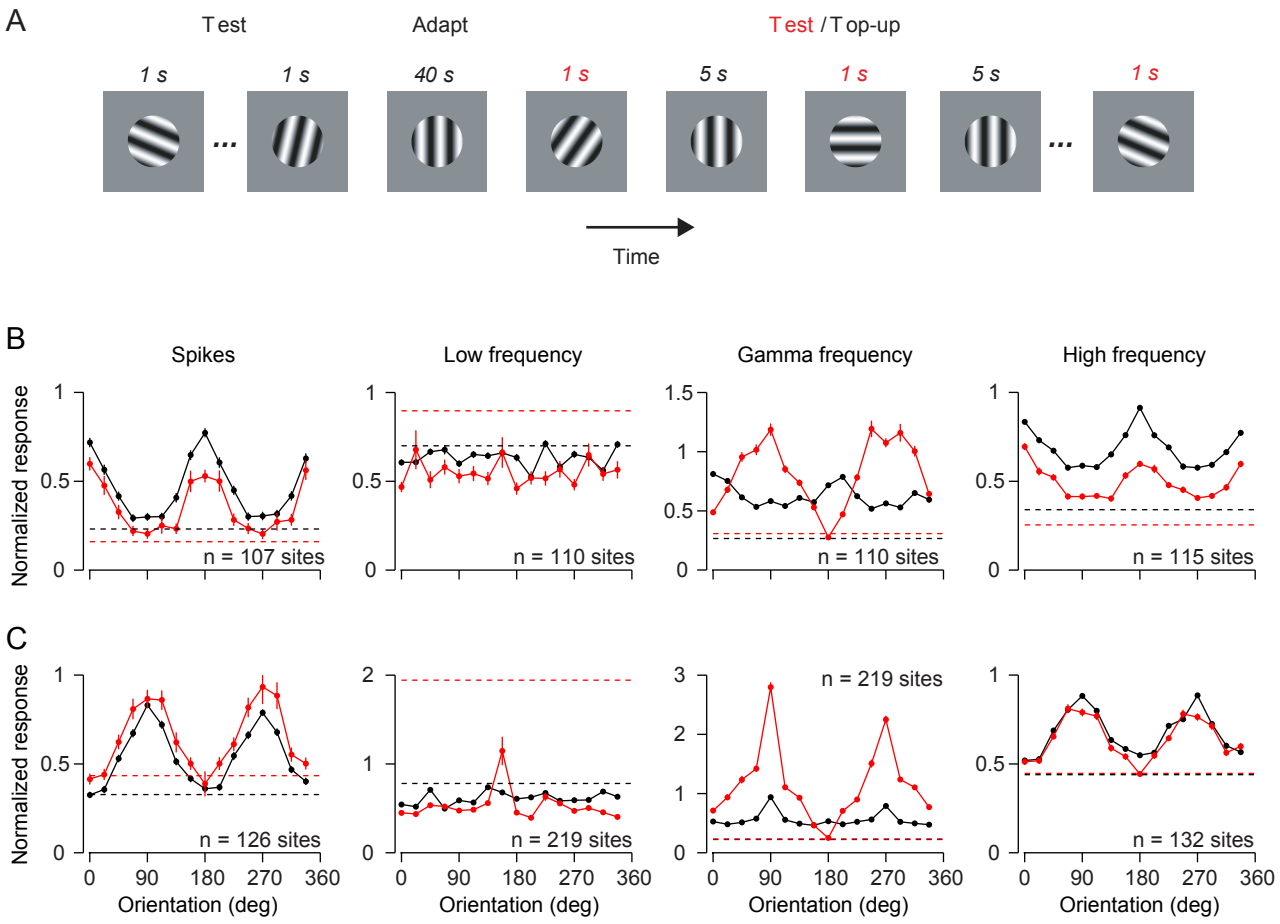
A
Test
Adapt
Test / Top-up
1 s
1 s
40 s
1 s
5 s
1 s
5 s
1 s
Time
B
Spikes
Low frequency
Gamma frequency
High frequency
Normalized response
n = 107 sites
n = 110 sites
n = 110 sites
n = 115 sites
C
n = 126 sites
n = 219 sites
n = 219 sites
n = 132 sites
Orientation (deg)

Figure 3.2 Shifts of gamma preference after adaptation with large gratings. (**A**) Scatter plot (from a single array) of orientation preferences before (black) and after (red) adaptation for gamma and MUA. Each dot represents the preferred orientation of MUA and gamma measured from the same electrode. Marginal distributions are shown as histograms to the side of the scatter plot. The circular variances of the orientation preference distributions before and after adaptation are indicated in the marginal histograms. (**B**) The shift of preferred orientation in the gamma frequency, as a function of the original preference relative to the adapter. Each dot represents one recording electrode. Positive shift means away from the adapter. (**C**) Distributions (from a single implant) of orientation preference for pre-adaptation, post-adaptation and recovery periods for gamma (upper) and MUA (lower). The circular variance is indicated at the upper-left of each histogram. Arrow indicates the orientation of the adapter. (**D**) Quantification of mean orientation preference of gamma, relative to the adapter, before and after adaptation (n=8 implants).

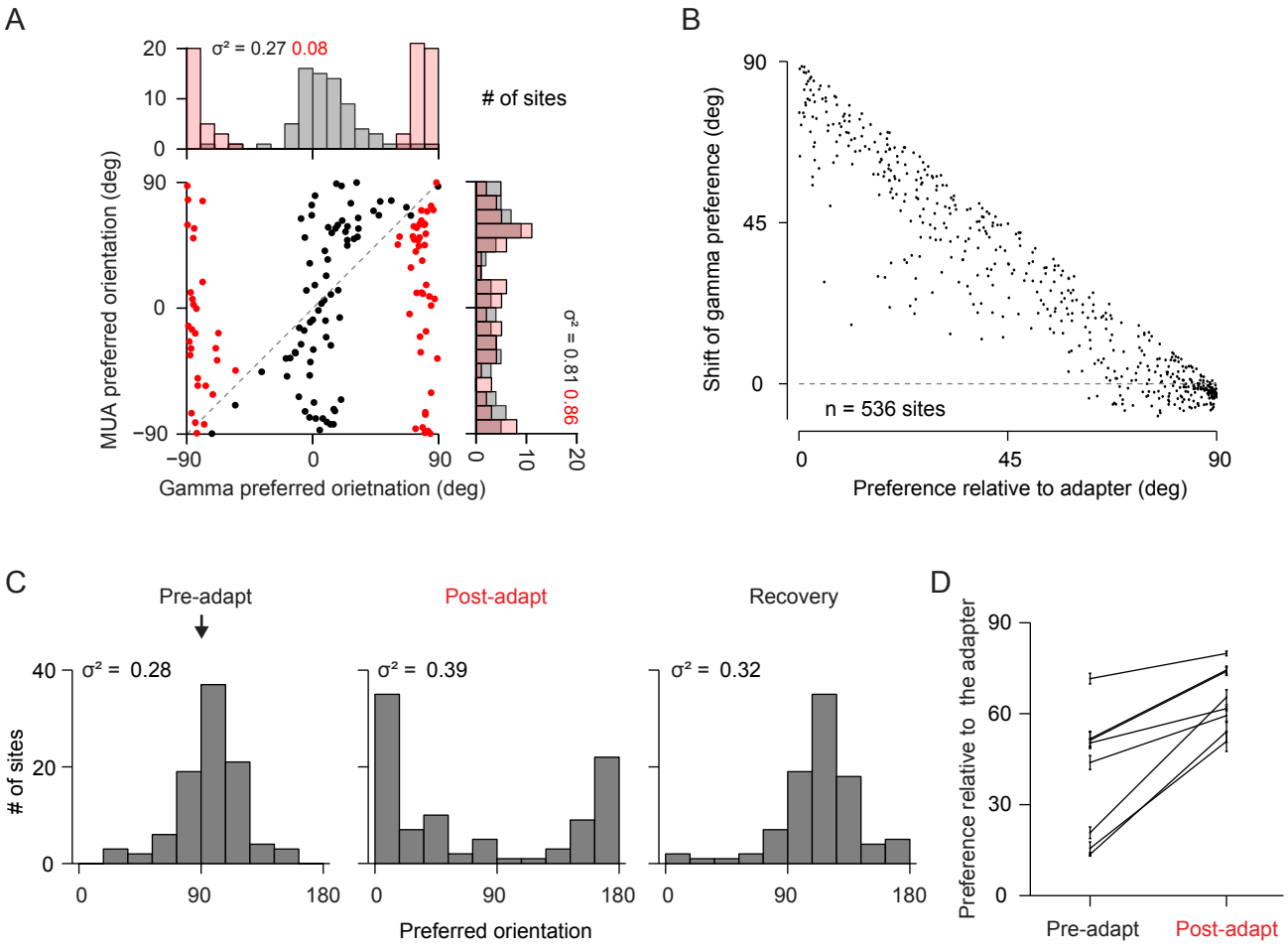
A
σ² = 0.27 0.08
# of sites
MUA preferred orientation (deg)
Gamma preferred orietnation (deg)
σ² = 0.81 0.86
B
Shift of gamma preference (deg)
n = 536 sites
Preference relative to adapter (deg)
C
Pre-adapt
Post-adapt
Recovery
σ² = 0.28
σ² = 0.39
σ² = 0.32
# of sites
Preferred orientation
D
Preference relative to the adapter
Pre-adapt
Post-adapt

Figure 3.3 Change in power spectra after adaptation. (**A**) The ratio of power spectra (post/pre-adaptation) for orientations identical to the adapter (0 degree, black; 180 degree, meaning the same orientation but opposite direction, in red) and orthogonal to the adapter (90 degree, blue; 270 degree, green). Dashed black line with errorbar indicates the changes in power during spontaneous activity (n=480 sites). The flat dashed line indicates value of 1, meaning no change in power. (**B**) Mean ratio of power spectrum post/pre adaptation as a function of orientation. 180 degree represents the adapted orientation.

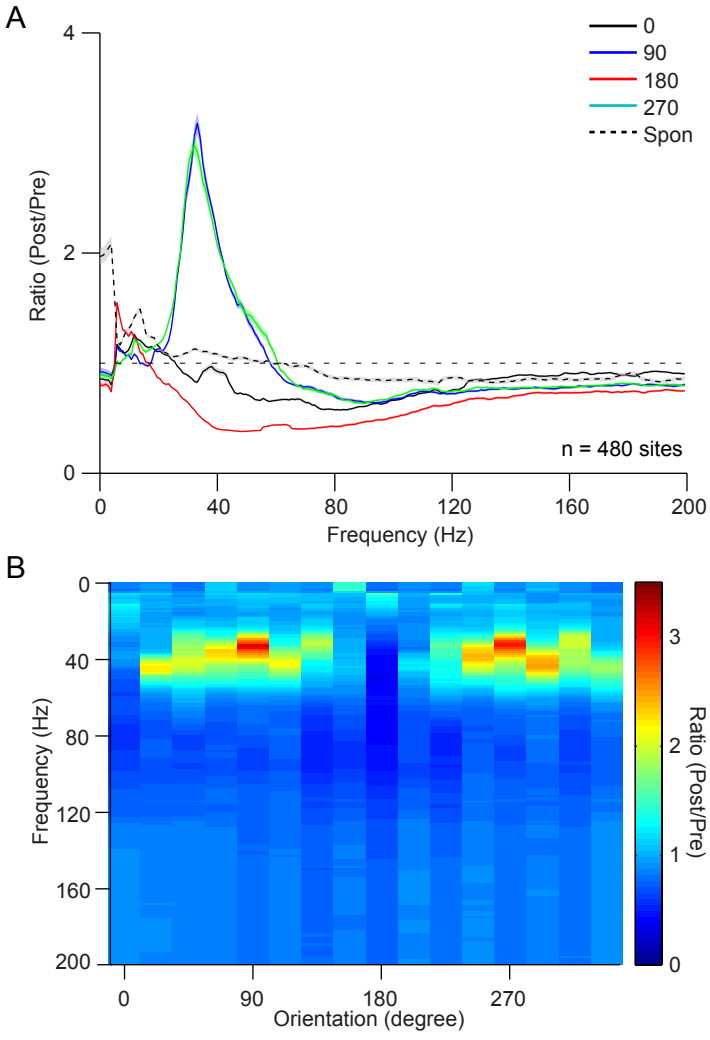
A
0
90
180
270
Spon
Ratio (Post/Pre)
n = 480 sites
Frequency (Hz)
B
Frequency (Hz)
Orientation (degree)
Ratio (Post/Pre)

Figure 3.4 Change of power spectra after adaptation with small gratings. (**A**) The ratio of power spectra (post/pre-adaptation) for orientations identical to the adapter (0 degree, black; 180 degree, red) and orthogonal to the adapter (90 degree, blue; 270 degree, green). Dashed black line indicates the changes in spontaneous activity (n = 238 sites). The flat dashed line indicates value of 1, indicating no change in power. (**B**) Mean ratio of power spectrum (post/pre adaptation) as a function of orientation. 180 degree represents the adapted orientation.

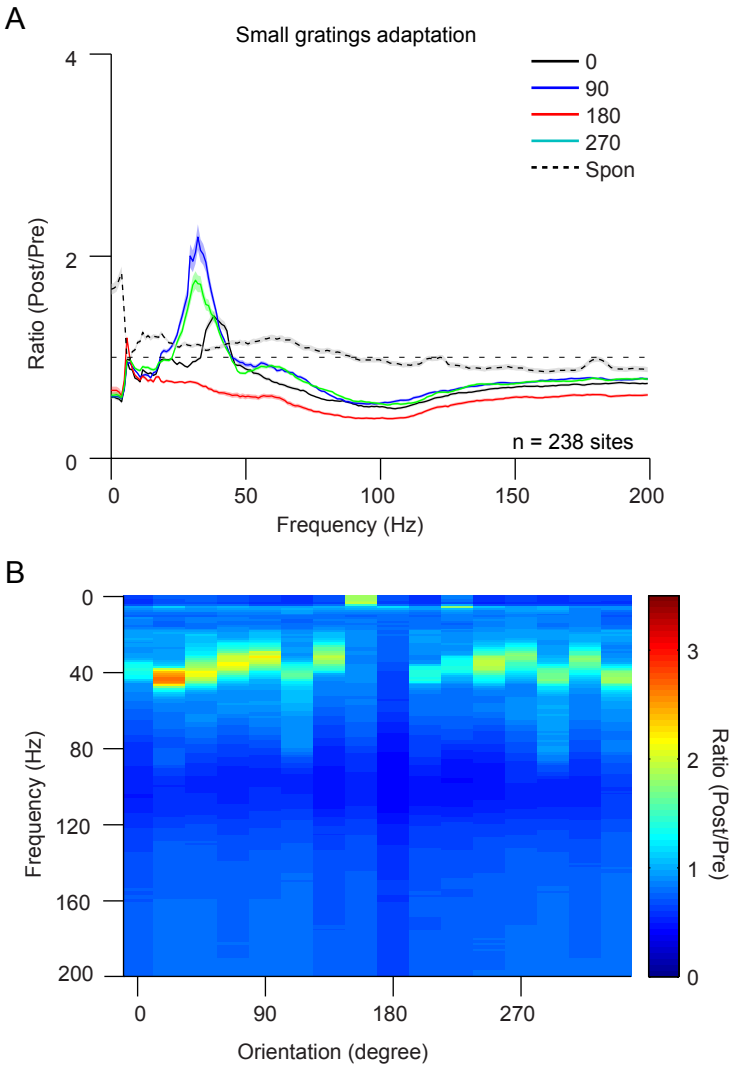
A
Small gratings adaptation
0
90
180
270
Spon
Ratio (Post/Pre)
4
2
0
n = 238 sites
0
50
100
150
200
Frequency (Hz)
B
Frequency (Hz)
0
40
80
120
160
200
0
90
180
270
Orientation (degree)
Ratio (Post/Pre)
3
2
1
0

Figure 3.5 Effects of adaptation on SFC. (**A**) Population average of difference in SFC after adaptation compared to before adaptation. The orientations identical (black and red) and orthogonal (blue and green) to the adapter, along with the spontaneous/blank stimuli condition (black dashed line) are plotted. Values above 0 indicate increased SFC. Dashed grey line at 0 indicates no change in SFC. (**B**) Averaged SFC in the low frequency (<10Hz) for all sites (n=480 sites) pre- (black) and post- (red) adaptation. Dashed lines indicate the low frequency SFC for spontaneous activity. (**C**) Averaged SFC in the gamma frequency band for all sites (n=480 sites) pre- (black) and post- (red) adaptation. Dashed lines indicate the gamma band SFC for spontaneous activity.

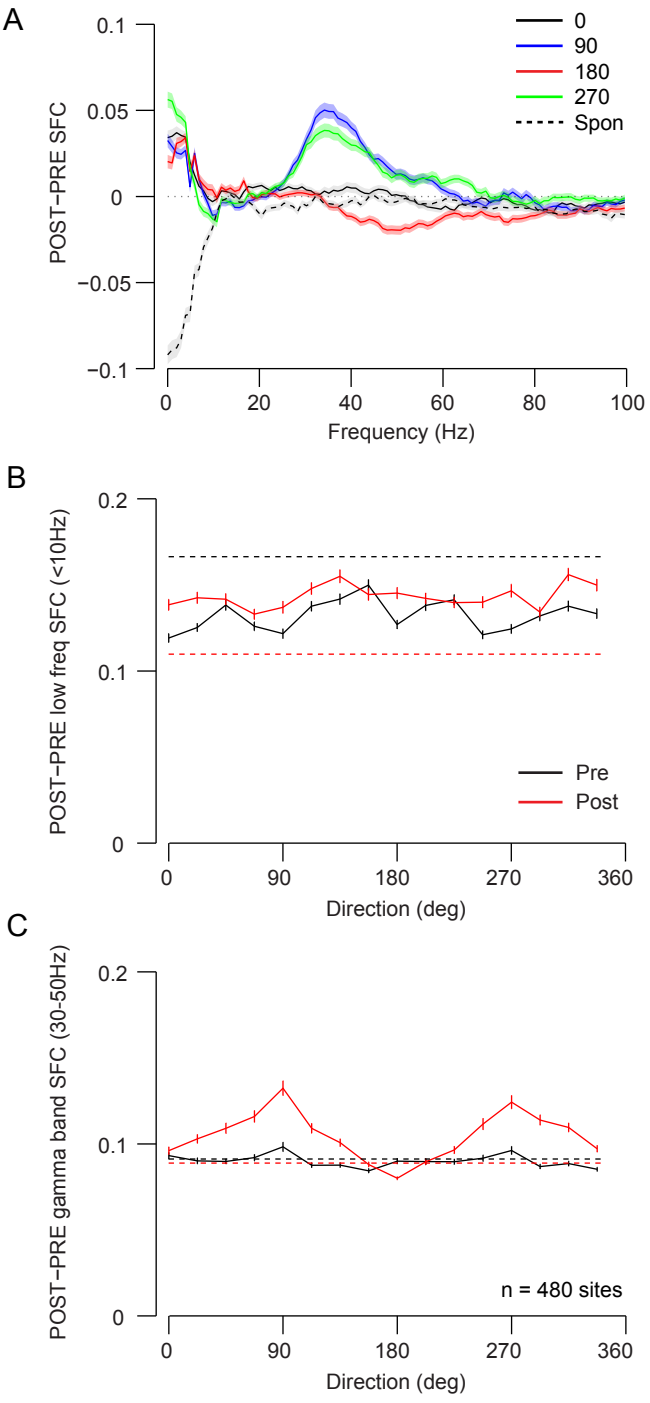
A
0.1
0.05
0
−0.05
−0.1
POST−PRE SFC
0
90
180
270
Spon
0
20
40
60
80
100
Frequency (Hz)
B
0.2
0.1
0
POST−PRE low freq SFC (<10Hz)
Pre
Post
0
90
180
270
360
Direction (deg)
C
0.2
0.1
0
POST−PRE gamma band SFC (30-50Hz)
n = 480 sites
0
90
180
270
360
Direction (deg)

Figure 3.6 Effect of adaptation on neuronal spike count correlation. (**A**) Distributions of pairwise neuronal correlation before (black) and after (red) adaptation with a large grating, for orientations identical to the adapter (n = 27208 pairs). (**B**) Distributions of neuronal correlations averaged across orientations, before and after adaptation. (**C**) Distributions of neuronal correlations during spontaneous activity, before and after adaptation.

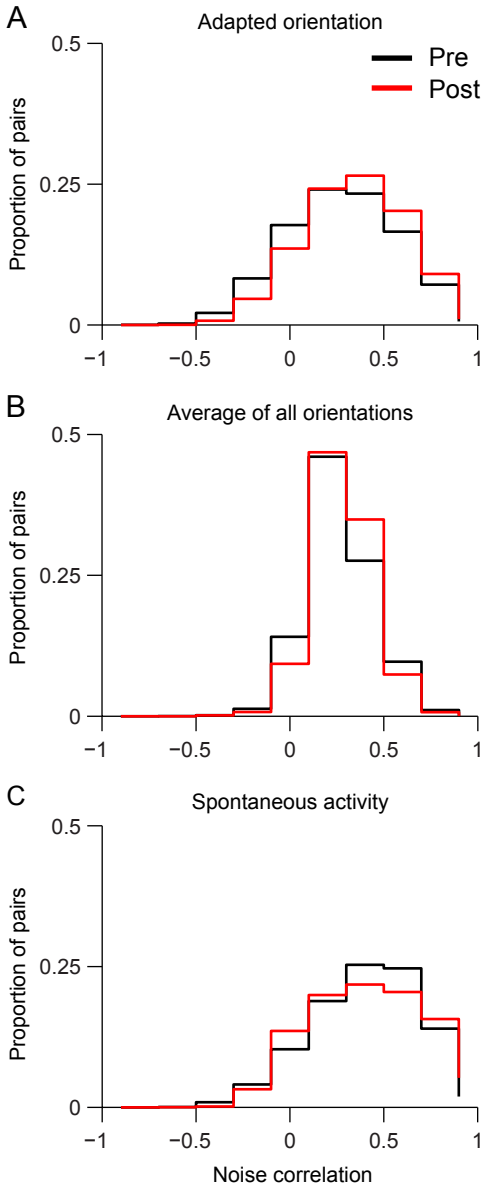
A
Adapted orientation
Pre
Post
Proportion of pairs
0.5
0.25
0
−1
−0.5
0
0.5
1
B
Average of all orientations
Proportion of pairs
0.5
0.25
0
−1
−0.5
0
0.5
1
C
Spontaneous activity
Proportion of pairs
0.5
0.25
0
−1
−0.5
0
0.5
1
Noise correlation

Chapter 4: Gamma rhythm, neuronal synchrony, and corticocortical communication in early visual cortex

Xiaoxuan Jia[1] and Adam Kohn[1,2]

[1] Dominick Purpura Department of Neuroscience

[2]Department of Ophthalmology and Vision Sciences

Albert Einstein College of Medicine, Bronx NY 10461

Acknowledgements: This work was supported by grants from the National Institutes of Health to AK (EY016774) and MAS (EY015958 and EY018894). We thank Amin Zandvakili, Stephanie Wissig, and Carlyn Patterson for assistance with data collection.

X.Jia designed and performed the experiments. X.Jia analyzed all the data in this section.

4.1 Abstract

Gamma frequencies of the local field potential (LFP) are elevated during cognitive and perceptual functions. A number of proposals have suggested that gamma can influence neuronal population synchrony and that this enhances the relaying of signals between cortical areas. However, the precise relationship between spiking activity and gamma LFP power remains unclear, and the influence of coordinated spiking activity on corticocortical signaling remains largely untested. We investigated these issues by simultaneously recording from populations of neurons in V1 and V2 in anesthetized macaque monkeys. We used stimulus manipulations to alter gamma power and spatial coherence systematically over a broad range. We found that visual stimuli that induce a strong, coherent gamma rhythm result in V1 spiking activity that is more temporally coordinated, leading to an enhancement of pairwise and higher-order synchrony. To test the functional consequence of this on corticocortical communication, we measured the correlation of activity between V1 and V2 neurons. We found coupling was enhanced in a retinotopically-specific manner, when gamma was elevated. This was due primarily to the gamma modulation of V1 firing, rather than an influence of the V2 rhythm. Our results show that changes in gamma power are indicative of altered population synchrony and that greater spike timing correlation can influence corticocortical signaling.

4.2 Introduction

Gamma band (~30-50 Hz) activity has been proposed to be an important coding mechanism in the brain. One proposal is that the timing of spiking activity relative to the phases of gamma cycle directly encodes sensory information ((Fries et al., 2007; Vinck et al., 2010), but also see (Kayser et al., 2009)). Gamma has also been proposed as a mechanism to link the distributed representation of sensory stimuli within a cortical area (Gray et al., 1989). A related, but distinct, proposal is that gamma determines a communication window to dynamically route information between neuronal populations (Colgin et al., 2009; Fries, 2009; Schoffelen et al., 2005a; Womelsdorf et al., 2007), particularly those in distinct cortical areas.

All of the proposed functions of gamma rely on an interaction between gamma rhythms and spike timing. The mechanistic basis for such a modulation lies in the fact that the activity of inhibitory neurons fluctuates rhythmically within the gamma cycle (see reviews by (Bartos et al., 2007) and (Whittington et al., 2011)). If neurons are embedded in networks with strong gamma activity, fluctuating inhibition could synchronize spiking activity, potentially leading to more effective drive to downstream targets (Fries, 2009; Salinas and Sejnowski, 2001; Singer, 1999). If the downstream network also has strong gamma activity, the efficacy of synaptic input may be modulated by its phase with respect to the local gamma cycle, being maximal when it arrives at the excitatory phase of the rhythm in the target area (Fries, 2009).

Gamma-band modulation of spike timing in visual cortex has been studied by numerous groups. Some studies have found gamma-modulation of single cell and MUA spiking activity, and the synchrony between pairs of such units, but others have not (see reviews by (Fries, 2009; Gray, 1999; Singer, 1999) and Discussion). This may be due in part to differences in stimulus conditions, which are now known to strongly modulate gamma power in the LFP (Berens et al., 2008; Frien et al., 2000; Gieselmann and Thiele, 2008; Henrie and Shapley, 2005; Jia et al., 2011; Lima et al., 2010; Liu and Newsome, 2006; Ray and Maunsell, 2010). Recent studies have used the coherence between the LFP and single neuron spiking activity in the gamma band as an arguably more sensitive method for detecting shared, weak fluctuations in a distributed population (Fries et al., 2008; Gregoriou et al., 2009; Pesaran et al., 2002). However, how altered gamma spike-field (or spike-spike) coherence is reflected the coordination of spiking responses in a distributed neuronal population remains unclear. Gamma components of the LFP represent a small fraction of the power in that signal, so changes in gamma coherence may have a small effect on spike timing coordination overall. Further, neurons may be gamma-phase modulated at different times, reducing the coordination of the ensemble. To understand the gamma-band coordination of distributed spiking activity requires simultaneous recordings from populations of neurons, and systematic and controlled manipulation of gamma power. Despite widespread interest and speculation into the function of gamma, no study has performed such measurements.

Knowing how changes in gamma power are reflected in altered ensemble activity provides a partial answer to its putative role in corticocortical communication. The

second issue is whether the strength of coordination is significant enough to affect the relaying of signals to downstream areas. Modeling studies suggest that signal transmission is more efficient when synchrony is enhanced (Akam and Kullmann, 2010; Knoblich et al., 2010; Salinas and Sejnowski, 2000, 2001), but these typically explore particularly strong gamma modulation, In vivo recordings have shown conditions under which interareal field-field or spike-field gamma coherence is elevated (Buschman and Miller, 2007; Frien et al., 1994; Gregoriou et al., 2009; Montgomery and Buzsaki, 2007; Popescu et al., 2009), but how this is reflected in altered coordination of spiking responses across areas is less clear. In particular, no study has provided a systematic, quantitative evaluation of how changes in gamma affect corticocortical coupling of spiking responses.

Here we study the relationship between gamma power in the LFP, spiking synchrony and corticocortical communication in early visual cortex. To evaluate the relationship between gamma and spike timing, we recorded LFP and spikes in the superficial layers of primary visual cortex (V1) using microelectrode arrays. We used manipulations of stimulus size and orientation to modulate gamma strength in a controlled and parametric manner. We find that stronger and more spatially coherent gamma is associated with stronger gamma-modulation of spike timing and enhanced pairwise and higher order synchrony. To test the consequence of this coordination, we paired our V1 measurements with simultaneous recordings in V2, a direct downstream target of the V1 population. We find that when V1 activity is more coordinated, each V1 spike is more likely to be

followed by one in V2 several milliseconds later. Our results show that elevated gamma is associated with enhanced synchrony and more effective corticocortical coupling.

4.3 Materials and methods

Animal preparation and electrophysiology

We recorded from seven anesthetized, adult male macaque monkeys (*Macaca fascicularis*). Anesthesia was induced with ketamine (10 mg/kg) and maintained with isoflurane (1.5-2.5% in 95% O_2) during venous cannulation. The animal was then placed in a stereotax and anesthesia was provided by intravenuous infusion of sufentanil citrate (6-18 μg/kg/hr, adjusted as needed for each animal), in normosol with dextrose (2.5%). Vecuronium bromide (0.1 mg/kg/hr) was administered to suppress eye movements. Temperature was maintained at 36-37 C°. Physiological signs (electrocardiogram, blood oxygen saturation, end-tidal CO_2, electroencephalogram, temperature, and urinary output and osmolarity) were monitored to ensure adequate anesthesia and animal well-being. A broad-spectrum antibiotic (Baytril, 2.5 mg/kg) and an anti-inflammatory steroid (dexamethasome, 1 mg/kg) were administrated daily. All procedures were approved by the Institutional Animal Care and Use Committee of the Albert Einstein College of Medicine at Yeshiva University.

We implanted a 100 multielectrode array (10x10 grid with 0.4 mm spacing and 1 mm electrode length) in the upper layers (0.6-0.8 mm deep) of primary visual cortex (V1), ~10 mm lateral to the midline and ~8 mm posterior to the lunate sulcus. The signal on each electrode was filtered between 250 Hz and 7.5 kHz to provide spiking activity. Events that exceeded a user-defined threshold were sampled at 30 kHz and saved for offline sorting. Raw signals were also filtered between 0.3 Hz and 250 Hz and sampled at 1 kHz to provide local field potentials (LFPs). To record responses in V2, a separate

multielectrode device was used, which consisted of up to 7 independent electrodes and tetrodes (305 micron spacing; Thomas Recording). Raw signals recorded from this device were filtered between 0.5 Hz and 200 Hz for LFPs (digitized at 1 kHz) and 500 Hz and 10 kHz for spiking activity (events exceeding a threshold were sampled at 40 kHz).

To remove 60 Hz noise from the LFP, we applied a fourth order Butterworth band-stop filter to the raw data. Spikes were sorted using commercial software (Plexon Offline Sorter) and standard algorithms and criteria. Only units with a signal-to-noise ratio (Kelly et al., 2007) larger than 2, corresponding to single units and small clusters of such cells, were used for further analysis. This typically corresponded to considering responses from the top half of recording sites, in terms of recording quality. Our results were not sensitive to the precise section of data considered.

Visual stimulation

Stimuli were generated with EXPO (https://corevision.cns.nyu.edu/) and presented on a linearized CRT monitor (1024x768 pixels; refresh rate 100 Hz) placed 110 cm from the animal. We mapped the receptive fields of V1 and V2 recording sites by briefly presenting small, full contrast drifting gratings (0.6 degree; 250 ms) of different orientations at a range of spatial positions. The spiking responses at each site were fit with a 2D Gaussian to determine the location and extent of the spatial receptive fields. We used these measurements to center full contrast gratings on the aggregate receptive field. Gratings had a fixed spatial frequency (1 cycle/degree) and temporal frequency (6.25 cycle/second).

We used two sets of stimuli. The first contained gratings drifting in 16 different directions, with sizes ranging from 1-10 degrees; each stimulus was presented for 1 second in pseudorandomized order (30 repetitions). These stimuli were viewed monocularly and used to characterize size-dependent effects (n=6 implants). The second set of stimuli used only small (2-3.5 degree) and large (10 degree) grating of 8 orientations, but each was presented 300-400 times (1.28 s with 1.5 interstimulus interval) to provide us with a sufficient number of spikes to investigate timing relationships in detail (n=5 implants). Large and small stimuli were presented in separate blocks of trials, so the number of recorded neurons varied slightly between conditions with this stimulus protocol. These stimuli were viewed binocularly.

Data analysis

We analyzed response epochs when gamma was prominent and firing rates were relatively stationary, which we defined as 100 ms after stimulus onset until the end of the stimulus presentation. For all comparisons involving stimuli of different sizes, we included only recording sites whose receptive field center was within the radius of the smallest grating.

We analyzed the power spectrum of the LFP and spiking activity with the multi-taper method, using the Chronux Toolbox. We applied k = 2WT-1 orthogonal Slepian tapers to the data, where T is the duration of the data and W is the half bandwidth of the smoothing

window, which we chose to be 5 Hz. The LFP signal was treated as a continuous signal and its power spectrum (S_{xx}) was calculated by computing the Fourier transform:

$$X_k(f) = \sum_{t=1}^{N} w_t(k) x_t e^{-2\pi i f t}, \quad (1)$$

where $w_t(k)$ is kth taper function and then averaging the modulus squared across tapers

$$S_{XX}(f) = \frac{1}{K} \sum_{k=1}^{K} \left| X_k(f) \right|^2 \quad (2)$$

Spike trains were treated as a discrete signal, binned with 1 ms resolution into a sequence of event times t_j in time window [0 T]. The spectrum was estimated using the Fourier transform of a counting process:

$$dN_k(f) = \sum_{j=1}^{N} w_{t_j}(k) e^{-2\pi i f t} - \frac{N(T)}{T} w_k(0), \quad (3)$$

where $N(T)$ is the total number of spikes in that time window and $w_k(0)$ is the Fourier transform of the tapers (Pesaran et al., 2002; Zhou et al., 2008).

We evaluated the relationship between spike timing and gamma using a number of complementary metrics. First, we evaluated spike-field coherence (SFC) by calculating the coherency, C_{xy}, as the cross-spectra between signals x and y normalized by the geometric mean of their auto-spectra:

$$C_{xy}(f) = \frac{S_{xy}(f)}{\sqrt{S_{xx}(f) S_{yy}(f)}}, \quad (4)$$

where S_{xx} and S_{yy} are calculated in equation 2 above, S_{xy} is calculated as:

$$S_{XY}(f) = \frac{1}{K}\sum_{k=1}^{K} X_k(f) Y_k^*(f) \tag{5}$$

where Y_k^* is the complex conjugate of Y_k. C_{xy} is a complex number. Its modulus represents the value of coherence, which lies between 0 and 1. The absolute value of the phase of this complex number is the relative phase difference between the two signals.

Estimating SFC using spike activity and LFPs recorded on the same electrode can result in spectral contamination due to leakage of the action potential waveform into the LFP. We therefore calculated SFC between the spiking activity on each electrode and the LFPs recorded at neighboring sites (0.4 mm distant). The SFC values in Fig 1B are the average of these SFCs. We confirmed visually that this procedure effectively removes spiking contamination of the SFC.

We analyzed the phase of spikes with respect to the gamma cycle by using a 4th order bandpass filter to isolate 30-50 Hz frequency component of the LFP. We then applied the Hilbert transform to estimate the phase of this complex signal at each time instant, and counting the number of spikes occurring in each 45 degree bin. The preferred phase, ϕ_{pref}, for each neuron was defined as:

$$\phi_{\text{pref}} = \arctan\left(\frac{\sum_{n=1}^{N} R_n \sin(\phi_n)}{\sum_{n=1}^{N} R_n \cos(\phi_n)}\right), \tag{6}$$

where R_n is the spike count of the n^{th} bin relative to the minimum spike counts across bins and ϕ_n is the center phase of the n^{th} bin. We determined the clustering of spikes in the gamma cycle, or phase bias, as:

$$\text{Bias} = \frac{\left|\sum_{n=1}^{N} R_n e^{i\phi_n}\right|}{\sum_{n=1}^{N} R_n}. \quad (7)$$

To evaluate the relationship between spike times in pairs of neurons, we calculated the cross-correlogram (CCG) between the two spike trains x_1 and x_2 (Kohn and Smith, 2005):

$$CCG(\tau) = \frac{\frac{1}{M}\sum_{i=1}^{M}\sum_{t=1}^{N} x_1^i(t)x_2^i(t+\tau)}{\theta(\tau)\sqrt{\lambda_1\lambda_2}}, \quad (8)$$

where M is the number of trials and N is the number of time bins in each trial. The CCG is normalized by (1) a triangle function $\theta(\tau) = T \pm \tau$, where T is the trial duration and τ is time lag; and (2) the geometric mean firing rate of the two neurons (λ_1 and λ_2). To correct for stimulus-locked correlations, we subtracted the shuffle corrected CCG from the raw CCG. To isolate brief timescale correlation (synchrony), we subtracted from the raw CCG a predictor calculated from surrogate data in which spike times were jittered in a 10 ms window (Harrison and Geman, 2009; Smith and Kohn, 2008). This predictor corrects for both stimulus-locked correlations and slow cofluctuations of responsivity (those occurring over epochs larger than the jitter window). Both calculations were normalized so that the units of the CCG were in coincidences/spike. We defined the strength of synchrony to be the area under the jitter-corrected CCG from time lags of -1 ms to 1 ms. For V1-V2 pairs, we defined the peak in the CCG to be most effective if the

sharp peak amplitude of the jitter-corrected CCG is larger than 5 fold of standard deviation at plus/minus 75-125 ms of the sharp peak.

Because large stimuli recruit surround suppression (Angelucci and Bressloff, 2006), the firing rate for large gratings was on average 51% of that for small gratings. Although each of the metrics we include a normalization factor for rate, we wished to be sure that issues of signal to noise at low rates would not affect our results. To control for trivial confounds due to differences in rate, we applied subsampling methods to rate-match responses from small grating with those evoked by large gratings. For experiments with 6 different sizes randomized in time, we matched to the lowest number of spikes across all stimulus conditions, whereas for experiments with more repetitions and two size conditions without randomized conditions, we down-sample the firing rate according to the average proportion of firing rate between large and small conditions. When comparing probability of V2 spike following each V1 spike for different gamma phases, we matched the number of spikes to the lowest firing rate bin among all phases for each trial and stimulus condition. For calculations that involved normalization by firing rate (SFC, SSC, and CCG), results were similar between rate-matched and raw data.

All indications of variance are standard errors of the mean, unless otherwise indicated. All tests of statistical significance are two-tailed t-tests, unless otherwise indicated.

4.4 Results

The relationship between spike timing and gamma components of the LFP

We used 10×10 multielectrode arrays implanted in the upper layers of primary visual cortex (V1), to record spiking activity and local field potentials (LFPs) simultaneously. Visual fields of the recorded units were 2-4° from the fovea, in the lower visual field. We collected data from 9 hemispheres of 7 anesthetized macaque monkeys.

Stimulus size has been shown to alter both gamma power and its peak frequency (Gieselmann and Thiele, 2008; Jia et al., 2011; Ray and Maunsell, 2011a), making it a potentially useful manipulation for investigating the relationship between spike timing and gamma. We therefore measured responses to full contrast drifting gratings ranging in size from 1-10 degrees. We analyzed responses only from those electrodes driven by the smallest grating, so that a common set of neurons could be compared across conditions. We averaged responses across all stimulus orientations (8 orientations, each drifting in one of 2 directions) and all sites, regardless of orientation preference.

Consistent with previous studies, we found gamma power (30-50 Hz) was enhanced and its peak frequency reduced for larger stimuli (Figure 4.1A, n=236 sites). Stimuli 1 degree in diameter (black line) induced little gamma power. Two degree stimuli (green) induced a weak gamma "bump" (Jia et al., 2011; Ray and Maunsell, 2011a) with a peak frequency of 43 Hz. For 10 degree stimuli, the peak frequency shifted to 37 Hz and gamma power increased 2-fold, compared to that induced by the smallest stimulus.

To test whether enhanced gamma power was reflected in a tighter relationship between spike timing in individual neurons and the gamma rhythm, we calculated the spike-field coherence (SFC) for each stimulus size (Figure 4.1B). The value of SFC reflects both amplitude covariation and the consistency of the relative phase of the two signals. We used the LFP recorded at electrodes adjacent to the one measuring spiking activity, to preclude direct spectral contamination of LFPs by spike waveforms (Ray and Maunsell, 2011a; Zanos et al., 2011).

Gamma-band SFC was 36% higher for activity driven by large (10 degree) gratings compared to small (1 degree gratings; 0.091±0.002 vs. 0.067±0.001; $p<0.0001$). Note that this was not the case for slightly higher frequency bands (e.g. 80-100 Hz). Like gamma, power in this frequency range was modulated by stimulus size (Figure 1A) but this was not paralleled by a change in SFC. In addition to an increase in gamma SFC, we observed a decrease in gamma peak frequency for larger stimuli, from 54 to 36Hz. Across sites, the correlation between the gamma-band peak frequency of SFC and power for stimuli of different sizes was 0.89±0.04, (n=236 sites). Thus, when gamma power is elevated, there is an enhanced relationship between gamma components of the LFP and gamma-band spiking activity.

To determine the spatial extent of elevated gamma-band SFC, we compared spikes and LFPs recorded by sites separated by a range of distances (n=10,212 pairings). Coherence was elevated across several millimeters for activity driven by 10 degree but not 1 degree gratings (Figure 4.1C). Note that we only considered a common set of sites for both

conditions--those for which the smallest stimulus covered a significant portion of the receptive field (see Methods)--so the difference in coherence does not reflect a trivial difference in the extent of activated cortex. For the larger grating, gamma coherence decayed from 0.091±0.003 for sites separated by 400 microns to 0.071±0.001 for sites separated by 3.2 mm, a trend that was well described as an exponential decay with a space constant of 2.8 mm. The spatially extensive gamma SFC is consistent with the long-range LFP-LFP coherence in the gamma band, for signals induced by large drifting gratings (Jia et al., 2011; Juergens et al., 1999).

To test how enhanced SFC was reflected in the gamma-modulation of spike timing, we measured the distribution of spikes within a gamma cycle. We bandpass filtered the raw LFP to isolate its gamma components and then applied the Hilbert transform to estimate the phase of this composite signal at each instant (Figure 4.2A; (Colgin et al., 2009; Galindo-Leon et al., 2009; Montemurro et al., 2008; Rajkai et al., 2008; Rubino et al., 2006); see Methods). The distribution of spikes evoked by a 10 degree grating, with respect to gamma phase, is shown for one neuron in Figure 4.2B. This cell had a slightly higher tendency to fire at a phase near 180 degrees, corresponding to the trough of the gamma rhythm.

To quantify effects across cells, we determined the preferred gamma phase and the phase bias for each neuron (see Methods). For the example neuron (Figure 4.2B), the preferred phase was 156 degrees (arrowhead) with a bias of 0.46, where a value of 0 indicates no phase modulation and 1 indicates perfect locking given the noisiness in spike timing.

Figure 4.2C shows the distribution of preferred phases for all neurons in one implant. Neurons had a tendency to fire at the trough of the gamma cycle when activity was driven by 10 degree gratings (red), but this was not evident for responses to 1 degree stimuli (gray). Correspondingly, the mean bias in this implant was 0.37±0.02 for activity driven by large gratings, compared to 0.24±0.03 for small ones (n=31 sites), a statistically significant difference ($p=0.0003$). Across implants, the bias observed for responses to large gratings (0.33±0.01) was significantly greater than small (0.25±0.01; n=236; $p<0.0001$). Consistent with this analysis, a test of the strength of modulation at individual sites showed that 25.4% of sites were significantly modulated when activity was driven by small gratings (Rayleigh test, significance level=0.05; n=236 sites), whereas for activity driven by large gratings 54.2% of sites were significantly modulated.

Our analysis shows that the clustering of spike times in the gamma cycle is more evident when gamma power in the LFP is more prominent. When driven by large gratings, spikes from individual neurons are more temporally coordinated and have a tendency to cluster at the same gamma phase. We next evaluated how this affected the strength of pairwise and higher-order spiking synchrony in the population.

Influence of gamma on neuronal synchrony in V1

Since individual neurons tend to fire at the same phase of the coherent gamma rhythm, the probability that these neurons fire synchronously should be elevated when gamma power is enhanced. We therefore compared the temporal coordination of spiking activity in a neuronal population driven by small and large gratings. Because accurate estimation

of spike timing correlation requires a large number of spikes, we measured responses to many presentations (300-400) of stimuli of two sizes: 10 degree gratings and ones 2-3.5 degrees in size. The smaller size was chosen to cover all of the spatial receptive fields, but induced a clearly weaker gamma rhythm than the larger stimulus (Figure 4.1A). As in our previous analysis, we rate matched the responses across conditions for all cells.

To measure pairwise spike timing correlation, we calculated cross-correlograms (CCGs) between all neuron pairings. The average shuffle-corrected CCG had a larger peak at 0 ms time-lag for activity evoked by large (Figure 4.3A; red line; n=24,167 pairs) compared to small gratings (black line; n=24,261 pairs). The CCG for the former condition also showed clear oscillatory side lobes, indicating rhythmicity in the coordinated firing. This was reflected in the power spectrum of the CCG: gamma power increased 45 fold, with a shift in peak frequency to 48 Hz for 39 Hz for activity driven by large gratings (Figure 4.3B). Gamma band spike-spike coherence (SSC) was also significantly stronger for large gratings than for small, and the peak frequency of SSC in the gamma band shifted from 47 Hz to 38 Hz when stimulus size was increased (Supplementary Figure 1A).

To isolate synchrony from co-fluctuations over longer time scales, we corrected the raw CCG with a predictor derived from jittered data. We chose a jitter winder of 10 ms to isolate fine-time scale synchrony (see Methods). This correction removes all correlations arising on timescales larger than the jitter window (Harrison and Geman, 2009; Smith and Kohn, 2008). Synchrony, measured as the area of the jitter-corrected CCG peak (±1

ms of 0 ms time lag), was 3.4 fold larger for large gratings than small ones (4.24±0.2E-4 vs. 1.23±0.04E-4, $p<0.0001$; Figure 4.3C). The stronger pairwise synchrony in the population arose from greater coordination between both nearby and more distant pairs (Figure 4.3D). Although the increase in synchrony was substantial, its magnitude remained small, meaning that synchronous events remained rare even when gamma power was elevated.

To extend our analysis beyond pairwise synchrony, we calculated the frequency of higher-order synchronous events: that is, events consisting of 3-7 neurons firing within 1 ms of each other. For activity driven by large gratings, there were more events consisting of several cells firing synchronously (Figure 4.3E), and fewer of events consisting of only one or two simultaneously active neurons, compared to responses driven by small gratings (Figure 4.3F, n=990,000 1 ms epochs). Note that events consisting of two neurons firing together (which become less frequent when stimulus size is increased) are not equivalent to measures of pairwise synchrony: the former is defined as *only* two cells in the recorded population firing (all others silent), whereas measures of pairwise synchrony do not consider activity in a broader population.

In complementary analysis, we found that higher-order synchronous events tended to occur at a more consistent phase of the gamma rhythm than lower-order ones. This was evident by greater gamma power in the event-triggered average of the LFP when events consisted of more co-active neurons (Supplementary Figure 2).

In conclusion, the gamma phase modulation of spike timing in individual neurons is associated with enhanced pairwise and higher-order synchrony. Increasing stimulus size, which results in more gamma power in the LFP and a shift in peak frequencies in the gamma range to lower frequencies, can enhance spiking synchrony with modulation at corresponding gamma frequencies.

Coupling of V1 and V2 spiking activity

A central tenet of the proposal that gamma influences corticocortical communication is that the temporal coordination of spiking activity in a neuronal population should result in stronger drive to downstream neurons (Akam and Kullmann, 2010; Knoblich et al., 2010; Salinas and Sejnowski, 2000, 2001). To determine how the coordination of V1 spiking activity affects its coupling with downstream networks, we paired our V1 recordings with simultaneous measurement of activity in V2 using arrays of tetrodes and electrodes (Figure 4.4A). We performed these experiments in 4 animals with 4 array implants in V1 and 7 recording sites in V2, which gives us 528 neurons in V1 and 181 neurons in V2 in total.

Areas V1 and V2 in the macaque monkey form a clear functional hierarchy (Felleman and Van Essen, 1991), with V2 entirely reliant on V1 input for its function: reversible cooling of V1 results in the abolition of visually-driven responses in V2 (Girard and Bullier, 1989; Schiller and Malpeli, 1977). Cooling of V2, on the other hand, has much weaker effects on V1 (Bullier et al., 1996). Corticocortical projections from V1 originate in layers 2/3 and 4B; fibers projecting to V2 terminate primarily in layer 4 and deep layer

3 (Felleman and Van Essen, 1991; Rockland, 1992; Van Essen et al., 1986). To target these sets of neurons, we implanted arrays roughly 600 microns into V1 (never more than 1 mm, the length of the electrodes) and lowered an array of tetrodes and electrodes to the middle layers of V2, at a nominal depth of 800-1200 microns from the layer 6/white matter border. We made use of the clear retinotopic organization of these two areas to target V2 neurons having spatial receptive fields that were aligned with those in V1 (Figure 4.4B). This provided groups of neurons that could be expected to be anatomically and functionally related.

We determined the effect of changes in population synchrony on corticocortical communication by measuring the relationship of V1 spiking activity with that in downstream V2 neurons, in pairs whose receptive fields were offset by less than 1 degree (center-to-center spacing; see Methods). The population average shuffle-corrected V1-V2 CCGs had two components (Figure 4.4C): a broad peak several hundred milliseconds wide, and a narrow peak. The broad peak indicates a tendency for the firing of the neurons to co-fluctuate on a time scale of a few hundred milliseconds (Kohn and Smith, 2005) whereas the narrow peak indicates tighter coupling of activity. For activity driven by large gratings (n=16,786 pairs; red line), the average V1-V2 CCG showed a suppressed broad component, an enhanced sharp peak, and an increase in the amplitude of the oscillatory side lobes, compared to CCGs calculated from responses to small gratings (n=16,128 pairs; black line). Gamma power in the V1-V2 CCG increased 5.9 fold for the larger stimulus, and gamma peak frequency decreased from 43 to 40 Hz.

To isolate the brief timescale component of the CCG, we corrected raw CCGs with a predictor using a 10 ms jitter window. The average jitter-corrected CCG showed a 68% increase in area for activity driven by large (Figure 4.4D, red trace) compared to small gratings (black; 1.4±0.1E-4 vs. 0.85±0.1E-4 coin/spk; p=0.0004). In 2.7% of V1-V2 pairs, the jitter-corrected CCG had a significant peak (see Methods), with a mean peak offset of 2.2±0.1 ms, indicating an increased tendency of the V2 cell to fire after the V1 cell with this delay. This is consistent with the conduction and synaptic delays for signals between these areas (Girard et al., 2001). In pairs for which the sharp peak was significant, we observed a 67% enhancement in area (p=0.04; Supplementary Figure 3).

To determine the specificity of the enhanced coupling between V1 and V2 spiking activity, we measured how the change in V1-V2 CCG depended on the RF separation between V1 and V2 recording sites. The amplitudes of the narrow and broad CCG peaks were larger at more overlapping locations, for both small and large grating conditions (Figure 4.4E-F). Subtracting the CCGs for activity driven by small gratings from those for large gratings revealed a suppression of the broad peak (blue colors in Figure 4.4G), facilitation of short timescale correlation (orange and yellow colors in Figures 4.4G), and stronger gamma-band side lobes in the CCG. Importantly, the modulation of V1-V2 CCGs by stimulus size was most apparent for sites separated by less than 1 degree, indicating that the effect was spatially specific. For pairs with RF offset of greater than 1 degree, sharp CCG peaks were infrequent, even when driven by large gratings.

Relationship between V1 and V2 gamma rhythm and their role in modulating coupling

The stronger V1-V2 coupling for spiking responses that are strongly gamma-modulated could arise from two distinct mechanisms. First, it could be that brief timescale V1-V2 spiking correlation is enhanced because each V1 spike is more likely to be accompanied by synchronous spikes in the presynaptic population (Figure 4.3). This would result in a higher probability that a V2 cell integrating these inputs would fire, causing a larger peak in the V1-V2 CCG at short time lags. A second possibility is that the V1-V2 coupling is enhanced because of modulation by the V2 gamma rhythm if V1 input arrives at a V2 gamma phase which is most advantageous for triggering a spike (e.g. when local inhibition within V2 is minimal) (Atallah and Scanziani, 2009; Cardin et al., 2009; Fries et al., 2007; Hasenstaub et al., 2005). We therefore aimed to determine whether V1 and V2 gamma rhythms were coordinated, and if so, how this played a role in the enhanced coupling of V1 and V2 spiking activity.

We first measured the coherence between V1 and V2 LFPs, as a function of the separation between the V1 and V2 spatial RFs of neurons recorded at each site (Figure 5A). Coherence was stronger between sites representing similar visual locations, and stronger in the gamma frequencies for large gratings which induce more gamma power both in V1 (Figure 4.1) and V2 (Supplementary Figure 4A). Gamma band coherence between sites with receptive fields separated by less than 1 degree was 0.424±0.002 for activity driven by large gratings, compared to 0.377±0.001 for small gratings ($p<0.0001$; n=2,197 pairs of sites, matched for small gratings; Figure 4.5B). This change in field potential coherence with stimulus size is accompanied by a change in the gamma band V1 spike-V2 LFP coherence (Supplementary Figure 1B).

We then used coherence analysis to measure the relative phase difference between V1 and V2 gamma rhythms. For activity induced by large gratings, the phase difference was 88.0±0.3 degrees (Figure 4.6A; n=2,213 pairs of sites). This is significantly higher than the relative phase of gamma rhythms recorded within each cortical area from the same sites, which had an average offset of 36.9±0.1 degrees for V1 sites (Figure 4.6B: n=17,167 pairs of sites; Bootstrap, $p<0.0001$ for difference with V1-V2 phase distribution) and 46.2±3.2 degrees for V2 sites (Figure 4.6C: n=65 pairs of sites; $p<0.0001$). Thus, there is a relationship between the gamma rhythms in V1-V2. This relationship is strengthened when gamma power is elevated, and there is a phase delay of roughly 90 degrees or ~6 ms between the two rhythms (corresponding to a gamma cycle of 4-8.3 ms or 30-50 Hz). Note that this temporal delay is higher than the peak offset in the V1-V2 CCGs which indicates a delay of ~2.5 ms between V1 spiking activity and that in V2.

Having found a relationship between the V1 and V2 gamma rhythms, we next determined whether the observed change in V1-V2 coupling was due to those inputs arriving at an optimal phase of V2 gamma, or whether changes in presynaptic coordination of spike timing were primarily responsible. We used responses to large gratings (when gamma was most prominent) and determined the phase of spikes relative to the gamma cycle by Hilbert transform of gamma band-limited signals (as in Figure 4.2). We defined the preferred V1 gamma phase for each cell as that at which the probability of V1 spikes was maximal (Figure 4.7B). We then normalized the distributions to unit area and averaged

across all cells. Consistent with the single cell analysis shown in Figure 4.2, V1 spiking activity was gamma modulated (ANOVA1 F=284.78 p=0). For each phase and V1-V2 pairing (n=17,518 pairs), we then calculated the proportion of V1 spikes that were followed by a spike in V2 1-3 ms later, a delay that reflects the offset of the narrow V1-V2 CCG peak offset. The proportion was significantly modulated by gamma (ANOVA1 F=3.81, p=3.8E−4) and highest at the gamma phase at which V1 spiking was maximal (Figure 4.7C), consistent with enhanced V1-V2 coupling arising from the temporal coordination of V1 spiking.

To test the influence of the V2 gamma rhythm, we determined the V2 preferred gamma phase, defined as the phase at which V2 cells were most likely to fire. V2 firing was less strongly gamma-modulated than in V1 (Figure 4.7D), but the modulation was significant (ANOVA1, F=8.98, p<0.0001). We then computed the proportion of V1 spikes that were followed by a V2 spike, based on their timing with respect to V2 gamma phase (Figure 4.7F). Modulation was notably weaker and not significant (ANOVA1 F=1.14, p=0.34), although there was a tendency for coupling to be slightly higher at phases 45-135 degrees offset from that at which V2 cells were most likely to fire. This is similar to the phase offset between V1 and V2 gamma determined by coherence analysis (Figure 4.6). This suggests that the coupling of V1-V2 spiking activity follows the V1 rhythm and not the V2 gamma rhythm. To confirm this, we calculated the phase distribution of V1 spikes with respect to V2 gamma. This revealed a significant modulation of V1 firing (ANOVA1 F = 65.16, p<0.0001), that was offset by 90 degrees from the preferred phase of V2 spiking (Figure 4.7E). The modulation of V1 firing (Figure 4.7E) was more

consistent than the modulation of V2 firing (Figure 4.7D) with the phase-modulation of V1-V2 coupling (Figure 4.7F; Pearson correlation r=0.85) than the modulation of V2 firing (Figure 4.7D; Pearson correlation r=-0.01).

Together our results suggest that a V1 spike is more likely to trigger a spike in V2 when the V1 cell fires at the V1 gamma phase at which V1 firing is maximal. This is consistent with the enhancement of V1-V2 correlation reflecting the coordination of the V1 population firing rate. In contrast, V1 spikes were not most likely to be followed by a V2 spike when they occurred at the V2 gamma phase at which V2 cells were most likely to fire. This can be attributed to a roughly 90 degree phase shift between the gamma rhythms in these two areas, longer than the delay for spike propagation between these networks. Thus, gamma-modulated V1 activity tends to arrive in V2 several milliseconds before the optimal V2 gamma phase.

Orientation dependence of the spike-gamma relationship

In addition to enhancing gamma power, increasing stimulus size suppresses the firing of many V1 neurons (Angelucci et al., 2002b; Cavanaugh et al., 2002b; Hubel and Wiesel, 1965), and effect that may involve an alteration in the balance of cortical excitation and inhibition (Haider et al., 2010; Ozeki et al., 2004). Larger stimuli also recruit activity in a more spatially distributed network. These effects complicate the interpretation of size-dependent changes in gamma, spiking activity, and V1-V2 coupling. It is unclear, for instance, whether these are associated directly with a change in gamma, or if both gamma

and spikes are co-modulated by some external factor (e.g. altered inhibitory tone) recruited by large stimuli.

We therefore investigated the relationship of gamma, population synchrony and V1-V2 coupling by comparing responses to stimuli of different orientations but of a fixed size. We have previously shown that the gamma induced by large gratings has a common orientation preference across recording sites (Jia et al., 2011): gamma power is up to two-fold stronger for some stimulus orientations than others (see (Berens et al., 2008) for a related result). This is illustrated in Figure 4.8A, which shows the orientation tuning of gamma power averaged across sites from the same array. In this example, gratings with an orientation of 112.5 degrees (red circle) induced 2.7-fold more power than gratings oriented at 45 degrees (gray circle). Firing rates in the neuronal population, however, were similar for these two stimuli, 9.17±0.35 for best orientation and 9.31±0.36 for worst (n = 957 neurons in V1; ttest2 p=0.7747). The orientation that induced more power also led to a more coherent gamma rhythm across electrode sites (Figure 4.8B; top), with a smaller range of phase delays (bottom). Across stimulus orientations, gamma power and coherence were significantly correlated (r = 0.89±0.02, n =8 implants).

To test whether the orientation-dependent changes in gamma power and coherence were associated with altered coordination of V1 spiking activity, we compared jitter-corrected V1-V1 CCGs for the stimulus orientations that induced the most and least gamma power (Figure 4.8C; n=28,251 pairs). The orientation that generated higher gamma power

resulted in nearly two-fold stronger population synchrony (15±1.2E-4 vs. 8.1±0.3E-4; $p<0.0001$).

To investigate the consequences for corticocortical communication, we compared V1 and V2 spiking activity for these two stimulus conditions. We first confirmed that the orientation that induced the strongest gamma power in V1 also did so in V2 (Supplementary Figure 4). We then computed jitter-corrected V1-V2 CCGs for the stimulus orientations that induced the most and least gamma power. The narrow-peak of the V1-V2 CCG showed a 39% enhancement of peak amplitude on average (Figure 4.8D, 15.2±0.7E-5 vs. 10.9±0.5E-5 coin/spk; $p<0.0001$, n=11,012 pairs). As with manipulations of stimulus size, the change in the V1-V2 CCG with orientation was accompanied by a change in the gamma band V1 spike-V2 LFP coherence (Supplementary Figure 1C).

It is worth noting that orientation preferences of neurons in V2 do not follow the orientation tuning of the global gamma rhythm in V1 (Supplementary Figure 4), even though efficacy depends on orientation. This is consistent with the fact that V2 neurons also retain surround suppression as V1 neurons, but the probability of individual spikes in V1 to drive V2 neuron is higher for large gratings.

We conclude that the relationship among gamma power, V1 population synchrony and coupling of V1-V2 spiking activity does not depend on changes in stimulus size. Manipulations of stimulus orientation reveal similar effects.

4.5 Discussion

We examined the interaction between the gamma components of the LFP and spike timing in a distributed neuronal population, and tested the influence of coordinated ensemble activity on corticocortical communication. We found that visual stimuli that induce a strong, coherent gamma rhythm in V1 also result in spiking activity that is more strongly gamma phase modulated. This is associated with enhanced V1 pairwise and higher-order synchrony. More coordinated activity in V1 was associated, in turn, with a higher probability that a V1 spike would be followed several milliseconds later by one in V2. This effect was retinotopically specific, and reflected more closely the gamma rhythm in the upstream (V1) than downstream (V2) area. Changes in gamma power are thus correlated with changes in spike timing of a neuronal population and that this can affect coupling between cortical areas.

Mechanisms of gamma generation

Two models have been proposed to explain the generation of gamma (see reviews by (Bartos et al., 2007; Tiesinga and Sejnowski, 2009; Whittington et al., 2011)) . The interneuron gamma (ING) model proposes that a network of inhibitory neurons synchronizes with external activation. This leads to gamma band synchronization of excitatory neurons because of the influence of rhythmic inhibition. The pyramidal-interneuron gamma (PING) model requires recurrent connections between inhibitory interneurons and excitatory neurons to generate gamma. In this model, excitatory neurons activate inhibitory neurons, which provide feedback to the excitatory neurons and coordinate their firing. We note that in these models, and our results, it is difficult to

determine whether stronger gamma leads to a tighter coordination of activity or whether stronger rhythmic firing of inhibitory and/or excitatory cells leads to stronger gamma. In this sense, gamma is best viewed as a marker of coordination, not a cause.

Although there are differences between these models, both involve rhythmic inhibitory network activity that can modulate spike timing. Either model could thus explain the relationship we observe between gamma power and spike timing. Because the modulation of V1 spike timing only occurs with strong and spatially coherent gamma, the relevant signal is presumably the aggregated activity of a distributed pool of inhibitory neurons. Both models also suggest that inhibitory and excitatory neurons fire at different phases of the gamma cycle. In our recordings, we did not distinguish between these cell types, which might underestimate the strength of gamma modulation in either population. However, the timing of inhibition and excitation is only offset by a fraction of a gamma cycle (Atallah and Scanziani, 2009; Hasenstaub et al., 2005), so pooling responses from excitatory and inhibitory cells should not strongly distort our measurements.

Gamma and neuronal synchrony

Numerous studies have investigated gamma-band modulation of spike timing in visual cortex (see (Gray, 1999; Singer, 1999) for review). In early work, measurements of gamma-modulation in single neurons provided mixed results, with some groups reporting that such modulation was common (Engel et al., 1991a; Friedman-Hill et al., 2000; Ghose and Freeman, 1992; Gray et al., 1990; Gray et al., 1989; Gray and Viana Di Prisco, 1997; Livingstone, 1996; Samonds and Bonds, 2005); whereas others found it was rare

(Tovee and Rolls, 1992; Young et al., 1992) or that it was due to burst firing (Bair et al., 1994). In studies of pairwise spike timing correlation, some studies reported gamma fluctuations in CCGs of pairs recorded in the same cortical area (Gray et al., 1989; Herculano-Houzel et al., 1999; Lima et al., 2010; Livingstone, 1996; Maldonado et al., 2000) whereas others did not (Bair et al., 2001; Kohn and Smith, 2005; Smith and Kohn, 2008).

Gamma fluctuations in neuronal responses can be difficult to detect because they vary in frequency and are not stimulus-locked (see Friedman-Hill et al., 2000 for discussion). Gamma power in the LFP, which reflects activity in an ensemble, has been suggested as an alternative and more sensitive measure (Gray and Singer, 1989). Gamma LFP power is sensitive to stimulus features such as contrast (Henrie and Shapley, 2005; Ray and Maunsell, 2010), size (Gieselmann and Thiele, 2008; Jia et al., 2011), masking noise (Jia et al., 2011) and orientation (Berens et al., 2008; Frien et al., 2000; Gray and Singer, 1989; Jia et al., 2011). Gamma LFP power is also elevated during cognitive events such as the allocation of attention (Fries et al., 2008) or working memory (Pesaran et al., 2002). Because gamma LFP power is a sensitive marker for such diverse manipulations, understanding its relationship to spike timing is critical.

Previous attempts to relate enhanced LFP gamma power to changes in spiking activity has relied primarily on measuring the LFP-spiking relationship, using either spike-triggered averaging of LFPs (Fries et al., 2001; Gregoriou et al., 2009), SFC (Fries et al., 2008; Gregoriou et al., 2009; Womelsdorf et al., 2006), or the gamma-phase modulation

of spiking activity in individual neurons (Colgin et al., 2009; Gregoriou et al., 2009). This has shown that enhanced gamma LFP power is paralleled by an increase in spike-field coupling in the gamma frequencies and gamma modulation of single neuron spike trains, consistent with our Figures 4.1 and 4.2. Few studies have attempted to relate these observations to changes in spike timing among pairs or larger populations of neurons. Enhanced gamma LFP power is correlated with greater spike-spike coherence (SSC) in the gamma frequencies (Fries et al., 2008; Lima et al., 2010; Womelsdorf et al., 2007).), but because gamma represents a small fraction of LFP power (Jia et al., 2011) the functional relevance of these effects is unclear. Indeed, Fries et al. (2008) showed that enhanced gamma SFC and SSC was not evident in measures of pairwise spike timing correlation (CCGs). Samonds and Bonds (2005) showed that gamma-modulation of single V1 neuron spiking activity was only weakly correlated with the strength of pairwise synchrony.

Our study focused, in part, on elucidating the relationship between gamma power of the LFP and population synchrony. We found that stimulus manipulations that led to elevated gamma LFP power also caused enhanced pairwise and higher-order synchrony. Further, the peak frequency of gamma-modulated spiking activity (evident in both SFC and CCG measures) shifted toward lower frequencies as stimulus size increased, in parallel with a similar shift in LFP peak gamma power.

The differences in gamma-modulation of spiking activity across stimulus conditions cannot be easily ascribed to differences in spike rate. Our metrics of coordination include

normalization for firing rate. More importantly, we equated firing rates across conditions to be sure there could be no statistical issues based on different number of spikes available for different stimuli. This procedure does not correct for differences in the underlying excitability of neurons in different conditions. However, for manipulations of stimulus size, we found the strongest correlation when rates were lowest, precisely when correlations are most likely to be underestimated (Cohen and Kohn, 2011). Further, we used a second stimulus manipulations to modulate gamma power, making use of the shared orientation tuning of the gamma rhythm recorded at different sites (Jia et al., 2011). We found that manipulating gamma strength and spatial coherence by changing stimulus orientation, for stimuli of a fixed size, also altered the coordination of V1 spiking activity and V1-V2 coupling. In this case, we observed no difference in population firing rate between the orientation that gave the strongest and weakest responses. There remains the possibility that firing in a broader pool of neurons was different for these two conditions (Jia et al., 2011). If this is the case, it would only strengthen our argument, as it would indicate stronger gamma modulation both for stimulus manipulations that lower rates (large gratings) and increase them (gamma-preferred orientation).

There are several possible reasons that we observed clearer gamma modulation of population synchrony than previous studies. First, using array recordings in the anesthetized animal provided us with a large number of pairings (and the ability to look at higher-order events). Whereas previous studies relied on, at most, a few hundred pairs, we investigated effects in roughly 20,000 pairs. Prolonged recording periods in the

anesthetized animal allowed us to record a large number of spikes, needed to measure accurately the strength of weak pairwise synchrony. In addition, the change in gamma LFP power we induced with our stimulus manipulations was much greater than that caused, for instance, by the allocation of attention (2-fold vs 20% in Fries et al. (2008)). The effects we observed were also associated with a gamma rhythm that was coherent across millimeters of cortex, so that it involved a broad population of cells. Small variations in the spatial similarity of a visual stimulus can disrupt gamma LFP coherence (Gail et al., 2000; Jia et al., 2011; Lima et al., 2010; Ray and Maunsell, 2010) and gamma-band neuronal synchrony (Gray et al., 1989; Lima et al., 2010; Zhou et al., 2008). Thus, naturalistic input which includes occlusions and image fragments is unlikely to generate the sort of strong, spatially coherent gamma rhythm we induce with large grating stimuli. The change in coordinated spiking activity we observed thus likely represents an upper bound on the physiological range over which gamma fluctuates *in vivo*.

Corticocortical coupling

Previous studies have found that gamma rhythms can become coherent between different cortical areas (Buschman and Miller, 2007; Gregoriou et al., 2009; Womelsdorf et al., 2007), subcortical networks (Montgomery and Buzsaki, 2007; Popescu et al., 2009), corticospinal networks (Schoffelen et al., 2005a), and hippocampal networks (Bragin et al., 1995; Colgin et al., 2009; Csicsvari et al., 2003). When this is the case, the spiking activity in one area can be coherent with the gamma components of the LFP recorded in another (Colgin et al., 2009; Gregoriou et al., 2009). These observations have been taken

as evidence that when gamma LFP power is elevated, this enhances communication efficiency between neuronal groups, perhaps serving as a dynamic mechanism for routing information between networks (Fries et al., 2007; Womelsdorf and Fries, 2006). As discussed above for intra-areal measurements, these observations are indicative of functional coupling. However, since gamma power is weak, how enhanced interareal gamma spike-field coupling translates into coordinated spiking activity has remained unclear.

Our study tackled this question by correlating spiking activity between V1 and V2, and measuring this coupling for stimulus manipulations that modulate gamma power. We find that when gamma power is elevated (large vs. small gratings or gamma-preferred orientation vs. the orthogonal) there is enhanced spike-spike correlation for subsets of neurons with retinotopically aligned spatial RFs (Figure 4). This relationship is also apparent in the gamma frequency range of field-field coherence and SFC (Figure 4.5; Supplementary Figure 1).

Our study is not the first to measure correlated spiking activity between cortical areas. For instance, correlated oscillatory firing between the retina, LGN and cortical areas 17 and 18 has been reported (Castelo-Branco et al., 1998; Neuenschwander and Singer, 1996), but some of this coordinated firing was in frequencies much higher than gamma and it was not retinotopically-specific. Engel et al. (1991) performed cross-correlation analysis between neurons in areas 17 and posteromedial lateral suprasylvian (PMLS) of the cat, and showed that these areas could display synchronous rhythmic activity in a

retinotopically specific manner. Curiously, the phase in area 17 lagged that in PMLS by 2 ms, although PMLS is a prestriate area that receives feedforward input from area 17 (Engel et al., 1991b).

In addition to quantifying effects using a much more extensive data set, our results extend these observations in several important ways. First, we link the inter-areal spiking relationship to changes in LFP power and peak frequency. Second, we record from specific networks whose connectivity is well-defined, and observed interactions in spike timing consistent with the propagation delays between these two networks (V1 leading V2 by roughly 2.5 ms). This interaction was also observed when gamma power was negligible (activity driven by small gratings) and thus does not require gamma coordination. Rather, gamma modulation appears to enhance an existing functional interaction. Finally, we investigated the relative influence of the V1 and V2 gamma rhythms on functional coupling.

The enhanced coupling of V1-V2 spiking activity could arise from the coordination of V1 population spiking activity, providing downstream networks with more synchronous input, or from timing excitatory inputs to arrive out of phase with local rhythmic gamma fluctuations in inhibition (Gregoriou et al., 2009; Schoffelen et al., 2005b; Womelsdorf et al., 2007). We therefore compared the probability that a V1 spike would be followed by one in V2, based on timing relative to the V1 and V2 gamma cycle. Comparing measurements across areas using separate recording systems can introduce distinct phase delays in the LFP (Nelson et al., 2008), so we used the local spiking activity to establish

the "preferred" gamma phase in each area. We found that coupling follows the V1 gamma rhythm more closely than the V2 rhythm. This implies that the temporal coordination of synaptic inputs is more relevant to modulate the strength of interareal coupling than the regulation of local inhibition. Consistent with this, the gamma rhythms in V1 and V2 are delayed by roughly 90 degrees (~5-8.3 ms for a 30-50 Hz signal). Since the delay in correlated spiking activity in these two networks is only 2 ms, inputs do not arrive at the optimal gamma phase. This additional delay likely reflects the recruitment of local V2 circuits that generate gamma in that area. Timing inputs to arrive at a non-optimal phase of the local rhythm may be necessary to prevent an accumulation of synchrony as signals are passed sequentially through feedforward networks (Reyes, 2003).

Our results differ from those of Gregoriou et al. (2009) who found a phase difference between the gamma rhythms in frontal eye field and area V4, corresponding to a temporal difference of about 8 to 13 ms (Gregoriou et al., 2009). The delay between FEF and V4 has been attributed to conduction delays (Gregoriou et al., 2009), but the coordination of spiking activity in these two areas was not measured. Further work will be needed to distinguish definitively the relative influence of these two mechanisms, for instance by comparing coupling between a single presynaptic network and two downstream ones, with different gamma signals.

Limitations of gamma

Our findings provide evidence that enhanced gamma power is associated with changes in the coordination of spiking activity in a neuronal ensemble, both within a cortical areas and between distinct networks. Whether this indicates that gamma plays an important functional role in sensory processing remains unclear. First, when gamma power is strongest, the rhythm is coherent across millimeters of cortex (Jia et al., 2011). Thus, when it is strongest, gamma lacks the spatial and functional specificity needed to select specific subgroups of neurons to be bound or to be preferentially routed to downstream targets. Second, the dynamics of gamma are relatively slow (Burns et al., 2010a; Jia et al., 2011; Kruse and Eckhorn, 1996), rising slowly after stimulus onset and peaking 200-300 ms later. Because the input to the visual system changes frequently, with each saccade, the slow onset of gamma may limit its functional role. Third, as discussed previously, gamma power is easily disrupted by occlusions or masking of visual input. Finally, while our results indicate fairly strong (2-fold) changes in temporal correlation of spiking activity, this correlation remains quite weak. Roughly 1-3 out of 1000 V1 spikes is synchronized with an event in another cell. The importance of modulating this weak synchrony, relative to potentially much stronger fluctuations in rate (100-fold), remains to be established. These limitations of gamma must also be taken into account when evaluating whether it plays an important functional role in cortical processing.

Summary

Our study extends our understanding of the relationship between gamma LFP power and spiking activity in several ways. First, we studied gamma in networks driven with visual input which manipulated the strength and spatial coherence of gamma over a broad range.

Second, we tested the relationship between gamma and spike timing in a spatially extensive network, allowing us to reveal the influence of gamma across the cortical surface and to characterize effects at the level of single neuron firing and pairwise and higher order synchrony. Finally, we measured the consequence of altered ensemble activity on relationship of V1 inputs and responses in a downstream network in the middle layers of V2. Together our findings show that the strongly elevated gamma is associated with altered temporal coordination of spiking activity in a distributed population and that this alters the coupling between cortical networks.

4.6 Figure legends:

Figure 4.1 Effects of stimulus size on gamma LFP power and spike-field coherence. (**A**) Power spectra of LFP for sites activated by the smallest grating (n=236 sites), with different colors indicating responses to grating ranging in diameter from 1 to 10 degrees. LFP power was dominated by low frequency (<20 Hz) power; only higher frequency components are illustrated for clarity of display. Shading indicates SEM. (**B**) Average spike-field coherence (SFC) of the spikes from each recording site and the LFP from neighboring sites (0.4 mm) for different sizes. Shading indicates SEM. Dashed lines indicate the coherence calculated after shuffling the trials. (**C**) SFC (0-140 Hz) as a function of inter-electrode distance for 1 degree (left) and 10 degree (right) gratings.

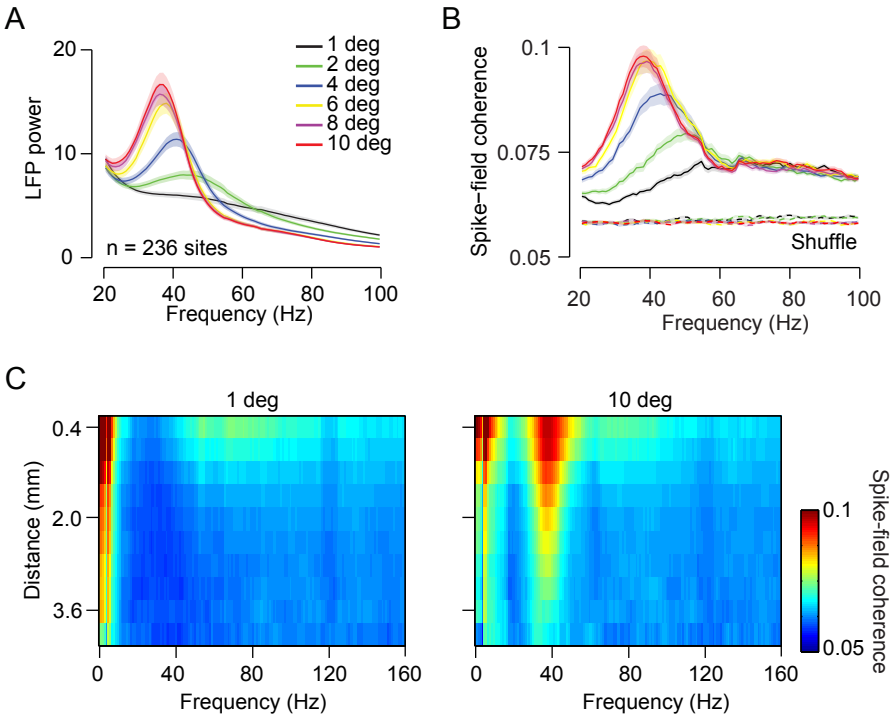
A
LFP power
20
10
0
1 deg
2 deg
4 deg
6 deg
8 deg
10 deg
n = 236 sites
20
40
60
80
100
Frequency (Hz)
B
Spike−field coherence
0.1
0.075
0.05
Shuffle
20
40
60
80
100
Frequency (Hz)
C
1 deg
10 deg
Distance (mm)
0.4
2.0
3.6
0
40
80
120
160
Frequency (Hz)
0.1
0.05
Spike-field coherence

Figure 4.2 Gamma phase modulation of spiking activity. (**A**) Illustration of the method to measure the phase of spiking activity relative to the gamma cycle. We band-pass filtered the LFP in the gamma range, and then applied the Hilbert transform to this signal to estimate spike phase. (**B**) Spike count distribution within the gamma cycle for an example site. The histogram is normalized to unit area. The preferred phase is indicated with a black triangle. Activity was driven by a 10 degree grating averaged across orientations. (**C**) The distributions of the preferred phase of individual sites from an example array, for activity driven by small (1 deg) and large (10 deg) gratings. (**D**) Example of the distribution of normalized spike counts with respect to the gamma cycle, for all neurons in one implant (n=148 neurons). Data for activity driven by large gratings is shown in red; for small gratings in black.

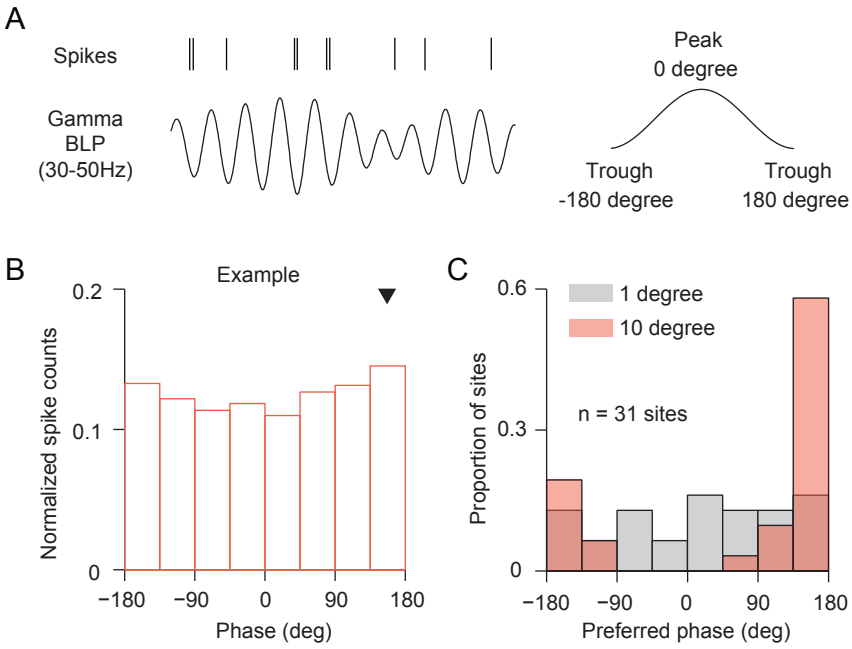
A
Spikes
Gamma
BLP
(30-50Hz)
Peak
0 degree
Trough
-180 degree
Trough
180 degree
B
Example
Normalized spike counts
0.2
0.1
0
−180
−90
0
90
180
Phase (deg)
C
1 degree
10 degree
n = 31 sites
Proportion of sites
0.6
0.3
0
−180
−90
0
90
180
Preferred phase (deg)

Figure 4.3 Population neuronal synchrony in V1. (**A**) Averaged shuffle-corrected CCGs for large (red; 10 deg; n=24,167 pairs) and small (black; <3.5 deg; n= 24,261 pairs) gratings. Shading, similar in size to the line thickness, indicates SEM. (**B**) Power spectra of the average shuffle-corrected CCGs in (A). (**C**) Average jitter-corrected (10 ms jitter window) CCGs for large and small gratings. Shading indicates SEM. (**D**) Average jitter-corrected CCG peak amplitude (+/- 1 ms), as a function of distance between recording sites. (**E**) Rate of occurrence of different multi-neuron spiking events (n = 990,000 time epochs). (**F**) Ratio between the rates shown in (**E**).

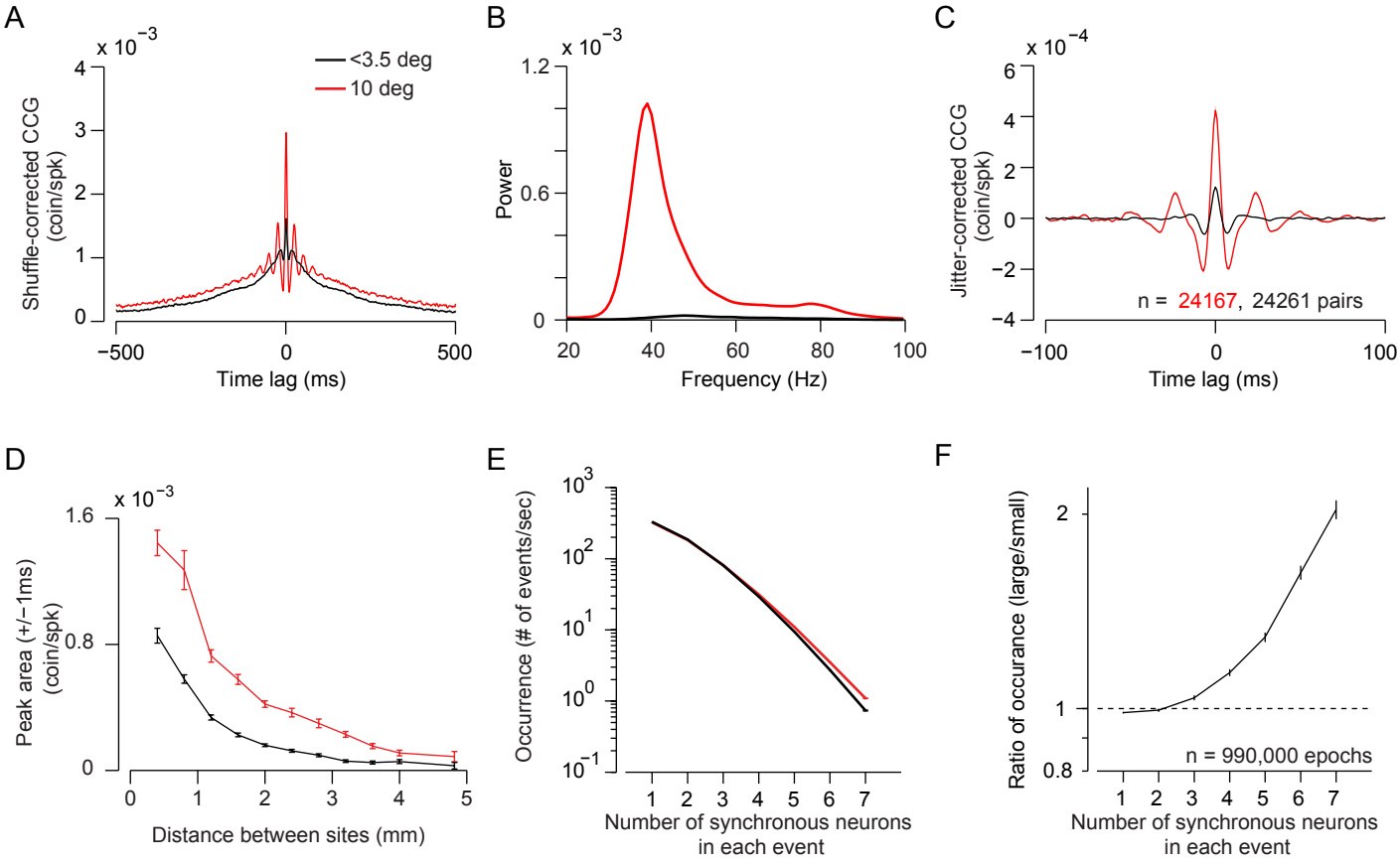
A
x 10^-3
<3.5 deg
10 deg
Shuffle-corrected CCG (coin/spk)
Time lag (ms)
B
x 10^-3
Power
Frequency (Hz)
C
x 10^-4
Jitter-corrected CCG (coin/spk)
n = 24167, 24261 pairs
Time lag (ms)
D
x 10^-3
Peak area (+/−1ms) (coin/spk)
Distance between sites (mm)
E
Occurrence (# of events/sec)
Number of synchronous neurons in each event
F
Ratio of occurance (large/small)
n = 990,000 epochs
Number of synchronous neurons in each event

Figure 4.4 Relating spiking activity in V1 and V2. (**A**) Illustration of the experimental approach. (**B**) Centers of the spatial receptive fields (RFs) in V1 (blue) and V2 (red). Each dot indicates the RF at a single recording site. The large circles indicate the sizes of an exemplar measured V1 and V2 RFs. (**C**) Average shuffle-corrected V1-V2 CCGs for large (red; 10 deg; n=16,367 pairs) and small (black; <3.5 deg; n=16,864 pairs) gratings. Shading indicates SEM. (**D**) Average jitter-corrected CCGs (jitter window = 10 ms) for the same V1-V2 pairings and stimulus conditions. Shading indicates SEM. (**E, F**) Shuffle-corrected (left) and jitter-corrected (right) V1-V2 CCGs as a function of the receptive field separation (distance between the RF centers) for small (**E**) and large (**F**) gratings. (**G**) For shuffle-corrected (left) and jitter-corrected (right) V1-V2 CCGs, the difference between CCGs of responses to large and small gratings.

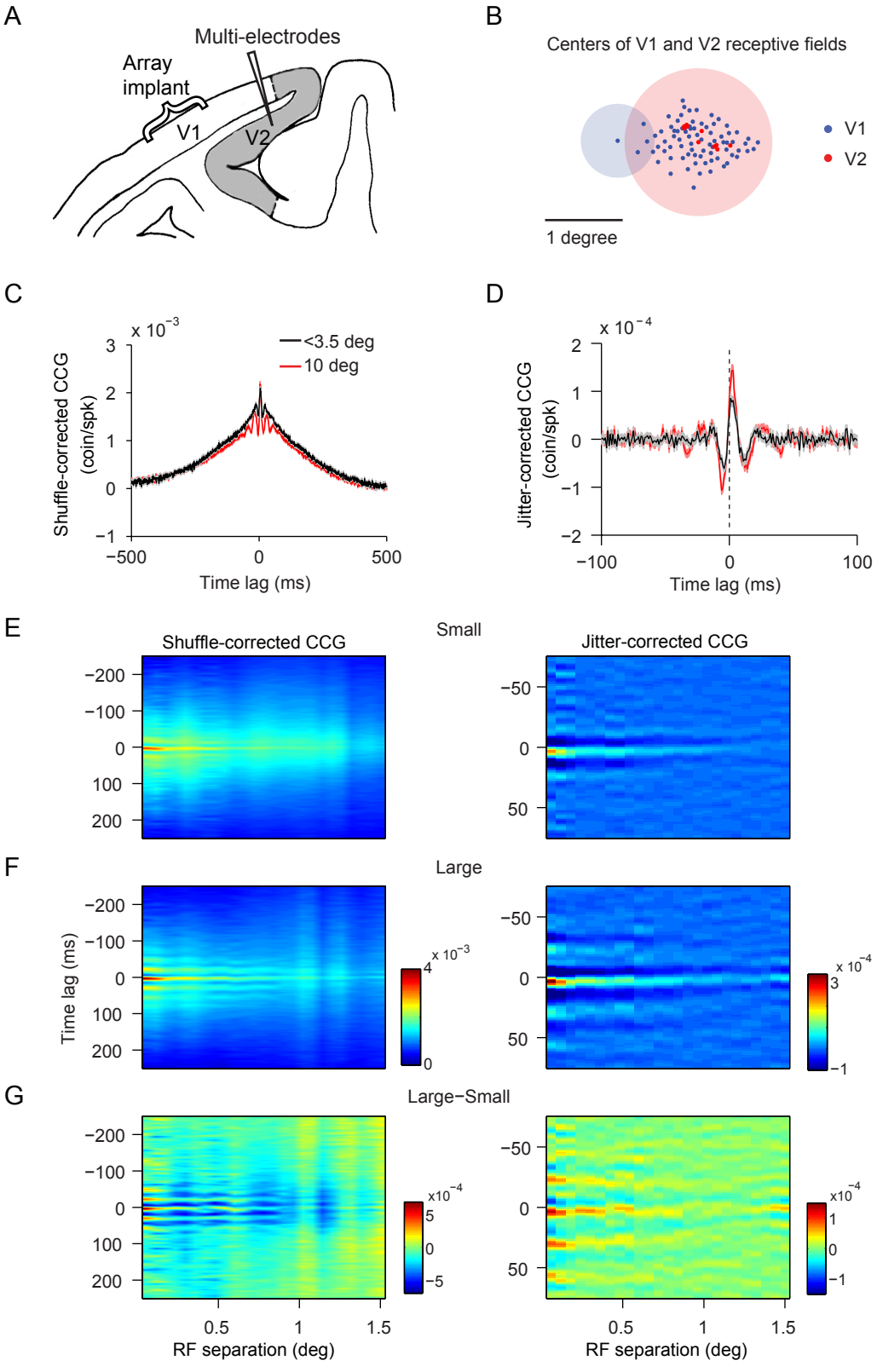
A
Multi-electrodes
Array implant
V1
V2
B
Centers of V1 and V2 receptive fields
V1
V2
1 degree
C
x 10^-3
<3.5 deg
10 deg
Shuffle-corrected CCG (coin/spk)
Time lag (ms)
D
x 10^-4
Jitter-corrected CCG (coin/spk)
Time lag (ms)
E
Small
Shuffle-corrected CCG
Jitter-corrected CCG
F
Large
Time lag (ms)
x 10^-3
x 10^-4
G
Large−Small
x10^-4
RF separation (deg)
RF separation (deg)

Figure 4.5 Coherence between V1 and V2 LFPs. (**A**) Coherence as a function of frequency and RF separation between the V1 and V2 recording sites for responses to small (left; n=3,793 pairs) and large (right; n=3,814 pairs) gratings. (**B**) Averaged coherence as a function of frequency, for sites for which RFs were separated by less than 1 degree. Coherence for responses to large gratings are shown in red; for small, in black.

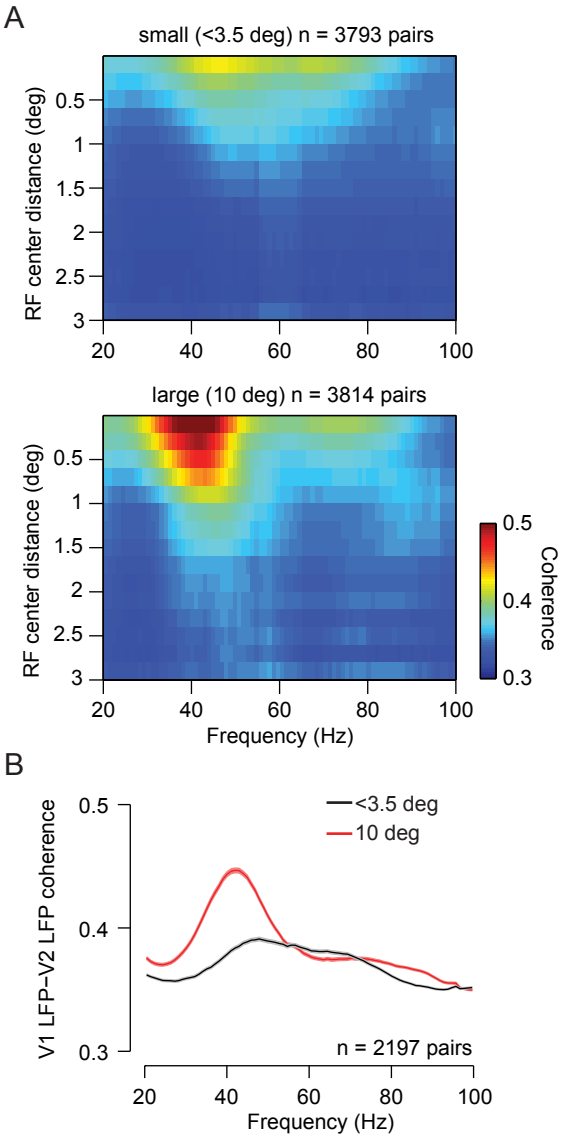
A
small (<3.5 deg) n = 3793 pairs
RF center distance (deg)
0.5
1
1.5
2
2.5
3
20
40
60
80
100
large (10 deg) n = 3814 pairs
RF center distance (deg)
Frequency (Hz)
Coherence
0.5
0.4
0.3
B
V1 LFP–V2 LFP coherence
<3.5 deg
10 deg
n = 2197 pairs
Frequency (Hz)

Figure 4.6 Relative phase difference in the gamma frequency within and between cortical regions with large gratings. (**A**) Relative phase difference between V1 and V2 gamma rhythms for sites for which RFs were separated by less than 1 degree (n=2213 pairs; bin size =22.5 deg). Mean of phase distribution is 87.9 degree. (**B**) Phase difference in the gamma frequency between pairs of V1 recording sites (n = 17167 pairs), for same V1 recording sites in (**A**). Mean of phase distribution is 36.9 degree. (**C**) Phase difference in the gamma frequency between pairs of V2 recording sites (n = 65 pairs), for same V2 recording sites in (**A**). Mean of phase distribution is 46.2 degree.

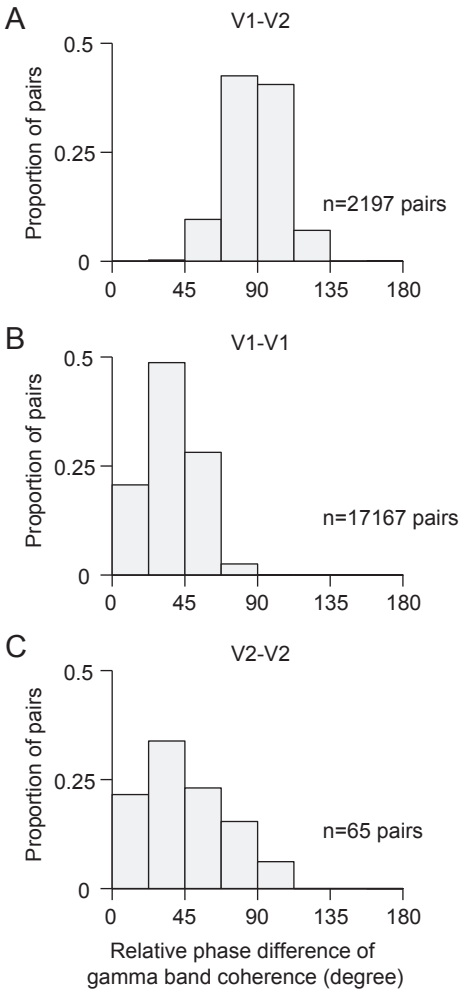
A
V1-V2
0.5
0.25
0
Proportion of pairs
n=2197 pairs
0
45
90
135
180
B
V1-V1
0.5
0.25
0
Proportion of pairs
n=17167 pairs
0
45
90
135
180
C
V2-V2
0.5
0.25
0
Proportion of pairs
n=65 pairs
0
45
90
135
180
Relative phase difference of
gamma band coherence (degree)

Figure 4.7 Coupling of V1 and V2 spiking activity, relative to the V1 and V2 gamma rhythms. (**A**) Illustration of method for determining the preferred gamma phase in V1 and V2. For the gamma rhythm in each area, we determined the preferred phase (ϕ), defined as the phase at which local spiking activity was most likely. (**B**) V1 spike counts relative to the V1 gamma cycle, with the preferred phase plotted as the first bin. Gamma-phase modulation was calculated for each cell, as in Figure 2, and then averaged across all neurons (n=770 cells). (**C**) Proportion of V1 spikes followed by a V2 spike 1-3 ms later, for each V1 gamma phase as defined in (**B**) (n = 17,518 pairs). (**D**) Normalized V2 spike counts relative to the V2 gamma cycle, with the preferred phase aligned to the first phase bin (n = 186 cells). (**E**) Normalized V1 spike counts aligned with respect to the V2 gamma phase at which V2 firing is most likely. Note that V1 neurons tend to fire at a phase offset from that preferred by V2 neurons (**F**) Proportion of V1 spikes that are followed by a V2 spike, with respect to the V2 gamma phase**.**

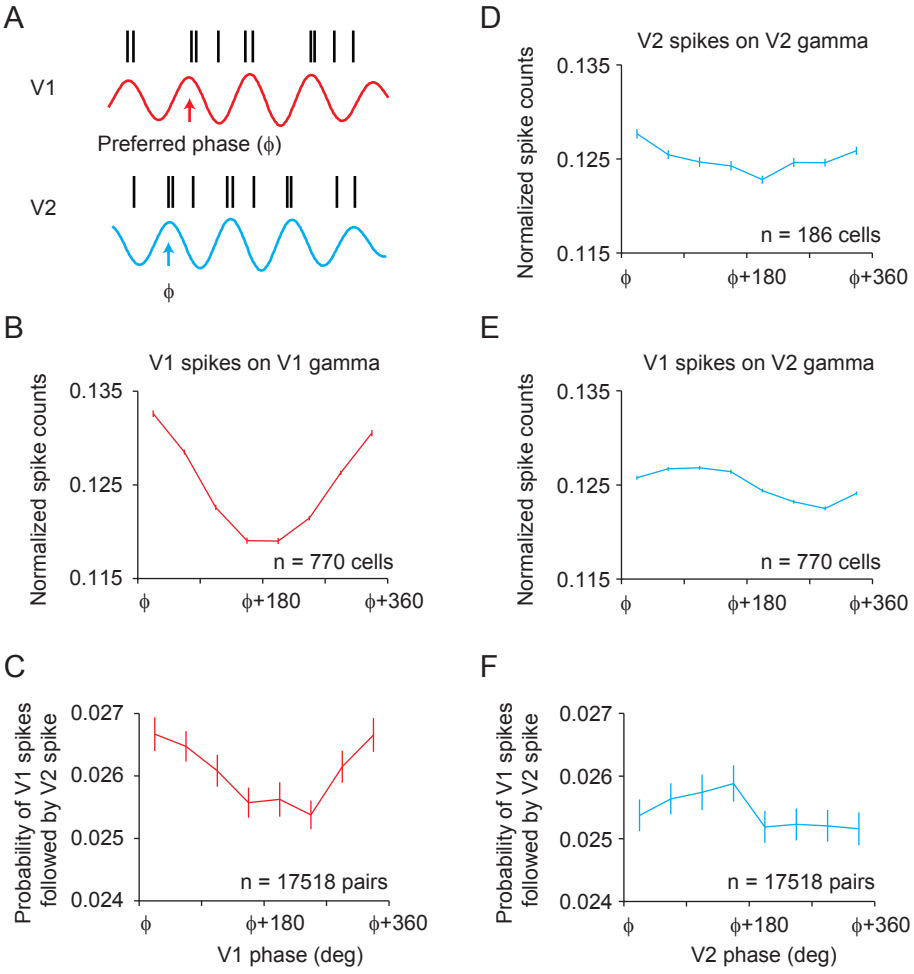
A
V1
Preferred phase (ϕ)
V2
ϕ
B
V1 spikes on V1 gamma
Normalized spike counts
0.135
0.125
0.115
n = 770 cells
ϕ
ϕ+180
ϕ+360
C
Probability of V1 spikes followed by V2 spike
0.027
0.026
0.025
0.024
n = 17518 pairs
ϕ
ϕ+180
ϕ+360
V1 phase (deg)
D
V2 spikes on V2 gamma
Normalized spike counts
0.135
0.125
0.115
n = 186 cells
ϕ
ϕ+180
ϕ+360
E
V1 spikes on V2 gamma
Normalized spike counts
0.135
0.125
0.115
n = 770 cells
ϕ
ϕ+180
ϕ+360
F
Probability of V1 spikes followed by V2 spike
0.027
0.026
0.025
0.024
n = 17518 pairs
ϕ
ϕ+180
ϕ+360
V2 phase (deg)

Figure 4.8 Dependence of gamma LFP power, neuronal synchrony and corticocortical coupling on stimulus orientation. (**A**) Population orientation tuning curve of gamma power from one example array (n = 86 sites), for activity induced with large gratings. The red dot indicates the best orientation, meaning the orientation that induced the most power; the grey dot indicates the worst orientation. (**B**) Coherence and phase difference between LFPs in V1, as a function of interelectrode distance and frequency. (**C**) Averaged jitter-corrected V1-V1 CCGs (n=28,251 pairs) for the best and worst stimulus orientations. (**D**) Averaged jitter-corrected V1-V2 CCGs (n=11,012 pairs) for the best and worst stimulus orientations.

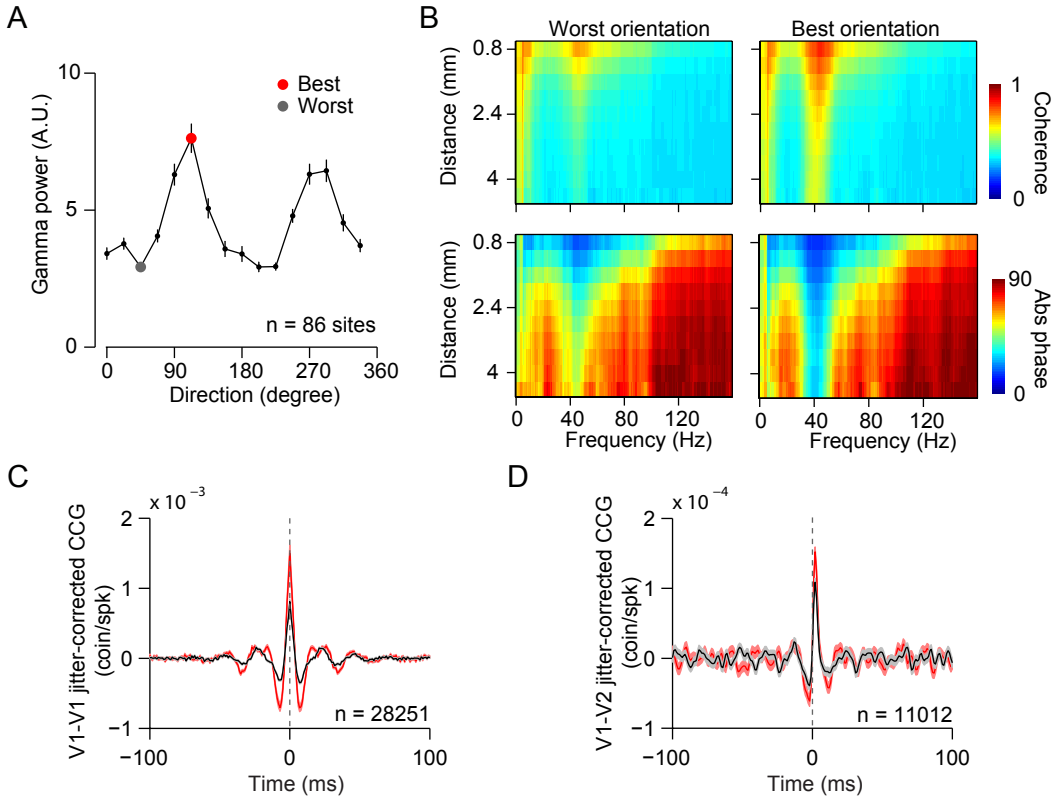
A
Gamma power (A.U.)
10
5
0
Best
Worst
n = 86 sites
0
90
180
270
360
Direction (degree)
B
Worst orientation
Best orientation
Distance (mm)
0.8
2.4
4
1
Coherence
0
90
Abs phase
0
0
40
80
120
Frequency (Hz)
C
x 10 −3
V1-V1 jitter-corrected CCG (coin/spk)
2
1
0
−1
n = 28251
−100
0
100
Time (ms)
D
x 10 −4
V1-V2 jitter-corrected CCG (coin/spk)
n = 11012

Supplementary Figure 1 Effects of stimulus size on spike-spike coherence in V1 and spike-field coherence between V1 and V2. (**A**) To measure coordination of spike timing in the frequency domain, to complement the CCG analysis in Figure 4.3, we calculated the spike-spike coherence (SSC) between all possible pairings of neurons. Gamma SSC was stronger for large gratings (0.0346±4E-5, n= 51980) than small gratings (0.0333±3.4E-5, n= 53463; $p<0.0001$), and the peak frequency of SSC in the gamma band shifted from 47 Hz to 38 Hz when stimulus size was increased. (**B**) Given the interaction between V1 spike timing and V1 gamma, the gamma coherence of V1-V2 LFPs implies a relationship between V1 spikes and V2 gamma, when the gamma rhythms in these two areas are coherent. We evaluated this by calculating the coherence between V1 spiking activity and V2 LFPs. Spike-field coherence was elevated at gamma frequencies and higher for responses to large (0.0203±0.0001; n=4374 pairs; red trace) compared to small gratings (0.0166±3E-005, n=4680 pairs; $p<0.0001$; black trace). (**C**) To investigate the interaction between V1 spikes and V2 gamma for large gratings, we measured the relationship between V1 spikes and V2 LFPs and spiking activity of different orientations. The best orientation, which induces most gamma power, showed higher V1 spike-V2 LFP coherence in the gamma band (n=3459 pairs), although both conditions induced a clear peak in gamma SFC.

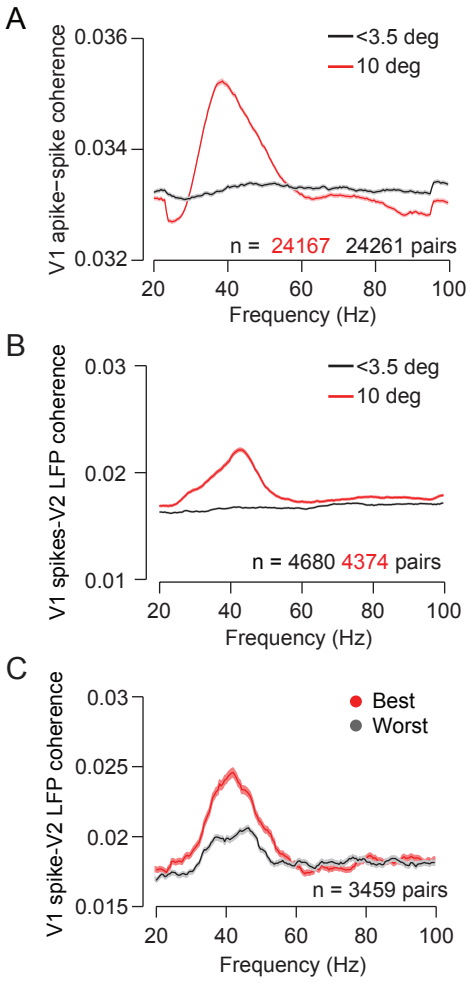
A
0.036
0.034
0.032
V1 apike−spike coherence
<3.5 deg
10 deg
n = 24167 24261 pairs
20
40
60
80
100
Frequency (Hz)
B
0.03
0.02
0.01
V1 spikes-V2 LFP coherence
<3.5 deg
10 deg
n = 4680 4374 pairs
20
40
60
80
100
Frequency (Hz)
C
0.03
0.025
0.02
0.015
V1 spike-V2 LFP coherence
Best
Worst
n = 3459 pairs
20
40
60
80
100
Frequency (Hz)

Supplementary Figure 2 Event-triggered averages of the global LFP. Our analysis shows that clustering of spike times in the gamma cycle is more consistent when gamma is more prominent. When driven by large gratings, spikes from individual neurons tend to cluster at the same phase. However, to determine how changes in gamma power affect the coordination of activity in a neuronal population, one must understand the timing relationships among large groups of neurons. We therefore examined the interaction between spike firing patterns in the population and the global gamma rhythm, defined as the average of the raw LFP signal across all electrodes at each point in time. (**A**) We computed event-triggered averages of the global LFP (ETA-LFP), where an event was defined as the number of neurons (regardless of identity) that fired in a 1 ms window. (**B**) Average global LFP triggered by events involving 1-7 neurons, for activity induced in a single array by a single grating. The LFPs triggered on 1 neuron events showed little structure, but we observed a notable increase in the amplitude of ETA-LFP as the number of co-active neurons increased. (**C**) The power spectrum of the ETA-LFPs was dominated by gamma frequencies when triggered by higher order events. (**D**) The average gamma band power in the ETA-LFP, normalized by the maximum gamma power for each implant, increased from 0.17±0.06 to 0.98±0.01 ($p<0.0001$; $n=8$ implants), for events involving 1 neuron compared to those involving 7 neurons. This result suggests that for higher-order synchrony to occur, spikes from individual neurons are more aligned at the same phase on the global gamma rhythm.

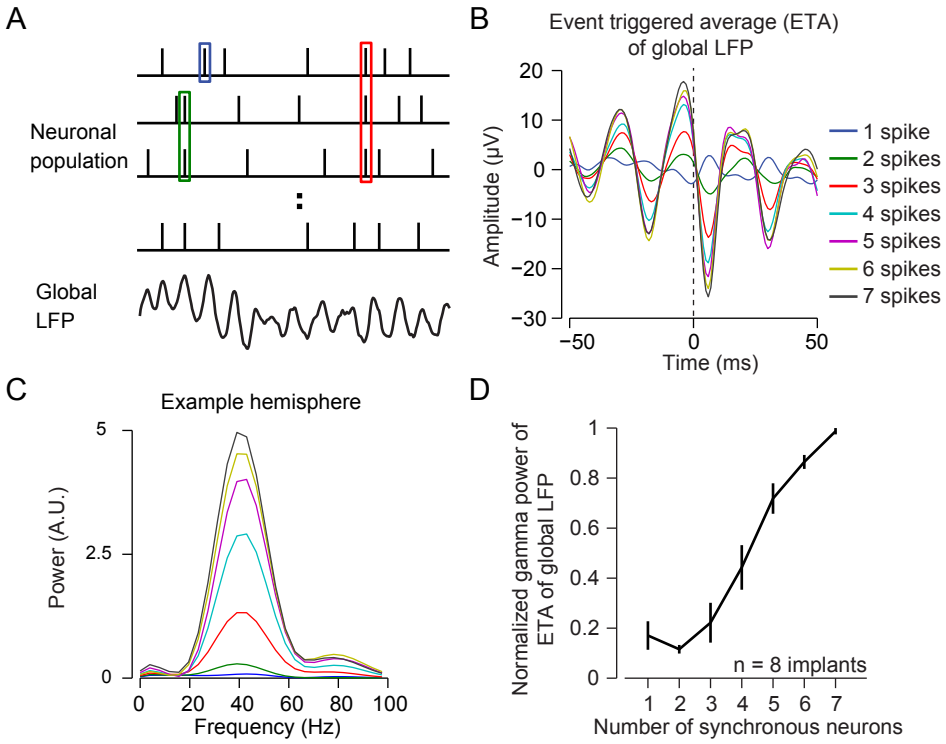
A
Neuronal population
Global LFP
B
Event triggered average (ETA) of global LFP
Amplitude (μV)
Time (ms)
1 spike
2 spikes
3 spikes
4 spikes
5 spikes
6 spikes
7 spikes
C
Example hemisphere
Power (A.U.)
Frequency (Hz)
D
Normalized gamma power of ETA of global LFP
n = 8 implants
Number of synchronous neurons

Supplementary Figure 3 CCGs of the most correlated V1 and V2 pairs. To evaluate the conduction time of the feedforward connections between V1 and V2, we quantified the most correlated pairs (sharp peak amplitude large than 5 fold of standard deviation at plus/minus 75-125 ms). (**A**) The resulted pairs showed 67% enhancement of CCG peak area for large compared to small. The distribution of the time lag of the sharp peak for small gratings (2-3.5 degree) is plotted in (**B**) and for large gratings (10 degree) is plotted in (**C**), with a mean peak offset of 2.20+/-0.10ms (n=459 pairs; 2.7% of total pairs) for small and 2.23+/-0.09ms for large (n=631 pairs; 3.9% of total pairs) and a median of 2 ms for small and 3 ms for large.

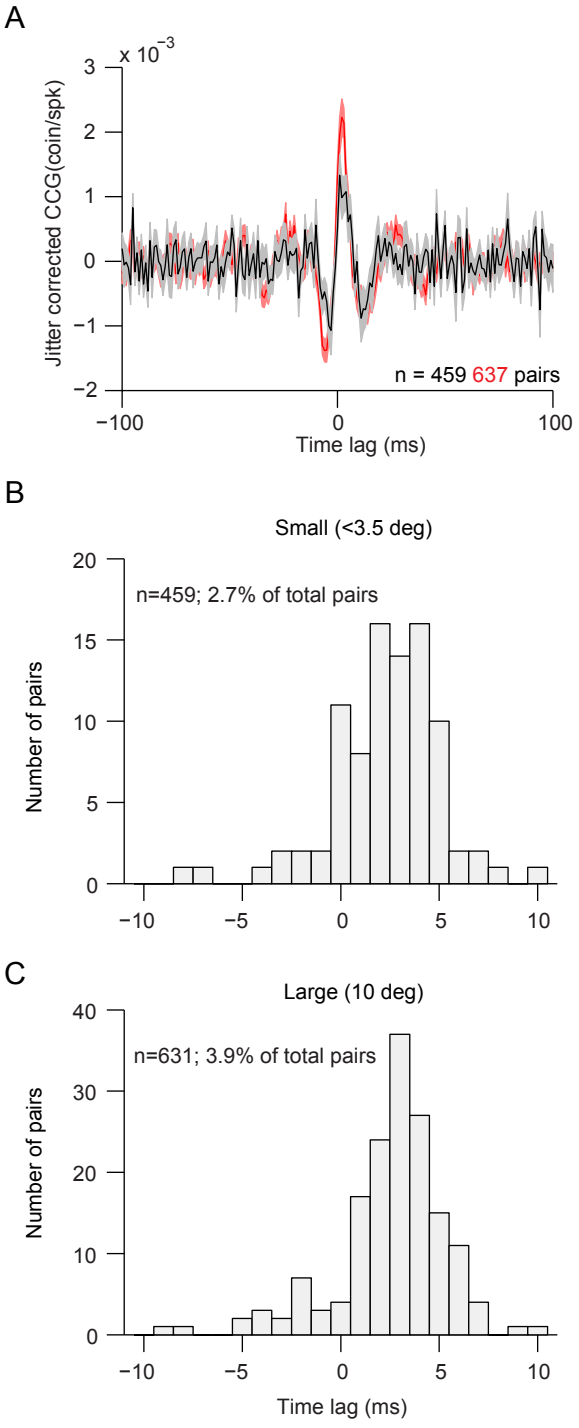
A
x 10^-3
3
2
1
0
−1
−2
Jitter corrected CCG(coin/spk)
n = 459 637 pairs
−100
0
100
Time lag (ms)
B
Small (<3.5 deg)
n=459; 2.7% of total pairs
Number of pairs
20
15
10
5
0
−10
−5
0
5
10
C
Large (10 deg)
n=631; 3.9% of total pairs
Number of pairs
40
30
20
10
0
−10
−5
0
5
10
Time lag (ms)

Supplementary Figure 4 Response properties of gamma power and neuronal responses in V2 compared to V1. (**A**) Power spectra of V2 LFP for large and small gratings (n=50 sites). (**B**) Upper panel shows the distribution of gamma preferred orientation in V1 with peak of the distribution centered at 90 degree (n=715 sites). Lower panel shows the distribution of orientation preferences of MUA in V1 shifted according to V1 gamma distribution. (**C**) Upper panel is the distribution of V2 gamma preferred orientation shifted according to the simultaneously recorded V1 gamma distributions. The preferred orientation of V2 gamma is the same as V1 (n = 50 sites). Lower panel shows the distribution of orientation preferences of V2 neurons shifted according to V1 gamma distribution. Clearly, the preferred orientation of V2 neurons is randomly distributed and does not follow the orientation tuning of V1 or V2 gamma rhythm.

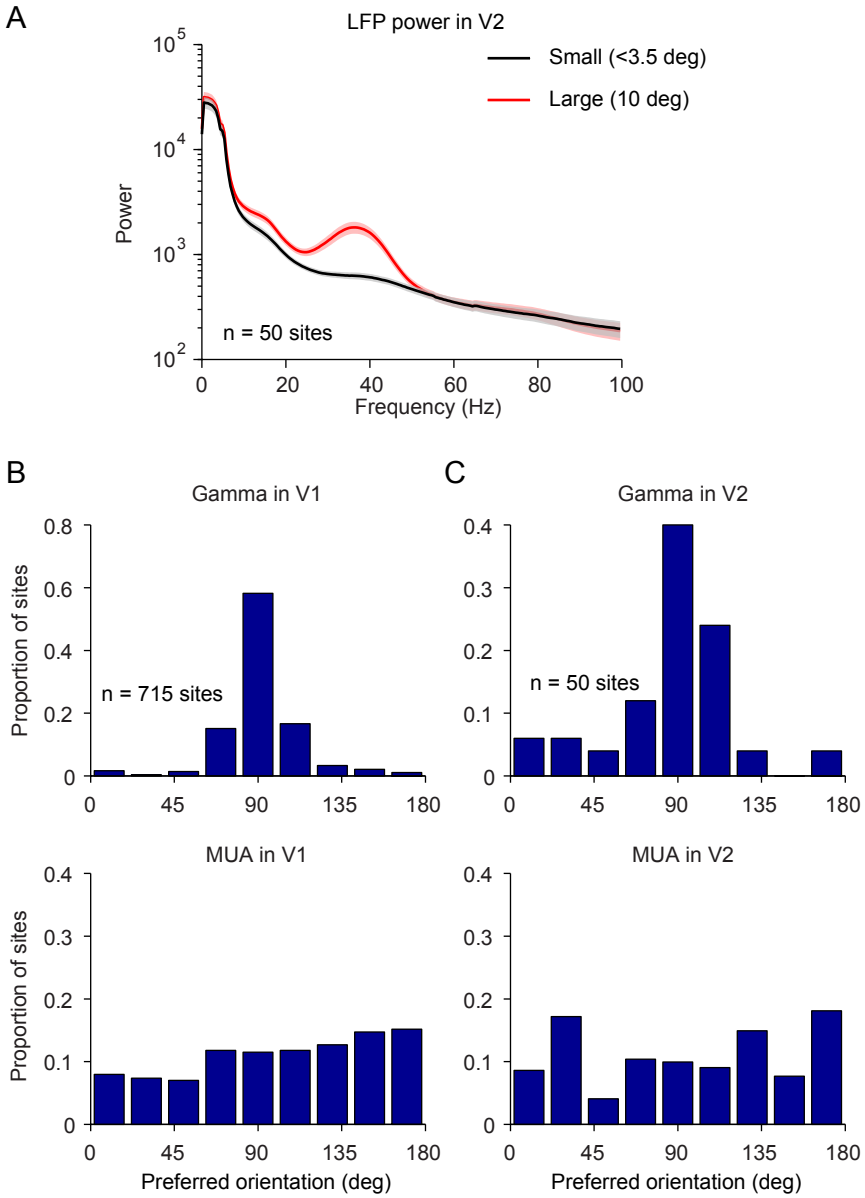
A
LFP power in V2
Small (<3.5 deg)
Large (10 deg)
Power
n = 50 sites
Frequency (Hz)
B
Gamma in V1
Proportion of sites
n = 715 sites
C
Gamma in V2
n = 50 sites
MUA in V1
Proportion of sites
Preferred orientation (deg)
MUA in V2
Preferred orientation (deg)

Chapter 5: Discussion

5.1 Summary

There are extensive observations of correlated changes between different brain rhythms and various brain states have been made (Buzsaki, 2006). Understanding the nature of brain rhythms and their potential functional roles has been an intriguing research topic in past decades. Decoding the message carried in these different rhythms may help us to read the brain, with higher spatial and temporal resolution compared to functional imaging.

Brain rhythms are slow rhythmic extracellular voltage fluctuations that can be detected on the scalp (EEG), underneath the dura (intracranial field potential; IFP) or within the brain (LFP). Among these the LFP has the finest spatial resolution. Many studies have focused on the gamma rhythm of the LFP, because that power in the low gamma range, typically 30 to 50 Hz, is enhanced with sensory drive and during active brain states, like attention and working memory. Similar to single neurons in sensory cortex, the gamma rhythm of the LFP is also tuned to stimulus properties. Findings on the relationship between the gamma rhythm and spike timing and the neuron substrate involved in generating gamma rhythm have led to many proposals on the functional role of gamma in signal transmission (see Introduction). However, the understanding of the basic properties of gamma is still poor, including its relationship to spiking activity and rigorous tests of proposals about its potential role in encoding and signaling information are lacking.

The main purpose of my thesis work is to elucidate the properties of gamma, its relationship to spiking activity, and its putative role in signal transmission in early visual cortex. I find that the spatial extent and selectivity of gamma rhythm is not fixed, but depends on the properties of the visual stimulus. When a visual stimulus is small, discontinuous in space or presented for a short period of time, the tuning of LFP in the gamma frequencies is dominated by broadband power, which is predictable from changes in higher frequencies of LFP. When a visual stimulus is a large drifting grating presented for sufficient time, a strong and spatially extensive gamma rhythm is generated, with a tuning preference that is shared across cortical distance. This global gamma rhythm is characterized by a spectral bump in the gamma range (Chapter 2). The preference of the global gamma rhythm could arise from a small representation bias of the neuronal population that generates the rhythm. In Chapter 3, I tested this proposal using adaptation and demonstrated that the global gamma rhythm is extremely sensitive to prolonged adaptation. This is consistent with the suggestion that the gamma rhythm reflects a neuronal bias. Having established the properties of the gamma rhythm, I then investigated the interaction between gamma and neuronal spiking activity. I find that when gamma is strong and spatially phase coherent, spikes tend to cluster at certain phases of the gamma rhythm and become synchronized. These synchronized outputs from V1 influence the efficacy of each V1 spike in driving downstream V2 neurons in a gamma-phase dependent manner (Chapter 4). These results suggest that strong gamma power with a distinctive spectral bump can indicate the formation of a global rhythm, enhanced

neuronal synchrony in a large network and increased signal propagation efficacy between cortical areas.

5.2 Factors contributing to the spatial resolution of the brain rhythms

The gamma rhythm is generated by coordinated subthreshold electrical activity of a neural ensemble (Jia and Kohn, 2011; Mitzdorf, 1985). It is important to emphasize that there are three potential factors contributing to the spatial resolution of the detected gamma rhythm. The first one is the structure of the physiological source of the signal. Correlated synaptic activity in each neuron is not enough to generate detectable rhythmic fluctuations in the extracellular field potential. The morphology of individual neurons, geometry of dendrites and axons, and the alignment and density of a neuronal population can all affect how effectively the extracellular electrical fields summate (Buzsaki, 2006). Only when the electrical fields generated in each neuron are aligned with each other can the extracellular electrical field sum to generate a signal that is detectable. For a given transmission medium (e.g. brain tissue), the detectable spatial extent of the passive conduction of the signal generated from the physiology source is related to its amplitude. Therefore, the structure of the neural ensemble can affect the spatial resolution of brain rhythms.

The second factor is the extent of neuronal network that generates the stimulus-induced gamma rhythm (Traub et al., 1996b; Wang and Buzsaki, 1996). We find that the broadband component of gamma rhythm has response properties similar to simultaneously recorded spiking activity from the same electrode. This component of

gamma could arise from local neural activity. On the contrary, the spatial extent of the actively generated gamma rhythm in the LFP is flexible and can reach to more than 4 mm around the recording site depending on properties of the visual stimulus. This suggest that there is a physiological source involved in the formation of the global rhythm because it has highly selective orientation tuning, which is hard to form with the random distribution and small spatial scale of the orientation map (Horton and Adams, 2005) if the gamma rhythm is passively aggregated from distinctive oscillators from a hundred-fold larger area. As a result, the spatial extent of the network involved in the global gamma rhythm formation contributes to the spatial specificity of the gamma rhythm. Unlike the structure of the physiology source, this factor is caused by the functional properties of the network and its extent is variable depending on visual input to the network.

The last factor is the physical property of brain tissue and of the recording electrodes. For example, the spatial resolution of the detected gamma rhythm could be dramatically different depending on whether the electrode is inside or outside the brain. However, it is important to note that our findings about the flexible extent of the actively generated gamma rhythm are physiological properties of the rhythm. They reflect a change in the neuronal activity. Even though we have a rough estimation and understanding of the flexible spatial extent of the gamma rhythm from the extracellularly recorded LFP, we cannot generalize this property to the gamma rhythm detected outside the brain with intracranial and EEG recordings, since the resistance, capacitance and volume conduction are different, not to mention the impedance and other properties of the sensing electrode.

Additionally, the relative location of the recording electrodes to the physiological source of the signal could also contribute to the spread of the sensed signal (Kajikawa and Schroeder, 2011; Linden et al., 2010). Therefore, although the physiological origin of these brain rhythms is the same, the spatial resolutions of rhythms detected with different recording methodologies can still different.

5.3 The meaning of changes in the gamma rhythm

5.3.1 Strength of gamma and spiking activity

The gamma rhythm mainly reflects subthreshold neural activity. Because the firing probability in each neuron is closely related to the subthreshold fluctuations of membrane potential, the strength of extracellular field potential could be related to the firing rate of individual neurons. However, as I have shown in Chapter 2, there are two components that contribute to gamma power: one comes from a broadband change in power; the other is an actively generated rhythm that can be dissociated from neighboring frequencies and can form a spatially extensive rhythm. The relationship between the total gamma power in the LFP and spiking activity depends on the relative contribution of these two components whose relationships with spiking activity are different.

Similar to power in higher frequencies (Ray and Maunsell, 2011a), the broadband component of gamma reflects changes in local neuronal firing rate. The actively generated gamma rhythm has a flexible relationship with local neuronal activity. When the spatial extent of the network generating this gamma rhythm is limited, its response is

more similar to local spiking activity, though not comparable to the broadband component (Chapter 2). However, when a spatially extensive network is involved, the gamma rhythm does not reflect the neuronal activity recorded at individual recording sites. Therefore, the relationship between total gamma power, which is the sum of these two components, and the spiking activity recorded at the same recording site depends on the relative contribution of the global gamma rhythm and how similar its response is to that of the local spiking activity.

Since the neural network that forms the global gamma rhythm is spatially extensive, the strength of the stimulus-induced gamma is determined by the total amount of excitation that the network receives and how strongly the inhibitory network is driven (Bauer et al., 1995; Gieselmann and Thiele, 2008). Under conditions when neuronal responses are similar across neurons, gamma power and firing rate behave similarly (e.g. with allocation of spatial attention (Fries et al., 2008) and manipulations of contrast (Henrie and Shapley, 2005)). On the other hand, when the neuronal responses to visual features are specific in individual neurons, they dissociate from each other, for example, with manipulation of stimulus size which is with respect to the classical receptive field of individual neurons (Gieselmann and Thiele, 2008) and orientation tuning comparison (Berens et al., 2008; Jia et al., 2011). Therefore, the locally recorded neuronal firing rate is often not closely related to the strength of gamma rhythm.

Although the strength of gamma may dissociate from firing rate, spike timing is more closely related to the amplitude and phase of the gamma rhythm. This is because when

firing rate is high, the neuronal network is not necessarily coordinated in the gamma frequency (Chapter 4). However, when gamma power is high, this suggests that the network is strongly synchronized in the gamma frequency, as evident by the observed phase-locking of spike timing to the gamma rhythm. As a result, the strength of gamma cannot reflect neuronal firing rate, but can be closely related to the firing pattern in individual neurons. Furthermore, since the strong gamma rhythm is phase coherent over distance, the phase-locking of spike times in individual neurons to a global rhythm indicates an enhanced brief timescale synchrony in the network. Therefore, changes in power of the actively generated gamma rhythm indicate changes in the temporal coordination of spike timing.

According to the independence between the two components of gamma, with one closely related to firing rate and the other more closely linked with spike timing, firing rate and spike timing relative to gamma cycle could be two independent signals as well (Huxter et al., 2003), different from previous proposals that rate and temporal coding are interrelated in the hippocampus (Harris et al., 2002; Mehta et al., 2002). Compared to spike timing, firing rate averaged over sufficiently long time intervals is more reliable and the information coded with firing rate has high signal to noise ratio, reflected in the selectivity of tuning curves. On the other hand, the spike timing relative to gamma cycle is an immediately available signal but less reliable in the visual cortex (Vinck et al., 2010). Since reduced firing rate does not mean a reduction in the reliability of spike timing, shown by the manipulation of stimulus size, the two signals could code independent information.

5.3.2 Peak frequency in the gamma range

Different visual stimulus features can regulate not only the strength of gamma power, but also its peak frequency in the gamma range. Since the spectrum of the broadband power can never have a peak, the peak frequency is by definition a property of the actively generated gamma rhythm. However, the strength of this gamma rhythm is not correlated with its peak frequency. For example, large gratings induce a strong gamma rhythm with a peak frequency in the lower gamma range, close to 30Hz. Small gratings induce less gamma power, with a peak frequency (when it exists) at the upper gamma range (50Hz) or even higher (Gieselmann and Thiele, 2008). Masking-noise (Appendix I) and stimulus contrast (Ray and Maunsell, 2010), on the other hand, show an opposite relationship between gamma strength and peak frequency. Lower contrast or higher level of masking noise will reduce the power of the gamma rhythm and also reduce the peak frequency in the gamma range. High contrast gratings with little noise will have more power and higher peak frequency. These observations suggest that the network mechanisms that determine the peak frequency in the gamma range and the strength of gamma rhythm are independent.

A modeling study (Brunel and Wang, 2003) has shown that the peak frequency of oscillation is critically dependent on the number of excitatory cells in a network, where the main oscillatory drive arises from electrically coupled interneurons. When larger stimuli excited additional pools of excitatory neurons, the reduction in frequency may have arisen from the larger pool of contributing principle cells with longer conduction

delays, while the increased oscillatory drive may have arisen from a larger pool of active (and coupled) interneurons.

Gieselmann and Thiele proposed that shifts of peak gamma to lower frequencies with larger stimuli could arise from longer conduction delays (Gieselmann and Thiele, 2008). If peak frequency reflects conduction delays in the network involved in generating the gamma rhythm, changes in contrast and noise-masking manipulations would suggest that lowering contrast and adding more noise also enlarge the network contributing to the actively generated gamma, even for stimuli of fixed size. This seems unlikely.

Recently, another network model has been proposed to explain the peak frequency shifts of the gamma rhythm when manipulating stimulus size (Kang et al., 2009). This model involves recurrent connections between excitation and inhibition, and a strong influence from cortical feedback. Given strong recurrent local inhibition, this model predicts that as more feedback is recruited by larger stimuli, the resonant frequency in the gamma range will shift lower.

These models suggest that the excitatory drive, conduction delays and feedback might play a role in determining peak frequency. Additionally, because lowering contrast can enlarge neuronal receptive fields and changes in stimulus size can manipulate the balance between excitation and inhibition (Kapadia et al., 1999; Sceniak et al., 1999), the separate mechanisms determining gamma power and peak frequency could be used as a window to study the properties of underlying neural network.

Since neural responses to different sizes, contrasts and levels of noise masking can be modeled by changes in the balance between excitation and inhibition, it is an attractive idea to speculate that the peak frequency shifts arise from changes in the balance between excitation and inhibition in a neuronal network. It has been shown that the balance between excitation and inhibition shifts to more proportion of inhibition with larger stimuli (Haider et al., 2010). Lowering contrast also has similar effects (Kapadia et al., 1999; Sceniak et al., 1999). I propose to predict the changing trend of peak frequency with various stimulus features by the difference between excitation and inhibition. With findings from previous studies, the difference between excitation and inhibition is larger for small than large stimuli, and the difference is also larger for high than low contrast. Then, the lower the peak frequency of gamma is, the less difference between excitation and inhibition. The hypothesized computational model may work only when one chooses the proper parameters for excitation and inhibition. Because surround suppression could involve feedback from other areas, the model can also include excitatory feedback as in previous modeling studies. Therefore, if the strength of gamma power is indicative of the total excitatory drive to a network or how strongly the inhibitory network is activated, the peak frequency of gamma could potentially reflect the relative balance between excitation and inhibition.

Whittington (2010) compared different circuitry models of gamma rhythm formation (ING, PING and persistent, introduced in General Introduction) and summarized the relationship between gamma power and peak frequency predicted by different models

(Whittington et al., 2010). Interestingly, the PING model can predict the changes of power and peak frequency with contrast and masking noise, but fails to explain the size effects. The other two models fail to predict any of the observed behaviors. Therefore, peak frequency changes in the gamma rhythm along with gamma power could impose strong constraints on the mechanisms involved in gamma formation. In evaluating the performance of a model, one should consider both its ability to predict power and peak frequency.

5.4 Orientation selectivity of gamma rhythm

Gamma, when induced with large drifting gratings, can form a spatially extensive global rhythm with stimulus selectivity that is comparable with multi-unit spiking activity. A study similar to ours found that the ocular dominance preference is more correlated between gamma power and local MUA than orientation tuning (Berens et al., 2008). This study thus estimated that the spatial extent of gamma is similar to ocular dominance columns, about 450-600 μm.

Berens et al. also found that the orientation selectivity of gamma power is highest when MUA and gamma rhythm recorded at the same electrode had a similar orientation preference. Because the distribution of the orientation preferences in primary visual cortex is not homogeneous, with pinwheels that consists of a wide range of orientations and linear zones which can extend up to several hundred micrometers for a single orientation (Bonhoeffer and Grinvald, 1991; Horton and Adams, 2005), Berens et al. propose that when a recording site is in the middle of a linear zone, it is more likely that

gamma will share a similar preference as MUA and that it will be more selective because it is summing over a region with similar orientation preference. When the recording site is near an orientation pinwheel, on the other hand, the signal reflects activity in a region with diverse tuning, resulting in less selective tuning that is less correlated with MUA.

Their proposal is based on the assumption that gamma rhythm reflects neural activity from a region about 450-600 μm, estimated by its similarity with spiking activity. However, I found that the spatial extent of gamma can cover many pinwheels and linear zones of the orientation map, and in such a situation its preference dissociates from local spiking activity. Therefore, the 'pinwheel' versus 'linear zone' hypothesis may not hold under this condition. However, we confirmed in our data set that with large grating stimuli, their observation of the selectivity changing trend as a function of the relative preference difference between gamma and local MUA still holds.

To explain this phenomenon, I propose that there is a competition between the broadband gamma, which is selective and always tuned similarly to local spiking activity, and the 'bump' gamma component, which is the selective global rhythm. When the orientation tuning of the global component happens to match that of the local spiking activity, the two components in the power spectrum of gamma rhythm will have similar tuning. Adding their power together will not reduce orientation selectivity. On the contrary, when the orientation tuning of the global gamma dissociates from local spiking activity, the selectivity of the tuning of the 'bump' and broadband components will be offset so their sum will be less selective. Thus, the simple sum of the two distinctive gamma

components could result in the dependence of gamma selectivity on its similarity with local spiking activity.

5.5 Preference of global gamma rhythm

What gives rise to the orientation preference of the global gamma rhythm is unclear. We have proposed that its preference could come from a magnified representation bias of the neuronal responses underlying the generation of the global gamma rhythm. Even though prolonged orientation adaptation has demonstrated that the orientation preference of gamma rhythm is sensitive to an externally induced bias in neuronal response (Chapter 3), it is still unclear where the preferred orientation comes from in the first place. There are two natural questions to ask: Do we consistently get the same preferred orientation in the global gamma rhythm that is induced by large gratings when we record from the same patch of visual cortex? Is there a certain orientation that gamma always prefers, for example vertical or horizontal in any cortical region?

The observation that the preferred orientation of global gamma recovers to its original preference before adaptation suggests that there is a physiological neuronal substrate that generates the preferred orientation of gamma (Chapter 3). This result seemingly supports the conclusion that the gamma preference recorded from the same cortical region is consistent. The aggregate receptive field size of our recording array is about 2-3 degrees, but the global gamma rhythm is not prominent until stimuli are at least 4 degrees in size. This allows us to present the large grating stimuli (10 degree) at different locations while keeping the recorded region driven. Results in Appendix II showed that even though the

recorded region is always stimulated by the large gratings, the preference of the global gamma changes systematically as the location of the large gratings in visual space changes.

This result argues against the possibility that the preference represents a hardwired neuronal population tuning property in the recorded cortical region. Instead, the orientation preference of the global gamma rhythm could be flexibly formed based on which visual cortical regions are activated coherently and contribute to the formation of the global gamma. Therefore, the answer to the first question is that the tuning of the global gamma detected at one cortical location or even a large cortical area is flexible depending on the network generating gamma.

To answer the second question, I compared the orientation preference of the global gamma rhythm from 22 hemispheres, but did not find a consistent preferred orientation (See Figure 2.15 in Appendix II). However, I did observe a tendency for the preferred orientation to cluster between 0 and 90 degree when the array was implanted in the right hemisphere, while the preferred orientation tended to reside between 90 and 180 when array was implanted in the left hemisphere.

Recent studies of the orientation tuning of the BOLD-fMRI signal have revealed that the each location in the primary visual cortex tends to prefer an orientation that is specified by its radial position relative to the fovea (Freeman et al., 2011; Sasaki et al., 2006). Because the BOLD-fMRI signal reflects neural activity at a coarse level, this suggests

that there is a general radial bias of the neuronal representation. If true, it is possible that this radial bias could underlie the orientation preference we observe in the global gamma rhythm. Our preliminary findings support this hypothesis. We observed that the global gamma preference followed the summed radial bias of the activated region (Appendix II: Figure 2). However, more evidence and analysis is required to fully test the radial bias theory, and to understand the preference of the global gamma rhythm more generally.

It is interesting to note the orientation preference of the gamma rhythm is not fixed at a given cortical location, which could be different from the radial bias observed in fMRI studies that showed similar orientation preference that is radial to the fovea across at the same visual cortical regions even in different individuals. Further tests using similar stimulus conditions and subjects are necessary to make the direct comparison, because the radial bias detected with fMRI could reflect a neuronal representation bias of a neural population which is the underlying source of the preferred orientation in global gamma rhythm, but cannot explain the network mechanism that gives rise to the preference in gamma.

5.6 Laminar dependency of LFP power

The strength of gamma is laminar dependent. The manuscript in Appendix IV (submitted manuscript) demonstrates that stimulus induced gamma power (30-50Hz) is higher in the middle layers of the visual cortex and lower in the superficial and deep layers. An opposite trend is seen in the low-frequency (0-10 Hz) power of the LFP: this is relatively weaker in the middle layers, but significantly stronger in the deep layers. These

observations suggest that the different neuronal circuits and architecture in different cortical layers of a single cortical area can generate different rhythms. The laminar dependence of the LFP power we observe is inconsistent with a recent paper, which suggested that the LFP signal originates from the infragranular layers rather than granular layers (Maier et al., 2011). However, their early work also showed similar trend as our gamma power across layers, but different changing trend for low frequency power (Maier et al., 2010). This discrepancy could be caused by several differences in experiment paradigms: First our analysis is based on induced LFP power, while the other study did not separate out the evoked component; Second, we used anesthetized monkeys while the other study used awake monkey (we used different visual stimulus conditions); Third, we recorded different depth independently while the other study used translaminar linear array; Finally, we computed power based on induced signals and the other study computed band-limited power and the second derivative of the band-limited power. Although more work is required to resolve this discrepancy, I will discuss the laminar circuitry with our observation which indicates that the induced gamma power is strongest in the middle layer.

There are two basic requirements for gamma generation: excitatory inputs and a coupled inhibitory neuronal network. Middle layers of primary visual cortex (layers IV), which is generally referred as the granular layer, contain different types of inhibitory interneurons and densely packed granule cells. These neurons receive excitatory inputs from thalamus (LGN) and infragranular layers (layers V and VI) and projects to supra and infra granular layers (III, V and VI) in the same column (Peters et al., 1994). Granule cells in layer IV

of primary visual cortex have spiny dendrites with most of their axons emerge from the side facing infragranular layer. This morphology would allow the neurons in layer IV to form dipole electrical field and the densely aligned structure of these neurons in the middle layer allows the accumulation of extracellular electrical field. The proportion of GABAergic interneurons is roughly consistent across cortical layers, which is about 20% of the total neurons, except some inconsistent higher proportion in layer IV (Hendry et al., 1987) or layer II-III (Fitzpatrick et al., 1987). Therefore, the strong excitatory feedforward inputs from thalamus and the existence of inhibitory interneurons (Lund, 1988; Lund et al., 1979) provides the cellular basis for gamma generation.

However, according to pyramidal interneuron gamma (PING) model which proposes that the generation of gamma rhythm involves the interaction between pyramidal neurons, which mostly present in the superficial and deep layers, and inhibitory interneurons, layer IV seems unlikely to be the signal source of gamma rhythm. However, most models of gamma formation are based on slice recording in the hippocampus(Bartos et al., 2007). Considering similar properties between pyramidal cells and granule cells, it is possible that if gamma originates from middle layer in the cortex, formation of the gamma rhythm uses granule cells instead of pyramidal neurons. Alternatively, since the pyramidal neurons are vertically orientated and have synapses terminate in the middle layer, it is important to consider that the majority of the inputs to layer IV originate from other layers in the same cortical column (Peters et al., 1994). Therefore, it is possible that recurrent connections provided by the microcircuitry across laminar can contribute to the formation of gamma rhythm. Nevertheless, why gamma is strongest in the middle layer is

still an open question that requires further dissection of the neuronal substrates and circuitry. Our finding of the laminar dependence of gamma power also provides more constrains on the micro-circuitry proposed in gamma formation.

In addition, the limited spatial extent of the neural circuitry in the middle layers is inconsistent with the spatial extent of the gamma. Compared with middle layers the superficial and deep layers are more richly interconnected horizontally, by lateral and long-range horizontal connections known to extend for several millimeters (Gilbert and Wiesel, 1983, 1989; Ts'o et al., 1986). It is possible that the generation of the strong gamma power involves the extensive horizontal connections in superficial and deep layers, which synchronize the neuronal activity from a broad region and feedback onto the neurons in the middle layers, but the higher gamma power in the middle layer stands out because the summed voltages that are passively conducted from other layers. Alternatively, it is also possible that the interneurons in the middle layers are coupled by gap junctions (Traub et al., 2001), which can synchronize and extend the inhibitory network and contribute to the formation of a global gamma rhythm, since the conduction delay by horizontal connections could be too slow to form gamma rhythm. However, it is important to note that the stimulus size we used in the depth experiments are intermediate sizes in the curve of the spatial extent of gamma. It is possible when gamma power is dominated by the global rhythm, the laminar distribution of gamma power will be different. It is also important to emphasize that the gamma power is highest in the middle layer but the range with significant gamma is much broader than a single layer in the

cortex. More studies targeting specific neuronal subtypes are required to tease apart these possibilities.

5.7 Laminar effects on array recordings

Although we can manipulate the strength of gamma with visual stimuli, the maximum gamma power induced by large gratings is variable across implants. In addition to variability caused by individual animals and anesthesia, the laminar dependency of gamma power could also in part explain this variability in gamma power. The length of each electrode on the array is 1 mm. We implant the electrodes to a nominal depth of about 600-800 μm, but it is difficult to control the precise depth of the insertion. If the implantation is not deep enough, gamma power would be expected to be significantly weaker, and the gamma 'bump' of the power spectrum absent. This could account for the differences in the degree of clustering of orientation preference in different implants.

When a rigid flat array is implanted into the brain, the depth of the recording electrodes on the same array could be slightly different depending on the angle of implantation and curvature of the brain surface. This could be potentially problematic for two reasons. One is that the strength of gamma power could be variable on the same array caused by the depth dependency of gamma power. The other problem is the potential influence of depth on the detected gamma phase. Assuming a global rhythm originating from the middle layers of the cortex that horizontally extends more than 9 mm, sensing the same rhythm in the superficial layers could artificially introduce a phase delay relative to its origin.

Under this condition, we might get less phase coherent gamma rhythm simply because of the unfair measurement of phase rather than an indication of less global gamma rhythm.

5.8 Active and resting states

During active states, the featured rhythms are different in different brain regions and have their own characteristic properties (Kopell et al., 2000). For example, the stimulus-induced rhythm is in the gamma frequency range in visual cortex, while beta rhythm (12-30Hz) is most distinctive in the motor cortex during motor tasks and the theta rhythm is prominent in the hippocampus. Based on our understanding of the network mechanisms generating gamma and theta, the reason that different brain areas possess different signature rhythms during active state could be caused by the different neuronal circuitry, properties and morphology of the neurons in those areas. Along the same line, if we understand the network mechanisms that give rise to the different rhythms, they can be used as a macroscopic indicator of the properties of the neuronal network. However, although different brain areas may have different rhythms during active states, the prominent fluctuation during resting state is always at low frequencies, and these are suppressed during the active state.

During resting state, brain rhythms are dominated by low frequency fluctuations. This suggests that the brain can self-generate long timescale oscillatory activity patterns in the absence of external or internal activation. The origin of these low frequency fluctuations (<5 Hz) could come from interactions between thalamus and cortex (Buzsaki, 2006). Studies using functional imaging have investigated the functional or structural

connectivity of default brain activity during resting state (<1Hz) (Greicius et al., 2009). However, the neuronal circuitry involved in the generation of slow low frequency fluctuations during resting state is still unclear, as is their potential functional role. It is thus interesting to ask the question why at default state low frequency power dominates. Does it mean the neural circuitry involved in the generation of different rhythms, for example low frequency and gamma rhythms, are mutually exclusive?

5.9 Weak anti-correlation between low frequency and gamma rhythms

Much evidence suggests a general anti-correlation between higher frequency power, especially gamma frequency, and low frequency activity of the LFP (<10Hz). For example, compared with spontaneous activity, visual stimuli induce more gamma power but reduce low frequency power. Enlarging stimulus size also increases gamma power and reduces low frequency power. Another consistent observation is the opposite laminar dependence of low frequency power of the LFP and the gamma rhythm. Unlike the gamma rhythm, low frequency fluctuations do not have clear receptive field properties. For example, power in this band is not orientation tuned and adaptation effects in these frequencies are also not specific to the adapted orientation. Therefore, although the general relationship between low frequency power and gamma are anti-correlated, the negative correlation may not apply during sensory-driven conditions for different feature selectivity, because the neuronal circuitry involved in slow fluctuations are more active during the spontaneous state and does not have significant selectivity for visual stimulus features.

5.10 LFP and neuronal correlation

It has been shown that long timescale correlated neuronal response, reflected in the broad peak of the cross-correlogram (CCG), is more prominent during spontaneous activity or with low contrast gratings, and suppressed during high contrast stimulus driven state (Kohn and Smith, 2005). I have introduced in the general Introduction that low frequency correlation in neural membrane potentials are stronger during resting state, and is decorrelated in the active state, whereas gamma-band synchronization of neuronal responses serve as a signature for active brain state. Together with our observations of similar depth laminar dependence of neuronal spike count correlation (r_{sc}), broad peak of CCG and low frequency power (Appendix IV), and the reduction of low frequency power of the LFP with sensory inputs compared to spontaneous (Jia and Kohn, 2009) and with large gratings compared with small suggest a potential link among low frequency correlated voltage fluctuations in the LFP, spike count correlation (rsc) and long timescale neuronal correlation (broad peak of CCG or low frequency of the spike-spike coherence).

Specifically, the energy in low frequency fluctuations of the extracellular field potential could reflect coordinated neuronal activity on long timescales and indicate that the network is less synchronized on brief timescales. What are the benefits of resting states to have long timescale neuronal correlation? One possibility is that in a highly interconnected neuronal network, the spontaneous neuronal activity in individual neurons (either stochastic or rhythmic at different frequency) will reach harmony every now and then, with the regulation of thalamic inputs at resting states during this process (Buzsaki,

2006). If this hypothesis of spontaneously generated slow fluctuation is true, then low frequency energy and the long timescale neuronal correlation may purely reflect the default state of the brain rather than serving any functional purpose. Alternatively, the slow timescale correlated fluctuations may be a default state and any interruption of this correlated activity will appear more distinguishable to the brain.

Previous work failed to establish a solid link between brief timescale neuronal correlation (synchrony) and neural activity in the gamma frequencies, reflected either in pairwise neuronal gamma-band synchronization or the gamma rhythm of LFP. Instead, there is only limited evidence for a relationship between synchrony and gamma, except for some weak or negative observations (Fries et al., 2008; Roy et al., 2007; Samonds and Bonds, 2005), even though this relationship has been implied and widely assumed. Chapter 4 of my thesis examined the relationship between strength of stimulus induced gamma rhythm and brief timescale neuronal correlation of a large neural population and found a strong correlation between these two.

In summary, the power in each frequency of the LFP is related to the neuronal correlation at different timescales: the power of the gamma rhythm reflects brief timescale neuronal correlation while lower frequency energy reflects long timescale neuronal correlation., The reduced low frequency activity with sensory inputs could reflect decorrelation on long timescale (Appendix IV) and allow more specificity of coding in the responses of individual neurons (Cohen and Maunsell, 2009; Mitchell et al., 2009). The enhanced stimulus selective gamma activity can carry more information of the sensory inputs,

increase neuronal synchrony and potentially influence signal propagation. Therefore, the ratio between gamma and slow fluctuations (<10Hz) could be used as an indication of neuronal network state.

5.11 Surround, cortical feedback and gamma rhythm

Neuronal responses within the classical receptive field are suppressed when simultaneously activating a surrounding area, which by itself does not evoke a response in the receptive field center (Cavanaugh et al., 2002a; Jones et al., 2001; Kapadia et al., 1999; Knierim and van Essen, 1992). Anatomical and physiological studies have shown that surround effects could involve horizontal connections within V1 and feedback connections from higher visual areas (Angelucci and Bressloff, 2006; Angelucci et al., 2002a; Angelucci et al., 2002b; Schwabe et al., 2006). Since gamma can form a global rhythm and gamma power increases monotonically with enlarging stimulus size (Gieselmann and Thiele, 2008; Jia et al., 2011), it is possible that feedback connections from higher cortical areas would contribute to the formation of global gamma rhythm.

Although there is no direct evidence of feedback connections in shaping the surround, it has been found that the effect of surround suppression propagates significantly faster than conduction delay of horizontal connections, which could be account for by the participation of feedback connections from higher cortical areas (Bair et al., 2003). Additionally, surround suppression has slower dynamics compared to responses within the classical receptive field (Smith et al., 2006; Webb et al., 2005). In Chapter 2, I have demonstrated that gamma power takes about 200ms to reach its maximum strength,

which is much slower than the dynamics of neuronal response in the center but closer to the dynamics of the surround response. Therefore, the slow dynamics of surround suppression and gamma power indicates that they might share similar network mechanisms, potentially involving feedback modulation from extrastriate cortex.

In Appendix III, I show with preliminary results that gamma power in V1 is enhanced with weak electrical stimulation of neurons in V2 that presumably send feedback connections to V1. These findings indicate that activating neurons in higher cortex can potentially increase the excitatory drive to the lower cortical neurons, enhancing the strength of the gamma rhythm. Even though microstimulation in a reciprocally connected networks could introduce changes that are not specific to feedback connections, these results provide additional supporting evidence for the proposed involvement of feedback connections in the formation of gamma activity.

Another piece of evidence in support of the involvement of feedback in gamma rhythm generation is the associated changes between gamma activity and the allocation of spatial attention (Fries et al., 2008). Attention is a cognitive process that involves effective concentration on one thing while ignoring others. The instructed allocation of attention is an active top-down mental process. Therefore, enhanced gamma power with attention suggests top-down process, which indicates stronger feedback regulation, could participate in gamma activity.

If gamma activity involves feedback from extrastriate cortex where receptive fields are larger and more complex, it is possible that the gamma activity could help with perceptual grouping of low-level visual features according to certain rules, like proximity, similarity and smoothness (Koffka, 1935; Roelfsema, 2006). It has been demonstrated that feedback projections from higher visual areas can facilitate figure-ground segregating in lower visual areas (Hupe et al., 1998), but see (Hupe et al., 2001a) for counter evidence. Similar to the slow dynamics of induced gamma power, the time-course of the perceptual grouping related phenomena in V1--figure-ground segregation (Lamme, 1995) and border ownership (Zhou et al., 2000)--are also slow and only distinguishable 200 ms after stimulus onset. This delayed response time is consistent with the dynamics of surround suppression and gamma, which is long enough to allow feedforward information to reach prefrontal cortex and feedback to V1 (Hupe et al., 2001b; Movshon and Newsome, 1996). More interestingly, gamma power is reduce on the boundary of two textures (Gail et al., 2000), suggesting a sensitivity of gamma to figure segregation. These findings imply a potential functional role of gamma activity in perceptual grouping and the possibility to study complex visual processing through changes in gamma activity.

5.12 Potential functions of gamma

5.12.1 Temporal reference--Binding

To resolve the perceptual binding problem (Treisman, 1996; Wolfe and Cave, 1999), previous studies have proposed a theory named ‘binding by synchrony’ (Engel et al.,

1997; Singer, 1999; Singer and Gray, 1995). This suggests that when neurons are synchronized in milisecond timescale, they are bound together as a neural ensemble for downstream processing. This theory was supported by the finding that neurons are more synchronized when they have similar orientation preferences or stimulated with a single bar stimulus (Freiwald et al., 1995; Gray et al., 1989). Because similarity and continuity belong to the criteria of perceptual binding proposed by *Gestalt* psychologists, synchrony among neurons could be used as a binding mechanism (Engel et al., 1999; Engel et al., 1997).

This theory was extended to 'binding by gamma-band synchronization' later because of observations of rhythmic activity in a neural ensemble synchronized in the gamma frequency, which is both selective for stimulus features (Fries et al., 2002; Gray and Singer, 1989; Liu and Newsome, 2006; Vinck et al., 2010) and sensitive to stimulus context (Fries et al., 1997; Jia et al., 2011; Lima et al., 2010; Zhou et al., 2008). It has also been proposed that the gamma rhythm can be used as a temporal reference which regulates spike timing and associates neural ensembles for further processing (Fries, 2009; Fries et al., 2007). However, given all these findings and proposals, there are two important questions that are still unanswered: the first one is how neuronal synchrony relates to gamma rhythm in the brain; the second one is the relationship among synchrony, gamma activty and the efficiency of signaling (Singer et al., 1996), which is the determinating evidence for the theory of binding.

Previous studies in awake monkeys have indicated a correlation between gamma LFP power and gamma band neuronal synchronization, seen as enhanced pairwise spike-spike coherence or spike-field coherence (Fries et al., 2008; Herculano-Houzel et al., 1999; Lima et al., 2010). However, few studies have compared neuronal synchrony in brief timescale with the strength of gamma, and those studies that have reported null (Fries et al., 2008) or weak (Samonds and Bonds, 2005) findings. Chapter 4 of my thesis addressed these questions and provided an extensive test of the relationship between gamma and pairwise and higher-order synchrony in a neuronal population with a wide range of stimulus manipulations, and revealed stronger effects than previous studies. One possible reason is that our experiment design allows us to manipulate gamma power up to 2-fold, which is significantly larger compared to previous studies. Our findings demonstrated correlated changes in brief timescale neuronal synchrony and gamma power, along with significant changes in transmission efficacy between V1 and V2. These findings suggest that the global gamma rhythm could be used as a temporal referencing frame to form a synchronized neural ensemble, with enhanced efficacy of the outputs from this neural ensemble in driving target neurons. These findings are thus in favor of the 'binding by synchronization' hypothesis.

The binding problem consists two parts: segregation of different features and grouping of similar features. Our finding of the spatial extent of the global gamma rhythm provided the possibility for gamma to group spatially segregated neurons together and potentially the mechanism of segregation, based on the sensitivity of gamma to spatial continuity of the visual stimuli. If gamma rhythm can be used as a mechanism in the 'binding' process,

it also needs to have specificity in the grouped neural ensemble, for example selectively grouping neurons representing features of the same object or with similar preferences. However, with our current understanding of the gamma rhythm, it is unlikely that gamma possesses fine spatial scale specificity, since the gamma rhythm with the potential to support neuronal synchrony over long distance (Chapter 4; see also (Konig et al., 1995)) is a global rhythm (Jia et al., 2011), with shared feature selection properties in different locations and does not have specificity for individual neurons. Therefore, our study not only provided supporting evidence for the potential functional role of gamma in perceptual binding but also restrictions. To evaluate the 'binding by gamma-band synchronization' hypothesis, it is of great importance to solve the specificity problem of gamma rhythm first.

5.12.2 Communication channel

Since selective attention can increase gamma power, it has been proposed that the gamma rhythm can function as a communication channel, which selectively routes information between cortical areas (Womelsdorf and Fries, 2006). Furthermore, enhanced cross-area coherence in the gamma frequency range has been observed in many cortical and sub-cortical regions during attention (Buschman and Miller, 2007; Gregoriou et al., 2009; Womelsdorf and Fries, 2006; Womelsdorf et al., 2007), learning (Popescu et al., 2009) and memory tasks (Jutras et al., 2009; Montgomery and Buzsaki, 2007). Additionally, the reaction time of human subjects is shortened with increased gamma band coherence between cortex and spine (Schoffelen et al., 2005a). All these evidences suggest that enhanced gamma coherence correlates with more effective communication and ultimately

leads to another proposed function of gamma: the 'communication through coherence' hypothesis. This hypothesis states that when the gamma rhythms in two neuronal groups are in good phase relationship, the communication efficiency between the two groups is maximal (Fries, 2009; Womelsdorf et al., 2007).

This proposal requires that the efficacy of signal transmission changes with gamma coherence (Akam and Kullmann, 2010; Knoblich et al., 2010; Salinas and Sejnowski, 2000, 2001). However, previous studies fail to demonstrate how gamma activity between neuronal networks affects the relaying of spiking activity. Our study is thus the first to demonstrate clearly that in synaptically-coupled networks, upstream inputs (V1) are more effective in driving downstream neurons (V2) when gamma power is enhanced in both areas, and this is accompanied by increased gamma band V1-V2 coherence.

The proposal of corticocortical communication through coherence (Schoffelen et al., 2005b; Womelsdorf et al., 2007) involves a postsynaptic mechanism--the downstream gamma rhythm--which can effectively gate, or modulate, the efficacy of input, depending on its arrival time with respect to the local gamma rhythm. It is important to note that the basis of this hypothesis is the interpretation of the gamma cycle (Fries et al., 2007). If different phases of gamma cycle reflect the relative strength of local excitation and inhibition, the timing of input spikes relative to the gamma cycle will affect their ability to drive the target neuron. Based on this, gamma band coherence of neuronal activity can dynamically group neurons into functional ensembles and select relevant information during attention (Womelsdorf and Fries, 2006, 2007). We directly tested synaptic

efficacy as a function of V2 gamma phase and found that it was more related to the temporal alignment by presynaptic inputs rather than regulation of postsynaptic gamma phase (Chapter 4).

When gamma is strongest in V1, this is reflected in a coherent, albeit phase-delayed, gamma rhythm downstream. Indeed, in a feedforward architecture in which population inputs are varying rhythmically at gamma frequencies, it would appear difficult to establish a local rhythm with independent phase relationship with respect to those inputs. In this sense, it may not be appropriate to consider the gamma rhythms in the two coherent areas as two independent signals, both capable of selecting specific subpopulations of neurons to be functionally channeled. With these arguments, I speculate that the enhanced coherence between cortical areas could be a pure epiphenomenon of rhythmic feedforward synaptic inputs and local network, rather than a functional channel of information transmission. Further work is needed to distinguish between the communication through coherence hypothesis and this alternative possibility.

5.13 Restrictions on potential functional role of gamma

5.13.1 Change in efficacy is different from firing rate

I have shown in Chapter 4 that the gamma rhythm induced with large gratings, especially its preferred orientation, correlates with enhanced neuronal synchrony in V1 and increased effectiveness of each spike in V1 in driving downstream V2 neurons. If gamma influences signal processing by manipulating spike efficacy, it is natural to expect that

large gratings should cause higher firing rates in downstream neurons and that the orientation preference of neurons in V2 should follow the orientation tuning of global gamma in V1. In fact, large gratings suppress neuronal firing in V2 as well as in V1, and the tuning of V2 neurons does not follow V1 global gamma activity. This suggests that a change in the efficacy of input spikes from one area to another do not indicate a change in the output firing rate of the target neurons. This could be caused by several reasons. First, although the efficacy of individual spikes in driving target neurons increased with large gratings, the total number of output spikes from V1 decreased with large gratings. The summed effect could be dominated by the number of spikes rather than the effectiveness of each spike. Second, the reduction of firing rate with large size is not only caused by a change in feedforward inputs, but also surround suppression coming from lateral connections and feedback. In other words, the firing probability of the V2 neuron could be higher after each synchronized V1 spike, but the inputs to V2 neurons can also involve other sources. As a result, input efficacy from one source cannot determine the fate of the target neuron. This reason could also explain why tuning of V2 neurons does not follow the orientation tuning of global gamma in V1. Third, it is important to note that although the change in single spike efficacy is significant, the absolute difference in efficacy is still small. Even without the effect of input firing rate, the consequence of such small changes in efficacy may not be functionally important.

5.13.2 Sensitivity of global gamma

The stimulus induced gamma rhythm is extremely sensitive to the spatial and temporal continuity of the visual stimuli. For example, compared with a constantly drifting large

grating stimulus, smaller stimulus size (Gieselmann and Thiele, 2008), abrupt changes in drifting speed (Kruse and Eckhorn, 1996), the boundary of two gratings with phase offset (Gail et al., 2000), noise-masking (Jia et al., 2011), gradual changes in the contrast of a grating (Ray and Maunsell, 2010) and super-imposing another grating (Lima et al., 2010) will reduce the power and coherence of the gamma rhythm. The sensitivity of gamma to visual stimuli properties make it hard to form in a continuously changing environment.

5.13.3 By-product or key-player

It is hard to distinguish whether the observed brain rhythms are pure by-product of the neural activity of the brain or has a functional role (Buzsaki and Draguhn, 2004; Fries, 2009; Ray and Maunsell, 2010). The magnitude of extracellular gamma rhythm, even when strongly induced (~200 μV), is much weaker compared to the strength of electrical field necessary to influence the firing of the neurons (Frohlich and McCormick, 2010), which is about 1mV. However, it is still possible that *in vivo* the large gamma rhythm might have some influence on membrane potential (e.g. through ephaptic effects).

Nevertheless, it is important to remember that even hypothetically, gamma could influence the firing pattern of individual neurons, the neural network needs to first generate the strong gamma rhythm. Given that only synchronized network has the potential to form a strong rhythm, the strong gamma rhythm is the consequence rather than the requirement for the formation of a synchronized network. However, after forming a global gamma, whether this rhythm could help regulate spike timing and maintain the network in the oscillatory state is unclear.

5.14 Technical factors affecting results

There are several technical factors that might affect the results in addition to stimulus paradigm. These include recording issues like electrode impedance, volume conduction and referencing, drift in eye position, and different calculation methods.

For electrode impedance, even if all electrodes are at the same depth, the variability of the impedance of electrodes from the same array can still change gamma power. However, since we always compare gamma under different conditions on the same electrode, this is not likely to strongly influence our results.

Volume conduction is often a concern when evaluating LFP studies. To make this problem clearer, I would like to introduce the circuitry of LFP measurement first. Consider the signal source of the detected LFP as an electrical power source with alternating current, our detecting electrode as a volt meter which measures voltage difference between the sensing point and a reference, and the brain tissue between the signal source and the sensing electrode as a resistor with certain conductance. What we measure from the recording electrode is actually signals that are volume conducted through brain tissue from the signal source. Because of the resistance of the brain tissue, the amplitude of the detected signal will decay as a function of distance between the sensing electrode and signal source. Therefore, volume conduction can affect the spatial resolution and amplitude of the measured LFP, which means it could potentially affect our characterization of the tuning and spatial extent of gamma rhythm. Some studies have

tried to estimate the spatial extent of passively propagated field potential signals and found various values. Some propose that the passive propagation of the evoked LFP potential, including gamma, is restricted to ~300 μm around the recording electrode, since its tuning is similar as local MUA and different from the tuning detected on the other electrode 400 μm apart (Katzner et al., 2009). Visual evoked potentials in another study revealed similar results, which is about 250 μm around the recording tip, with variations across laminae (Xing et al., 2009). A recent study further demonstrated that laminar structure can affect volume conduction but found a much broader extent of volume conducted voltage (Kajikawa and Schroeder, 2011). Therefore, it is possible that at any location, the detected LFP is a mixture of local signal and many other signals passively conducted there. However, even though the signals from other sources can ultimately reach the sensing electrode, the extracellular signal detected by the recording electrode is a summed signal and the contribution of other signals could diminish after summation because of phase offset and only remain the signal originate from local neural activity which gets effectively aggregated. This is supported by the fact that tuning of the evoked potential is similar as local spiking activity but different on neighboring electrodes (Katzner et al., 2009). For the stimulus induced gamma oscillation which is spatially coherent, it is still impossible for signals that originate from other sources to aggregate. Since the global gamma is phase coherent at any location at a given time point, the passive propagation of signals from different distances will cause different phase delays and in the end fail to accumulate. In addition, the high orientation selectivity index of the global gamma rhythm that is comparable to MUA suggests a limited contribution from volume conduction (For additional arguments against the volume

conduction contribution, please see discussion section in Chapter 2). Therefore, the spatial extent of our observed global gamma rhythm is not a result of volume conducted signals from a spatially extensive region, but is generated from a synchronized neural network. However, since the passive volume conduction always exists, it is necessary to evaluate its contribution in the results and separate it from any active process.

Another relevant technical issue is referencing. The voltage signal is always measured as a difference between the recording electrodes relative to a reference. In the array recordings, we place two independent wires underneath the dura at different locations and use either of them as a reference for data collection. Since the reference wire can be treated as a measure of intracranial field potential, our detected local field potential from the array is actually a difference between local field potential and the intracranial field potential. Because the intracranial field potential is dominated by very slow fluctuations and is much weaker, the difference has less influence on the gamma rhythm. To rule out the potential contribution of referencing in our results on the global gamma properties, we did two independent controls. First, we simultaneously recorded the global gamma rhythm from both multi-electrode array and the Thomas system, whose reference is the guide tube of each electrode. We found that the tuning of global gamma was the same in these two systems. Second, we compared the orientation tuning of the global gamma with recordings using different referencing wires of the array. If the orientation bias is introduced by a potential tuning of gamma detected in the referencing wire, we would notice a difference under this condition. We found exactly similar orientation tuning of global gamma rhythm from the two independent referencing wires (data not shown).

Therefore, different referencing and recording systems can only alter the amplitude of the signal but not its preference.

A final consideration is that drift in eye position can affect the tuning of gamma detected at a particular location on the cortex. Because the preferred orientation of global gamma depends on the region of visual cortex that is involved in the generation of this rhythm, when there is significant eye movement while the visual stimulus is presented at the same location on the monitor, different visual cortical region relative to fovea gets activated and will change the tuning of gamma rhythm. Throughout my thesis, all tuning evaluation is based on stimuli centered on the aggregated receptive field of the array. Since we use norcuron (vecuronium) to prevent eye movement and frequently monitor the receptive field location during our experiments, it is unlikely eye movement strongly affected our data. However, it is important to be aware of this issue in awake monkey experiment and during long recording sessions.

Except for recording issues, it is possible that different approaches of analysis would result in different results. I would like to point out that different windowing methods of the power spectrum estimation of the LFP and different normalization methods of the LFP power will not alter our findings. To be sure of this, I compared tuning of the LFP with power spectrum calculated with different windowing methods and found similar tuning with all methods. Since we compute the power spectrum using Fourier transform on a time limited chunk of signal, we need to apply smoothing window function to prevent energy leakage. It is important to note that different window sizes can affect the

resolution of the estimated power spectrum. For a given window size, different window functions can also alter the shape of the spectrum. Therefore, for a given signal, choosing a proper window size and function is critical for a good estimation (enough resolution but not noisy) of the power spectrum. We used multi-taper method that has been widely used and proven to be sufficient (Mitra and Pesaran, 1999; Pesaran et al., 2002). However, as I have mentioned, our findings do not depend on the method of power spectrum estimation.

To evaluate stimulus-driven changes in LFP power, some studies normalize the power spectrum by subtracting or dividing by the power spectrum of spontaneous activity (Berens et al., 2008; Gieselmann and Thiele, 2008; Henrie and Shapley, 2005; Logothetis et al., 2001), others used the raw power (Jia et al., 2011; Liu and Newsome, 2006). I compared orientation tuning of gamma based on raw power with normalized data and did not observe a major difference. However, I presented the power spectra of both stimulus-driven and spontaneous activity rather than normalizing, since the origin of different frequency components of spontaneous activity is unclear, it is not easy to justify the meaning of power after normalization.

5.15 Speculation: potential applications

My thesis focused on the properties of gamma rhythm of the LFP and its relationship with neuronal activity. Regardless of the potential functions that the gamma rhythm serves in the brain, there is a neural network that is actively involved in generating this rhythm. Therefore, with our understanding of the neuronal network activity underlying

the changes of gamma rhythm, we can use gamma as an indicative signal of changes in neuronal response when we cannot record directly. For example, abnormal gamma could reflect abnormal inhibition and thus suggest an abnormality in GABAergic interneurons or the synaptic coupling among inhibitory neurons. This link could be useful in the studies of brain disease, since unusual gamma activity has been observed in Alzheimer's disease, Schizophrenia and autism (Uhlhaas et al., 2006; Uhlhaas and Singer, 2006).

Additionally, it has been noticed that the cross area synchrony and magnitude of gamma is trainable by mental practice like meditation (Lutz et al., 2004). The effect of phase synchronization and the strength of gamma are significantly higher in Buddhist practitioners than newcomers during meditation. This suggests that meditation can induce long-term changes in a large scale neural network. However, it is unclear why mental practice can induce this fast timescale synchronization and how continuously strong gamma activity would affect the neuronal responses. Another interesting observation is that the gamma activity recorded in the practitioners during meditation is the strongest gamma rhythm recorded by EEG so far. In traditional Chinese medicine, there is a mental practice called '气功 (qi gong)', which refers to the mentally guided circulation of imaginary flow around the body. During practice, the person can be more sensitive to environmental changes with eyes closed and the electrical magnetic field around that person is enhanced. Since this is also an attention based process, I wonder whether gamma synchronization could explain the mental change after practice.

Last but not least, the ability of individuals to control the strength of attention related gamma rhythm could be used as an indicative signal in brain-machine interface and can also be potentially useful in designing interactive computer games.

5.16 Future directions

I recorded neuronal response and LFPs from a large neural population extracellularly *in vivo*. However, although we are able to study simultaneously recorded neuronal response in a large network and compare its changes with LFP, our recordings cannot control for different neuron types in the network. With newly developed genetic tools, manipulating the activity of different subtypes of neurons in a neuronal network that give rise to the global gamma with (Fenno et al., 2011) while recording large number of neurons simultaneously will allow us to study the cellular mechanism underlying global gamma generation *in vivo.*

Appendix III: Feedback from V2 to V1

Xiaoxuan Jia[1] and Adam Kohn[1,2]

1 Dominick Purpura Department of Neuroscience

[2]Department of Ophthalmology and Vision Sciences

Albert Einstein College of Medicine, Bronx NY 10461

Acknowledgements: We thank Amin Zandvakili and Stephanie Wissig for assistance with data collection.

X.Jia designed and performed the experiments. X.Jia analyzed all the data in this section.

Abstract

Cerebral cortex is a hierarchical structure, with feedforward, feedback and horizontal connections. Understanding the function of feedback is critical to understanding information processing in the cerebral cortex. Feedback has been proposed to underlie perceptual grouping, figure-ground segregation, contour integration, visual attention, awareness and other forms of top-down regulation. However, compared with feedforward connections, most of these proposals are speculative and the functional properties of feedback are still unclear. The reciprocal connections between primary cortex (V1) and V2 make it an ideal system for this study because of the abundance of the connections and the relatively well-known neuronal properties. We recorded V1 neurons with multi-electrode array while simultaneously microstimulating V2 neurons under different conditions. We found significant enhancement in the gamma power in V1 when stimulating V2 neurons which retinotopically overlapping. This effect is affected by stimulus size the contrast, and is laminar dependent in V2. Since feedback connections are weak and diffuse, I propose that feedback modulates neural activity by changing the relative gain of excitation and inhibition, which is reflected in changes in the gamma rhythm of the local field potential (LFP).

Introduction

It is commonly accepted that cerebral cortex is organized in a hierarchical way (Felleman and Van Essen, 1991). Based on their laminar origin and termination, intercortical connections are generally categorized into feedforward, feedback and horizontal pathways (Rockland and Pandya, 1979).

Histology and physiology have revealed some basic properties of feedback connections: 1. Feedback connections originate in supragranular and infragranular layers in higher cortical areas and project to supragranular layers in earlier cortical areas (Felleman and Van Essen, 1991); 2. The neurons providing feedback are excitatory and synapse on pyramidal neurons (Angelucci et al., 2002b; Shao and Burkhalter, 1996; Shmuel et al., 2005; Stettler et al., 2002); 3. Feedback connections generate smaller EPSPs compared with feedforward and horizontal connections (Shao and Burkhalter, 1996); 4. The conduction velocity of feedback is the same as the feedforward connections, about 3.5m/s (Girard et al., 2001); 5. Feedback connections are more diffuse than feedforward connections and form few (Angelucci et al., 2002b; Shmuel et al., 2005) or no clusters (Stettler et al., 2002) in the target region; 6. Feedback connections are as numerous as those in the forward direction (Stettler et al., 2002). In summary, feedback connections are weak, excitatory, fast, diffuse and extensive.

Feedback is believed to be important for top-down attentional modulation, discriminating figure from ground (Lamme, 1995; Lamme et al., 1999; Lamme et al., 1998b, 2002), integrating collinear contours over large regions of visual space (Hess and Dakin, 1997;

Kovacs and Julesz, 1993; Lamme et al., 1993), assigning borders to objects (Qiu and von der Heydt, 2007; von der Heydt et al., 2005; Zhou et al., 2000) and generating surround suppression (Angelucci and Bressloff, 2006; Bair et al., 2003; Schwabe et al., 2006). These proposals are exciting but speculative, because most of them have been inferred from responses to different visual stimuli rather than based on direct measurement (Lamme, 1995; Lee and Nguyen, 2001).

As a signal reflecting population activity, the LFP is in some cases more sensitive than spikes to changes in neural activity related to perception (Gail et al., 2004; Wilke et al., 2006), movement intention (Donoghue et al., 1998; Pellerin and Lamarre, 1997; Rickert et al., 2005; Scherberger et al., 2005) and attention (Fries et al., 2001; Jensen et al., 2007). Because it arises from low-frequency extracellular currents that are thought to reflect synchronized synaptic activity, to understand the modulatory effects of feedback, I focused on changes in local field potential (LFP).

We used the massive feedback projections between V2 and V1 as a model system. In the macaque monkey, V1 has been extensively studied and is relatively well understood. Visual area V2 is almost the same size as V1 and is reciprocally connected with V1 (Felleman and Van Essen, 1991; Girard et al., 2001). The extensive feedback connections projecting from V2 to V1 make this an ideal system to study the properties of cortical feedback. The major obstacle in feedback research is that it is hard to measure and separate feedback from feedforward and horizontal effects, because feedback connections are diffuse with weak synaptic strength. Previous studies using cooling or lesions in V2

to silence feedback and showed a reduction in V1 tuning acuity, with no change in orientation preference (Merigan et al., 1993; Sandell and Schiller, 1982). However, the non-specific silencing of an entire cortical area and the low temporal resolution of these techniques make it hard to interpret the results.

To solve this problem, I used electrical microstimulation in V2 while recording in both V2 and V1. Microstimulation is an effective technique for studying functional connectivity in vivo. It allows us to activate neurons in a temporally precise manner and directly activate neurons in a local region. This allows me to recruit the activity of a small neuronal population and to measure their effects on target neurons in V1. This makes it possible to assess the functional specificity of feedback effects in V1 and to detect direct feedback connections from V2 to V1. However, there are two major obstacles to study feedback with microstimulation. One is that it is hard to measure and separate feedback from feedforward and horizontal effects, because information is processed in a loop and feedback connections are diffuse with weak synaptic strength. The second problem with microstimulation is the possible recruitment of antidromic effects. Although we attempted to avoid V1 axons terminating in layer 4 of V2, we cannot rule out antidromic activity. Alternatively, the complementary approaches will be to make use of glutamate injection, uncaging glutamate with laser beam or optogenetics tools.

In addition to the electrical microstimulation, I also used a more physiological approach. Illusory contours of the *Kanizsa* figures evoke strong responses in V2 but not in V1 (Lee

and Nguyen, 2001). I therefore used contour stimuli to drive V2 neurons strongly and evoke strong feedback to V1.

Method

Animal preparation

We recorded from 3 anesthetized, adult male macaque monkeys (Macaca fascicularis). Anesthesia was induced with ketamine (10 mg/kg) and maintained with isoflurane (1.5-2.5% in 95% O2) during venous cannulation. The animal was then placed in a stereotax and anesthesia was provided by intravenuous infusion of sufentanil citrate (6-18 μg/kg/hr, adjusted as needed for each animal), in normosol with dextrose (2.5%). Vecuronium bromide (0.1 mg/kg/hr) was administered to suppress eye movements. Temperature was maintained at 36-37 C°. Physiological signs were monitored (electrocardiogram, blood oxygen level, end-tidal CO2, electroencephalogram, temperature, and urinary output and osmolarity) to ensure adequate anesthesia and animal well-being. A broad-spectrum antibiotic (Baytril, 2.5 mg/kg) and an anti-inflamatory steroid (dexamethasome, 1 mg/kg) were administrated daily. All procedures were approved by the Institutional Animal Care and Use Committee of the Albert Einstein College of Medicine at YeshivaUniversity and were in compliance with the guidelines set forth in the United States Public Health Service Guide for the Care and Use of Laboratory Animals.

Electrical microstimulation

We implanted multielectrode microarrays in the superficial layers in V1 (layer 2/3), while simultaneously placing multiple stimulating and recording electrodes in V2 (interelectrode spacing of 300 microns). One pulse of biphasic electrical current with duration of 100 μs in each phase was delivered by a constant current source (STG 1001)

at the desired time point relative to visual stimulus onset. The amplitude of the electrical currents ranged between 30 μA to 100 μA. If not specified, the stimulated location is roughly layers 5/6 in V2, which we define as around 100-300 μm into V2, where neurons are supposed to project back to V1 layers 2/3.

Visual stimuli

Visual stimuli were generated with EXPO and presented on a CRT monitor (resolution 1024 by 768 pixels; refresh rate 100 Hz) placed 110 cm from the animal. Because there is a higher probability of feedback connections between retinotopically overlapping regions in areas V1 and V2, we mapped the receptive fields by briefly presenting small, full contrast drifting gratings (0.6 degree; 250 ms duration) at different locations on the monitor. The spiking responses at each site were fitted with a 2D Gaussian to determine the receptive field location and extent.

We used these measurements to center gratings on the aggregate receptive field. Visual stimuli consisted of sinusoidal gratings with a fixed spatial (1 cycle/degree) and temporal frequency (6.25 cycle/second) drifting at 4 directions (0, 45, 90 and 135 degree). In general, we used low contrast (contrast=0.33) drifting sinusoidal gratings to drive V1 neurons to a moderate firing level, which allowed us to detect excitatory or inhibitory effects of the feedback induced by microstimulation. Microstimulation was delivered 300 or 500 ms after stimulus onset if not specified (red arrow in Figure 1A). Visual stimuli were presented for 2 second with 1 second inter-stimulus interval. Control conditions,

which are same visual stimuli without microstimulation, are randomized with stimulation trials.

Data analysis

In general, data are analyzed in two different epochs: 100ms after stimulus onset till the time of microstimulation (pre epoch) and 100 ms after microstimulation till the end of stimulus presentation (post epoch). Identical epochs were used for control trials, as indicated by a grey box in Figure 1B. Since LFP power shows dynamics over time, I compared the LFP power on stimulated and non-stimulated (control) trials across the array by calculating the ratio between the power spectra of stimulation and control conditions (Figure 2A).

Results and discussion

We used electrical microstimulation to activate V2 neurons that provide feedback projections to V1. Data reported here are form array implants in V1 from 4 hemispheres, two monkeys. I recorded spiking activity and local field potential (LFP) simultaneously from a large population of neurons in V1 to measure the impact of feedback.

Spatial specificity of feedback effects in V1

We found that single pulse of microstimulation in V2 can induce a strong facilitation in LFP power for gamma and higher frequencies relative to control trials (Figure 2A). Figure 2B plots the power ratio between stimulation and control in low frequency power (0-10Hz) and high gamma frequencies (80-120Hz) according to the electrode location on one example array in V1 for 4 different stimulus orientations. Both low frequency and high gamma power showed inhomogeneous distribution of changes in power. This result suggests that there could be a spatial specificity of the microstimulation effect on V1 LFP power.

Location specificity of feedback effects in V2

We compared the effects of stimulating at different locations in V2. The three electrodes shown in Figure 3A are at roughly the same nominal depth in V2, and spaced horizontally over a distance of 900 microns. We found that the stimulation location in V2 could influence the change in LFP power in V. To optimize our stimulation protocol, we compared the power ratio with or without stimulation with different amplitudes of

electrical stimulation current. Figure 3A showed that effect of stimulation saturate with 100 μA current. The largest change in power is induced by 60 μA stimulation.

Feedback projections are laminar specific (Felleman and Van Essen, 1991). We used this to evaluate the specificity of electrical stimulation in V2. We stimulated at different depth in V2 while monitoring the change in LFP power in V1. On one electrode (E1), we stimulated at 5 different depths with 200-300 microns spacing in V2. On average, we found that the power ratio changes for the first site and second to last site were very similar: both showed suppression in the low frequency power and facilitation in higher frequency power. On the contrary, the two depths in the middle showed suppression for higher frequency power as well as the last site. This result suggested that only when stimulating the infragranular and supragranular layers, which are the output layers in V2, can we get enhanced higher frequency power in V1. Stimulating at depths around the granular layer (input layer) in V2, had opposite effects. This result suggests that the power spectra changes we observe in V1 are specific to stimulating neurons that project to V1 instead of neurons that receive feedforward connections from V1.

Comparison for different contrasts and sizes

Feedback effects have been proposed to be modulatory, but how this input affects the balance of excitation and inhibition in the target area is unclear. Gamma power requires activation of inhibitory network (Bartos et al., 2007) and the monotonic enhancement of gamma power with enlarging size suggest that its power mainly reflects the strength of network inhibition. Moreover, there are physiological evidence showing the balance

between excitation and inhibition could be altered by stimulus size (Haider et al., 2010). Therefore, we used two different visual stimuli to alter the balance between network excitation and inhibition: one is stimulus contrast and the other is stimulus size.

We found that the increase of gamma power with stimulation was higher for low contrast (0.33; thin black line) compared to high contrast (0.67; wide black line; Figure 5A) stimuli, indicating that feedback is stronger when the network is less active, meaning less excitation and inhibition. The size comparison revealed that microstimulation in V2 enhanced gamma and higher frequency power in V1 when the network was driven with a small grating, but reduced gamma and higher frequency power when activity was driven with a large stimulus (Figure 5B). This suggests that when the network is dominated by excitation, feedback induces stronger inhibition, but when the network is already strongly suppressed, feedback connections will reduce inhibition. However, this conclusion is speculative and requires further experimental validation.

Time of electrical stimulation relative to stimulus onset alters dynamics of firing rate in V1

It has been suggested that the feedback effect is delayed relative to the response latency of neurons to response onset in lower visual cortex (Webb et al., 2005). We recruited feedback by stimulating V2 neurons with different delays relative to stimulus onset. Figure 6 illustrates the firing rate evoked by a low contrast large grating combined with either no stimulation or microstimulation applied with different delays. When stimulation was applied simultaneously with stimulus onset (0 ms), the response onset is earlier than

under the control condition. When microstimulation is applied 50 ms after stimulus onset, the response was delayed compared to control. As expected, when stimulation occurs 500 ms after the presentation of the visual, there is no effect on response latency and the time course is similar to control condition.

Correlation between V1 and V2 neurons to illusory contour

We also tried complicated visual stimuli that supposed to drive V2 neurons more than V1 neurons to study the effect of feedback without microstimulation. The stimulus we used are adapted from Lee and Nguyen (Lee and Nguyen, 2001), which are shown in Figure 7A. The V2 neurons we recorded from in this experiment are roughly in layers 5/6. To calculate correlation between V1 and V2 neurons under different conditions, we calculated the average crosscorrelograms (CCGs) between V1 and V2 neuron pairs for different corresponding conditions (Figure 7B) and noise correlation (r_{sc}) between V1 and V2 neurons. We did see a tendency of illusory contour to elicit stronger correlation between V1 and V2 neurons than control conditions. However, we have collected very limited data set with overlapping receptive fields between V1 and V2, which makes it hard to generate a conclusion.

In summary, our preliminary results indicate that the effect induced by microstimulation in V2 causes a weak and specific enhancement of LFP gamma band power, although very low frequency bands of the LFP show a decrease in power. This effect is dependent on horizontal and laminar location of the V2 stimulating site. The effects of feedback depend on the original balance between excitation and inhibition driven by visual stimuli and its

timing relative to visual stimulus onset. These results suggest that the modulatory effect of feedback could alter balance between excitation and inhibition depending on visual stimuli and may be more specific than previously thought.

Figure legends

Figure 1 Illustration of experiment methods. (A) Illustration of visual stimuli and the onset of electrical stimulation (red arrow). (B) LFPs averaged across trials to show the duration of the stimulation artifact. The gray area indicates the time epoch 100ms after stimulation, which is used for comparison of LFP power between stimulation and control conditions. (C) Power spectra of the post stimulation epoch for microstimulation and control conditions.

A

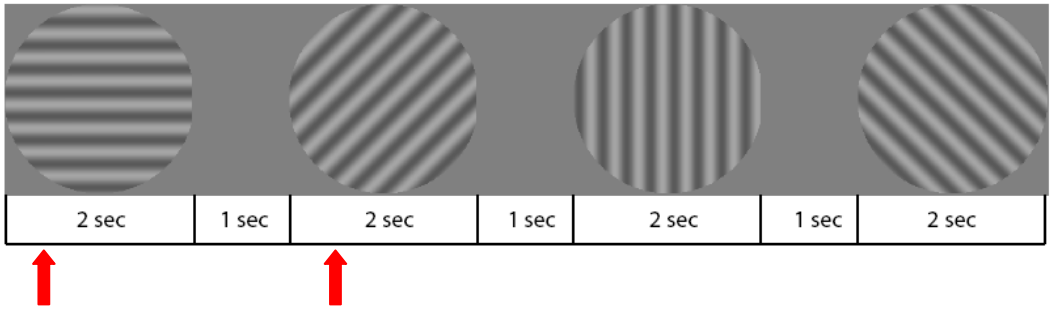
2 sec
1 sec
2 sec
1 sec
2 sec
1 sec
2 sec

B

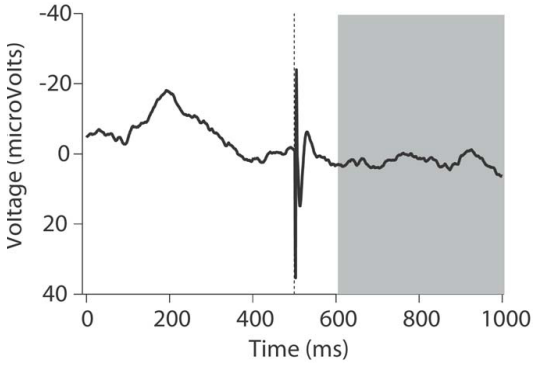
-40
-20
0
20
40
Voltage (microVolts)
0
200
400
600
800
1000
Time (ms)

C

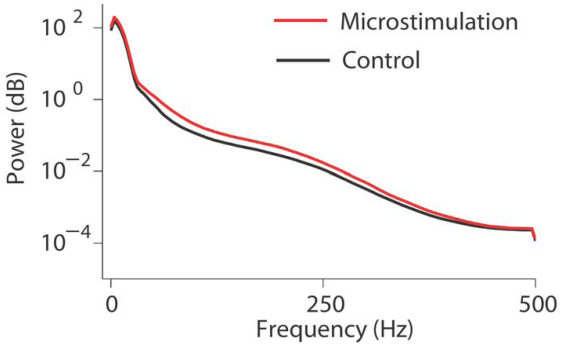
Microstimulation
Control
10 2
10 0
10−2
10−4
Power (dB)
0
250
500
Frequency (Hz)

Figure 2 Effect of feedback on LFP power. (A) Ratio of power between stimulation and control conditions from an example electrode. (B) Average power ratio for low frequency (0-10Hz) and high gamma frequency (80-120Hz) plotted according to the electrode location in V1.

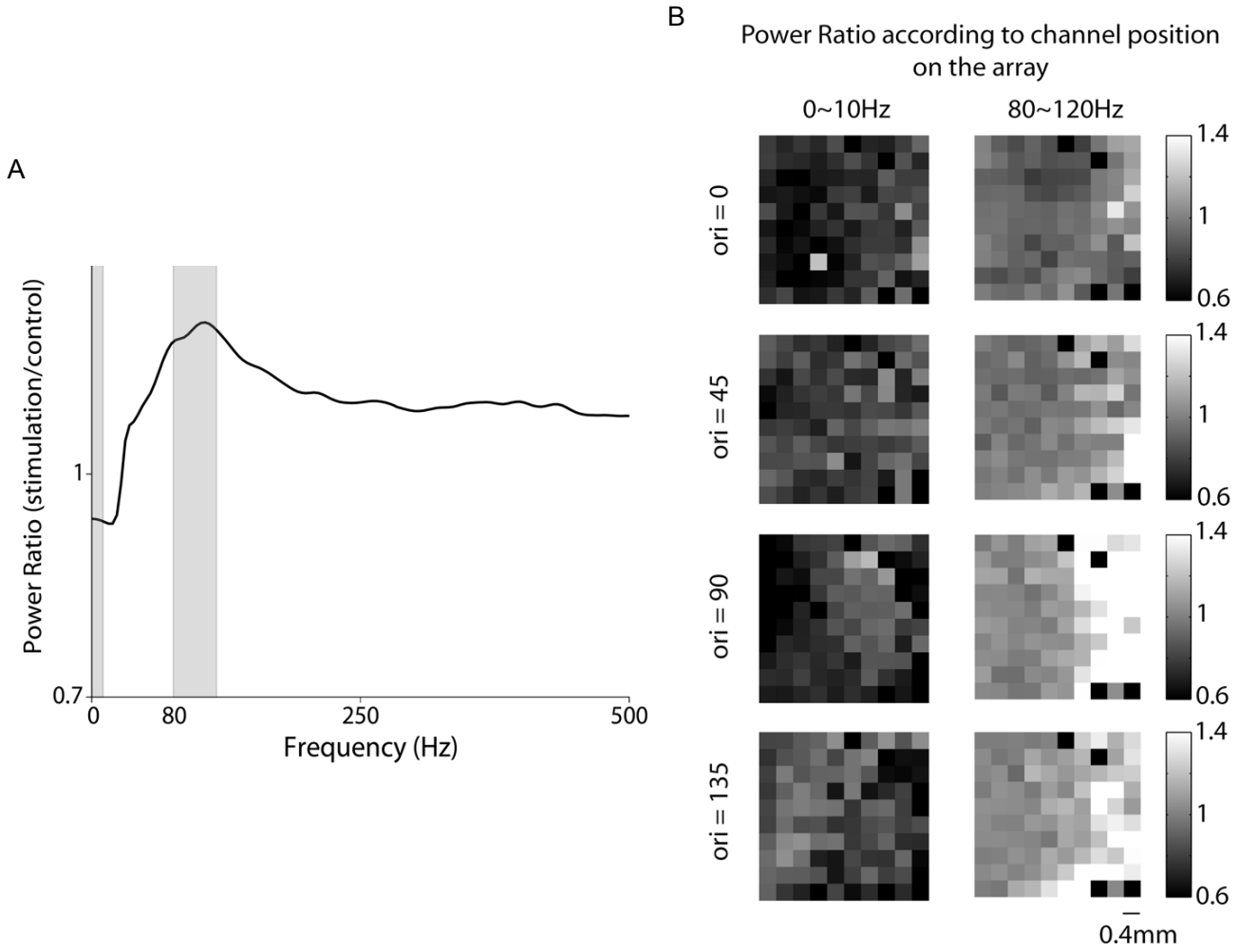
A
Power Ratio (stimulation/control)
1
0.7
0
80
250
500
Frequency (Hz)
B
Power Ratio according to channel position on the array
0~10Hz
80~120Hz
ori = 0
ori = 45
ori = 90
ori = 135
1.4
1
0.6
0.4mm

Figure 3 Effect of feedback on LFP power depends on the amplitude of current and electrode location. (A) Ratio of power between stimulation and control conditions. Average for one V1 array for different stimulating electrodes (contrast=0.33, current = 100 μA, stimulating 300ms after visual stimulus onset). (B) Power ratio for different amplitude of stimulation current (contrast=0.33, stimulating 300ms after visual stimulus onset).

A

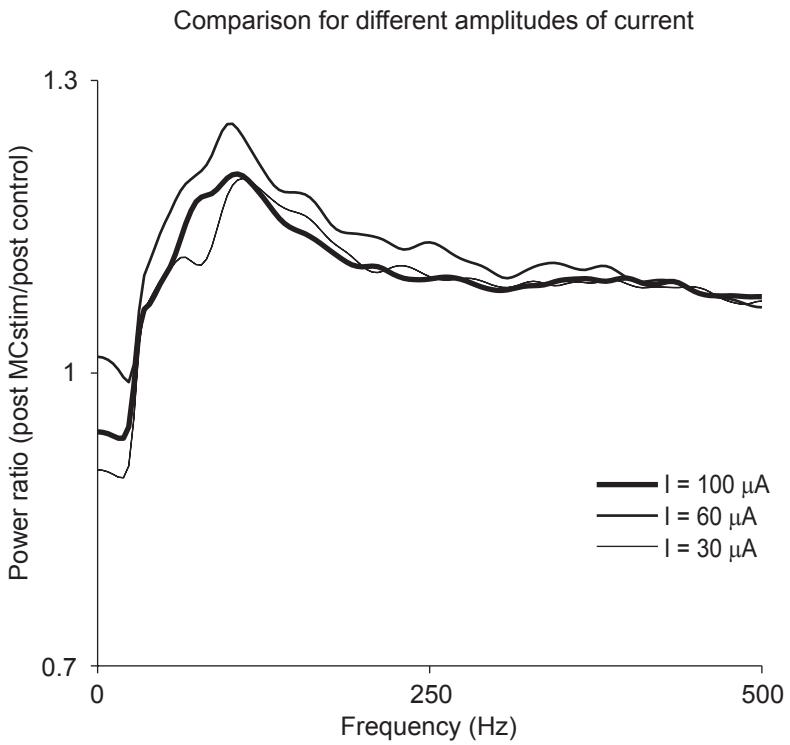

Note: Contrast = 0.33, electrical current delivered at 300ms after stimulus onset

B

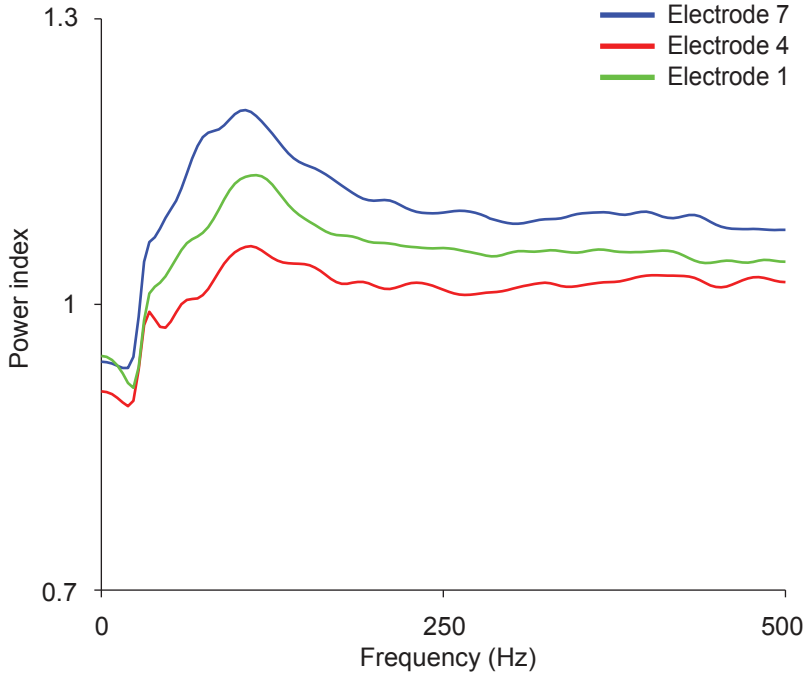

Note: current = 100microamps, delivered at 300ms

Figure 4 Laminar specificity of feedback effect. Power ratio in V1 organized as a function of depth of the stimulating electrode in V2.

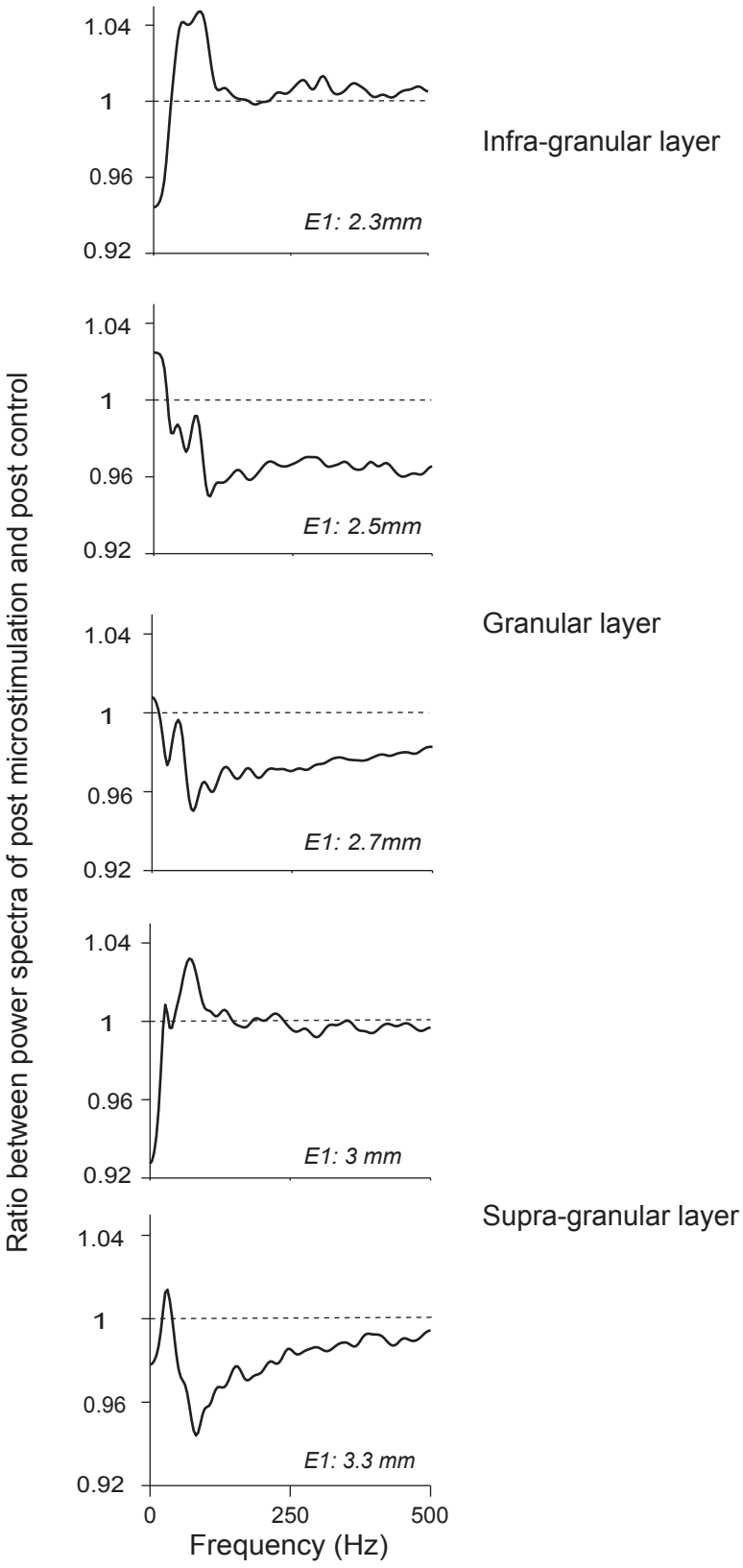
Ratio between power spectra of post microstimulation and post control
1.04
1
0.96
0.92
E1: 2.3mm
E1: 2.5mm
E1: 2.7mm
E1: 3 mm
E1: 3.3 mm
Infra-granular layer
Granular layer
Supra-granular layer
0
250
500
Frequency (Hz)

Figure 5 Effect of feedback on LFP power depends on stimulus contrast and size. (A) Ratio of power between stimulation and control conditions average for one V1 array for different visual stimulus contrasts (current = 30 μA). (B) Ratio of power for different amplitudes of stimulation current (contrast=0.67, current = 100 μA).

A

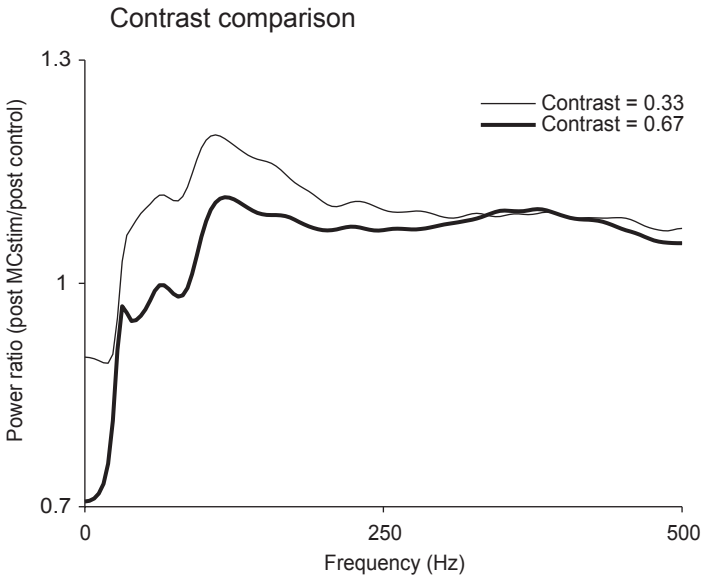

Note: Electrode 7, current = 30 μA

B

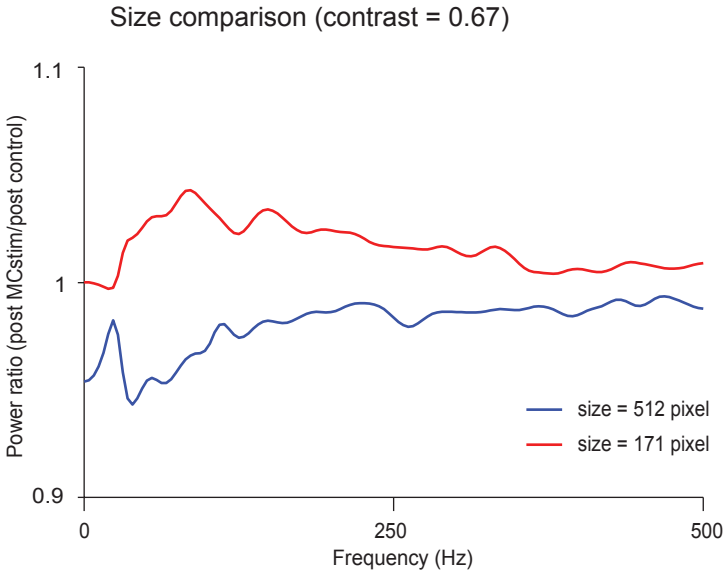

Note: current = 100; position = 3.3 mm

Figure 6 Changes in response latency with time of microstimulation relative to visual stimulus onset.

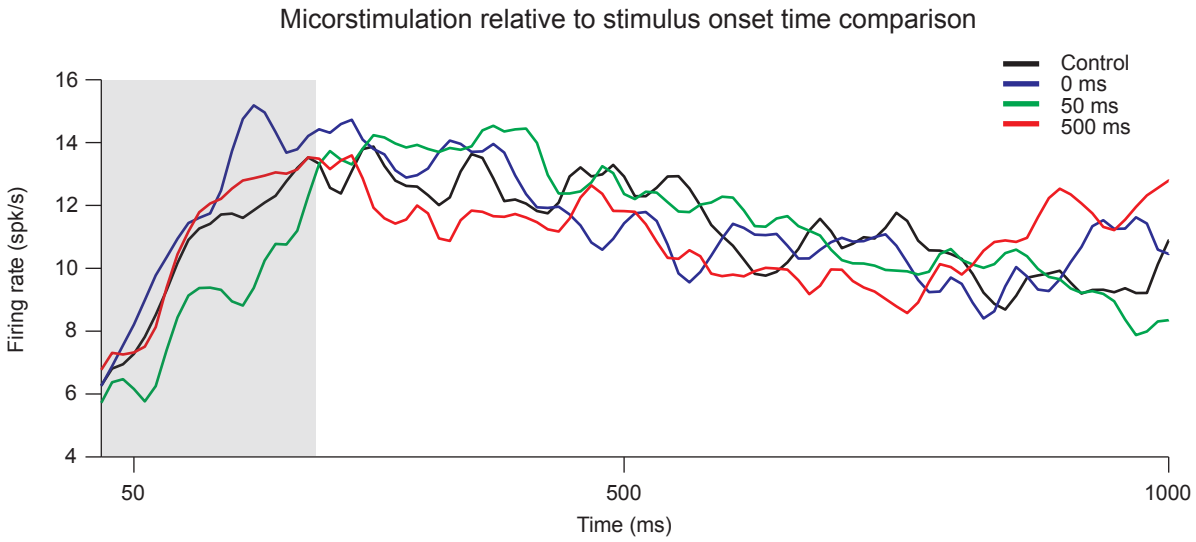
Micorstimulation relative to stimulus onset time comparison
Control
0 ms
50 ms
500 ms
Firing rate (spk/s)
16
14
12
10
8
6
4
50
500
1000
Time (ms)

Figure 7 Effect of illusory contour on V1-V2 neuronal correlation. (A) Illustration of different contour and control stimuli. (B) V1-V2 CCGs for different stimulus conditions. (C) Noise correlation for different stimulus conditions.

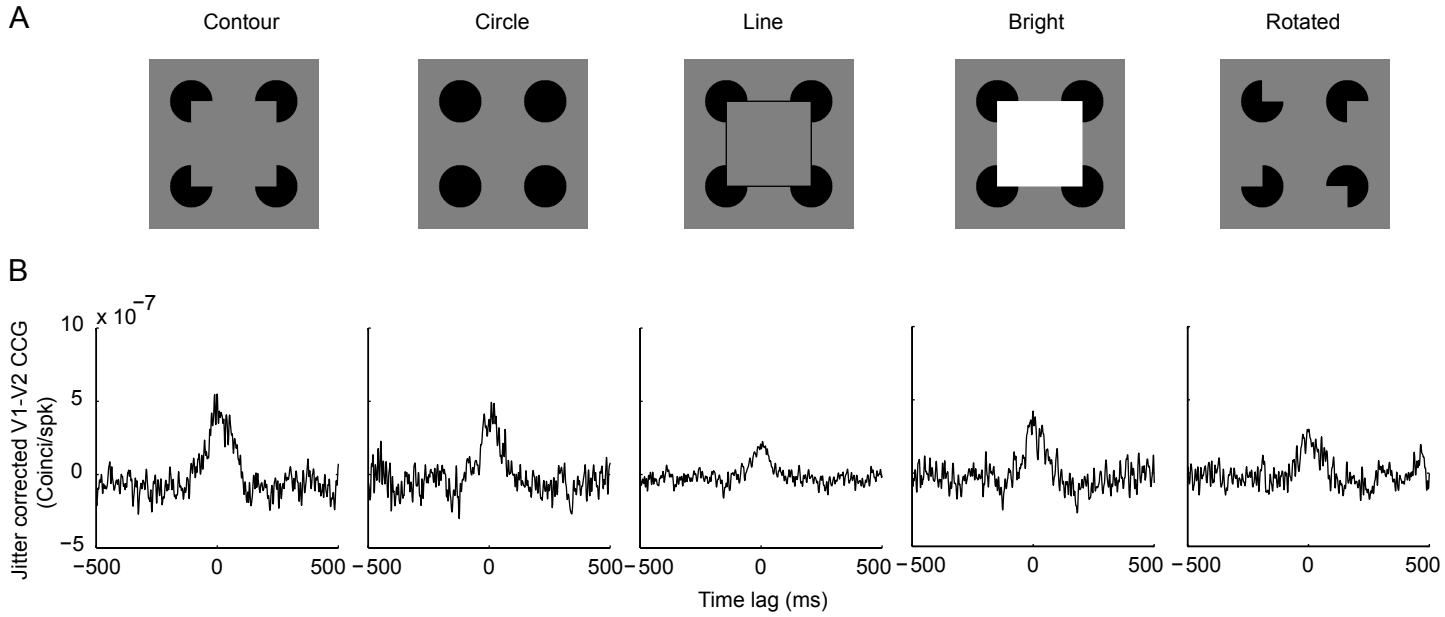
A
Contour
Circle
Line
Bright
Rotated
B
x 10^−7
10
5
0
−5
Jitter corrected V1-V2 CCG
(Coinci/spk)
−500
0
500
Time lag (ms)

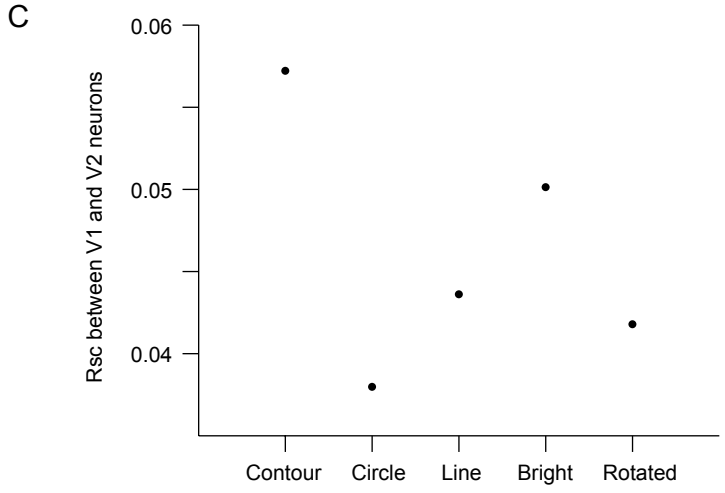
C
0.06
0.05
0.04
Rsc between V1 and V2 neurons
Contour
Circle
Line
Bright
Rotated

Appendix IV: Laminar dependence of neuronal correlations in visual cortex (submitted manuscript)

Matthew A. Smith[1], Xiaoxuan Jia[2*], Amin Zandvakili[2*], and Adam Kohn[2,3]

[1] Departments of Ophthalmology and Bioengineering,

Center for the Neural Basis of Cognition and

Fox Center for Vision Restoration

University of Pittsburgh, Pittsburgh PA 15213

[2] Dominick Purpura Department of Neuroscience

[3]Department of Ophthalmology and Vision Sciences

Albert Einstein College of Medicine, Bronx NY 10461

*These authors contributed equally.

X. Jia contributed to part of the data collection, data analysis of LFP and CSD; contributed to making Figure 1C and Figure 5.

The Journal of Neuroscience

http://jneurosci.msubmit.net

Laminar dependence of neuronal correlations in visual cortex

JN-RM-4874-11

Matthew Smith, University of Pittsburgh

Xiaoxuan Jia, Albert Einstein College of Medicine

Amin Zandvakili, Albert Einstein College of Medicine

Adam Kohn, Albert Einstein

Commercial Interest: No

Laminar dependence of neuronal correlations in visual cortex

Matthew A. Smith[1], Xiaoxuan Jia[2*], Amin Zandvakili[2*], Adam Kohn[2,3]

[1] Departments of Ophthalmology and Bioengineering,
Center for the Neural Basis of Cognition and
Fox Center for Vision Restoration
University of Pittsburgh, Pittsburgh PA 15213

[2] Dominick Purpura Department of Neuroscience
[3] Department of Ophthalmology and Visual Sciences
Albert Einstein College of Medicine, Bronx NY 10461

*These authors contributed equally.

Correspondence: Matthew A. Smith
Department of Ophthalmology
University of Pittsburgh
203 Lothrop St
Eye and Ear Institute, Room 914
Pittsburgh, PA 15213
Phone: (412) 647-2313
Fax: (412) 647-5880
E-mail: smithma@pitt.edu

Acknowledgements: This work was supported by grants from the National Institutes of Health (NIH) to AK (EY016774) and MAS (EY018894). MAS was also supported by NIH Core Grant P30 EY008098, the Eye and Ear Foundation of Pittsburgh, PA, and an Unrestricted Grant from Research to Prevent Blindness (New York, NY). We thank Stephanie Wissig and Carlyn Patterson for assistance with data collection, Ryan Kelly and Amie DiTomasso for technical assistance, and Nathan Urban for comments on an earlier draft of this manuscript.

ABSTRACT

Neuronal responses are correlated on a range of timescales. Correlations can affect population coding and may play an important role in cortical function. Correlations are known to depend on stimulus drive, behavioral context, and experience, but the mechanisms that generate and control their strength and properties are poorly understood. Here we make use of the laminar organization of cortex—with its variations in sources of input, local circuit architecture, and neuronal properties—to test whether networks engaged in similar functions but with distinct properties generate different patterns of correlation. We find that slow timescale correlations are prominent in the superficial and deep layers of primary visual cortex (V1) of macaque monkeys, but are near zero in the middle layers. A similar pattern is seen in the low-frequency (0-10 Hz) power of the LFP, which is weakest in the middle layers. Fast timescale correlation, or synchrony, differs in its laminar dependence: it is maximal in the middle layers of V1, although evident at most cortical depths. The gamma (30-50 Hz) power of the LFP follows a similar trend. To test whether these patterns hold in extrastriate cortex, we performed additional recordings in area V2, targeting the input layers. We found a laminar dependence similar to V1 for synchrony, but slow timescale correlations were not different between the input layers and nearby locations. Our results reveal that cortical circuits in different laminae can generate remarkably different patterns of correlations, despite being tightly interconnected.

The responses of cortical neurons are not independent. Fluctuations in responses – either in spike timing or count – are shared between nearby neurons and those with similar functional properties. These correlations can strongly affect population coding. In a pooled population signal, correlations reduce signal-to-noise since shared fluctuations cannot be averaged away (Zohary et al., 1994). Under other scenarios, correlated variability can either improve or reduce population encoding (Averbeck et al., 2006) and decoding performance (Graf et al., 2011). Spike timing correlation on briefer timescales (synchrony) has been suggested to underlie the binding of distributed sensory representations (Gray, 1999), and the temporal coordination of activity by gamma rhythms suggested to influence corticocortical communication and the dynamic routing of information through cortical circuits (Fries, 2009).

A simple explanation for correlations is that they arise when cells receive common input from a presynaptic neuron or pool of neurons. However, modeling work has shown that correlations can be near zero, even in highly recurrent networks, if excitatory and inhibitory inputs are balanced appropriately (Salinas and Sejnowski, 2000; Renart et al., 2010). The relationship between correlations and patterns of synaptic input is thus not straightforward. More generally, how correlations depend on network architecture and the intrinsic properties of neurons remains unclear, an issue that must be addressed if we are to understand why correlations vary across brain areas, stimulus conditions and behavioral states (see Cohen and Kohn, 2011).

The laminar organization of cortex provides an opportunity to compare correlations in networks engaged in similar computations but with distinct properties. First, circuit architecture differs among layers. For instance, the middle layers (layers 4C alpha and beta) of primary visual cortex (V1) are driven by feedforward input from the thalamus, and have recurrent circuitry of a limited spatial extent (Lund et al., 1979; Blasdel and Lund, 1983). Signals are then relayed to the superficial and deep layers, where neurons are richly interconnected, in part by horizontal connections known to extend for several millimeters (Gilbert and Wiesel, 1983; Ts'o et al., 1986; Gilbert and Wiesel, 1989). Second, the electrophysiological properties of neurons and synapses differ among layers, due to the expression of different configurations of receptors and ion channels (Markram et al., 2004; Nelson et al., 2006; Thomson and Lamy, 2007). Finally, different layers generate different rhythmic fluctuations, which are observable in the local field potential (LFP; Bollimunta et al., 2008; Maier et al., 2010) and may contribute strongly to correlations (Kohn et al., 2009).

To determine whether different laminar circuits give rise to neuronal correlations with distinct properties, we recorded from groups of neurons in V1 of macaque monkeys at locations sampled systematically across the cortical depth. To relate our findings to network rhythms, we also recorded the LFP and compared its power in different laminae. To test whether the laminar differences in V1 correlations reflect universal properties of visual cortical networks, we performed similar measurements in area V2. We find that the strength and properties of neuronal correlations can be remarkably different in nearby and interlinked cortical circuits.

This work has been published previously in abstract form (Smith and Kohn, 2009).

MATERIALS AND METHODS

General methods

We recorded data from 6 anesthetized, adult male macaque monkeys (*Macaca fascicularis*). The techniques we use have been described in detail previously (Smith and Kohn, 2008). In brief, anesthesia was induced with ketamine (10 mg/kg) and maintained during preparatory surgery with isoflurane (1.0-2.0% in 95% O2). Anesthesia during recordings was maintained with sufentanil citrate (6-18 μg/kg/hr, adjusted as needed for each animal). Vecuronium or pancuronium bromide (0.1-0.15 mg/kg/hr) was used to suppress eye movements. Drugs were administered in normosol with dextrose (2.5%) to maintain physiological ion balance. Physiological signs (ECG, blood pressure, SpO2, end-tidal $C0_2$, EEG, temperature, and urinary output and osmolarity) were monitored to ensure adequate anesthesia and animal well-being. Temperature was maintained at 36-37 C°. The pupils were dilated with topical atropine and the corneas protected with gas-permeable hard contact lenses. We used supplementary lenses to bring the retinal image into focus. At the end of the recording session, animals were sacrificed with sodium pentobarbital (65 mg/kg) and perfused with phosphate buffer solution followed by formalin. Tissue was processed histologically to verify recording locations (see also below).

All procedures were approved by the Institutional Animal Care and Use Committee of the Albert Einstein College of Medicine at Yeshiva University and were in compliance with the guidelines set forth in the United States Public Health Service Guide for the Care and Use of Laboratory Animals.

We recorded with a group of 5-7 linearly arranged (305 μm spacing) platinum-tungsten electrodes, which consisted of both conventional electrodes and tetrodes (Thomas Recording, Giessen, Germany). In V1, we inserted recording electrodes normal to the cortical surface within a craniotomy centered 10 mm lateral to the midline and 5 mm posterior to the lunate sulcus, where neuronal receptive fields are within 5° of the fovea. The electrodes were aligned using a microscope to the end of the guide tube, and advanced together through cortex, sampling in 200 μm intervals until all electrodes had exited into white matter.

V2 recordings were performed by angling the electrodes 20° from vertical, in the sagittal plane, and advancing through V1 into the white matter. Entry into the deep layers of V2 was apparent from the reappearance of neuronal signals. We advanced the electrodes roughly 700 μm into cortex and began recording. We sampled 3-5 depths (approximately 200 μm spacing) which spanned the layers receiving input from V1 (Van Essen et al., 1986; Rockland and Virga, 1990). V2 recordings were performed while monitoring the activity of a population of neurons in the superficial layers of V1, using microelectrode array recordings (described in Smith and Kohn, 2008).

Signals from the electrodes were bandpass filtered between 0.3 and 10 kHz and sampled at 40 kHz. Waveform segments that exceeded a user-defined threshold were stored for offline

analysis and sorting (Offline Sorter; Plexon; Dallas, TX). An initial sort was performed using the "T-Distribution E-M" automated sorting mode, which was then refined by hand, taking into account the waveform shape, clustering in principle component space and interspike interval distribution.

We quantified sort quality using the signal to noise ratio (SNR) of each candidate unit, defined as the ratio of the average waveform amplitude to the SD of the waveform noise (Kelly et al., 2007). We started with 685 candidate units in V1 and 647 in V2. Candidates with a SNR less than 2.3 were discarded as multi-unit recordings (215 V1 and 347 V2 units removed). We also eliminated neurons for which the best grating stimulus did not evoke a response of at least 2 spikes/s (69 V1 and 94 V2 units removed). The remaining candidate waveforms (401 units in V1 and 206 in V2) were deemed to be of sufficient quality and visual responsiveness to warrant further analysis. Changing the SNR or responsivity threshold did not qualitatively change any of the results described herein. In addition, the mean SNR was similar across layers (mean of 3.29, 3.43, and 3.26 in the superficial, middle and deep layers, respectively, $p > 0.30$ for all comparisons).

At each recording site, we also acquired the local field potential (LFP) by band-pass filtering the raw signal between 0.3 Hz and 250 Hz and sampling at 1 kHz. For tetrodes, we acquired the LFP from only one of the four contacts.

Visual stimulation

Visual stimuli were generated using EXPO (corevision.cns.nyu.edu) and displayed on a linearized CRT monitor (mean luminance 40 cd/m^2) with a resolution of 1024 by 768 pixels and a refresh rate of 100 Hz. The monitor was placed 110 cm from the animal. Stimuli were presented in a circular aperture surrounded by a gray field of average luminance. We mapped the spatial receptive field of units on each electrode by presenting small, drifting gratings (0.6 degrees; 250 ms duration) at a range of spatial positions. We centered our stimuli on the aggregate receptive field of the recorded units. Stimuli were viewed binocularly and presented for 1.28 seconds, separated by 1.5 s intervals during which we presented an isoluminant gray screen (except in one penetration, where we used an interval of 10 s). We presented full-contrast drifting sinusoidal gratings at 8 or 12 orientations spaced equally (30˚ or 45˚ increments). The spatial frequency (1-1.3 cpd) and temporal frequency (3 or 6.25 Hz) values were chosen to correspond to the typical preference of parafoveal V1 neurons (De Valois et al., 1982; Foster et al., 1985; Smith et al., 2002). The position and size (3.9–5.3˚) of the grating were sufficient to cover the receptive fields of all the neurons. Stimulus orientation was block randomized, and blocks were repeated 30-100 times.

Measures of correlation

A detailed discussion of the measures of correlation can be found in previous publications (Kohn and Smith, 2005; Smith and Kohn, 2008). Briefly, r_{sc}, or spike count correlation, is the Pearson correlation coefficient of the spike counts of two cells to repeated presentations of a particular stimulus – it captures shared trial-to-trial variability. For each

stimulus orientation, we Z-scored the responses and calculated r_{sc} after combining responses to all stimuli. We removed trials on which the response of either neuron was > 3 SDs different from its mean (Zohary et al., 1994) to avoid contamination by outlier responses.

To measure spike timing correlations, we computed the spike train cross-correlogram (CCG; Perkel et al., 1967), normalized by the geometric mean spike rate. We computed the CCG of each stimulus condition and corrected it using an all-way shuffle correction. To isolate the narrow peak of the CCGs we used a jitter correction method (Harrison et al., 2007; Smith and Kohn, 2008; Harrison and Geman, 2009) with a window of 10 ms, removing all correlation on a timescale greater than that window size. We then averaged CCGs across stimulus condition. We smoothed these CCGs with a Gaussian kernel (SD=1.0 ms) before using them in further analysis.

Determining recording locations

Although we took care to align our electrodes and determine carefully their entry into the brain, we could not prevent slight deviations in alignment across depths, due to variations in the cortical surface, a penetration angle that was not precisely perpendicular to cortex, imprecision in the microdrive motor, and other factors. To be certain of the recording locations we therefore performed current source density (CSD) analysis (Nicholson and Freeman, 1975). Although CSD analysis is typically performed on data recorded simultaneously across cortical layers, this is not required, as the analysis is based on signals that are averaged across trials.

We computed the average, evoked (stimulus-locked) LFP at each site, smoothed these signals across sites, and then calculated the second spatial derivative, as in Stoelzel et al. (2009). We used CSD analysis for two purposes. First, we used it to determine which electrode penetrations were well aligned. We computed the Pearson's correlation between the CSD values of each pair of electrodes. We only kept pairings for which this value was 0.5 or larger, indicating similar profiles. Second, we used the CSD profile to determine the location of the middle layers, which are distinguishable by the presence of a distinct current sink/source (Givre et al., 1995; Schroeder et al., 1998; Rajkai et al., 2008; Maier et al., 2010; 2011). We first averaged the CSDs from all aligned electrodes recorded on a single penetration and then determined the minimum value of the CSD in the first 100 msec. We defined the middle layer sink to be the depth and time that first reached 40% of that value, if this was followed by a source (defined as a signal that was at least 50% of the maximum CSD value and that occurred within 100 ms of the sink). We only accepted for analysis penetrations in which this method provided a clear assignment of the middle layers.

Using the 401 recorded V1 units, we paired each neuron with all other simultaneously recorded neurons, excluding pairs from the same electrode or tetrode. This resulted in 2369 pairs. Based on the CSD similarity criterion described above, we eliminated 478 pairs. We also discarded the data from a depth in which we only recorded 11 pairs (1200 μm above the middle layers) and a depth in which we recorded some individual neurons but

no pairs that met our criteria (1000 μm below the middle layers). Our final data set thus consisted of 1880 pairs of V1 neurons recorded from 19 electrode or tetrode tracks, grouped in 4 ensemble penetrations.

In 2 of the 4 penetrations, we made electrolytic lesions (2 μA for 5-10 s) at the last recording sites and 250 μm deeper, in white matter. We did not make lesions in the middle layers as we did not want to alter responses at deeper sites in the same penetration. We recovered a subset of the lesions, which were consistently at the expected location (an example is shown in Fig 1B).

For our analysis of LFP power, we simply aligned the recordings on different electrodes based on depth identified as the middle layers from the CSD on each electrode. This is because our analysis of LFP power did not require computing quantities across electrodes. We used LFP signals acquired from all depths at which we recorded single neurons that met the above criteria. We evaluated differences in the raw amplitude spectrum. Normalizing the spectra from individual sites before analysis provided qualitatively similar results.

In V2, we employed a different strategy to align the electrodes and to identify the input layers. We paired our V2 recordings with simultaneous recordings from neurons in the superficial layers of V1 with retinotopically-aligned receptive fields. We calculated CCGs between every pairing of V1 and V2 neurons and averaged across all conditions and pairs. We defined the input layers to be those V2 sites at which we observed evidence that neurons received direct input from V1 (Tanaka, 1983; Reid and Alonso, 1995): namely, that the average jitter-corrected CCG had a significant peak (5 standard deviations above the value at time lags of ±75-125 ms). These locations were typically 800-1000 μm from our entry into V2 at the layer V1/white matter border. V2 recording sites were defined to be deep/superficial, if the average CCGs lacked a sharp peak and these sites were recorded before/after an input layer site. Penetrations in which sharp peaks were not observed were not analyzed further. Before computing correlations, we applied the same rate and sort quality criteria as for our V1 data.

All indications of variation in the graphs and text are standard errors of the mean (s.e.m). The statistical significance of all results was evaluated with two-tailed t-tests, unless otherwise noted. Significance of r_{sc} was assessed after applying the Fisher Z-transform to the data.

RESULTS

We recorded 1880 pairs of V1 neurons, using linear arrays consisting of 5-7 electrodes and tetrodes (305 micron spacing) inserted normal to the cortical surface (Fig 1A). The electrodes were aligned at their entry into the brain, and then advanced until we observed neuronal spiking activity. We recorded at that position and every 200 um thereafter, until the electrodes reached white matter (Fig 1B)

FIGURE 1 ABOUT HERE

The dependence of correlations on cortical layer

Along with spiking activity, we simultaneously recorded the local field potential (LFP) from each electrode. We used these signals to compute the laminar current source density (CSD) profile, which measures the location, direction and strength of current flow (Fig 1C). In this plot, sinks and sources of current flow are shown in red and blue, respectively. The earliest sink is found in layer 4C, reflecting the arrival of input from the lateral geniculate nucleus (LGN), and activation in superficial and deep layers follows (Givre et al., 1995; Schroeder et al., 1998; Rajkai et al., 2008; Maier et al., 2010; 2011). We identified the depth at which the earliest sink was present (Fig 1C, dashed circle), and designated that as the input or middle layers of V1 (see Methods). The sink was usually confined to 1-2 recorded depths, consistent with the known thickness of layer 4C in the macaque (300-400 μm, Lund, 1988).

FIGURE 2 ABOUT HERE

To determine whether spike count correlations (r_{sc}, also known as noise correlations or correlated variability) are laminar dependent, we calculated values between all pairs of neurons recorded at each depth, using spike counts measured in 1.28 s trials. Figure 2A shows the average r_{sc} values for neuronal pairs grouped by recording depth (number of pairs is indicated above each bin). We found substantial variation in r_{sc}, with higher values in the superficial (depths of -1000 to -200 microns relative to the middle layers) and deep layers (depths of 200 to 800 microns) and lower values in the middle layers. We then divided the data into three groups—superficial, middle, and deep—based on depth (Fig 2B). The r_{sc} values were highest in the superficial layers (peak of 0.125 ± 0.011 at 400 μm above the middle layers, mean of 0.104 ± 0.006, n = 965). In the deep layers, r_{sc} was slightly weaker on average (peak of 0.109 ± 0.010 at 400 μm below the middle layers, mean of 0.070 ± 0.008, n = 656), due to a drop in strength at the deepest recording sites, presumably in layer 6. The value of r_{sc} in the middle layers was notably lower, with values not significantly different from zero (0.016 ± 0.013, n = 259, p=0.24). All of the differences between groupings were statistically significant ($p<0.001$). Data from individual penetrations were consistent with the trends in the population average, but more variable due to a lower number of observations at each depth.

FIGURE 3 ABOUT HERE

To explore the laminar dependence of spike timing correlations, we computed shuffle-corrected cross-correlograms (CCGs) for the same pairs of neurons. At each depth we averaged the CCG from all pairs to produce a grand average for that depth (Fig 3A). Since r_{sc} is proportional to the integral of the shuffle-corrected CCG (Bair et al., 2001), the laminar dependence of r_{sc} should be reflected in the CCGs. Consistent with this, CCGs in the superficial and deep layers had broad peaks, and these were more prominent in the superficial layers. CCGs in the middle layers lacked broad peaks, but showed oscillatory

side lobes (arrows) around the peak. We quantified the gamma power in the CCG (30-50 Hz, calculated from the full shuffle-corrected CCG within ±100 ms of zero time lag), for each pair of neurons, and found significantly more power for the middle layers than the superficial ($p=1.8x10^{-7}$) and deep ($p=1.5x10^{-4}$) layers. Low frequency power (0-10 Hz, calculated from the full shuffle-corrected CCG over all time lags), on the other hand, was higher in the superficial (p=0.034) and deep (p=0.014) layers than the middle layers, consistent with the broad peak evident at many locations in those layers.

To measure precise timing correlation or synchrony, we computed jitter-corrected CCGs (see Methods; Smith and Kohn, 2008). This correction removes all correlations in the CCGs on timescales larger than the jitter window (in this case 10 ms), thus isolating synchronous activity from more loosely coordinated activity. Laminar differences were less distinct than for r_{sc}, but the most prominent peaks in the average CCGs were in the middle layers (Fig 3B, note change in scale). We quantified the synchrony in the CCG by measuring the area under the CCG within ± 5 ms of zero time lag. This value was slightly higher in the middle layers ($8.8x10^{-4}$ coinc./sp.) than in the superficial layers ($6.1x10^{-4}$ coinc./sp., p=0.05) or deep layers ($7.2x10^{-4}$ coinc./sp., p=0.33).

Effects of rate and tuning similarity on r_{sc}

When the firing rate of either neuron in a pair is low, r_{sc} will be small, even when the underlying membrane potentials are strongly correlated (de la Rocha et al., 2007; Cohen and Kohn, 2011). One possible explanation for the laminar variation in r_{sc} could thus be laminar differences in firing rate. We therefore compared the dependence of r_{sc} on firing rate for pairs of neurons in the middle layers with those in all other layers. For this analysis, we computed r_{sc} for each stimulus and pair separately. Figure 4A shows the average r_{sc} values plotted as a function of the firing rate of each neuron in each pair, in the superficial and deep layers. The value of r_{sc} was higher when both neurons fired at a higher rate (upper right corner). In the middle layers, r_{sc} was small even when both neurons fired at high rates (Fig 4B). Considering only cases in which both neurons had a mean firing rate of at least 5 sp/s, r_{sc} in the middle layers was -0.015±0.031 compared to 0.116±0.009 in the other layers ($p=3.3x10^{-6}$). We also compared mean firing rates across layers, but found no trend that could explain the laminar variations in r_{sc}, except at the most superficial sites (depths of -1000 and -800 μm) where there was a clear decrease in rate. In fact, firing rates were slightly higher in the middle layers when compared with the superficial and deep layers (13.1 vs. 9.5 sp/s, p=0.025), consistent with previous studies (Gur et al., 2005). We conclude that differences in firing rate cannot explain the small values of r_{sc} in the middle layers.

FIGURE 4 ABOUT HERE

Correlations are stronger between neurons with similar response properties (Zohary et al., 1994; Bair et al., 2001; Kohn and Smith, 2005; Smith and Kohn, 2008). Thus, a second explanation for the low values of r_{sc} in the middle layers is that the sampled neurons have more diverse functional properties than those sampled in other layers. We did not fully characterize the receptive field properties of the recorded neurons, so we could not provide a thorough account of their similarity. However, we did compare the similarity of orientation tuning between pairs of cells, quantified by the Pearson's correlation (signal

correlation). Signal correlations for the middle layers (0.026±0.023, n = 259) were only slightly smaller than at other sites (0.066±0.011, n=1621, p=0.21). Further, even among pairs with high signal correlation (>0.5), indicating quite similar tuning, r_{sc} was low in the middle layers (0.050±0.036, n=33, compared to 0.121±0.011 in other layers). Note that although r_{sc} was weak in the middle layers, values were larger for pairs with similar tuning (0.050 compared to 0.016 on average), consistent with the "limited-range" dependence seen in the superficial layers (Smith and Kohn, 2008). We conclude that the low r_{sc} we observe in the middle layers is unlikely to be due to lower signal correlations among the sampled neurons.

Laminar trends in the LFP

Low frequency cortical rhythms are thought to contribute to slow timescale correlations (Kohn and Smith, 2005; Poulet and Petersen, 2008; Smith and Kohn, 2008; Kohn et al., 2009; Mitchell et al., 2009; Kelly et al., 2010), whereas higher frequency rhythms (e.g. gamma) have been associated with spike timing correlations (Samonds and Bonds, 2005; Fries et al., 2008). We therefore determined whether the laminar dependence of r_{sc} and timing correlations were also reflected in the LFP.

FIGURE 5 ABOUT HERE

We measured the power of the LFP for frequencies from 0-80 Hz, and found substantial laminar variation. Low frequency (0-10 Hz) power was most prominent in the superficial and deep layers, and substantially weaker in the middle layers (Fig 5A and C), although this trend was not statistically significant because of reduced power for very superficial recordings (p=0.11 for the difference between middle and all other layers). For gamma frequencies (30-50 Hz), power was highest in the middle layers (Fig 5B and D; p=0.011 for difference between middle and all other layers). Note that in these experiments we used gratings of an intermediate size (3-5 degrees); gamma power is higher for larger stimuli and may display a different laminar pattern under those conditions (Gieselmann and Thiele, 2008; Jia et al., 2011).

To quantify the relationship between LFP power and spiking correlations, we compared the average power measured from the same electrode pairings used to compute r_{sc}. Across pairings, r_{sc} was correlated with low-frequency (r=0.12, $p=4.8\times10^{-7}$) but not gamma power (r=-0.02, p=0.44). Synchrony showed the opposite trend – the area under the CCG was correlated with gamma (r=0.21, $p=1.4\times10^{-19}$) but not low-frequency power (r=0.03, p=0.22).

We conclude that, like r_{sc} and synchrony, LFP frequency content is laminar dependent. Low frequency fluctuations are weakest in the middle layers, where r_{sc} is near zero, and elevated in the superficial and deep layers. Gamma power, on the other hand, peaks in the middle layers, where we observed the strongest synchrony as well as the most gamma power in the CCG. However, the correspondence between the properties of the LFP and spiking correlations is not absolute: low frequency power was strong at the deepest recording sites where r_{sc} had an intermediate strength.

Laminar trends outside V1

Our finding that r_{sc} is weak in the middle layers of V1 may represent a general principle that the circuits in the input layers are designed to minimize slow timescale correlations. Alternatively, this finding may represent a specialization of V1; for instance, because it is driven directly by the thalamus or because of neural architecture unique to layer 4C. To test whether inputs layers in extrastriate cortex have similarly weak values of r_{sc}, we targeted these layers in additional recordings performed in V2 (7 electrode penetrations in 4 animals).

Because CSD analysis and its relationship to input layers is less well-established in extrastriate cortex, we used an alternative strategy for determining the location of the inputs layers from that used in our V1 recordings: we measured directly whether a particular location in V2 received input from V1 by pairing our V2 recordings (made with 5-7 microelectrodes or tetrodes, advanced as a group) with microelectrode array recordings in the superficial layers of V1. In a small proportion of V1-V2 pairs (~1%), we observed sharp peaks in the CCG that were offset by 2.2 ms, on average, indicating that the V2 cell had an enhanced probability of spiking after a V1 spike with this delay (Zandvakili and Kohn, 2010). These peaks were observed only when the spatial receptive fields were precisely aligned, with a center-to-center spacing of less than 1 degree. The average jitter-corrected V1-V2 CCGs for 4 recording sites sampled sequentially in a single penetration are shown in Fig 6A. At deep (top) and superficial (bottom) sites, CCGs did not have sharp peaks. At intermediate locations—typically at one or two sites—sharp peaks were evident. We interpret these peaks as indicating a functional connection from V1 to V2 (see Reid and Alonso, 1995, for a related approach) and defined those sites at which we observed a sharp peak in the average V1-V2 CCG (across all pairs and stimulus orientations) as being in the input layers of V2.

FIGURE 6 ABOUT HERE

We then measured correlations among V2 pairs recorded simultaneously at each depth. In contrast to our observations in V1, we found no trend for r_{sc} to differ significantly across layers (Fig 6B). In layers with sharp peaks, the mean r_{sc} was 0.157±0.014, while in superficial and deep layers it was 0.142±0.021 and 0.120±0.030, respectively ($p>0.2$ for all comparisons). Thus, r_{sc} in the input layers of V2 is similar to that observed in other layers. Consistent with this, low frequency(0-10 Hz) LFP power recorded from the same electrodes was slightly higher in the input layers than other layers ($p=0.03$, data not shown).

We also compared the laminar dependence of spike timing correlations for V2-V2 pairs (Figure 6C). We found broad peaks in shuffle-corrected CCGs at all three locations (data not shown). As in V1, synchrony was stronger in the input layers than in nearby locations ($p=0.08$ for comparison with superficial layers, and $p=0.05$ for the deep layers, based on the area within ±5ms of zero lag in the jitter-corrected CCG). LFP gamma power was also maximal in the input layers, although this trend was not statistically significant ($p=0.10$, data not shown).

Our data do not provide a full characterization of the laminar dependence of correlations and LFP power in V2. Further, our method for determining the input layers may have misassigned recording sites to the superficial or deep layers if the number of functionally-connected V1-V2 pairs was low. Nevertheless, these data show clearly that the low values of r_{sc} and low-frequency LFP power observed in the middle layers of V1 are not evident in the V2 layers receiving the strongest input from V1. Thus, we conclude that it is not a universal principle that input layers of cortex show weakly correlated responses. Spike synchrony and gamma LFP power, on the other hand, were elevated in the input layers of V2 (as in V1), suggesting this property might be shared across cortical areas.

DISCUSSION

We have shown that correlations vary significantly among layers in V1. Spike count correlations are prominent in the superficial and deep layers, but near zero in the middle layers. The laminar dependence of r_{sc} in V1 was reflected in the broad peak of the CCG and in the low frequency power of the LFP, both of which were weak in the middle layers. Fine timescale correlations, on the other hand, were evident in all cortical layers but slightly stronger in the middle layers, where gamma LFP power was also most elevated. In V2, r_{sc} in the input layers was similar to nearby layers, but synchrony was elevated, as in the middle layers of V1. Our results show that cortical layers can display distinct patterns of correlations, despite strong interlaminar circuitry linking them together. This indicates that the local network properties are a critical factor in determining the strength of correlations in neuronal populations.

Relation to previous studies

Previously we have reported that correlations on fast and slow timescales have a different stimulus dependence (Kohn and Smith, 2005) and spatial extent (Smith and Kohn, 2008). We show here that correlations vary in different ways among layers in V1 for different timescales. We are aware of only two previously published studies that compared correlations across cortical layers. The first compared r_{sc} in the superficial and deep layers of rat auditory cortex, and found a similar strength but different spatial extent (Sakata and Harris, 2009). It did not target the middle layers, where we find the most striking differences. The second study focused on synchrony, which was weakest in the middle layers of rat somatosensory cortex (Zhang and Alloway, 2004), unlike our findings in primate V1.

In the visual system, r_{sc} is typically found to be in the range of 0.1-0.2, for neurons that are well-driven and responses that are measured over hundreds of milliseconds or seconds (see Cohen and Kohn, 2011, for review). A notable exception is a recent study which reported r_{sc} values of ~0.01 in V1 of awake, fixating macaques (Ecker et al., 2010). The authors propose this discrepancy reflects a host of artifacts in all previous studies. Our findings offer an alternative explanation – that their recordings were biased toward the input layers of V1, as in a previous study by the same group (Berens et al., 2008). More broadly, the laminar trends in correlations that we observe point to an important source of potential variation in measurements, and a critical variable to control in future studies. We note that weak correlations have been reported in the motor cortex (Averbeck and Lee, 2006; Stark et al., 2008), further emphasizing that cortical circuits can generate different strengths of correlations.

Mechanisms

Previous studies have established that correlations depend on the strength of neuronal responses, the time epoch over which they are measured, the distance between recorded neurons, the quality of spike isolation and sorting, and the tuning similarity of the constituent neurons (see Cohen and Kohn, 2011, for review). The laminar differences in V1

r_{sc} values cannot be ascribed to any of these factors. In the middle layers, r_{sc} was low even between the most responsive neurons, and the firing rates there were higher on average than in the superficial and deep layers. We counted spikes over the same epoch and, in each penetration, measured responses under identical stimulus conditions in all layers. The distance between recorded pairs was the same in all layers, as we recorded at all sites using the same array of electrodes, inserted normal to the cortical surface. We cannot rule out differences in spike isolation, although we used tetrodes and high-impedance electrodes to ensure high quality recordings (Gray et al., 1995). However, if isolation quality varied, it would be expected to be worst in the middle layers because of the high packing density and relatively small size of stellate cells in layer 4C (Peters, 1994). This would cause r_{sc} there to be higher than in other layers (Cohen and Kohn, 2011), opposite to our findings. Finally, our analysis revealed no consistent difference in the tuning similarity between layers, as expected given the normal penetration we used to sample neurons within the same cortical column.

There are three, not mutually exclusive, sets of mechanisms that may contribute to the laminar dependence of correlations. First, the low r_{sc} values in the middle layers of V1 may arise in part from the unique inputs provided to this network – namely feedforward input from the LGN, where responses are relatively independent (Cheong et al., 2011). This would also explain the drop in r_{sc} we observed at the deepest recording sites, presumably in layer 6, which also receives substantial thalamic input (Casagrande and Kass, 1994). Interestingly, the koniocellular layers of the LGN, which project to the superficial layers of cortex (Chatterjee and Callaway, 2003) are more strongly correlated, particularly on slow timescales (Cheong et al., 2011).

It is unlikely, however, that r_{sc} values in V1 simply reflect the properties of LGN input. First, independent upstream neurons can lead to correlated responses in downstream neurons that pool common sets of inputs, as middle layer neurons do (Reid and Alonso, 1995). Second, neurons in the middle layers provide the dominant input to layers 2/3; although r_{sc} is weak in the source population (Casagrande and Kass, 1994; Douglas and Martin, 2004; Thomson and Lamy, 2007), correlations for pairs of superficial neurons are substantially stronger. Thus the strength of r_{sc} in a particular layer is unlikely to be solely a function of the dependencies in the feedforward input it receives.

A second explanation for the low values of r_{sc} in the middle layers of V1 is the properties of the local circuitry. Stellate cells in the middle layers have limited dendritic arbors (Lund et al., 1979; Blasdel and Lund, 1983), and do not give rise to long-range (several millimeters) horizontal connections found in the superficial and deep layers (Lund, 1988). Feedback connections from extrastriate cortex, which target widely separated neurons, terminate in all cortical layers except the middle layers (Felleman and Van Essen, 1991; Salin and Bullier, 1995). It is thus possible that the richer recurrent circuitry outside the middle layers leads to higher r_{sc} values. Networks in the middle layers may conform more closely to the homogeneous random connectivity patterns that generate weak r_{sc} values in recurrent network models (van Vreeswijk and Sompolinsky, 1996; Renart et al., 2010), whereas the spatial and functional dependencies of connections in other layers generate

rhythmic activity (see also below) that leads to higher values of r_{sc} (Litwin-Kumar et al., 2011; Rasch et al., 2011).

A third possibility is that laminar differences in correlations arise in part from differences in the intrinsic properties of neurons. For instance, neurons in layers 5 and 2/3 generate ~10 Hz rhythmic activity (Silva et al., 1991; Flint and Connors, 1996). Layer 5 neurons also generate 0.1-1 Hz oscillations (Sanchez-Vives and McCormick, 2000; Sakata and Harris, 2009)) which may propagate via patchy horizontal connections (Compte et al., 2003). While it would be premature to link these findings directly to our results, they do indicate the existence of laminar differences in neuronal (and presumably circuit) properties that could contribute to laminar variations in correlations. A related possibility is that there is a greater diversity in the electrophysiological properties of middle-layer neurons, a factor that contributes to decorrelation in the olfactory bulb (Padmanabhan and Urban, 2010).

We have previously suggested that slow timescale correlations arise from low frequency fluctuations in responsivity (Kohn and Smith, 2005; see also Poulet and Petersen, 2008 and Mitchell et al., 2009, for related findings; and Kohn et al., 2009, for review). Low frequency LFP fluctuations have been shown to be predictive of spike rate fluctuations in V1 (Kelly et al., 2010) and computational work suggests these fluctuations require horizontal connections (Rasch et al., 2011). Consistent with this, we observed enhanced low frequency LFP power in the superficial and deep layers, and a notable reduction in power in the middle layers.

The laminar trends we observed for r_{sc} computed from full trial counts were distinct from those for fine timescale correlations, or synchrony. Synchrony was slightly higher in the middle layers than outside, suggesting distinct mechanisms generating correlations on different timescales. Gamma power was also highest near the middle layers (Maier et al., 2010), presumably related to the oscillatory side lobes in the CCGs there. However, synchrony was also observed at sites in the superficial and deep layers, where gamma was much weaker. This suggests a weak coupling between gamma and synchrony (Roy et al., 2001; Samonds and Bonds, 2005; Fries et al., 2008).

The laminar trends in V1 were only partially evident in V2. Unlike V1, r_{sc} and low-frequency power in the LFP were similar in input and nearby layers. Synchrony and gamma LFP power, on the other hand, were elevated in the input layers, as in V1. The difference between V1 and V2 could reflect differences in local circuitry, neuronal properties, or the fact that feedforward input from V1 may be more strongly correlated or show a different pattern of convergence from thalamocortical input to V1.

Given that the correlations found in cortex appear detrimental to population coding accuracy, one could ask why they exist: our results show that cortical networks can be wired to provide relatively independent responses. One possibility is that correlations arise invariably from providing neurons with diverse sources of input (distant neurons connected via inter- or intra-areal connections). This connectivity may allow neurons to participate in diverse computations and functions, although some inputs will be irrelevant for a particular situation or computation. Because they are not recruited by the stimulus or

task at hand, these inputs may provide a source of shared, fluctuating drive that results in correlations (Churchland et al., 2010).

FIGURE LEGENDS

Figure 1. Experimental methods. **A**, A diagram of the recording procedure. A linear array of 5-7 microelectrodes or tetrodes was inserted normal to the opercular surface of V1, shown in a sagittal section of macaque cortex. The red dashed rectangle indicates the approximate location of the histological section show in panel **B** for one penetration. **B**, A Nissl-stained section from an example penetration in V1. Recordings were made every 200 μm throughout the cortical layers. The four black arrowheads indicate lesions made by electrodes at the far ends of the array at the last recording site in V1 and again 250 μm into white matter. The scale bar indicates 500 μm (uncorrected for tissue shrinkage). **C**, A CSD analysis of the LFP signals from an individual penetration, showing the location, direction and strength of current flow. Sinks are shown in red and sources in blue. The middle layers are identifiable as the earliest current sink followed by a source.

Figure 2. Dependence of r_{sc} on laminar location. **A**, The value of r_{sc} for pairs of neurons grouped based on the depth of recording. The middle layers, determined by the CSD analysis, are defined as depth zero, with superficial and deep layers indicated as negative and positive depths, respectively. The number of neuronal pairs that contribute to each depth is indicated above the histogram bar. Error bars on this and all subsequent plots indicate ± 1 SEM. **B**, Neuronal pairs were grouped so that the recording site at depth zero included in the middle layers and all other neuronal pairs were labeled as superficial or deep relative to this site. The three frequency histograms show the distribution of r_{sc} in each of these groups.

Figure 3. Dependence of timing correlations on laminar location. **A**, Average shuffle-corrected CCGs for pairs of neurons grouped by recording depth (shown at the right). Broad peaks are present in the superficial and deep layers, while sharp peaks with oscillatory side lobes (black arrows) are more notable in the middle layers. The tick marks to the left of the CCGs indicate a value of 0 coinc./sp. The tick marks at the bottom of the CCGs indicate zero time lag. **B**, Average jitter-corrected CCGs for the same data as in **A**. The axes scales are adjusted for clearer display. The peak of the CCG is highest in the middle layers, although evident across most depths.

Figure 4. Effect of firing rate on r_{sc}. **A**, For superficial and deep layer pairs, this color plot shows r_{sc} as a function of the mean firing rate of the two cells (on the x and y axes). Only bins with at least 10 observations are shown. For pairs and stimuli in which both neurons had high firing rates (upper right corner of the panel), r_{sc} was higher. **B**, This plot is the same as **A** except for pairs in the middle layers. Here, even when both neurons had high firing rates, r_{sc} was low.

Figure 5. Dependence of LFP power on laminar location. **A**, The power in the LFP as a function of electrode depth (on the y-axis) and frequency (on the x-axis). Low-frequency power (0-10 Hz) peaks in the superficial and deep layers. **B**, Power in the 30-80 Hz band is

highest in the middle layers. Note the change in scale for the two panels. **C** and **D**, Collapsed across frequencies in the low (0-10 Hz) and gamma (30-50 Hz) range, these frequency histograms show the average LFP power vs. depth in the bands where the layer differences are most pronounced.

Figure 6. Dependence of correlations in V2 on laminar location. **A**, Jitter-corrected CCGs (averaged across all pairs) at four V2 sites, recorded in one V2 penetration with simultaneous recording in the superficial layers of V1. Sharp peaks in the CCG were evident at the second and third depth, but only the amplitude of the former reached our criterion of significance (horizontal dotted lines indicating 5 SDs). The horizontal and vertical dashed lines indicate 0% synchrony and zero time lag, respectively. **B**, Using the presence of sharp peaks as an indicator of the middle layers of V2, these frequency histograms show the distribution of r_{sc} for V2-V2 pairs in superficial, middle and deep layers. **C**, For the same pairs shown in **B**, average jitter-corrected CCGs in the superficial, middle and deep layers. The vertical scale bar indicates 0.0002 coinc./sp. for panel **C** and 0.01% efficacy (normalized only by the presynaptic rate) for panel **A**. The horizontal bar indicates 25 ms for both panels.

REFERENCES

Averbeck BB, Latham PE, Pouget A (2006) Neural correlations, population coding and computation. Nat Rev Neurosci 7:358–366

Averbeck BB, Lee D (2006) Effects of noise correlations on information encoding and decoding. J Neurophysiol 95:3633–3644

Bair W, Zohary E, Newsome WT (2001) Correlated firing in macaque visual area MT: time scales and relationship to behavior. J. Neurosci. 21:1676–1697

Berens P, Keliris GA, Ecker AS, Logothetis NK, Tolias AS (2008) Feature selectivity of the gamma-band of the local field potential in primate primary visual cortex. Front Neurosci 2:199–207

Blasdel GG, Lund JS (1983) Termination of afferent axons in macaque striate cortex. J. Neurosci. 3:1389–1413

Bollimunta A, Chen Y, Schroeder CE, Ding M (2008) Neuronal mechanisms of cortical alpha oscillations in awake-behaving macaques. J. Neurosci. 28:9976–9988

Casagrande VA, Kass JH (1994) The afferent, intrinsic, and efferent connections of primary visual cortex in primates In A. Peters & K. Rockland, eds. Cerebral Cortex New York: Plenum Press, p. 201–259.

Chatterjee S, Callaway EM (2003) Parallel colour-opponent pathways to primary visual cortex. Nature 426:668–671

Cheong SK, Tailby C, Martin PR, Levitt JB, Solomon SG (2011) Slow intrinsic rhythm in the koniocellular visual pathway. Proc. Natl. Acad. Sci. U.S.A. 108:14659–14663

Churchland MM et al. (2010) Stimulus onset quenches neural variability: a widespread cortical phenomenon. Nat. Neurosci. 13:369–378

Cohen MR, Kohn A (2011) Measuring and interpreting neuronal correlations. Nat. Neurosci. 14:811–819

Compte A, Sanchez-Vives MV, McCormick DA, Wang X-J (2003) Cellular and network mechanisms of slow oscillatory activity (< 1 Hz) and wave propagations in a cortical network model. J Neurophysiol 89:2707–2725

de la Rocha J, Doiron B, Shea-Brown E, Josić K, Reyes A (2007) Correlation between neural spike trains increases with firing rate. Nature 448:802–806

De Valois RL, Albrecht DG, Thorell LG (1982) Spatial frequency selectivity of cells in macaque visual cortex. Vision Res 22:545–559

Douglas RJ, Martin KAC (2004) Neuronal circuits of the neocortex. Annu Rev Neurosci

27:419–451

Ecker AS, Berens P, Keliris GA, Bethge M, Logothetis NK, Tolias AS (2010) Decorrelated neuronal firing in cortical microcircuits. Science 327:584–587

Felleman DJ, Van Essen DC (1991) Distributed hierarchical processing in the primate cerebral cortex. Cereb Cortex 1:1–47

Flint AC, Connors BW (1996) Two types of network oscillations in neocortex mediated by distinct glutamate receptor subtypes and neuronal populations. J Neurophysiol 75:951–957

Foster KH, Gaska JP, Nagler M, Pollen DA (1985) Spatial and temporal frequency selectivity of neurones in visual cortical areas V1 and V2 of the macaque monkey. J. Physiol. (Lond.) 365:331–363

Fries P (2009) Neuronal gamma-band synchronization as a fundamental process in cortical computation. Annu Rev Neurosci 32:209–224

Fries P, Womelsdorf T, Oostenveld R, Desimone R (2008) The effects of visual stimulation and selective visual attention on rhythmic neuronal synchronization in macaque area V4. J. Neurosci. 28:4823–4835

Gieselmann MA, Thiele A (2008) Comparison of spatial integration and surround suppression characteristics in spiking activity and the local field potential in macaque V1. Eur J Neurosci 28:447–459

Gilbert CD, Wiesel TN (1983) Clustered intrinsic connections in cat visual cortex. J. Neurosci. 3:1116–1133

Gilbert CD, Wiesel TN (1989) Columnar specificity of intrinsic horizontal and corticocortical connections in cat visual cortex. J. Neurosci. 9:2432–2442

Givre SJ, Arezzo JC, Schroeder CE (1995) Effects of wavelength on the timing and laminar distribution of illuminance-evoked activity in macaque V1. Vis Neurosci 12:229–239

Graf ABA, Kohn A, Jazayeri M, Movshon JA (2011) Decoding the activity of neuronal populations in macaque primary visual cortex. Nat. Neurosci. 14:239–245

Gray CM (1999) The temporal correlation hypothesis of visual feature integration: still alive and well. Neuron 24:31–47, 111–25

Gray CM, Maldonado PE, Wilson M, McNaughton B (1995) Tetrodes markedly improve the reliability and yield of multiple single-unit isolation from multi-unit recordings in cat striate cortex. J Neurosci Methods 63:43–54

Gur M, Kagan I, Snodderly DM (2005) Orientation and direction selectivity of neurons in V1 of alert monkeys: functional relationships and laminar distributions. Cereb Cortex

15:1207–1221

Harrison M, Amarasingham A, Geman S (2007) Jitter methods for investigating spike train dependencies. Computational and Systems Neuroscience Abstracts

Harrison MT, Geman S (2009) A rate and history-preserving resampling algorithm for neural spike trains. Neural Comput 21:1244–1258

Jia X, Smith MA, Kohn A (2011) Stimulus selectivity and spatial coherence of gamma components of the local field potential. J. Neurosci. 31:9390–9403

Kelly RC, Smith MA, Samonds JM, Kohn A, Bonds AB, Movshon JA, Lee TS (2007) Comparison of recordings from microelectrode arrays and single electrodes in the visual cortex. J. Neurosci. 27:261–264

Kelly RC, Smith MA, Kass RE, Lee TS (2010) Local field potentials indicate network state and account for neuronal response variability. J Comput Neurosci 29:567–579

Kohn A, Zandvakili A, Smith MA (2009) Correlations and brain states: from electrophysiology to functional imaging. Curr. Opin. Neurobiol. 19:434–438

Kohn A, Smith MA (2005) Stimulus dependence of neuronal correlation in primary visual cortex of the macaque. J. Neurosci. 25:3661–3673

Litwin-Kumar A, Azeredo da Silveire R, Doiron B (2011) Slow dynamics in balanced networks with spatially dependent connections. Computational and Systems Neuroscience Abstracts

Lund JS (1988) Anatomical organization of macaque monkey striate visual cortex. Annu Rev Neurosci 11:253–288

Lund JS, Henry GH, MacQueen CL, Harvey AR (1979) Anatomical organization of the primary visual cortex (area 17) of the cat. A comparison with area 17 of the macaque monkey. J Comp Neurol 184:599–618

Maier A, Adams GK, Aura C, Leopold DA (2010) Distinct superficial and deep laminar domains of activity in the visual cortex during rest and stimulation. Front Syst Neurosci 4

Maier A, Aura CJ, Leopold DA (2011) Infragranular sources of sustained local field potential responses in macaque primary visual cortex. J. Neurosci. 31:1971–1980

Markram H, Toledo-Rodriguez M, Wang Y, Gupta A, Silberberg G, Wu C (2004) Interneurons of the neocortical inhibitory system. Nat Rev Neurosci 5:793–807

Mitchell JF, Sundberg KA, Reynolds JH (2009) Spatial attention decorrelates intrinsic activity fluctuations in macaque area V4. Neuron 63:879–888

Nelson SB, Hempel C, Sugino K (2006) Probing the transcriptome of neuronal cell types.

Curr. Opin. Neurobiol. 16:571–576

Nicholson C, Freeman JA (1975) Theory of current source-density analysis and determination of conductivity tensor for anuran cerebellum. J Neurophysiol 38:356–368

Padmanabhan K, Urban NN (2010) Intrinsic biophysical diversity decorrelates neuronal firing while increasing information content. Nat. Neurosci. 13:1276–1282

Perkel DH, Gerstein GL, Moore GP (1967) Neuronal spike trains and stochastic point processes. II. Simultaneous spike trains. Biophys J 7:419–440

Peters A (1994) The organization of the primary visual cortex in the macaque In A. Peters & K. Rockland, eds. Cerebral Cortex New York: Plenum Press, p. 1–35.

Poulet JFA, Petersen CCH (2008) Internal brain state regulates membrane potential synchrony in barrel cortex of behaving mice. Nature 454:881–885

Rajkai C, Lakatos P, Chen C-M, Pincze Z, Karmos G, Schroeder CE (2008) Transient cortical excitation at the onset of visual fixation. Cereb Cortex 18:200–209

Rasch MJ, Schuch K, Logothetis NK, Maass W (2011) Statistical comparison of spike responses to natural stimuli in monkey area V1 with simulated responses of a detailed laminar network model for a patch of V1. J Neurophysiol 105:757–778

Reid RC, Alonso JM (1995) Specificity of monosynaptic connections from thalamus to visual cortex. Nature 378:281–284

Renart A, de la Rocha J, Bartho P, Hollender L, Parga N, Reyes A, Harris KD (2010) The asynchronous state in cortical circuits. Science 327:587–590

Rockland KS, Virga A (1990) Organization of individual cortical axons projecting from area V1 (area 17) to V2 (area 18) in the macaque monkey. Vis Neurosci 4:11–28

Roy SA, Dear SP, Alloway KD (2001) Long-range cortical synchronization without concomitant oscillations in the somatosensory system of anesthetized cats. J. Neurosci. 21:1795–1808

Sakata S, Harris KD (2009) Laminar structure of spontaneous and sensory-evoked population activity in auditory cortex. Neuron 64:404–418

Salin PA, Bullier J (1995) Corticocortical connections in the visual system: structure and function. Physiol Rev 75:107–154

Salinas E, Sejnowski TJ (2000) Impact of correlated synaptic input on output firing rate and variability in simple neuronal models. J. Neurosci. 20:6193–6209

Samonds JM, Bonds AB (2005) Gamma oscillation maintains stimulus structure-dependent synchronization in cat visual cortex. J Neurophysiol 93:223–236

Sanchez-Vives MV, McCormick DA (2000) Cellular and network mechanisms of rhythmic recurrent activity in neocortex. Nat. Neurosci. 3:1027–1034

Schroeder CE, Mehta AD, Givre SJ (1998) A spatiotemporal profile of visual system activation revealed by current source density analysis in the awake macaque. Cereb Cortex 8:575–592

Silva LR, Amitai Y, Connors BW (1991) Intrinsic oscillations of neocortex generated by layer 5 pyramidal neurons. Science 251:432–435

Smith MA, Bair W, Movshon JA (2002) Signals in macaque striate cortical neurons that support the perception of glass patterns. J. Neurosci. 22:8334–8345

Smith MA, Kohn A (2008) Spatial and temporal scales of neuronal correlation in primary visual cortex. J. Neurosci. 28:12591–12603

Smith MA, Kohn A (2009) Laminar dependence of neuronal correlation in macaque V1. Society for Neuroscience Abstracts

Stark E, Globerson A, Asher I, Abeles M (2008) Correlations between groups of premotor neurons carry information about prehension. J. Neurosci. 28:10618–10630

Stoelzel CR, Bereshpolova Y, Swadlow HA (2009) Stability of thalamocortical synaptic transmission across awake brain states. J. Neurosci. 29:6851–6859

Tanaka K (1983) Cross-correlation analysis of geniculostriate neuronal relationships in cats. J Neurophysiol 49:1303–1318

Thomson AM, Lamy C (2007) Functional maps of neocortical local circuitry. Front Neurosci 1:19–42

Ts'o DY, Gilbert CD, Wiesel TN (1986) Relationships between horizontal interactions and functional architecture in cat striate cortex as revealed by cross-correlation analysis. J. Neurosci. 6:1160–1170

Van Essen DC, Newsome WT, Maunsell JH, Bixby JL (1986) The projections from striate cortex (V1) to areas V2 and V3 in the macaque monkey: asymmetries, areal boundaries, and patchy connections. J Comp Neurol 244:451–480

van Vreeswijk C, Sompolinsky H (1996) Chaos in neuronal networks with balanced excitatory and inhibitory activity. Science 274:1724–1726

Zandvakili A, Kohn A (2010) Linear summation of feedforward corticocortical inputs. Society for Neuroscience Abstracts

Zhang M, Alloway KD (2004) Stimulus-induced intercolumnar synchronization of neuronal activity in rat barrel cortex: a laminar analysis. J Neurophysiol 92:1464–1478

Zohary E, Shadlen MN, Newsome WT (1994) Correlated neuronal discharge rate and its implications for psychophysical performance. Nature 370:140–143

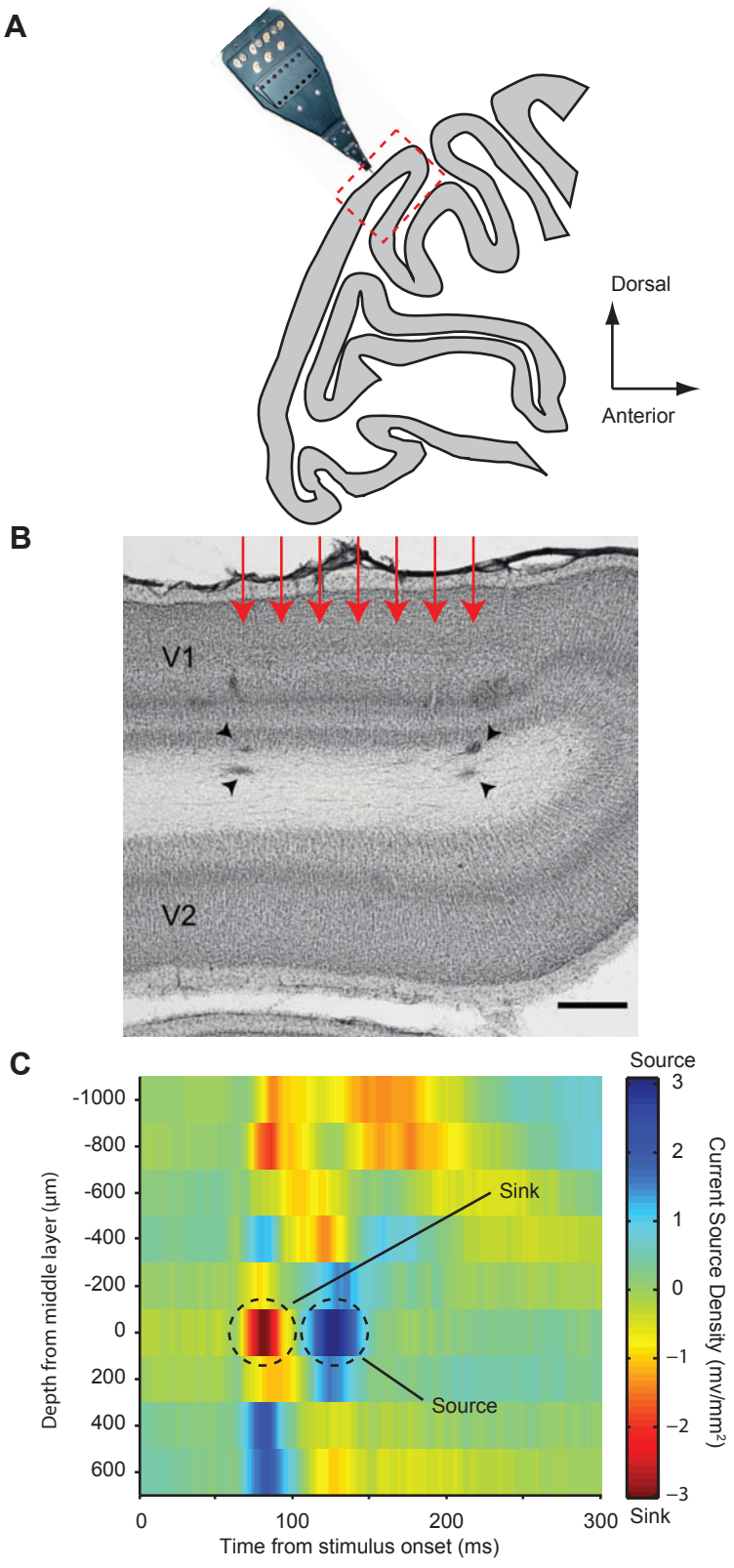

Figure 1 - Smith et al.

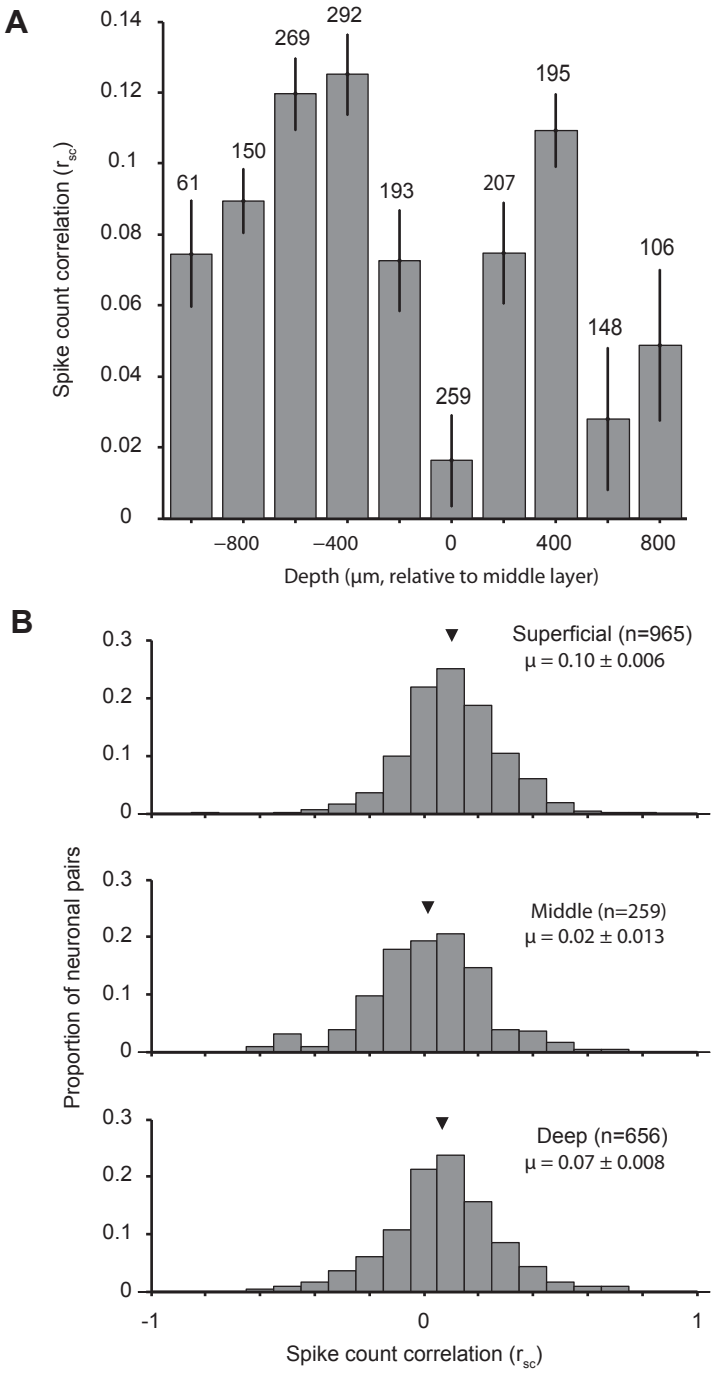

Figure 2 - Smith et al.

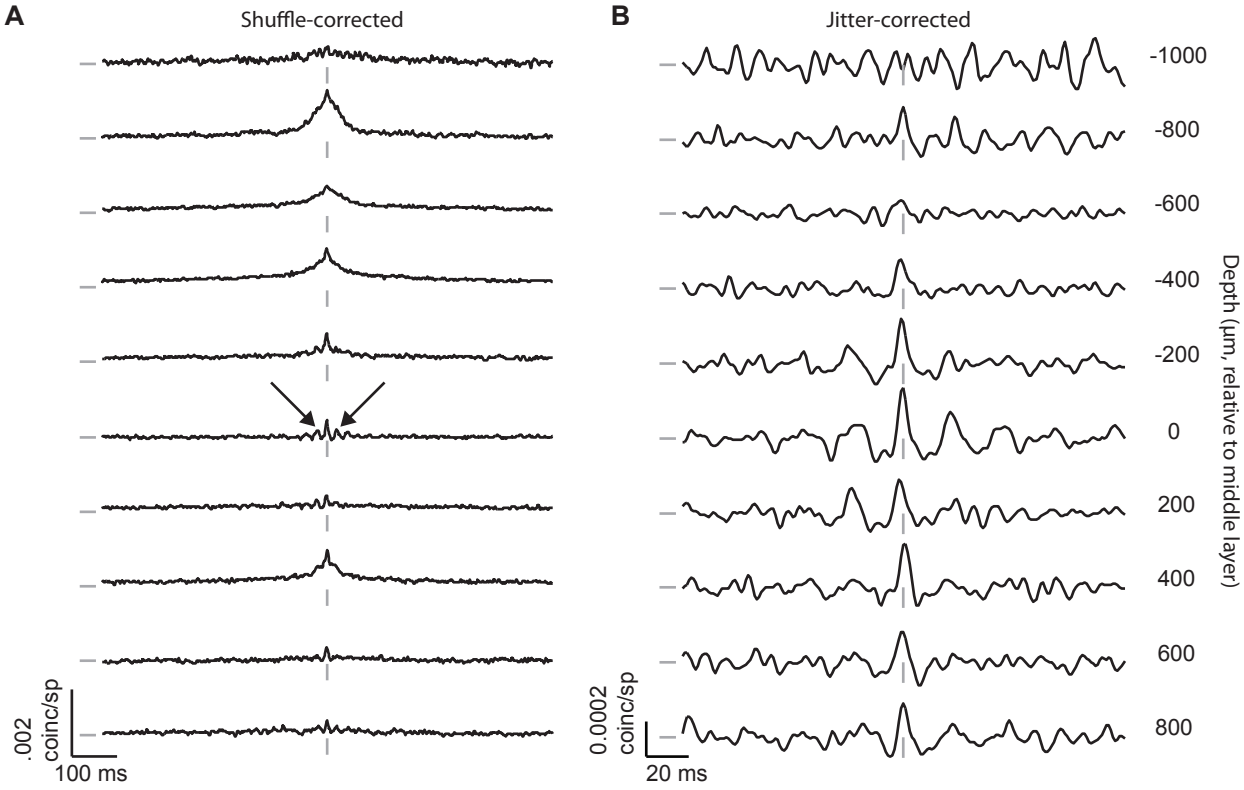

Figure 3 - Smith et al.

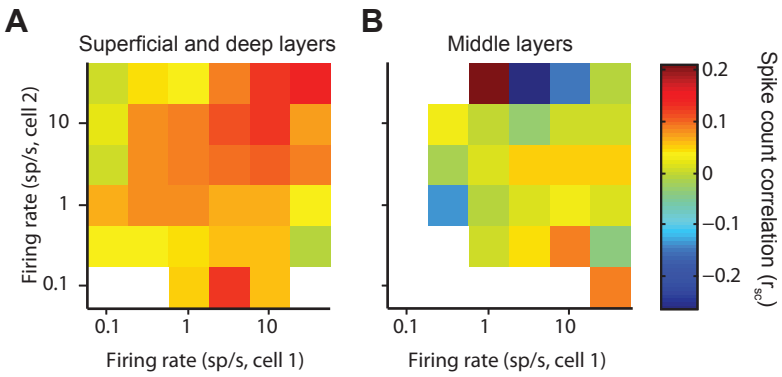

Figure 4 - Smith et al.

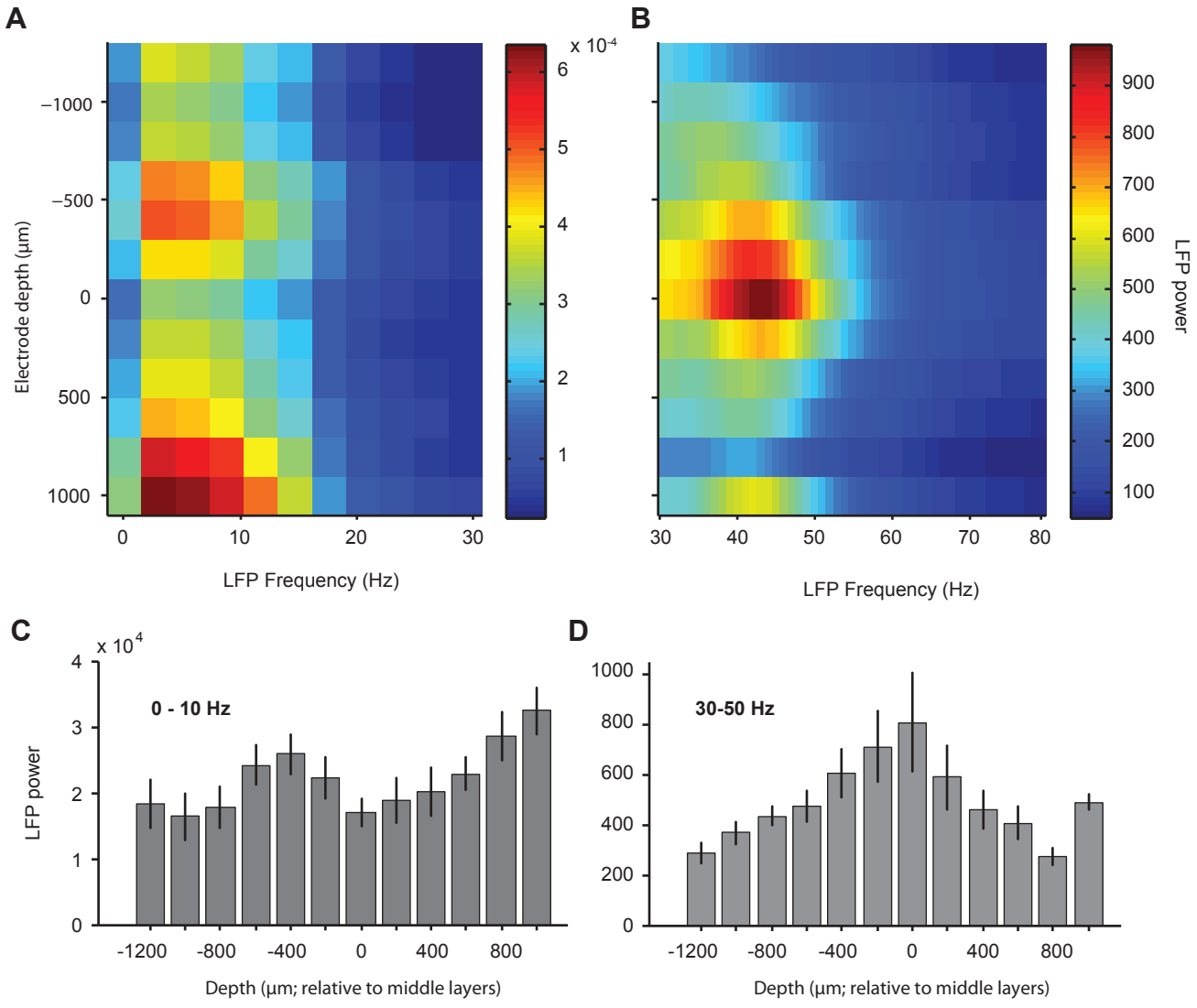

Figure 5 - Smith et al.

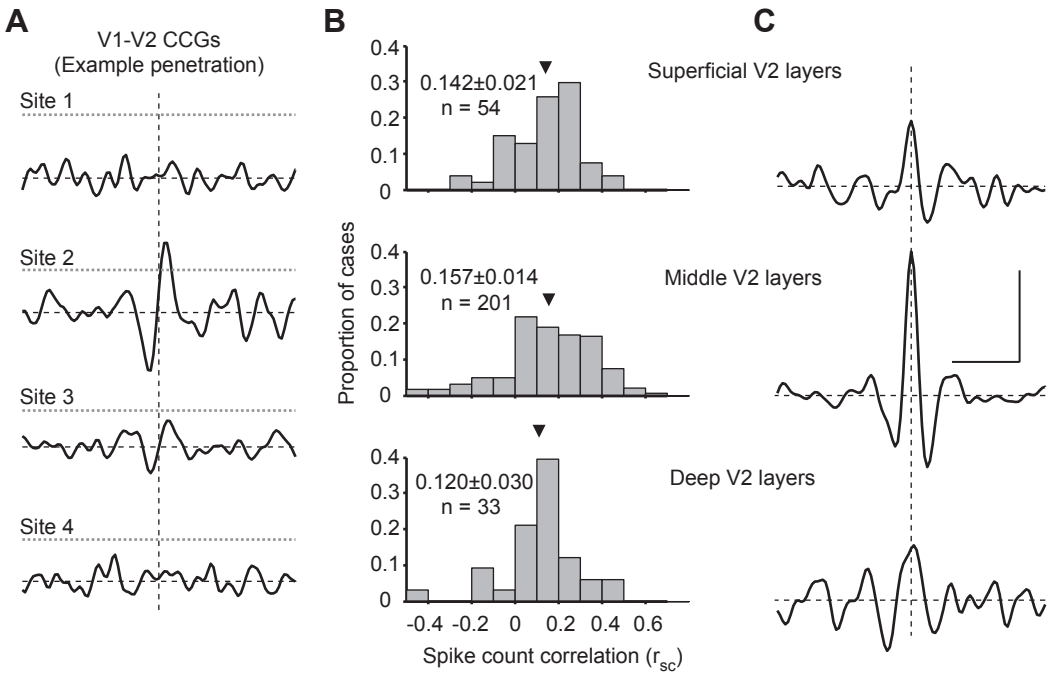

Figure 6 - Smith et al.

Appendix V: Previously published papers

OPEN ACCESS Freely available online

PLoS BIOLOGY

Primer

Gamma Rhythms in the Brain

Xiaoxuan Jia[1]*, Adam Kohn[1,2]

1 Dominick P. Purpura Department of Neuroscience, Albert Einstein College of Medicine, Bronx, New York, United States of America, **2** Department of Ophthalmology and Visual Sciences, Albert Einstein College of Medicine, Bronx, New York, United States of America

Brain rhythms are activity fluctuations shared in populations of neurons. They are evident in extracellular electric fields and detectable through recordings performed within the brain or on the scalp. The gamma rhythm, a relatively high frequency (30–80 Hz) component of these fluctuations, has received a great deal of attention. Gamma is modulated by sensory input and internal processes such as working memory and attention. Numerous theories have proposed that gamma contributes directly to brain function, but others argue that gamma is better viewed as a simple byproduct of network activity. Here we provide a basic introduction to this enigmatic signal, the mechanisms that generate it, and an accompanying paper in *PLoS Biology* attempting to elucidate its potential function.

Hans Berger first successfully measured the brain waves of humans in 1924 using the electroencephalogram (EEG) [1]. His goal was to demonstrate that the electromagnetic fields of the human brain could be used for telepathy. Although the signals he detected were unsuccessful for this purpose, the EEG was widely adopted by clinicians and scientists. This is because the recordings are easy to perform and the rhythms detected are informative of brain state. For example, when we are in a deep sleep, the EEG consists of low-frequency, large-amplitude oscillations; when we are awake and attentive, it consists primarily of fast, small amplitude rhythms.

Brain rhythms are evident as extracellular voltage fluctuations. These arise from summed electrical activity (primarily, but not exclusively, inputs) in populations of neurons, and are shaped by the geometry and alignment of those neurons [2]. The resultant fluctuations can be measured on the scalp by EEG or magnetoencephalography (MEG), and intracranially with subdural electrodes (electrocorticography). They can also be measured, on a more local basis, with a high impedance electrode placed in the brain (Figure 1A). The voltage fluctuations detected are then low-pass filtered (<250 Hz) to capture the slower fluctuations of brain rhythms (Figure 1B). The resultant signal—termed the local field potential (LFP)—was frequently used to study brain function, until it fell in popularity with the advent of single-cell electrophysiology in the late 1950s. Over the last decade, however, LFPs have attracted renewed interest as a potentially useful signal for studying the behavior of ensembles of neurons.

The LFP is a continuous voltage signal that can vary in amplitude and frequency content. Like the EEG, it can be decomposed into different frequency components—delta (<4 Hz), theta (4–8 Hz), alpha (8–12 Hz), beta (12–30 Hz), gamma (30–80 Hz), and high-gamma or high-frequency activity (>80 Hz)—although the precise frequency ranges associated with these terms vary across studies. The relative contribution of these different components to the measured signal is quantified by their relative power (Figure 2). In quiescent networks, most of the power in the LFP is found at low frequencies, indicating that rhythms like delta and theta contribute more significantly than high frequency ones. This is still the case when networks are activated, but less so: the power in higher frequencies increases, whereas that in lower frequencies is suppressed. The enhancement of gamma power in this driven state is particularly striking and is evident as a distinct "bump" in the power spectrum (Figure 2; right panel, solid line).

A prominent gamma rhythm provides a signature of engaged networks. Gamma has been observed in a number of cortical areas, as well as subcortical structures, in numerous species. In sensory cortex, gamma power increases with sensory drive [3,4], and with a broad range of cognitive phenomena, including perceptual grouping [5] and attention [6]. At a given recording site, gamma is stronger for some stimuli than others, generally displaying selectivity and a preference similar to that of nearby neuronal spiking activity [7,8]. In higher cortex, gamma power is elevated during working memory [9] and learning [10]. Interestingly, irregular gamma activity has been observed in neurological disorders such as Alzheimer's disease, Parkinson's disease, schizophrenia, and epilepsy [11].

To interpret the meaning of changes in gamma requires an understanding of the cellular and network mechanisms that generate it. Fast-spiking GABAergic inhibitory interneurons are known to be crucial, with their activity being both necessary and sufficient to generate gamma [12–14]. Network models suggest that this process may be enhanced by interactions with excitatory neurons [15] and that local gamma-generating networks can be coupled by long-range horizontal connections [16] or gap junctions among inhibitory interneurons [17]. Such coupling would seem necessary, as gamma has been shown to be coherent across millimeters of cortex [18–20].

It is well established that gamma correlates with engaged or driven networks, but it is less clear whether it is a simple byproduct of network activity or has an important functional role. This is not for lack of proposals: numerous functions have been attributed to this rhythm. Most of these hinge on a relationship between gamma and the timing of spiking activity in nearby neurons. Spikes are actively generated signals in individual neurons and relay information between neural networks. Gamma activity is not actively propagated. It is a component of an extracellular field

Primers provide a concise introduction into an important aspect of biology highlighted by a current *PLoS Biology* research article.

Citation: Jia X, Kohn A (2011) Gamma Rhythms in the Brain. PLoS Biol 9(4): e1001045. doi:10.1371/journal.pbio.1001045

Published April 12, 2011

Funding: This work was supported in part by a grant from the National Institutes of Health to AK (EY016774). The funders had no role in study design, data collection and analysis, decision to publish, or preparation of the manuscript.

Competing Interests: The authors have declared that no competing interests exist.

Abbreviations: EEG, electroencephalogram; LFP, local field potential

* E-mail: jxiaoxuan@gmail.com

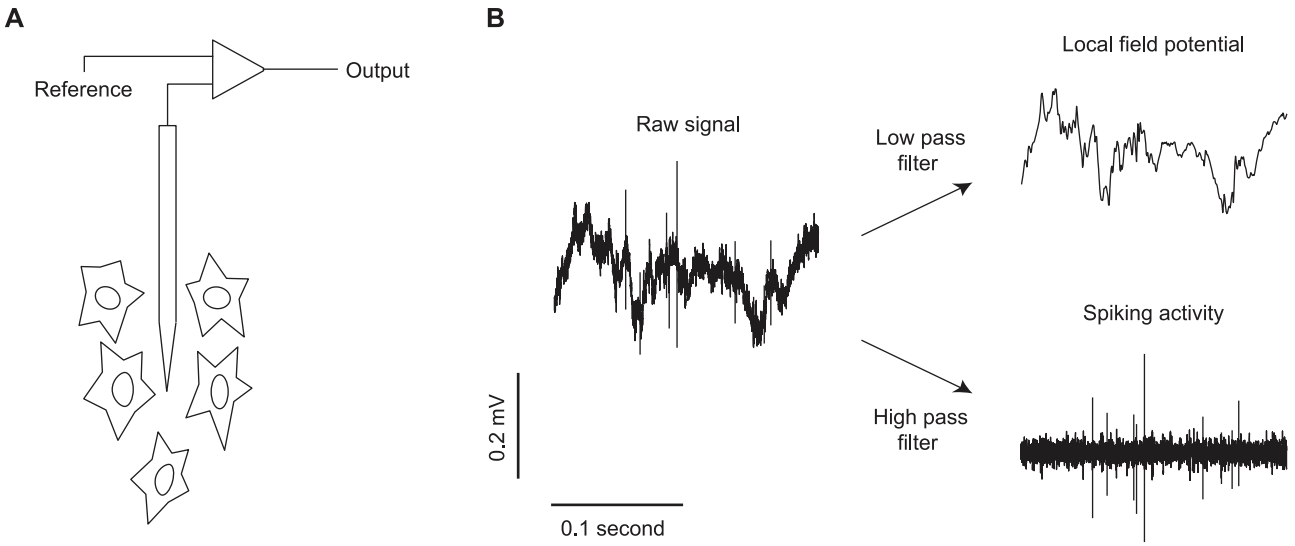

Figure 1. Illustration of LFP recordings. (A) A high impedance electrode detects extracellular electrical activity of nearby neurons. (B) This raw signal is low-pass filtered (e.g., <250 Hz) to provide the local field potential (LFP), and high-pass filtered (e.g., 0.5–10 kHz) to isolate spiking activity.
doi:10.1371/journal.pbio.1001045.g001

potential that reflects primarily the synaptic input to a collection of neurons. Because of this, gamma can only play a role in processing if it is linked to spiking activity in a meaningful way. A coupling between gamma and spike timing could arise because local inhibitory neurons—which contribute strongly to gamma—fire preferentially at the trough of the gamma cycle [21]. This makes the spiking of excitatory projection neurons more likely to occur at an offset phase, when inhibition is weaker.

Based on this mechanism—in some cases, predating its discovery—numerous theories have suggested that the gamma coordination of spiking activity is central to cortical processing. One purports that gamma acts as a temporal reference frame, with the gamma phase at which spikes occur encoding stimulus strength [22]. Consistent with this suggestion, neurons in visual cortex can encode stimulus orientation in "phase-of-firing" relative to gamma [23]. Another theory proposes that gamma may influence the communication between neuronal populations [24,25]. Here the suggestion is that when field potentials and spiking activity in two groups of neurons are phase coherent, the communication between them will be maximal. A third hypothesis, "binding by synchrony", suggests gamma can link the representation of a single sensory input (e.g., a visual object) whose features are processed by

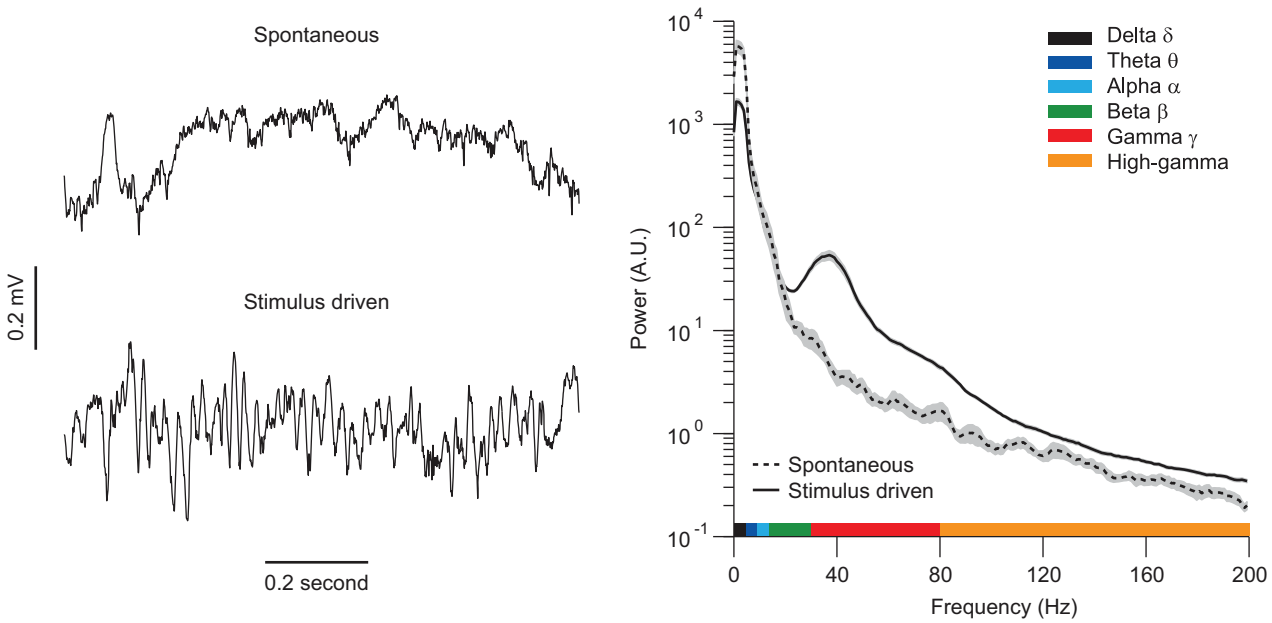

Figure 2. LFPs for spontaneous and stimulus-driven activity. (Left) Example traces of the LFP during spontaneous activity and visually driven activity in primary visual cortex. (Right) The corresponding power spectra for the two conditions, with the frequency ranges of different rhythms indicated.
doi:10.1371/journal.pbio.1001045.g002

different groups of neurons [26]. At the heart of these proposals is the concept that gamma influences spike timing and that this affects cortical computation and function.

A number of recent studies have taken a more critical view of the role of gamma, testing whether it has the properties required for its purported functions. One study showed that the frequency of gamma can vary between nearby sets of neurons, limiting its ability to function as a global timing reference [27]. Another has shown that, at a single site, the gamma rhythm is not "auto-coherent", meaning that its absolute phase changes with time, a pernicious feature for a reference clock or integrative signal [28]. In this vein, it is also worth noting that gamma fluctuations are small, roughly 10–20 microvolts on average, and account for only 0.5%–10% of the total power in the LFP. These observations raise the possibility that gamma is simply a resonant frequency that has no special function, a byproduct of a recurrently connected neuronal network.

To test existing proposals, and to understand the function of gamma more generally, it is critical to analyze the temporal relationship between spikes and gamma. This is typically done using spike-field coherence analysis or by spike-triggered averaging of the LFP, both of which provide a measure of the temporal or phase relationship between spike trains and the LFP. These measures have revealed weak but measurable coupling, which increases when gamma power is elevated [6,9,29]. This coupling is only meaningful, however, if the two signals are measured independently. LFPs and spikes are often recorded from a single electrode. Because extracellular action potential waveforms have a broad frequency spectrum, including power below 250 Hz, their energy can leak into the LFP signal [30,31]. That is, the low-pass filtering of the extracellular voltage signal, which is used to isolate the LFP (Figure 1), may not entirely remove action potential waveforms. The resultant contamination would introduce spurious correlations: the timing of spikes will appear to be related to fluctuations in LFP power for the simple reason that a remnant of the spike waveform remains in that signal.

The paper by Ray and Maunsell in this issue of *PLoS Biology* carefully examines the interaction between spikes and the LFP [32]. Using clever analysis, they provide rigorous quantification of the contamination of LFP signals by spike waveforms and spike-related transients. They show this contamination can contribute to the high frequency components of the LFP, and has a measurable effect on frequencies extending down to 50 Hz. For studies that have focused on spike–gamma interactions in the lower gamma rhythm range (30–50 Hz), contamination is thus less likely to be an issue, although the precise frequency range over which contamination occurs will depend on the specific properties of the filters used to separate spikes from LFPs. However, for frequencies above this range (>50 Hz), which include the higher frequencies of gamma and the full range of high-gamma, spike–LFP correlations might be inflated by spike contamination. More generally, the findings of Ray and Maunsell suggest the need for a re-evaluation of the spike–LFP timing relationship, particularly in cases where this has been established using signals recorded from the same electrode.

In a related analysis, Ray and Maunsell tested the relationship between high-gamma and gamma power. To do so, they manipulated stimulus size. It is well known that many neurons in primary visual cortex are less responsive to large stimuli than small ones [33]. Gamma power, in contrast, increases with stimulus size [34]. Building on this work, Ray and Maunsell show that high-gamma power is modulated similarly to spiking activity by stimulus size (i.e., suppressed by large stimuli), and thus differently from gamma. The authors also show that high-gamma power has similar temporal dynamics as spiking activity, whereas gamma does not. Together, this strongly suggests that the proposed functions of gamma do not apply to high-gamma, even in situations where both signals are similarly enhanced. Rather, high-gamma may best be viewed as a reliable and convenient signal to represent multi-unit activity (MUA).

The findings of Ray and Maunsell help clarify the relationships among gamma, high-gamma, and spiking activity. But much remains unclear. It is certain that gamma, like other brain rhythms, can provide a signature of cognitive state, as well as network dysfunction. To move beyond the interesting correlation between these rhythms and brain state, like those first described by Berger, we need a better understanding of the underlying generative mechanisms, the way in which these signals modulate spiking activity, and the effect they have on the computations performed by neuronal networks. Only then will we know what role, if any, gamma plays in cortical function.

References

1. Haas LF (2003) Hans Berger (1873–1941), Richard Caton (1842–1926), and electroencephalography. J Neurol Neurosurg Psychiatry 74: 9.
2. Buzsaki G (2006) Rhythms of the brain. New York: Oxford University Press.
3. Adrian ED (1942) Olfactory reactions in the brain of the hedgehog. J Physiol 100: 459–473.
4. Henrie JA, Shapley R (2005) LFP power spectra in V1 cortex: the graded effect of stimulus contrast. J Neurophysiol 94: 479–490.
5. Tallon-Baudry C, Bertrand O (1999) Oscillatory gamma activity in humans and its role in object representation. Trends Cogn Sci 3: 151–162.
6. Fries P, Reynolds JH, Rorie AE, Desimone R (2001) Modulation of oscillatory neuronal synchronization by selective visual attention. Science 291: 1560–1563.
7. Berens P, Keliris GA, Ecker AS, Logothetis NK, Tolias AS (2008) Feature selectivity of the gamma-band of the local field potential in primate primary visual cortex. Front Neurosci 2: 199–207.
8. Liu J, Newsome WT (2006) Local field potential in cortical area MT: stimulus tuning and behavioral correlations. J Neurosci 26: 7779–7790.
9. Pesaran B, Pezaris JS, Sahani M, Mitra PP, Andersen RA (2002) Temporal structure in neuronal activity during working memory in macaque parietal cortex. Nat Neurosci 5: 805–811.
10. Bauer EP, Paz R, Pare D (2007) Gamma oscillations coordinate amygdalo-rhinal interactions during learning. J Neurosci 27: 9369–9379.
11. Uhlhaas PJ, Singer W (2006) Neural synchrony in brain disorders: relevance for cognitive dysfunctions and pathophysiology. Neuron 52: 155–168.
12. Whittington MA, Traub RD, Jefferys JG (1995) Synchronized oscillations in interneuron networks driven by metabotropic glutamate receptor activation. Nature 373: 612–615.
13. Cardin JA, Carlen M, Meletis K, Knoblich U, Zhang F, et al. (2009) Driving fast-spiking cells induces gamma rhythm and controls sensory responses. Nature 459: 663–667.
14. Bartos M, Vida I, Jonas P (2007) Synaptic mechanisms of synchronized gamma oscillations in inhibitory interneuron networks. Nat Rev Neurosci 8: 45–56.
15. Whittington MA, Cunningham MO, LeBeau FE, Racca C, Traub RD (2011) Multiple origins of the cortical gamma rhythm. Dev Neurobiol 71: 92–106.
16. Traub RD, Whittington MA, Stanford IM, Jefferys JG (1996) A mechanism for generation of long-range synchronous fast oscillations in the cortex. Nature 383: 621–624.
17. Gibson JR, Beierlein M, Connors BW (1999) Two networks of electrically coupled inhibitory neurons in neocortex. Nature 402: 75–79.
18. Leopold DA, Murayama Y, Logothetis NK (2003) Very slow activity fluctuations in monkey visual cortex: implications for functional brain imaging. Cereb Cortex 13: 422–433.
19. Frien A, Eckhorn R (2000) Functional coupling shows stronger stimulus dependency for fast oscillations than for low-frequency components in striate cortex of awake monkey. Eur J Neurosci 12: 1466–1478.
20. Murthy VN, Fetz EE (1992) Coherent 25- to 35-Hz oscillations in the sensorimotor cortex of awake behaving monkeys. Proc Natl Acad Sci U S A 89: 5670–5674.
21. Hasenstaub A, Shu Y, Haider B, Kraushaar U, Duque A, et al. (2005) Inhibitory postsynaptic potentials carry synchronized frequency information in active cortical networks. Neuron 47: 423–435.
22. Masquelier T, Hugues E, Deco G, Thorpe SJ (2009) Oscillations, phase-of-firing coding, and spike timing-dependent plasticity: an efficient learning scheme. J Neurosci 29: 13484–13493.

23. Vinck M, Lima B, Womelsdorf T, Oostenveld R, Singer W, et al. (2010) Gamma- phase shifting in awake monkey visual cortex. J Neurosci 30: 1250–1257.
24. Fries P (2009) Neuronal gamma-band synchronization as a fundamental process in cortical computation. Annu Rev Neurosci 32: 209–224.
25. Womelsdorf T, Schoffelen JM, Oostenveld R, Singer W, Desimone R, et al. (2007) Modulation of neuronal interactions through neuronal synchronization. Science 316: 1609–1612.
26. Singer W (1999) Neuronal synchrony: a versatile code for the definition of relations? Neuron 24: 49–65, 111–125.
27. Ray S, Maunsell JH (2010) Differences in gamma frequencies across visual cortex restrict their possible use in computation. Neuron 67: 885–896.
28. Burns SP, Xing D, Shelley MJ, Shapley RM (2010) Searching for autocoherence in the cortical network with a time-frequency analysis of the local field potential. J Neurosci 30: 4033–4047.
29. Fries P, Womelsdorf T, Oostenveld R, Desimone R (2008) The effects of visual stimulation and selective visual attention on rhythmic neuronal synchronization in macaque area V4. J Neurosci 28: 4823–4835.
30. Zanos TP, Mineault PJ, Pack CC (2011) Removal of spurious correlations between spikes and local field potentials. J Neurophysiol 105: 474–486.
31. David SV, Malaval N, Shamma SA (2010) Decoupling action potential bias from cortical local field potentials. Comput Intell Neurosci: 393019.
32. Ray S, Maunsell JHR (2011) Different origins of gamma rhythm and high-gamma activity in macaque visual cortex. PLoS Biol 9(4): e1000610. doi:10.1371/journal.pbio.1000610.
33. Angelucci A, Bressloff PC (2006) Contribution of feedforward, lateral and feedback connections to the classical receptive field center and extra-classical receptive field surround of primate V1 neurons. Prog Brain Res 154: 93–120.
34. Gieselmann MA, Thiele A (2008) Comparison of spatial integration and surround suppression characteristics in spiking activity and the local field potential in macaque V1. Eur J Neurosci 28: 447–459.

Behavioral/Systems/Cognitive

Stimulus Selectivity and Spatial Coherence of Gamma Components of the Local Field Potential

Xiaoxuan Jia,[1] Matthew A. Smith,[3] and Adam Kohn[1,2]

[1]Dominick Purpura Department of Neuroscience and [2]Department of Ophthalmology and Vision Sciences, Albert Einstein College of Medicine, Bronx, New York 10461, and [3]Center for the Neural Basis of Cognition and Department of Neuroscience, University of Pittsburgh, Pittsburgh, Pennsylvania 15213

The gamma frequencies of the local field potential (LFP) provide a physiological correlate for numerous perceptual and cognitive phenomena and have been proposed to play a role in cortical function. Understanding the spatial extent of gamma and its relationship to spiking activity is critical for interpreting this signal and elucidating its function, but previous studies have provided widely disparate views of these properties. We addressed these issues by simultaneously recording LFPs and spiking activity using microelectrode arrays implanted in the primary visual cortex of macaque monkeys. We find that the spatial extent of gamma and its relationship to local spiking activity is stimulus dependent. Small gratings, and those masked with noise, induce a broadband increase in spectral power. This signal is tuned similarly to spiking activity and has limited spatial coherence. Large gratings, however, induce a gamma rhythm characterized by a distinctive spectral "bump," which is coherent across widely separated sites. This signal is well tuned, but its stimulus preference is similar across millimeters of cortex. The preference of this global gamma rhythm is sensitive to adaptation, in a manner consistent with its magnifying a bias in the neuronal representation of visual stimuli. Gamma thus arises from two sources that reflect different spatial scales of neural ensemble activity. Our results show that there is not a single, fixed ensemble contributing to gamma and that the selectivity of gamma cannot be used to infer its spatial extent.

Introduction

Local field potentials (LFPs) reflect coordinated synaptic input and slow intrinsic conductances in neurons (Mitzdorf, 1985; Buzsaki, 2006) and thus provide a potentially useful view of neuronal ensemble activity. Gamma components of the LFP provide a physiological correlate of perceptual and cognitive phenomena (Pesaran et al., 2002; Gail et al., 2004; Wilke et al., 2006; Womelsdorf et al., 2006; Fries et al., 2008) and have been suggested to play an active role in cortical processing.

The spatial extent and functional specificity of gamma are critical constraints on the role it may play in cortical processing. To function as a global reference signal (e.g., an internal clock) (Hopfield, 2004; Fries et al., 2007), gamma would need to form a widespread, coherent rhythm, potentially shared among neuronal ensembles with different response properties. To select specific subsets of neurons [e.g., those representing an attended location (Fries, 2009)], gamma would need to be limited in extent. To link distributed neurons into an ensemble [e.g., binding or dynamically routing information (Gray, 1999; Buzsaki, 2006; Colgin et al., 2009)], gamma would need to target specific subsets of cells but also be coherent across locations.

The spatial extent and functional specificity of gamma are unclear. Recently, Katzner et al. (2009) showed that the evoked LFP, a stimulus-locked transient response, reflects neural activity within 250 μm of the recording site. Xing et al. (2009) showed that this "spatial footprint" reflects the volume conduction of extracellular fields (estimated to be 250 μm) and the extent of the neural ensemble generating the signal. However, these measures of passive propagation and the evoked LFP do not directly address the extent of gamma. This is because gamma is an induced signal—an intrinsic rhythm generated by specific neurons and circuits (for review, see Bartos et al., 2007; Whittington et al., 2011) that are modulated by, but not time locked to, stimulus drive (Kruse and Eckhorn, 1996; Juergens et al., 1999; Brosch et al., 2002; Siegel and König, 2003; Tallon-Baudry, 2003).

Previous studies have provided disparate views of the extent and functional specificity of gamma. In primary visual cortex (V1), gamma is stimulus selective (Gray and Singer, 1989; Frien et al., 2000; Siegel and König, 2003; Henrie and Shapley, 2005; Liu and Newsome, 2006; Berens et al., 2008), suggesting that the relevant circuits have a limited extent: a spatially distributed origin would involve averaging ensembles with different preferences and should thus produce a relatively unselective signal. However, gamma has sometimes (Liu and Newsome, 2006; Katzner et al., 2009), but not always (Kreiman et al., 2006; Berens et al., 2008), been found to have the same preference as spiking activity recorded at the same site. As a result, it has been suggested

Received Feb. 5, 2011; revised April 13, 2011; accepted April 29, 2011.

Author contributions: X.J. and A.K. designed research; X.J., A.K., and M.A.S. performed research; X.J. analyzed data; X.J. and A.K. wrote the paper.

This work was supported by National Institutes of Health Grant EY016774 (A.K.) and Grants EY015958 and EY018894 (M.A.S.). We thank Amin Zandvakili, Stephanie Wissig, and Carlyn Patterson for assistance with data collection; Ryan Kelly for technical assistance; and members of the laboratory, Ruben Coen Cagli, Franco Pestilli, Jason Samonds, and Robert Shapley, for comments on an earlier version of this manuscript. We are grateful to Tai Sing Lee in whose laboratory we recorded data from an awake behaving macaque.

The authors declare no competing financial interests.

Correspondence should be addressed to either Xiaoxuan Jia or Adam Kohn, Department of Neuroscience, Kennedy Center, Room 822, Albert Einstein College of Medicine, 1410 Pelham Parkway South, Bronx, NY 10461. E-mail: jxiaoxuan@gmail.com or adam.kohn@einstein.yu.edu.

DOI:10.1523/JNEUROSCI.0645-11.2011

 0270-6474/11/319390-14$15.00/0

to reflect activity within a few hundred micrometers up to millimeters of the electrode. Another approach to estimating the extent of gamma is to measure it simultaneously at different locations. This has revealed a signal that is coherent across many millimeters of cortex (Juergens et al., 1999; Frien and Eckhorn, 2000; Leopold et al., 2003) and even across regions (Murthy and Fetz, 1992; Pesaran et al., 2002; Schoffelen et al., 2005; Popescu et al., 2009). The presence of gamma in scalp recordings also suggests a widespread coherent signal (Tallon-Baudry, 2003).

To clarify the spatial extent of gamma and its relationship to neuronal activity, we measured both signals simultaneously using multielectrode arrays implanted in the superficial layers of macaque V1. We compared the response properties of gamma across locations and, at each site, with local spiking activity, for a range of stimulus manipulations.

Materials and Methods

Animal preparation and electrophysiology. We recorded data from eight anesthetized, adult male macaque monkeys (*Macaca fascicularis*). The techniques we use have been described in detail previously (Smith and Kohn, 2008). In brief, anesthesia was induced with ketamine (10 mg/kg) and maintained during preparatory surgery with isoflurane (1.5–2.5% in 95% O_2). Anesthesia during recordings was maintained with sufentanil citrate (6–18 $\mu g \cdot kg^{-1} \cdot h^{-1}$, adjusted as needed for each animal). Vecuronium bromide (0.1 $mg \cdot kg^{-1} \cdot h^{-1}$) was used to suppress eye movements. Drugs were administered in normosol with dextrose (2.5%) to maintain physiological ion balance. Physiological signs (ECG, blood pressure, SpO_2, end-tidal CO_2, EEG, temperature, and urinary output and osmolarity) were monitored to ensure adequate anesthesia and animal well-being. Temperature was maintained at 36–37 C°.

Data were also obtained from an awake behaving male rhesus macaque monkey (*Macaca mulatta*). Detailed methods regarding our procedures for training and recording from awake behaving macaques can be found in a previous publication (Smith et al., 2007). All procedures were approved by the Institutional Animal Care and Use Committee of Carnegie Mellon University (awake recordings only) and the Albert Einstein College of Medicine at Yeshiva University (anesthetized recordings only) and were in compliance with the guidelines set forth in the United States Public Health Service *Guide for the Care and Use of Laboratory Animals.*

We implanted a 4 × 4 mm multielectrode array (0.4 mm spacing and 1 mm electrode length) with 100 electrodes into the upper layers of primary visual cortex (~0.6–0.8 mm deep in anesthetized animals; 1 mm for awake recordings), ~10 mm lateral to the midline and ~8 mm posterior to the lunate sulcus. Two reference wires were placed between the brain surface and the dura. Events larger than a user-defined threshold were recorded (Cyberkinetics Neurotechnology Systems). We applied additional voltage thresholding off-line (Plexon Offline Sorter) to remove any remaining noise. Units from the same electrode were then combined to form multiunit activity (MUA). The peak firing rate of this signal was on average 20.7 ± 0.5 ips, suggesting it arose from a handful of neurons at most. LFPs were obtained by bandpass filtering the same signal between 0.3 and 250 Hz and sampling at 1 or 2 kHz.

In some experiments, a separate linearly arranged multielectrode device (Thomas Recording) was positioned between the lunate sulcus and the array, with each electrode referenced to the guide tubes. Raw signals recorded from this device were bandpass filtered between 0.5 and 250 Hz, and digitized at 1 kHz. To remove 60 Hz noise, we applied a fourth-order Butterworth band-stop filter to the raw data.

Visual stimulation. Visual stimuli were generated using custom software (EXPO or Matlab Psychtoolbox) and displayed on a monitor with a resolution of 1024 × 768 pixels, viewed at a distance of 110 cm (58 cm for awake recordings). We mapped the spatial receptive field of each channel by presenting small, drifting gratings (0.6°; 250 ms duration) at a range of spatial positions. We centered our stimuli on the aggregate receptive field of the recorded units. Stimuli were viewed binocularly and presented for 1 s at full contrast. We presented each stimulus 25 times (100 times for measurements of dynamics), in a pseudorandom sequence. In awake recordings, the animal was required to maintain fixation within a 1° window during the 1 s stimulus presentation and to make a saccade to a random target location at stimulus offset.

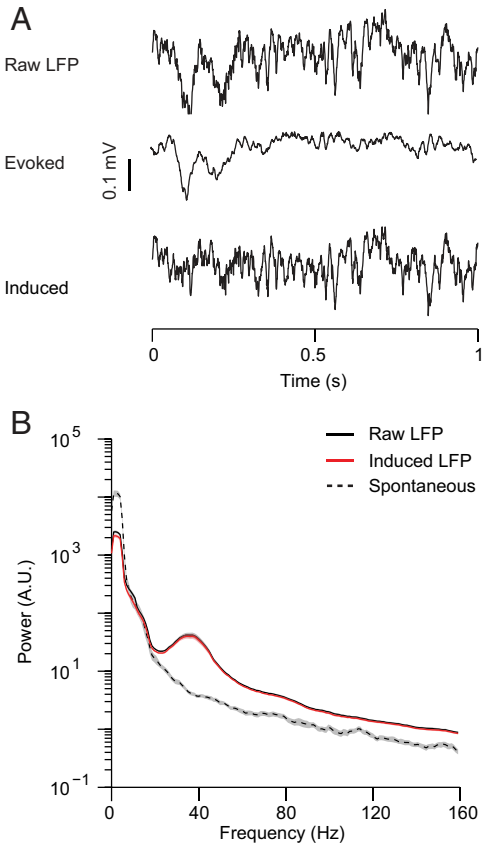

Figure 1. Evoked and induced components of the LFP. ***A***, Single epoch examples of the raw LFP (top) and the induced component (bottom). The induced component is calculated by subtracting the evoked component (middle) from the raw signal. ***B***, Example of the power spectrum of the induced LFP (red), compared with the raw LFP (black). Spontaneous activity was measured with a uniform luminance screen (gray dashed).

For our measurements of tuning at different sizes, stimuli were viewed monocularly. In these experiments, we included only those sites whose receptive field center was within 0.5° of the stimulus center. This yielded typically approximately one-half of the recorded sites, with a maximal separation of 3.57 ± 0.02 mm on average. In our noise-masking experiments, spatial noise was created by selecting small patches (0.06 × 0.06°) randomly in the original image, computing the mean luminance of each patch, and then randomly permutating the patches (Zhou et al., 2008). The noise level (20, 50, and 80%) was defined by the proportion of total area replaced by noise. Noise was randomly distributed on each frame.

Data analysis. We isolated the induced components of the LFP by subtracting the evoked signal (the average response across trials, for each stimulus) from the raw signal on each trial (Fig. 1*A*). We then analyzed responses 100–1000 ms after stimulus onset, when the magnitude of the evoked component was minimal. We did this to separate these two different components of the LFP (Katzner et al., 2009), but the power spectra of the raw LFPs (i.e., not subtracting the evoked component) were in fact similar to the induced LFPs, except at low frequencies (<20 Hz) (Fig. 1*B*). All of the findings reported here were thus similar when based on raw responses, even when we included the onset transient.

We calculated the power spectrum with a multitaper method (Mitra and Pesaran, 1999), which uses a set of orthogonal Slepian tapers to provide a good estimate of power for a limited number of trials and small time windows. For a signal of duration T and a desired half-bandwidth of W (determining the smoothness of the spectrum), the taper number is given by $k = 2TW - 1$. For most of our analysis, the duration of the analyzed epoch was 0.9 s, so we used eight tapers to provide a half-

bandwidth equal to 5 Hz. For the analysis of dynamics, we used a 129 ms sliding window (25 ms steps) and three tapers.

Tuning of the LFP was based on its average power within 4 Hz bins, spanning the range from 0 to 160 Hz. Orientation preference was determined by the vector sum of responses to 16 test directions (22.5° step). An orientation selectivity index (OSI) was calculated as the vector sum of the response vectors (combining responses to different drift directions of the same orientation), normalized by the sum of lengths of the vectors (Leventhal et al., 1995). For computing the OSI, we defined response strength with respect to that driven (MUA) or induced (LFP) by the least preferred orientation. Using spontaneous activity as a baseline was precluded because its power could be either greater or less than the stimulus-induced power, depending on the frequency band of interest.

Only sites with an OSI >0.2 for both MUA and gamma were kept for tuning-related analysis (i.e., for determining the orientation preference of the site or for the correlation between tuning curves). To determine the preference of individual sites, we used the best tuned frequency band [i.e., the 4 Hz band with highest selectivity (Berens et al., 2008)] in the gamma range (30–50 Hz).

We quantified the variance of orientation preferences in the population, σ^2, as follows:

$$1 - \frac{\sqrt{\left(\sum_{i=1}^{n}\cos(2\theta_i)\right)^2 + \left(\sum_{i=1}^{n}\sin(2\theta_i)\right)^2}}{n},$$

where θ_i is the orientation preference for channel i and n is the number of sites.

To determine the tuning similarity between MUA and LFP from the same channel ($r_{\text{MUA-LFP}}$ or $r_{\text{MUA-}\gamma}$ when comparing only to the gamma components) or between two LFP sites ($r_{\text{LFP-LFP}}$ or $r_{\gamma\text{-}\gamma}$), we calculated the Pearson correlation between their tuning. We found that the peak gamma frequency was lower for large gratings (Gieselmann et al., 2008) and for stimuli masked by noise [similar to the effect of lowering stimulus contrast (Ray and Maunsell, 2010)]. To enable a meaningful comparison across conditions, we therefore computed tuning correlations (and all other measures, except orientation preferences) based on the average gamma power in 30–50 Hz. We obtained similar results if our analysis was based on any subband in this frequency range.

To measure the spatial coherence of the LFP, we calculated the coherency between signals measured at different sites (x and y) as follows:

$$C_{xy}(f) = \frac{S_{xy}(f)}{\sqrt{S_{xx}(f)S_{yy}(f)}},$$

where S_{xy} is the cross-spectrum calculated with the multitaper method (duration of 0.9 s, half-bandwidth of 5 Hz, and taper number of 8), and S_{xx} and S_{yy} are the respective autospectra (Pesaran et al., 2002). C_{xy} is a complex number. Its modulus is the coherence (ranging from 0 to 1), a measure of the relationship between two signals as a function of frequency (f). The phase of C_{xy} is the relative phase difference between the two signals, as a function of frequency.

All indications of variation in the graphs and text are SEMs. The statistical significance of all results was evaluated with two-tailed t tests, unless otherwise noted. Significance of correlation values was assessed after applying the Fisher Z-transform to the data.

Results

We implanted microelectrode arrays in the upper layers of V1 of eight anesthetized macaque monkeys and recorded spiking activity and LFPs (0.3–250 Hz) simultaneously on each electrode. Each array covered roughly a 4 × 4 mm cortical region, corresponding to the representation of ~2–3° of the lower visual field (2–5° from the fovea).

Orientation tuning of gamma power

To compare the tuning of gamma power to local spiking activity, we measured responses to large gratings (7.4 or 10° in diameter) drifting in 16 different directions. Gratings had a spatial frequency (1 cycle/deg) and drift rate (6.25 Hz) chosen to evoke robust activity in parafoveal V1 (Foster et al., 1985). Spiking activity was isolated from the filtered voltage signal (250 Hz-10 kHz) with a user-defined threshold and sorted off-line to yield MUA. Tuning of the LFP was generated by computing the power spectrum of the induced signal on each trial and measuring how power in gamma and other frequency bands depended on stimulus orientation. Consistent with previous studies, we found that the LFP was stimulus selective. An example of its tuning at one site (for frequencies between 32 and 36 Hz) is shown in Figure 2*A*, together with that of the local MUA.

We quantified tuning quality using a selectivity index, for which a value of 0 indicates an equal response to all orientations and a value of 1 indicates an elevated response to a single orientation, relative to all others. The low-frequency components of the LFP were poorly tuned, but for frequencies in the gamma range and higher (above ~30 Hz) selectivity was relatively high (Fig. 2*B*, black line) ($n = 680$ sites in 8 implants), albeit lower than that of MUA (0.47 ± 0.01; indicated with black dot to the right).

To quantify the similarity of LFP orientation tuning to local MUA, we computed the correlation between their tuning at each site (termed $r_{\text{MUA-LFP}}$). A value of $r_{\text{MUA-LFP}}$ near 1 indicates very similar tuning; a value near −1 would indicate the opposite. For the tuning curves in Figure 2*A*, $r_{\text{MUA-LFP}}$ was 0.22. Consistent with previous V1 studies (Frien et al., 2000; Siegel and König, 2003; Berens et al., 2008), we found that high-frequency components of the LFP were more similarly tuned to local spiking activity than low-frequency components (Fig. 2*B*, red trace). However, despite the tendency for $r_{\text{MUA-LFP}}$ to increase for higher frequencies, we observed a clear deviation in the range of 30 to 50 Hz (low gamma frequencies, hereafter "gamma"; indicated by box): tuning of gamma was relatively distinct from that of MUA. A similar effect was observed at harmonics of these frequencies (70–90 Hz) in some, but not all, implants.

To explore this further, we compared the preferred orientation of gamma and MUA at each tuned site (selectivity index, ≥0.2). The two signals had a similar preference at some sites but not at others (Fig. 2*C* for data from an example implant). Strikingly, this occurred because the orientation preference of gamma was often similar across sites. This is evident in the marginal histograms (Fig. 2*C*), which show a roughly uniform distribution of preferences for spikes (circular variance, σ^2, of 0.73) and a clearly biased distribution for gamma (σ^2 of 0.23), with a preference of ~110° being the most common. We found a similar pattern in other implants: the distribution of preferences was consistently uniform for spikes (σ^2 of 0.75 ± 0.03; $n = 8$) but strongly biased for gamma (0.23 ± 0.06; $p \ll 0.001$ for the difference between the two signals; Wilcoxon's rank sum test). The orientation preferred by gamma, however, was different in each implant.

We considered that our results might be due to anesthesia, so we recorded responses using the same type of microelectrode arrays and visual stimuli in an awake monkey (see Materials and Methods). The data are consistent with, but more striking than, those observed in anesthetized animals (Fig. 2*D*). In this data set, the orientation preference of gamma was always near 60° (σ^2 of 0.07), whereas simultaneously recorded MUA showed a wide range of preferences (σ^2 of 0.80).

To evaluate the cortical distance over which orientation tuning is similar for gamma and other frequency components, we computed the correlation between its tuning ($r_{\text{LFP-LFP}}$) at all se-

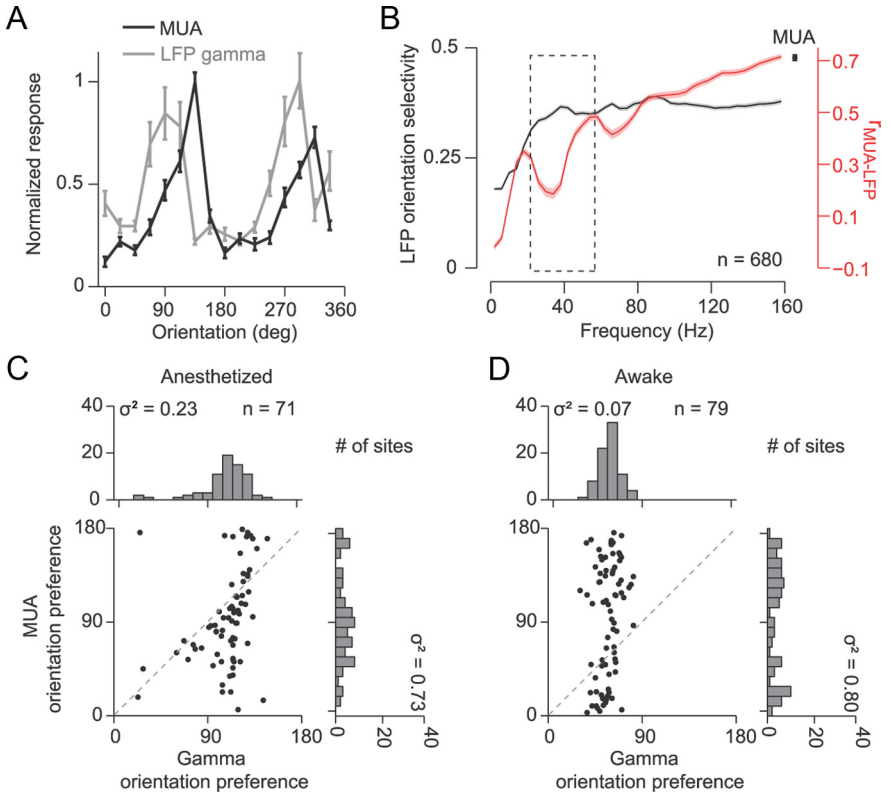

Figure 2. Comparison of the orientation tuning of the LFP with local spiking activity. ***A***, Example tuning curves for MUA (black) and gamma power (gray) at the same site ($n = 25$ repeats). ***B***, Population average trends for LFP orientation selectivity (black) and correlation between the tuning of MUA and the LFP ($r_{MUA\text{-}LFP}$; red), as a function of frequency ($n = 680$ sites). The mean orientation selectivity index for MUA is indicated to the right side (black dot). ***C***, Comparison of orientation preferences for gamma and MUA ($n = 71$ sites from one implant). The circular variance (σ^2) of the distributions was 0.23 for gamma and 0.73 for MUA. ***D***, Similar example for data from an awake monkey ($n = 79$ sites).

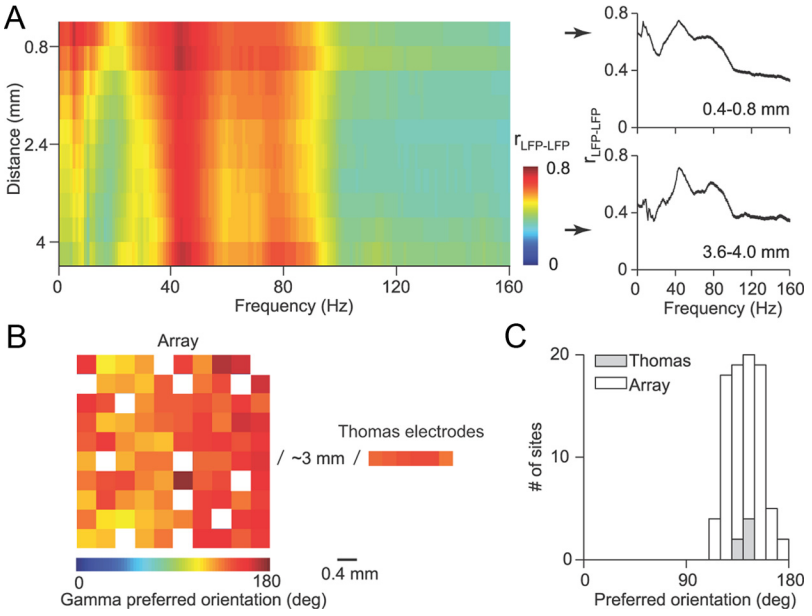

Figure 3. Relationship between orientation tuning of the LFPs measured at different sites. ***A***, Population average of $r_{LFP\text{-}LFP}$ as a function of distance, for sites with orientation selectivity ≥0.2. Cross sections of the color plot for distances of 0.4–0.8 mm ($n = 2233$ pairs) and 3.6–4.0 mm ($n = 1347$ pairs) are shown on the right. ***B***, An example of orientation preference in the gamma band, from simultaneous recordings using two multielectrode systems. Each square represents the orientation preference of one recording site, plotted according to its spatial position. ***C***, Distributions of orientation preference for the example in ***B***.

lective sites and sorted the data according to the distance between electrodes (Fig. 3*A*) ($n = 31{,}211$ pairs of sites). The value of $r_{LFP\text{-}LFP}$ was well maintained across a distance of >4 mm for frequencies between ~35 and 90 Hz. In the 30–50 Hz band, it decayed only 10.2%, from 0.69 ± 0.01 for nearby sites (0.4–0.8 mm; $n = 2233$) to 0.62 ± 0.01 at distances of 4–5 mm ($n = 571$). At lower frequencies (<30 Hz), $r_{LFP\text{-}LFP}$ decayed more rapidly (35% over the same distance). At higher frequencies (>100 Hz), $r_{LFP\text{-}LFP}$ was significantly smaller, even for nearby electrodes, as each site had a different preference.

Because gamma tuning was similar across the entire spatial extent of the array, we performed simultaneous recordings with a separate multielectrode device (Thomas Recording) positioned ~3 mm away (five penetrations in four monkeys). These electrodes were arranged linearly and oriented orthogonally to the nearest edge of the array, providing neurons that were 3–9 mm from those sampled by the array. We used large gratings covering the receptive fields of all neurons to induce gamma activity. The tuning measured at these additional sites had a similar preference to those measured by the array (example shown in Fig. 3*B* with each square representing the preference at one recording site and the respective distributions shown in Fig. 3*C*), with a difference in mean preference of 4.5 ± 1.0°. The orientation preference of gamma can thus be shared over many millimeters of cortex. Note that these recordings used independent multielectrode systems, with distinct electrical references (see Materials and Methods). As a result, these observations preclude the possibility that shared tuning involved an array-specific artifact (e.g., cross talk between electrodes) or arose from a common referencing of array electrodes (for related findings and further discussion, see also Berens et al., 2008).

Our results show that, when gamma is induced by large gratings, it is orientation selective but with a preference distinct from local spiking activity and similar across millimeters of cortex. Since its tuning is distinct, its power is thus not indicative of the strength of activity in local ensembles.

Dependence of gamma tuning on stimulus size

The similar tuning of gamma we observed across sites was based on responses to large gratings. Previous studies have shown that gamma power is weakened by reducing stimulus size (Bauer et al., 1995; Gie-

selmann and Thiele, 2008). We therefore tested how this manipulation affects the similar tuning of gamma across sites and the relationship between its tuning and that of local spiking activity.

To determine the influence of stimulus size, we measured orientation tuning with gratings ranging from 1 to 10° in diameter. Stimuli were centered on the aggregate receptive field of the MUA, as determined by a separate mapping procedure (see Materials and Methods). We analyzed only those sites driven by our smallest stimulus so that the same locations would be compared across conditions. Consistent with previous observations (Bauer et al., 1995; Gieselmann and Thiele, 2008), gamma power increased with stimulus size (Fig. 4*A*), nearly doubling over the range measured. In contrast, the spiking activity at these sites was suppressed by stimuli >1° (Fig. 4*A*), as expected given the prevalence of surround suppression in V1 (Angelucci and Bressloff, 2006).

We found that the relationship between the orientation tuning of MUA and gamma depended strongly on stimulus size. When driven with small gratings (1°), gamma power had a similar preference to MUA at all sites, as shown in Figure 4*B* for a single implant. When stimulated with larger gratings (10°), the preference of gamma changed: it became more similarly tuned across sites, and its preference at many sites became distinct from the local MUA (Fig. 4*C*). Across our data set, we found $r_{\gamma\text{-}\gamma}$, the tuning similarity of gamma, increased strongly with stimulus size (Fig. 4*D*), from 0.11 ± 0.01 to 0.50 ± 0.01 ($n = 2961$ pairs of sites in 3 implants). The similarity between the tuning of MUA and gamma ($r_{\mathrm{MUA}\text{-}\gamma}$), however, decreased from 0.42 ± 0.03 to 0.25 ± 0.03 ($n = 129$ sites), indicating these two signals became more distinct for large stimuli. Although the preference of gamma changed dramatically with stimulus size, its selectivity did not: the mean selectivity for small stimuli was 0.31 ± 0.01 compared with 0.37 ± 0.01 for large gratings, a small but statistically significant increase in tuning quality for the more global signal ($p = 0.007$).

Our results show that gamma has a different preference for small stimuli (i.e., one matched to local spiking activity) and large ones (i.e., one shared across sites). This suggests that gamma does not reflect ensemble activity of a fixed extent. The shared preference we observed across millimeters of cortex, when gamma is induced by large stimuli, suggests a spatially extensive mechanism underlying the signal. For small stimuli, the close match between the preference of spiking activity and gamma measured at the same site strongly suggests a local basis for the signal. Note that small gratings activated ~10 mm^2 of cortex, but the preference of gamma matched the spiking activity at each measured location. Thus, the close match between the preferences of these two signals is not a trivial consequence of small gratings only driving circuits near a particular electrode.

Two components of gamma power

The change in the tuning of gamma with stimulus size was paralleled by a change in the form of the LFP spectra. Small gratings induced a broadband (20–160 Hz) increase in power, which was stronger for some orientations than others (Fig. 5*A*). The preference for gamma frequencies was similar to that of both higher (>50 Hz) and nearby lower (20–30 Hz) frequencies. Large gratings induced a notable increase in power at gamma frequencies, which strongly exceeded the power of both high and lower (20–30 Hz) frequencies (Fig. 5*B*) (Gieselmann et al., 2008; Ray and Maunsell, 2010). The tuning of this gamma "bump" was

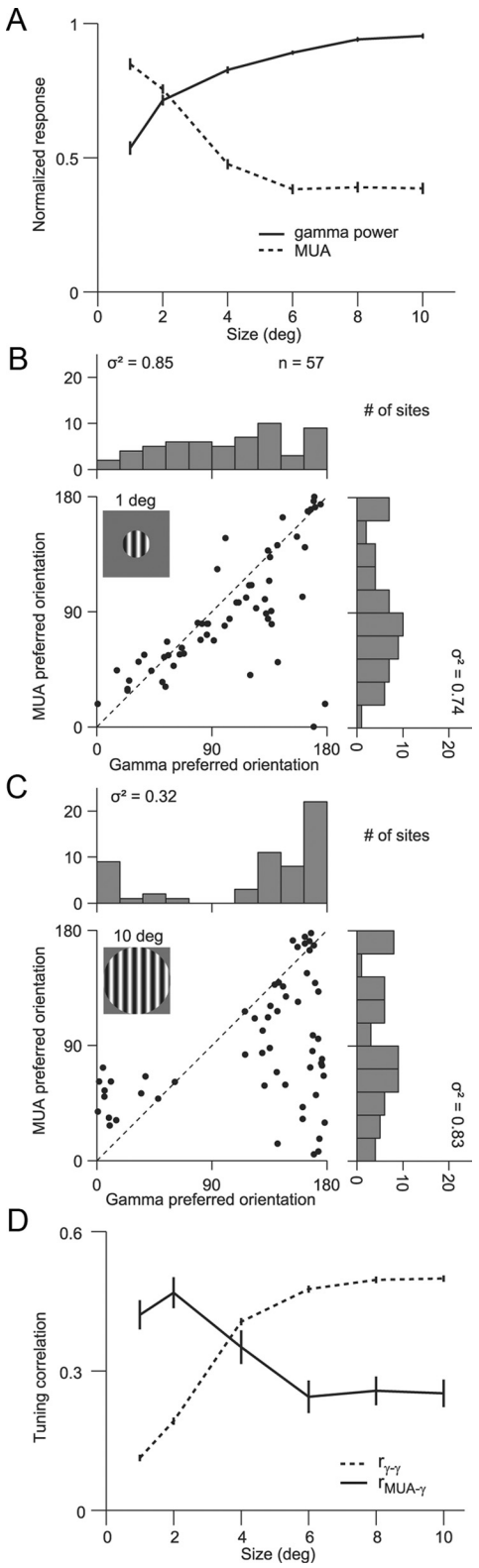

Figure 4. Effect of stimulus size on gamma power and its tuning. ***A***, Normalized firing rate (dashed trace) and gamma power (solid black trace) as a function of stimulus size. Data are shown only for sites driven by the smallest stimulus ($n = 129$ sites). ***B***, Comparison of orientation preference for activity driven by a 1° grating ($n = 57$ sites), for a single implant. The preference of gamma was similar to the MUA at all sites, and the distribution of preferences had a similar variance (0.85 and 0.74, respectively). ***C***, Orientation preferences for the same sites as in ***B***, but when stimulated with a large grating (10°). Gamma preferences dissociated from MUA and became more uniformly tuned, with circular variance equal to 0.32. ***D***, Dependence of $r_{\mathrm{MUA}\text{-}\gamma}$ (solid trace; $n = 129$ sites) and $r_{\gamma\text{-}\gamma}$ (dashed trace; $n = 2961$ pairs) on stimulus size.

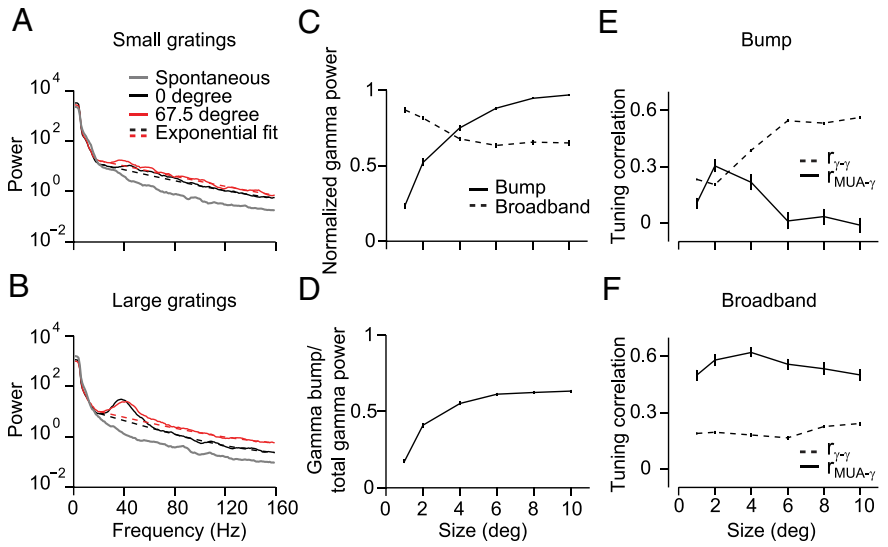

Figure 5. Two components of gamma power and their dependence on stimulus size. ***A***, ***B***, Power spectra of LFPs from one recording site, for large (10°; ***A***) and small (1°; ***B***) stimuli for two orientations (red and black lines) and spontaneous activity (gray lines). Estimate of broadband component of gamma power is provided by the exponential fit indicated with dashed lines. ***C***, Normalized power of the gamma bump and broadband component, as a function of stimulus size ($n = 129$ sites). ***D***, Proportion of total power attributable to the gamma bump. ***E***, ***F***, Dependence of $r_{MUA\text{-}\gamma}$ (solid trace; $n = 129$ sites) and $r_{\gamma\text{-}\gamma}$ (dashed trace; $n = 2961$ pairs), for the gamma bump (***E***) and broadband component (***F***), on stimulus size.

often distinct from neighboring frequencies, suggesting a distinct origin.

We estimated the strength of the broadband component of gamma using an exponential fit to the power measured between 20–26 and 80–160 Hz (outside the range of gamma) (Fig. 5*A*,*B*, dashed lines). For activity induced by small stimuli, this fit captured 92 ± 2% of the variance in the spectra over the 20–160 Hz range. The gamma power estimated by this fit was 87 ± 1% of that measured, and it was strongly correlated with the measured gamma across orientations ($r = 0.64 \pm 0.02$). The remaining power—that exceeding this prediction—we refer to as the gamma bump. The broadband component of gamma decreased for larger stimuli (Fig. 5*C*), much like spiking activity (Fig. 4*A*); the gamma bump, however, grew with stimulus size (Fig. 5*C*). The proportion of total gamma power attributable to the bump thus increased with stimulus size (Fig. 5*D*).

To compare the tuning of these two components of gamma and their relationship to local spiking activity, we calculated $r_{MUA\text{-}\gamma}$ and $r_{\gamma\text{-}\gamma}$ separately for each component (Fig. 5*E*,*F*). We found that the gamma bump for large stimuli (for which it was most accurately measured) had a similar preference across sites ($r_{\gamma\text{-}\gamma}$ of 0.56 ± 0.007) and thus a distinct preference from local spiking activity ($r_{MUA\text{-}\gamma}$ of −0.01 ± 0.04). The broadband component of gamma, however, was always similarly tuned to local spiking activity ($r_{MUA\text{-}\gamma}$ ranging 0.50 to 0.62) and thus tuning across sites was only weakly correlated ($r_{\gamma\text{-}\gamma}$ ranging from 0.18 to 0.24).

We conclude that there is a component of gamma that arises from broadband changes in power. This component behaves similarly to local spiking activity. Large stimuli induce a second component, which has a shared preference across millimeters of cortex. The flexible relationship between the tuning of gamma and local spiking activity, revealed by changes in stimulus size, can be explained by the relative contribution of these two components to total gamma power.

Manipulations that do not alter stimulus size can also change the preference of gamma

Manipulating stimulus size shows that the preference of gamma and its relationship to local spiking activity are flexible, but leaves unclear when gamma is likely to display a shared preference across sites. It could be that shared tuning involves mechanisms that are recruited whenever an extensive region of cortex is visually driven, as with large gratings. Alternatively, shared tuning may occur because of the gamma bump induced by such stimuli. If so, manipulations that reduce the power of this component—without altering the extent of visually driven cortex—would be expected to result in tuning similar to that of local multiunit activity.

To distinguish between these possibilities, we manipulated gamma power by masking large gratings with noise (Zhou et al., 2008). This manipulation had a limited effect on V1 firing rate, with the response evoked by unmasked gratings and those masked with 80% noise being nearly indistinguishable in strength (Fig. 6*A*, dashed trace): the mean firing rate across stimuli was 8.9 ± 0.7 spikes/s for unperturbed grating compared with 8.4 ± 0.7 for those masked with 80% noise ($n = 248$ sites in 3 implants). With high levels of noise, however, gamma power was reduced more than twofold (Fig. 6*A*) (from a normalized value of 0.99 ± 3E-4 to 0.42 ± 5E-3; $n = 248$ sites) (for related findings, see Lima et al., 2010). This was due primarily to a loss of the gamma bump, as evident in the small proportion of the total power provided by this component with high masking noise (Fig. 6*B*).

The relationship between the tuning of gamma and local spiking activity depended on the strength of masking noise. Figure 6*C* shows the orientation preference for one array at three noise levels. For unmasked gratings (0% noise; top panel), the preference of gamma was similar across sites (σ^2 of 0.12 and $r_{\gamma\text{-}\gamma}$ of 0.67) and distinct from local multiunit activity ($r_{MUA\text{-}\gamma}$ of 0.15). With high masking noise (80% noise; bottom panel), the tuning of the two signals became more similar ($r_{MUA\text{-}\gamma}$ of 0.56), and, thus, the preference of gamma was no longer shared across sites (σ^2 of 0.59 and $r_{\gamma\text{-}\gamma}$ of 0.33). Across implants, as masking noise was increased, $r_{\gamma\text{-}\gamma}$ decreased from 0.74 ± 3E-3 to 0.48 ± 2E-3; $p \ll 0.001$; $n = 8911$ pairs of sites) and gamma became more similarly tuned to the local MUA ($r_{MUA\text{-}\gamma}$ increased from 0.14 ± 0.02 to 0.46 ± 0.02; $p \ll 0.001$; $n = 228$ sites).

These results show that noise masking disrupts the gamma bump induced by large stimuli and results in gamma whose tuning is similar to local spiking activity. Compared with manipulations of stimulus size, masking required a larger decrease in gamma power to generate a signal with similar preference to local spiking activity: it is only at the highest level of masking noise, when the gamma bump is nearly entirely suppressed (Fig. 6*B*), that the two signals become more similarly tuned. Thus, while the trends for size and noise masking manipulations are similar, the point at which gamma switches from a shared preference to a local one is different. This is presumably because of numerous differences in the drive provided by these two stimuli. Neverthe-

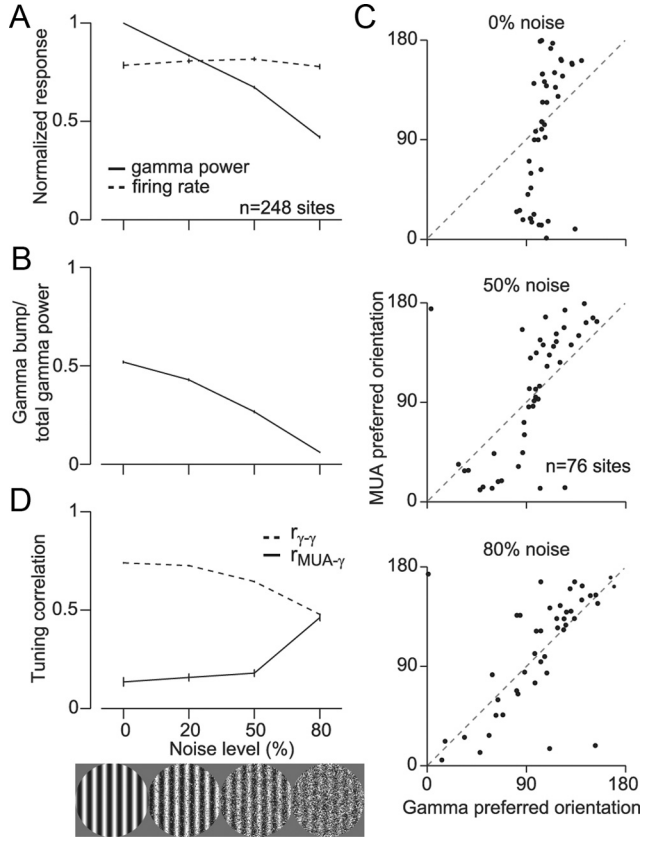

Figure 6. Masking noise modulates gamma power and its tuning. ***A***, Effect of masking noise on normalized gamma power (solid trace; $n = 248$ sites) and firing rate (dashed trace). ***B***, Proportion of total power attributable to the gamma bump. ***C***, Comparison of orientation preference of gamma and MUA for three noise levels ($n = 76$ sites in one array). Gamma is more dissociated from local spiking activity when the gamma bump is more prominent. ***D***, Dependence of $r_{MUA\text{-}\gamma}$ (solid trace; $n = 228$ sites) and $r_{\gamma\text{-}\gamma}$ (dashed trace; $n = 8911$ pairs; error bars are smaller than the line thickness) on the amount of masking noise. Stimuli size is 10°. Representation of stimuli is shown at the bottom.

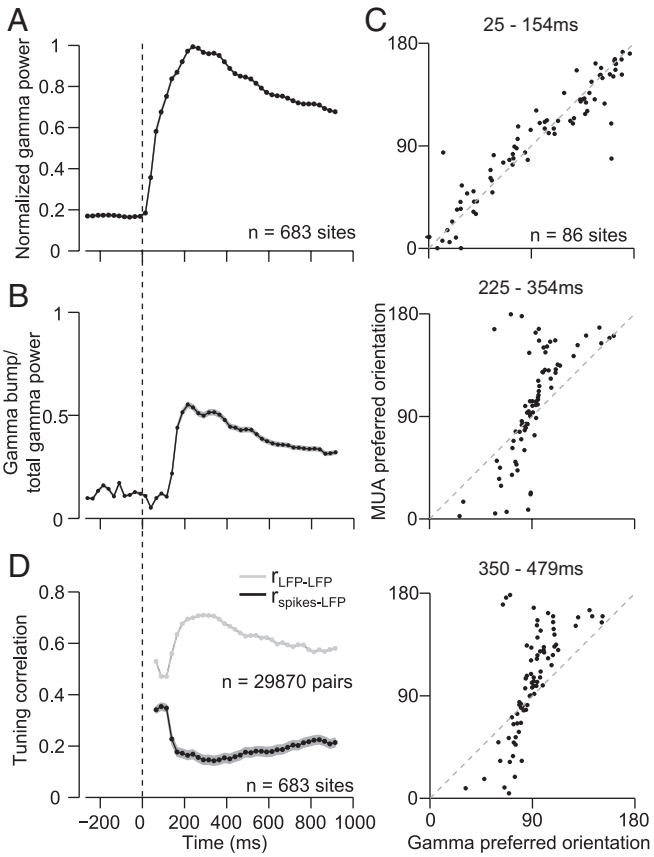

Figure 7. Dynamics of gamma power and its tuning. ***A***, Population average of normalized gamma power, as a function of time relative to stimulus onset ($n = 683$ sites; error bars are smaller than the line thickness). Power peaks around 250 ms after stimulus onset. Each point represents the center of one epoch (129 ms window). The dashed vertical line, to facilitate comparisons across plots, indicates stimulus onset at 0 ms. ***B***, Dynamics of the proportion of total power attributable to the gamma bump. ***C***, Orientation preference of gamma and MUA for epochs 25–154, 225–354, and 350 – 479 ms after stimulus onset ($n = 86$ sites). ***D***, Dynamics of $r_{MUA\text{-}\gamma}$ (black; $n = 683$ sites) and $r_{\gamma\text{-}\gamma}$ (gray trace; $n = 29{,}870$ pairs; error bars are smaller than the line thickness). Negative values indicate time before stimulus onset.

less, our masking results clearly show that the change in the tuning of gamma does not require reducing stimulus size or the spatial extent of activated cortex.

To test further the flexible relationship between the tuning of gamma and local spiking activity, we made use of the slow buildup of induced gamma after stimulus onset (Bauer et al., 1995; Ray and Maunsell, 2010). We analyzed responses to large gratings drifting in different directions, with interleaved blank stimuli, using a sliding window (129 ms epoch length with 25 ms steps). Gamma power increased soon after stimulus onset (Fig. 7*A*, vertical dashed line) but reached its maximum ~250 ms later, on average ($n = 683$ sites). The proportion of power attributable to the gamma bump reached its maximum at a similar time, but its onset was delayed, revealing that the initial enhancement of gamma reflects a broadband increase in power (Fig. 7*B*).

During the initial epoch of the response (25–154 ms after stimulus onset) (Fig. 7*C*, top), gamma tuning was well matched to the local spiking activity ($r_{MUA\text{-}\gamma}$ of 0.47) and had a wide range of preferences (σ^2 of 0.87). In later epochs, gamma tuning changed to a common preference across sites (σ^2 of 0.25 for the epoch from 350 to 479 ms). Across implants, we found that $r_{\gamma\text{-}\gamma}$ increased markedly over the first few hundred milliseconds of response (from 0.47 ± 2E-3 to 0.71 ± 2E-3; $p \ll 0.001$) (Fig. 7*D*, gray line). Over the same period, $r_{MUA\text{-}\gamma}$ fell more than twofold (from 0.35 ± 0.01 to 0.14 ± 0.02; $p \ll 0.001$) (Fig. 7*D*, black line). The relationship between the tuning of gamma and local MUA is thus dynamic, and these dynamics mirror the relative contribution of the gamma bump to its total power.

In conclusion, there are two components to stimulus-induced increases in gamma power, and the relative weight of these determines the relationship between gamma tuning and that of local spiking activity. Stimuli that induce strong gamma bumps (large, unperturbed gratings) result in similar tuning across sites and a preference that is distinct from that of local MUA. Small gratings, or those masked with noise, induce gamma that arises from a broadband increase in power, resulting in a signal with similar tuning to the local spiking response. Similarly, the dynamic relationship between the tuning of gamma and local spiking activity reveals that, as the contribution of the gamma bump to total gamma power increases, the preference of gamma switches from that of the local MUA to a common orientation across sites.

Spatial coherence of the gamma rhythm

When gamma power is high and the spectral bump prominent, tuning is similar across sites. This suggests that, under these conditions, the preference of locally measured signals arises from a shared rhythm. To test this directly, we measured the spatial coherence and phase difference of gamma across sites, for different

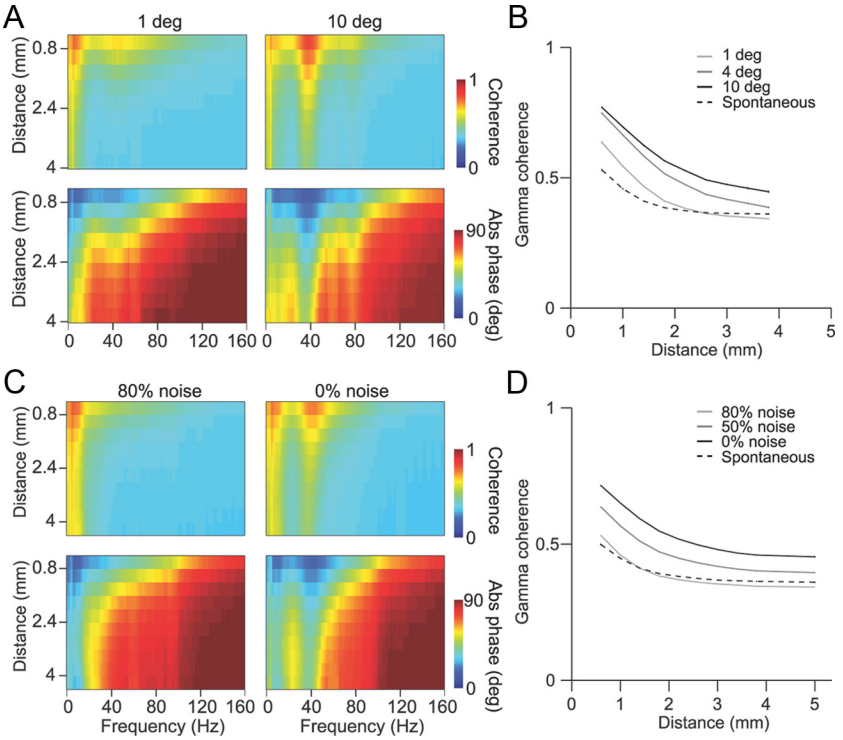

Figure 8. Dependence of gamma coherence and phase alignment on distance. ***A***, Coherence (top panels) and absolute phase difference (bottom panels) of the LFP, as a function of the distance between recording sites ($n = 2961$ pairs). Results are shown for signals induced by small gratings (1°; left) and large gratings (10°, averaged across stimulus orientations; right). Gamma coherence is weak and has a limited spatial extent when stimuli are small; gamma coherence increases markedly in both magnitude and spatial extent when stimuli are large, especially for the preferred orientation, and gamma activity shows a smaller phase difference across sites. ***B***, Coherence of gamma (averaged across orientations) induced by 1, 4, and 10° gratings as a function of distance between recording sites, compared with that observed in the absence of visual stimulation (spontaneous; dashed line). Error bars, where not visible, are within the line thickness. ***C***, Coherence (top panel) and absolute phase difference (bottom panel) of LFPs induced by 80% noise masked large grating ($n = 9891$ pairs; left) and unperturbed large gratings (right). ***D***, Coherence of gamma induced by 50 and 80% noise-masked and unperturbed gratings as a function of distance, compared with that observed for spontaneous activity.

stimulus conditions. A shared gamma rhythm would be indicated by higher coherence and smaller phase offsets.

We computed the coherence between signals induced by both large and small stimuli ($n = 2961$ pairs; averaging across different stimulus orientations), using the same set of driven sites. Small gratings (1°) induced a small increase in gamma coherence, relative to spontaneous conditions, with a limited spatial extent of ~2 mm (Fig. 8*A*, left column; *B*). Large gratings induced a more substantial increase in coherence and signals were also more phase aligned (Fig. 8*A*, right column). This enhanced coherence extended across all measured distances (Fig. 8*B*) and decayed more slowly for large gratings than small ones (exponential decay with a space constant of 1.6 mm, compared with 1.0 mm for small gratings). The enhanced coherence for activity induced by large gratings was strongest for the shared, preferred orientation (data not shown).

We also compared coherence for large, unperturbed gratings with those masked with noise. Gamma coherence was weaker and more localized for signals induced by masked gratings (Fig. 8*C*, left column; *D*) ($n = 9891$ pairs). For 80% masking noise, coherence was nearly indistinguishable from that measured under spontaneous conditions (without stimulus drive), although gamma and spiking responses were selective for such stimuli (as evidenced by the enhanced value of $r_{\mathrm{MUA}\text{-}\gamma}$ in Fig. 6).

Our coherence analysis suggests that large gratings induce a single, global gamma rhythm with little phase lag across sites. If so, gamma activity should be maintained after averaging the signals recorded at different sites on each trial—a signal we term the global LFP. Figure 9*A* shows single-trial examples of the global LFP induced by large (10°; top) and small (1°; bottom) gratings of the same orientation, averaged across the same sites. The large stimulus induced a prominent gamma rhythm; this was absent from the signal induced by the small stimulus. This result was not due to an undue influence of the signal recorded at a few electrodes, as *Z*-scoring the LFP before averaging yielded essentially identical results. We quantified the power in the global LFP for all frequencies and stimulus sizes we presented ($n = 3$ implants) (Fig. 9*B*). For small gratings, gamma components of the global LFP had minimal power. For larger stimuli, however, power in the gamma band increased nearly sixfold over the range measured. Other frequency bands did not show this behavior. The global LFP showed strong orientation selectivity for gamma power induced by large but not small stimuli (Fig. 9*C*). Across implants ($n = 3$), the selectivity of the gamma component of the global LFP was 0.32 ± 0.08, comparable with the selectivity at each individual site (0.37 ± 0.01), and its preferred orientation closely matched the mean preference of signals measured at individual sites (mean offset of 1.7 ± 0.7°; $n = 8$ implants).

Together, these results show that the gamma measured at each electrode reflects a spatially extensive rhythm, when activity is induced by large but not small gratings. The power in this signal is stronger for some orientations than others, giving rise to a common preference across sites. A potential explanation for the extensive coherence of gamma induced by large stimuli is that it reflects volume conduction, which could in principle explain its similar tuning across sites as well (i.e., if the signal measured by each electrode reflects a spatial average of distantly generated gamma signals). Several pieces of evidence argue against this. First, recent estimates of volume conduction suggest it is limited to 250 μm (Xing et al., 2009), ~20-fold smaller than the extent of spatially coherent gamma that we observe. Consistent with this, annular gratings induce no gamma power at sites where spiking activity is not elevated (Gieselmann and Thiele, 2008) (X. Jia and A. Kohn, unpublished observations), showing that gamma from distant sites does not passively propagate over large distances. Second, because high-amplitude signals should conduct more effectively (i.e., remain measurable despite the attenuation associated with passive propagation through the extracellular space), one would expect low frequencies to be more coherent than gamma frequencies, as their power is substantially higher (Fig. 1*B*). However, when induced by large gratings, gamma was slightly more coherent than low frequencies (Fig. 8*A*) (mean of 0.599 ± 0.002 for gamma vs 0.583 ± 0.002 for frequencies <10 Hz), although gamma power was 26-fold lower. Note also that the change in the preference and coherence of gamma with stimulus conditions

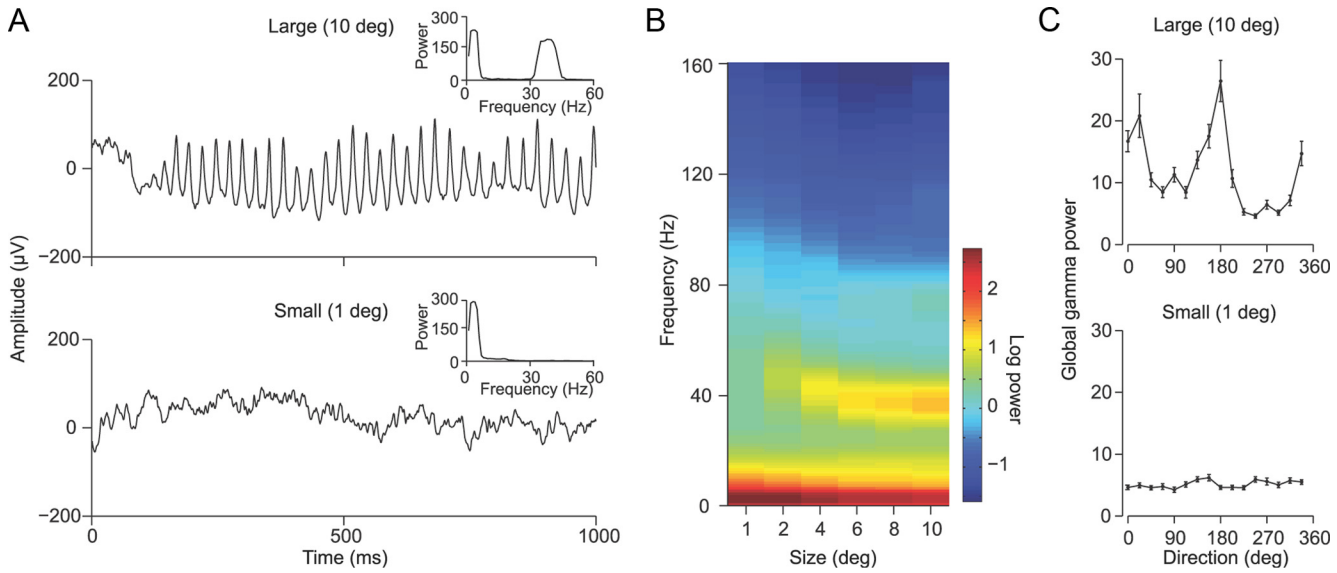

Figure 9. The global LFP. ***A***, Single trial examples of the global LFP averaged across 31 sites of one implant, for activity induced by a large (top) and small (bottom) stimulus of the same orientation. The insets show the power spectrum of the signal. ***B***, Average of the global LFP power spectra for different sizes ($n = 3$ implants). Value indicated is the average across orientations. ***C***, Orientation tuning of the gamma component of the global LFP, for 10° (top) and 1° (bottom) stimuli of an array implant.

involved roughly twofold changes in power (Figs. 4*A*, 6*A*). It seems unlikely that this would result in a signal whose tuning was different at sites separated by 400 μm, in one case, but shared up to 9 mm in another. Third, when a strong gamma rhythm is induced, spike–spike coherence in gamma frequencies is elevated across the array (Jia et al., 2011). Since volume-conducted fields have little influence on membrane potential—compared with those locally generated—the enhanced coordination of neuronal activity argues strongly against an important contribution of volume conduction (Bauer et al., 2007). Fourth, if the gamma rhythm induced by large gratings involved simple volume conduction of distant signals, one would expect little or no selectivity, because each site would represent the average of locally generated signals with different preferences. In fact, tuning was more selective for gamma induced by large gratings than small ones (as described above).

An adaptable bias underlies the preference of the global gamma rhythm

We have shown that large stimuli induce a spatially extensive gamma rhythm that is both well tuned and has a common preference across millimeters of cortex. We wondered why some orientations would induce a stronger rhythm than others, over such a large region. One possibility is that this preferred orientation reflects or magnifies a small bias in the neuronal representation of orientation. An obvious source for this bias would be the purported systematic overrepresentation of cardinal orientations in primary visual cortex (Li et al., 2003). However, we observed a shared preference for noncardinal orientations in a number of implants, such as those in Figure 2, *C* and *D*. Alternatively, the shared preference could arise from an inhomogeneous representation within a more limited region, such as the bias seen in fMRI voxels that are orientation-tuned despite reflecting activity averaged over several (or even many) cubic millimeters (Kamitani and Tong, 2005; Haynes and Rees, 2006).

We attempted to detect this potential representational bias with our neuronal recordings by comparing the preference of the gamma induced by large gratings to the most common preference of the spiking activity detected by our array. Figure 10*A* shows the range of MUA preferences from one array ($\sigma^2 = 0.88$; $n = 89$ sites, arranged according to their position on the array), measured with large gratings. Figure 10*B* shows the orientation preference of gamma from the same array, with its characteristic narrow distribution of preferences ($\sigma^2 = 0.26$). In this implant, there is no obvious relationship between the preference distribution of gamma and that of the recorded spiking responses: the preferred orientation of gamma is near 0°, but there is no bias for this orientation in the spiking responses. We quantified this relationship by computing the correlation between the population-averaged tuning of MUA and gamma, after normalizing the data for each site by the maximal response. For the example implant, this correlation was 0.28 (Fig. 10*C*). Across implants the mean correlation was 0.27 ± 0.24 ($n = 8$), not significantly different from zero ($p = 0.72$). We were thus unable to detect a bias in the spiking representation of orientation that could underlie the shared preference of gamma. However, this failure is perhaps not surprising given the limited sample of recording sites provided by the array.

Because we could not observe a relationship between the preferences of the sampled spiking activity and the shared preference of gamma, we used an alternative strategy of manipulating the representation of orientation with adaptation. Adaptation is well known to reduce the responsivity of cortical neurons whose preferences match the adapter and to have little effect on cells with offset preferences (Kohn, 2007). If gamma magnifies a presumed bias in the neuronal representation of orientation, adaptation-induced changes in neuronal response should have a strong consequence for gamma tuning.

We measured tuning with our standard grating stimuli, before and after adapting with a single orientation for 40 s. To maintain the effects of adaptation, we used brief (5 s) "top-up" adaptation between test stimuli (Fig. 11*A*). An illustration of how adaptation affects the orientation preference of gamma is shown in Figure 11*B* for a recording in which the adapter (indicated by the arrow) was well aligned with the most commonly preferred orientation. Adaptation caused a striking shift in the preference of gamma to

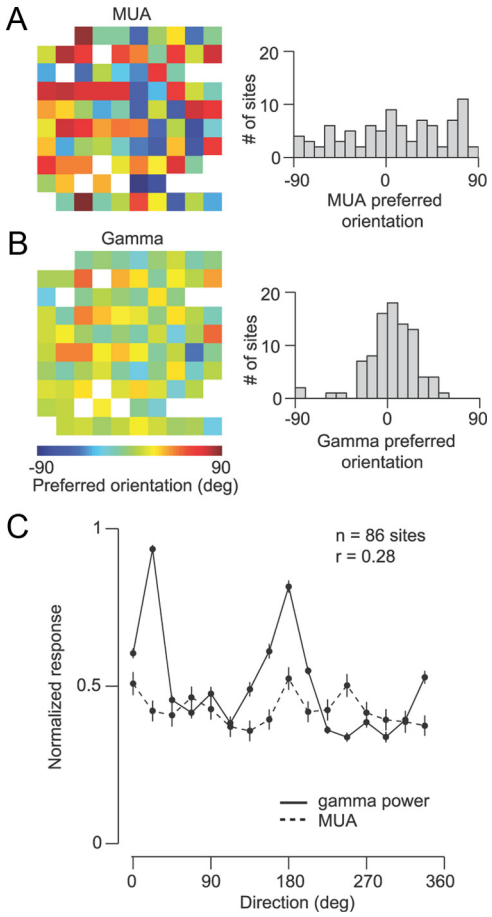

Figure 10. Relationship between neuronal preferences sampled by the array and the preference of gamma. ***A***, MUA orientation preferences plotted according to electrode positions on the array (left) and corresponding distribution (right). ***B***, Gamma preferences from the same array as in ***A*** and their distribution ($n = 86$ sites). ***C***, Population tuning curves of MUA (dashed) and gamma (solid) calculated by averaging normalized tuning curves of all sites from the same array. The two tuning curves are only weakly related, with a correlation of 0.28.

the orthogonal orientation (mean offset increasing from 20.7 ± 1.9° to 65.4 ± 2.5°; $p \ll 0.001$). After a period of several minutes without visual stimulation, the distribution of preferences nearly fully recovered to its preadaptation form. Across implants ($n = 8$), there was a pronounced tendency for the preference to shift toward the orientation orthogonal to the adapter (Fig. 11*C*). In those cases in which the preference was nearly orthogonal to the adapter before adaptation, we observed smaller shifts.

A similar effect of adaptation was visible in the population tuning curves, computed by averaging data from sites with similar preadaptation preferences (bins of 22.5°) after normalizing the responses at each site by its maximum. Adaptation caused a dramatic shift of preference to the orthogonal orientation when the adapter was well matched to the initial preference (Fig. 11*D*, top) ($n = 127$ sites; shift of 65.4°). This was due to a strong suppression of the gamma induced by stimuli similar to the adapter, and a facilitation of the signal induced by orthogonal orientations. In recordings for which the preadaptation gamma preference was orthogonal to the adapter, these effects led to little change in preference but a clearer shared tuning (Fig. 11*D*, bottom) ($n = 138$ sites; shift of 4.0°). These results suggest that the global gamma rhythm is extremely sensitive to adaptation-induced changes in neural representation, consistent with its preference magnifying a weak bias in that representation.

We tested our explanation for the shared preference of gamma in an additional, independent manner: by measuring tuning for grating spatial and temporal frequency. Whereas the representation of orientation would be expected to be at most weakly biased, neuronal preferences for spatial and temporal frequency are well known to be nonuniformly distributed (Foster et al., 1985; Hawken et al., 1996; O'Keefe et al., 1998). We reasoned that, if a biased representation underlies the preference of gamma, its tuning for spatial and temporal frequency should be similar both across sites and implants.

We measured tuning using large gratings drifting at a fixed drift rate (6.25 cycles/s) and with spatial frequencies ranging from 0.1 to 8.6 cpd, or with a fixed spatial frequency (1 cpd) and a range of drift rates (0.3–25 cycles/s). Sites for which the minimal response was not at least 50% smaller than the peak response were deemed untuned (Foster et al., 1985) (6.3% of 567 MUA sites for spatial frequency and 9.6% of 732 MUA sites for temporal fre-

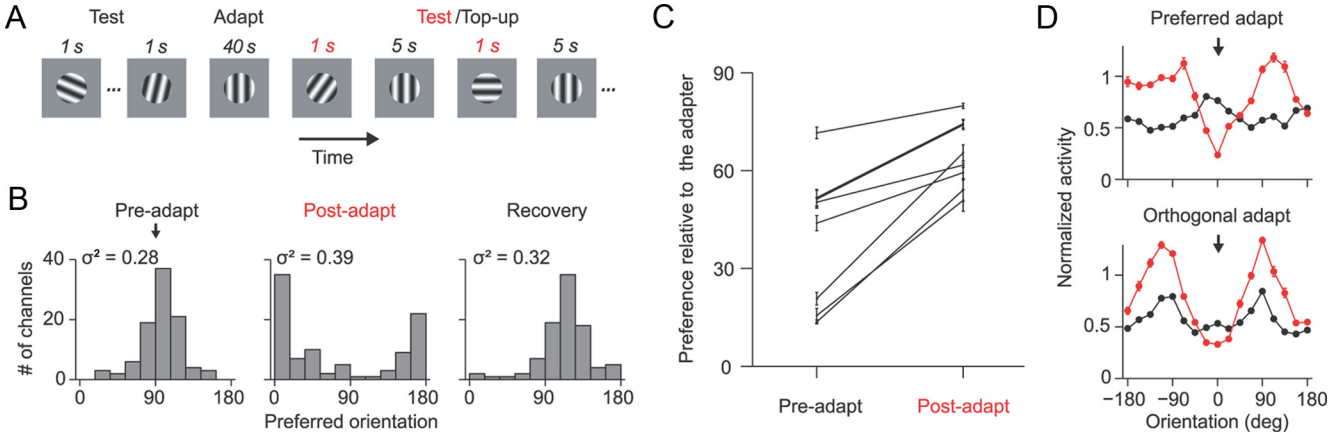

Figure 11. Effect of adaptation on the tuning of gamma. ***A***, Illustration of the adaptation protocol. ***B***, Distributions (from a single implant) of orientation preference for preadaptation, postadaptation, and recovery periods for gamma (top) and MUA (bottom). The circular variance is indicated at the top left of each histogram. The arrow indicates the orientation of the adapter. ***C***, Quantification of mean orientation preference of gamma, relative to the adapter, before and after adaptation ($n = 8$ implants). ***D***, Population-averaged orientation tuning curves before (black) and after (red) adaptation for gamma. All tuning curves are aligned so that 0 represents the adapting orientation (indicated by arrow). The top panels represent cases in which the tuning preference was within 22.5° of the adapter ($n = 127$ sites). The bottom panels are cases in which the preference was orthogonal to the adapter ($n = 138$ sites).

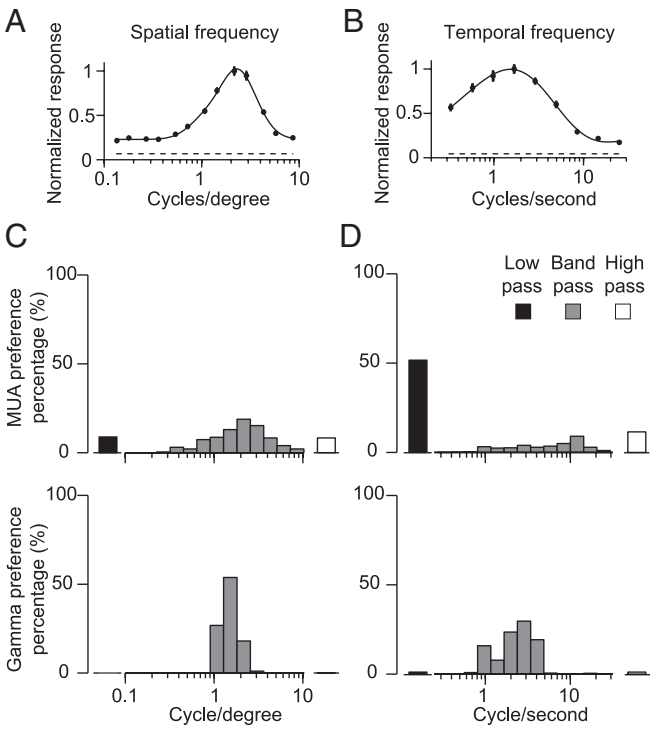

Figure 12. MUA and gamma tuning for stimulus spatial and temporal frequency. ***A***, An example of gamma tuning for spatial frequency for a single site. ***B***, Same as ***A*** for temporal frequency tuning. ***C***, Distribution of spatial frequency preferences across all implants (567 sites from 7 implants), for tuned sites of MUA (top) and gamma (bottom). ***D***, Same as ***C*** for temporal frequency preferences (732 sites from 9 implants).

quency). At selective sites, MUA often had high-pass or low-pass tuning (Fig. 12*C*,*D*) (7.9 and 9.1%, respectively, for spatial frequency; and 10.3 and 36.0% for temporal frequency), defined as a response at the lowest or highest measured frequency that was >75% of the peak response (Levitt et al., 1994; Movshon et al., 2005). At the remaining bandpass sites, we estimated the preference based on the fit of a difference-of-Gaussians function to the data. MUA had a wide range of spatial and temporal frequency preferences (Fig. 12*C*,*D*).

Unlike the tuning of MUA, gamma power had bandpass tuning for both stimulus parameters at almost all sites (Fig. 12*A*,*B*) (99.8% of sites for spatial frequency tuning and 97.8% for temporal frequency). There were no untuned gamma sites. Remarkably, gamma preferences for spatial and temporal frequency were similar across sites and implants (Fig. 12*C*,*D*). For instance, across 567 sites recorded in seven implants, 86% of sites preferred a spatial frequency between 1 and 3 cpd; for MUA, these preferences were most common but they accounted for only 29% of sites. The similarity of spatial and temporal frequency tuning of gamma, across sites and implants, is consistent with its preference arising from the biased representation for these stimulus features.

Discussion

To determine the spatial extent of gamma and its relationship to spiking activity, we recorded LFPs and MUA simultaneously in the upper layers of macaque V1. We found that gamma could have similar tuning to local spiking activity, when it reflected a broadband increase in power. Under other conditions, gamma could form a coherent, spatially extensive rhythm with similar tuning across millimeters of cortex. This latter behavior was evident for stimuli that induced a distinct spectral bump, a signal that grew slowly after stimulus onset and that could be disrupted by reducing stimulus size, or using masking noise. Our results suggest two distinct components to gamma power, with very different relationships to neuronal activity. The relative weight of these two components is stimulus dependent, resulting in a flexible relationship between the tuning of gamma power and local spiking activity.

This flexible relationship offers an explanation for previous disparate findings. Some previous comparisons of the tuning of gamma and local MUA have found matched preferences, but others have not. This has led to estimates that gamma reflects activity within 250 μm up to 3 mm of the electrode (Gray and Singer, 1989; Kreiman et al., 2006; Liu and Newsome, 2006; Berens et al., 2008; Gieselmann and Thiele, 2008). Our findings show stimulus conditions under which each of these descriptions is accurate. Similarly, studies of the relationship between gamma and the BOLD fMRI signal have found both strong correlation [Kayser et al., 2004; Goense and Logothetis, 2008 (who both used prolonged presentations of large gratings)] and a weak one [Maier et al., 2008 (who used briefly flashed noise stimuli)]. These differences could be explained by the two components of gamma we observe, assuming the global gamma rhythm is more directly related to the macroscopic measurement afforded by BOLD. More generally, our results emphasize that one must carefully consider stimulus properties—and the relative weight of broadband increases in power to the spectral bump—in understanding and interpreting the behavior of gamma.

When induced by large gratings, gamma is coherent over millimeters of cortex, consistent with previous studies (Juergens et al., 1999; Frien and Eckhorn, 2000; Leopold et al., 2003). Despite this spatial extent, it remains remarkably well tuned. Our observations thus reconcile previous work emphasizing the extent of gamma coherence with seemingly inconsistent claims that gamma is well tuned. Importantly, our results show that inferring the spatial extent of gamma rhythms from their selectivity is problematic: a well tuned signal does not mean a local one. Only by measuring tuning and coherence across sites—a novel feature of our study—can one accurately determine the extent and functional specificity of gamma rhythms.

Our findings do not contradict recent reports that the evoked LFP reflects neural activity within 250 μm of recording site (Katzner et al., 2009) and that the passive propagation of extracellular fields has a similarly limited spatial extent (Xing et al., 2009). We focused on an induced signal whose extent is influenced by passive propagation but ultimately determined by the circuits generating it. Katzner et al. (2009) did compare the orientation tuning of the induced and evoked LFP and concluded they were similar. However, activity was driven by brief stimuli (32 ms) that do not induce a strong gamma rhythm (Fig. 7) (Kruse and Eckhorn, 1996). To be sure that our different conclusions concerning induced gamma were not due to other factors, we recorded responses to similarly brief (40 ms) presentations and confirmed that the induced gamma power is weak, contains little evidence of a bump, and that both this signal and the evoked response are similarly tuned to local MUA (data not shown), entirely consistent with Katzner et al. (2009).

A previous study by Berens et al. (2008) conducted in awake macaque V1 using large gratings, reported findings similar to a subset of ours. Namely, they found that the orientation preference of gamma was similar across nearby sites (separated by 1 mm or less) and inferred that gamma reflects activity within 500–1000 μm of the electrode tip, due to a combination of extensive circuits generating the rhythm and the volume conduction of

those signals. Our interpretation differs from theirs in part because we show that gamma power consists of two components. Shared tuning across sites is not a fixed property of gamma; it occurs only when a prominent bump is induced. Furthermore, our data suggest that, when tuning is similar across sites, this is not due to simple volume conduction of nearby signals (for reasons described in Results), but rather because of the formation of a spatially extensive, coherent rhythm. Our different interpretation arises because we considered a wider range of stimulus manipulations (size, noise masking, dynamics, and spatial and temporal frequency), sampled across a ~10-fold higher range of distances, and because we analyzed both coherence and tuning across sites.

Berens et al. (2008) also reported that the selectivity of gamma is positively correlated with its similarity to local spiking activity. They propose that this relationship reflects the spatially extensive ensemble contributing to gamma and whether the recording site is situated in an iso-orientation domain (similar preference to MUA and high selectivity) or at a pinwheel center. We observe a similar relationship between selectivity and the match to local MUA (Jia and Kohn, unpublished observations), even when gamma was induced by large gratings and extends over many pinwheels. In this case, the correlation may arise because when gamma preference is matched to local spiking activity, the gamma bump and its broadband component will have a similar preference, resulting in higher selectivity; at sites where gamma is different from local spiking activity, these two components will have different preferences, resulting in weaker selectivity.

Mechanisms

The mechanisms of gamma generation have been studied extensively, both in the hippocampus and neocortex. GABAergic interneurons have been shown to play a critical role in generating gamma (Whittington et al., 1995, 2011; Traub et al., 1996a; Hasenstaub et al., 2005; Bartos et al., 2007; Atallah and Scanziani, 2009; Cardin et al., 2009), and this is perhaps enhanced by interactions with excitatory neurons (Buzsaki, 2006; Tiesinga and Sejnowski, 2009). In cortex, "chattering cells" may also contribute (Gray and McCormick, 1996; Cunningham et al., 2004).

These mechanisms do not appear to contribute strongly to the gamma induced by small stimuli and large, masked gratings, or at response onset. This is because gamma in these cases reflects a broadband increase in power, rather than a mechanism specific to gamma frequencies (Ray and Maunsell, 2010). Instead, the broadband increase in power likely arises from a general elevation of synaptic and spiking activity in local circuits because this signal behaves similarly to local MUA (e.g., similar orientation tuning and suppression by large gratings). This component of gamma may also include direct spectral contamination of the LFP by spiking activity, although previous work suggests this is limited to frequency components >50 Hz (David et al., 2010; Zanos et al., 2011).

The traditional inhibitory (or excitatory–inhibitory) mechanisms of gamma generation presumably do underlie the spectral bump we observe for activity induced by large stimuli. However, the global nature of this rhythm suggests additional spatially extensive mechanisms that coordinate or drive this inhibitory network. One possibility is that this involves feedback connections, which extend over long distances and are thought to contribute to the surround suppression recruited by large stimuli (Bair et al., 2003; Angelucci and Bressloff, 2006). Alternatively, the global gamma rhythm may be an emergent rhythm that involves the coordination of local generators through mechanisms such as long-range lateral connections or gap-junction coupling among inhibitory neurons (Traub et al., 1996b; Gibson et al., 1999; Buzsaki, 2006; Tiesinga and Sejnowski, 2009). Finally, the global gamma rhythm may arise from an altered balance between excitatory and inhibitory activity in cortex, because inhibitory cells may be only weakly surround suppressed (Brunel and Wang, 2003; Haider et al., 2010).

Whichever mechanisms contribute, they must be more effective for some stimuli than others, a property we suggest may be due to biased representations for these features (e.g., stronger feedback or an enhanced local representation). An intriguing possibility is that this bias involves a recently described overrepresentation of orientations corresponding to the radial position of the spatial receptive fields [a radial bias (Freeman et al., 2011)]. The sites we recorded represented similar positions in the visual field across animals, so one might expect to observe similar preferences. However, the gratings we used were positioned slightly differently in each animal, and given the proximity of our recordings to the fovea, these small differences could alter the net bias in the recruited population. These explanations for our findings are, of course, speculative, and additional work is needed to address the mechanisms underlying the novel properties of gamma we report.

Functional role of gamma rhythms

Through its suggested influence on spike timing, gamma has been proposed to provide a temporal window for communication (Fries, 2009), encode the amplitude of stimulus drive in response phase (Fries et al., 2007), bind distributed representations (Gray, 1999), or dynamically route information (Pesaran et al., 2002; Colgin et al., 2009; Fries, 2009). The spatially extensive, coherent gamma rhythm we observe seems better suited for an integrative function than one that requires targeting specific subsets of neurons. For instance, the gamma induced by a large vertical grating is similar at sites where neurons prefer vertical or horizontal structure. Thus, it could not be expected to emphasize or group specific subset of neurons. Only when gamma power is limited (reflecting a broadband increase in power), is it spatially and functionally selective. However, precisely because it is weak, it is unlikely to have a strong influence on spike timing under these conditions (Sohal et al., 2009; Okun et al., 2010).

As an integrative signal, the global gamma rhythm could, in principle, function as an internal reference. For instance, it seems well suited to modulate spike timing in a large region of cortex. However, this rhythm is much stronger for some stimuli than others, in a patch of cortex representing several degrees of visual field. Unless perceptual performance is similarly biased, this would suggest a limited functional role, at least for stimulus-induced gamma activity in V1. Under this interpretation, the global gamma rhythm may simply be a resonant frequency arising from the interaction between excitation and inhibition (Burns et al., 2010; Ray and Maunsell, 2010), albeit one that can reflect a much more extensive ensemble than previously considered.

References

Angelucci A, Bressloff PC (2006) Contribution of feedforward, lateral and feedback connections to the classical receptive field center and extra-classical receptive field surround of primate V1 neurons. Prog Brain Res 154:93–120.

Atallah BV, Scanziani M (2009) Instantaneous modulation of gamma oscillation frequency by balancing excitation with inhibition. Neuron 62:566–577.

Bair W, Cavanaugh JR, Movshon JA (2003) Time course and time-distance relationships for surround suppression in macaque V1 neurons. J Neurosci 23:7690–7701.

Bartos M, Vida I, Jonas P (2007) Synaptic mechanisms of synchronized gamma oscillations in inhibitory interneuron networks. Nat Rev Neurosci 8:45–56.

Bauer EP, Paz R, Paré D (2007) Gamma oscillations coordinate amygdalorhinal interactions during learning. J Neurosci 27:9369–9379.

Bauer R, Brosch M, Eckhorn R (1995) Different rules of spatial summation from beyond the receptive field for spike rates and oscillation amplitudes in cat visual cortex. Brain Res 669:291–297.

Berens P, Keliris GA, Ecker AS, Logothetis NK, Tolias AS (2008) Feature selectivity of the gamma-band of the local field potential in primate primary visual cortex. Front Neurosci 2:199–207.

Brosch M, Budinger E, Scheich H (2002) Stimulus-related gamma oscillations in primate auditory cortex. J Neurophysiol 87:2715–2725.

Brunel N, Wang XJ (2003) What determines the frequency of fast network oscillations with irregular neural discharges? I. Synaptic dynamics and excitation-inhibition balance. J Neurophysiol 90:415–430.

Burns SP, Xing D, Shelley MJ, Shapley RM (2010) Searching for autocoherence in the cortical network with a time-frequency analysis of the local field potential. J Neurosci 30:4033–4047.

Buzsaki G (2006) Rhythms of the brain. New York: Oxford UP.

Cardin JA, Carlén M, Meletis K, Knoblich U, Zhang F, Deisseroth K, Tsai LH, and Moore CI (2009) Driving fast-spiking cells induces gamma rhythm and controls sensory responses. Nature 459:663–667.

Colgin LL, Denninger T, Fyhn M, Hafting T, Bonnevie T, Jensen O, Moser MB, Moser EI (2009) Frequency of gamma oscillations routes flow of information in the hippocampus. Nature 462:353–357.

Cunningham MO, Whittington MA, Bibbig A, Roopun A, LeBeau FE, Vogt A, Monyer H, Buhl EH, Traub RD (2004) A role for fast rhythmic bursting neurons in cortical gamma oscillations in vitro. Proc Natl Acad Sci U S A 101:7152–7157.

David SV, Malaval N, Shamma SA (2010) Decoupling action potential bias from cortical local field potentials. Comput Intell Neurosci 393019.

Foster KH, Gaska JP, Nagler M, Pollen DA (1985) Spatial and temporal frequency selectivity of neurones in visual cortical areas V1 and V2 of the macaque monkey. J Physiol 365:331–363.

Freeman J, Brouwer GJ, Heeger DJ, Merriam EP (2011) Orientation decoding depends on maps, not columns. J Neurosci 31:4792–4804.

Frien A, Eckhorn R (2000) Functional coupling shows stronger stimulus dependency for fast oscillations than for low-frequency components in striate cortex of awake monkey. Eur J Neurosci 12:1466–1478.

Frien A, Eckhorn R, Bauer R, Woelbern T, Gabriel A (2000) Fast oscillations display sharper orientation tuning than slower components of the same recordings in striate cortex of the awake monkey. Eur J Neurosci 12:1453–1465.

Fries P (2009) Neuronal gamma-band synchronization as a fundamental process in cortical computation. Annu Rev Neurosci 32:209–224.

Fries P, Nikolić D, Singer W (2007) The gamma cycle. Trends Neurosci 30:309–316.

Fries P, Womelsdorf T, Oostenveld R, Desimone R (2008) The effects of visual stimulation and selective visual attention on rhythmic neuronal synchronization in macaque area V4. J Neurosci 28:4823–4835.

Gail A, Brinksmeyer HJ, Eckhorn R (2004) Perception-related modulations of local field potential power and coherence in primary visual cortex of awake monkey during binocular rivalry. Cereb Cortex 14:300–313.

Gibson JR, Beierlein M, Connors BW (1999) Two networks of electrically coupled inhibitory neurons in neocortex. Nature 402:75–79.

Gieselmann MA, Thiele A (2008) Comparison of spatial integration and surround suppression characteristics in spiking activity and the local field potential in macaque V1. Eur J Neurosci 28:447–459.

Goense JB, Logothetis NK (2008) Neurophysiology of the BOLD fMRI signal in awake monkeys. Curr Biol 18:631–640.

Gray CM (1999) The temporal correlation hypothesis of visual feature integration: still alive and well. Neuron 24:31–47, 111–125.

Gray CM, McCormick DA (1996) Chattering cells: superficial pyramidal neurons contributing to the generation of synchronous oscillations in the visual cortex. Science 274:109–113.

Gray CM, Singer W (1989) Stimulus-specific neuronal oscillations in orientation columns of cat visual cortex. Proc Natl Acad Sci U S A 86:1698–1702.

Haider B, Krause MR, Duque A, Yu Y, Touryan J, Mazer JA, McCormick DA (2010) Synaptic and network mechanisms of sparse and reliable visual cortical activity during nonclassical receptive field stimulation. Neuron 65:107–121.

Hasenstaub A, Shu Y, Haider B, Kraushaar U, Duque A, McCormick DA (2005) Inhibitory postsynaptic potentials carry synchronized frequency information in active cortical networks. Neuron 47:423–435.

Hawken MJ, Shapley RM, Grosof DH (1996) Temporal-frequency selectivity in monkey visual cortex. Vis Neurosci 13:477–492.

Haynes JD, Rees G (2006) Decoding mental states from brain activity in humans. Nat Rev Neurosci 7:523–534.

Henrie JA, Shapley R (2005) LFP power spectra in V1 cortex: the graded effect of stimulus contrast. J Neurophysiol 94:479–490.

Hopfield JJ (2004) Encoding for computation: recognizing brief dynamical patterns by exploiting effects of weak rhythms on action-potential timing. Proc Natl Acad Sci U S A 101:6255–6260.

Jia X, Zandvakili A, Kohn A (2011) Gamma rhythms, neuronal synchrony, and corticocortical communication in early visual cortex. Paper presented at COSYNE 2011, Salt Lake City, February.

Juergens E, Guettler A, Eckhorn R (1999) Visual stimulation elicits locked and induced gamma oscillations in monkey intracortical- and EEG-potentials, but not in human EEG. Exp Brain Res 129:247–259.

Kamitani Y, Tong F (2005) Decoding the visual and subjective contents of the human brain. Nat Neurosci 8:679–685.

Katzner S, Nauhaus I, Benucci A, Bonin V, Ringach DL, Carandini M (2009) Local origin of field potentials in visual cortex. Neuron 61:35–41.

Kayser C, Kim M, Ugurbil K, Kim DS, König P (2004) A comparison of hemodynamic and neural responses in cat visual cortex using complex stimuli. Cereb Cortex 14:881–891.

Kohn A (2007) Visual adaptation: physiology, mechanisms, and functional benefits. J Neurophysiol 97:3155–3164.

Kreiman G, Hung CP, Kraskov A, Quiroga RQ, Poggio T, DiCarlo JJ (2006) Object selectivity of local field potentials and spikes in the macaque inferior temporal cortex. Neuron 49:433–445.

Kruse W, Eckhorn R (1996) Inhibition of sustained gamma oscillations (35–80 Hz) by fast transient responses in cat visual cortex. Proc Natl Acad Sci U S A 93:6112–6117.

Leopold DA, Murayama Y, Logothetis NK (2003) Very slow activity fluctuations in monkey visual cortex: implications for functional brain imaging. Cereb Cortex 13:422–433.

Leventhal AG, Thompson KG, Liu D, Zhou Y, Ault SJ (1995) Concomitant sensitivity to orientation, direction, and color of cells in layers 2, 3, and 4 of monkey striate cortex. J Neurosci 15:1808–1818.

Levitt JB, Kiper DC, Movshon JA (1994) Receptive fields and functional architecture of macaque V2. J Neurophysiol 71:2517–2542.

Li B, Peterson MR, Freeman RD (2003) Oblique effect: a neural basis in the visual cortex. J Neurophysiol 90:204–217.

Lima B, Singer W, Chen NH, Neuenschwander S (2010) Synchronization dynamics in response to plaid stimuli in monkey V1. Cereb Cortex 20:1556–1573.

Liu J, Newsome WT (2006) Local field potential in cortical area MT: stimulus tuning and behavioral correlations. J Neurosci 26:7779–7790.

Maier A, Wilke M, Aura C, Zhu C, Ye FQ, Leopold DA (2008) Divergence of fMRI and neural signals in V1 during perceptual suppression in the awake monkey. Nat Neurosci 11:1193–1200.

Mitra PP, Pesaran B (1999) Analysis of dynamic brain imaging data. Biophys J 76:691–708.

Mitzdorf U (1985) Current source-density method and application in cat cerebral cortex: investigation of evoked potentials and EEG phenomena. Physiol Rev 65:37–100.

Movshon JA, Kiorpes L, Hawken MJ, Cavanaugh JR (2005) Functional maturation of the macaque's lateral geniculate nucleus. J Neurosci 25:2712–2722.

Murthy VN, Fetz EE (1992) Coherent 25- to 35-Hz oscillations in the sensorimotor cortex of awake behaving monkeys. Proc Natl Acad Sci U S A 89:5670–5674.

O'Keefe LP, Levitt JB, Kiper DC, Shapley RM, Movshon JA (1998) Functional organization of owl monkey lateral geniculate nucleus and visual cortex. J Neurophysiol 80:594–609.

Okun M, Naim A, Lampl I (2010) The subthreshold relation between cortical local field potential and neuronal firing unveiled by intracellular recordings in awake rats. J Neurosci 30:4440–4448.

Pesaran B, Pezaris JS, Sahani M, Mitra PP, Andersen RA (2002) Temporal

structure in neuronal activity during working memory in macaque parietal cortex. Nat Neurosci 5:805–811.
Popescu AT, Popa D, Paré D (2009) Coherent gamma oscillations couple the amygdala and striatum during learning. Nat Neurosci 12:801–807.
Ray S, Maunsell JH (2010) Differences in gamma frequencies across visual cortex restrict their possible use in computation. Neuron 67:885–896.
Schoffelen JM, Oostenveld R, Fries P (2005) Neuronal coherence as a mechanism of effective corticospinal interaction. Science 308:111–113.
Siegel M, König P (2003) A functional gamma-band defined by stimulus-dependent synchronization in area 18 of awake behaving cats. J Neurosci 23:4251–4260.
Smith MA, Kohn A (2008) Spatial and temporal scales of neuronal correlation in primary visual cortex. J Neurosci 28:12591–12603.
Smith MA, Kelly RC, Lee TS (2007) Dynamics of response to perceptual pop-out stimuli in macaque V1. J Neurophysiol 98:3436–3449.
Sohal VS, Zhang F, Yizhar O, Deisseroth K (2009) Parvalbumin neurons and gamma rhythms enhance cortical circuit performance. Nature 459:698–702.
Tallon-Baudry C (2003) Oscillatory synchrony and human visual cognition. J Physiol Paris 97:355–363.
Tiesinga P, Sejnowski TJ (2009) Cortical enlightenment: are attentional gamma oscillations driven by ING or PING? Neuron 63:727–732.
Traub RD, Whittington MA, Colling SB, Buzsáki G, Jefferys JG (1996a) Analysis of gamma rhythms in the rat hippocampus in vitro and in vivo. J Physiol 493:471–484.
Traub RD, Whittington MA, Stanford IM, Jefferys JG (1996b) A mechanism for generation of long-range synchronous fast oscillations in the cortex. Nature 383:621–624.
Whittington MA, Traub RD, Jefferys JG (1995) Synchronized oscillations in interneuron networks driven by metabotropic glutamate receptor activation. Nature 373:612–615.
Whittington MA, Cunningham MO, LeBeau FE, Racca C, Traub RD (2011) Multiple origins of the cortical gamma rhythm. Dev Neurobiol 71:92–106.
Wilke M, Logothetis NK, Leopold DA (2006) Local field potential reflects perceptual suppression in monkey visual cortex. Proc Natl Acad Sci U S A 103:17507–17512.
Womelsdorf T, Fries P, Mitra PP, Desimone R (2006) Gamma-band synchronization in visual cortex predicts speed of change detection. Nature 439:733–736.
Xing D, Yeh CI, Shapley RM (2009) Spatial spread of the local field potential and its laminar variation in visual cortex. J Neurosci 29:11540–11549.
Zanos TP, Mineault PJ, Pack CC (2011) Removal of spurious correlations between spikes and local field potentials. J Neurophysiol 105:474–486.
Zhou Z, Bernard MR, Bonds AB (2008) Deconstruction of spatial integrity in visual stimulus detected by modulation of synchronized activity in cat visual cortex. J Neurosci 28:3759–3768.

References

1. Adrian, E.D. (1942). Olfactory reactions in the brain of the hedgehog. J Physiol *100*, 459-473.
2. Akam, T., and Kullmann, D.M. (2010). Oscillations and filtering networks support flexible routing of information. Neuron *67*, 308-320.
3. Albrecht, D.G., and Hamilton, D.B. (1982). Striate cortex of monkey and cat: contrast response function. J Neurophysiol *48*, 217-237.
4. Alonso, J.M., Usrey, W.M., and Reid, R.C. (1996). Precisely correlated firing in cells of the lateral geniculate nucleus. Nature *383*, 815-819.
5. Andersen, R.A., Snowden, R.J., Treue, S., and Graziano, M. (1990). Hierarchical processing of motion in the visual cortex of monkey. Cold Spring Harbor symposia on quantitative biology *55*, 741-748.
6. Angelucci, A., and Bressloff, P.C. (2006). Contribution of feedforward, lateral and feedback connections to the classical receptive field center and extra-classical receptive field surround of primate V1 neurons. Prog Brain Res *154*, 93-120.
7. Angelucci, A., Levitt, J.B., and Lund, J.S. (2002a). Anatomical origins of the classical receptive field and modulatory surround field of single neurons in macaque visual cortical area V1. Prog Brain Res *136*, 373-388.
8. Angelucci, A., Levitt, J.B., Walton, E.J., Hupe, J.M., Bullier, J., and Lund, J.S. (2002b). Circuits for local and global signal integration in primary visual cortex. J Neurosci *22*, 8633-8646.
9. Atallah, B.V., and Scanziani, M. (2009). Instantaneous modulation of gamma oscillation frequency by balancing excitation with inhibition. Neuron *62*, 566-577.
10. Babiloni, C., Ferri, R., Moretti, D.V., Strambi, A., Binetti, G., Dal Forno, G., Ferreri, F., Lanuzza, B., Bonato, C., Nobili, F.*, et al.* (2004a). Abnormal fronto-parietal coupling of brain rhythms in mild Alzheimer's disease: a multicentric EEG study. Eur J Neurosci *19*, 2583-2590.
11. Babiloni, C., Miniussi, C., Moretti, D.V., Vecchio, F., Salinari, S., Frisoni, G., and Rossini, P.M. (2004b). Cortical networks generating movement-related EEG rhythms in Alzheimer's disease: an EEG coherence study. Behav Neurosci *118*, 698-706.
12. Bair, W., Cavanaugh, J.R., and Movshon, J.A. (2003). Time course and time-distance relationships for surround suppression in macaque V1 neurons. J Neurosci *23*, 7690-7701.
13. Bair, W., Koch, C., Newsome, W., and Britten, K. (1994). Power spectrum analysis of bursting cells in area MT in the behaving monkey. J Neurosci *14*, 2870-2892.
14. Bair, W., Zohary, E., and Newsome, W.T. (2001). Correlated firing in macaque visual area MT: time scales and relationship to behavior. J Neurosci *21*, 1676-1697.

15. Barr, D.S., Lambert, N.A., Hoyt, K.L., Moore, S.D., and Wilson, W.A. (1995). Induction and reversal of long-term potentiation by low- and high-intensity theta pattern stimulation. J Neurosci *15*, 5402-5410.
16. Bartos, M., Vida, I., and Jonas, P. (2007). Synaptic mechanisms of synchronized gamma oscillations in inhibitory interneuron networks. Nat Rev Neurosci *8*, 45-56.
17. Bash, K.W. (1968). [On alpha conditions in relaxed wakefulness, dreams, hallucinosis, twilight state and psychosis]. Psychiatria clinica *1*, 152-174.
18. Bauer, E.P., Paz, R., and Pare, D. (2007). Gamma oscillations coordinate amygdalo-rhinal interactions during learning. J Neurosci *27*, 9369-9379.
19. Bauer, R., Brosch, M., and Eckhorn, R. (1995). Different rules of spatial summation from beyond the receptive field for spike rates and oscillation amplitudes in cat visual cortex. Brain Res *669*, 291-297.
20. Berens, P., Keliris, G.A., Ecker, A.S., Logothetis, N.K., and Tolias, A.S. (2008). Feature selectivity of the gamma-band of the local field potential in primate primary visual cortex. Front Neurosci *2*, 199-207.
21. Bland, B.H. (2004). The power of theta: providing insights into the role of the hippocampal formation in sensorimotor integration. Hippocampus *14*, 537-538.
22. Bland, B.H., Jackson, J., Derrie-Gillespie, D., Azad, T., Rickhi, A., and Abriam, J. (2006). Amplitude, frequency, and phase analysis of hippocampal theta during sensorimotor processing in a jump avoidance task. Hippocampus *16*, 673-681.
23. Bland, B.H., and Oddie, S.D. (2001). Theta band oscillation and synchrony in the hippocampal formation and associated structures: the case for its role in sensorimotor integration. Behav Brain Res *127*, 119-136.
24. Blasdel, G.G., and Salama, G. (1986). Voltage-sensitive dyes reveal a modular organization in monkey striate cortex. Nature *321*, 579-585.
25. Bonds, A.B. (1982). An "oblique effect" in the visual evoked potential of the cat. Exp Brain Res *46*, 151-154.
26. Bonhoeffer, T., and Grinvald, A. (1991). Iso-orientation domains in cat visual cortex are arranged in pinwheel-like patterns. Nature *353*, 429-431.
27. Borgers, C., Epstein, S., and Kopell, N.J. (2005). Background gamma rhythmicity and attention in cortical local circuits: a computational study. Proc Natl Acad Sci U S A *102*, 7002-7007.
28. Boynton, G.M., and Finney, E.M. (2003). Orientation-specific adaptation in human visual cortex. J Neurosci *23*, 8781-8787.
29. Bragin, A., Jando, G., Nadasdy, Z., Hetke, J., Wise, K., and Buzsaki, G. (1995). Gamma (40-100 Hz) oscillation in the hippocampus of the behaving rat. J Neurosci *15*, 47-60.
30. Brincat, S.L., and Connor, C.E. (2004). Underlying principles of visual shape selectivity in posterior inferotemporal cortex. Nat Neurosci *7*, 880-886.
31. Brosch, M., Budinger, E., and Scheich, H. (2002). Stimulus-related gamma oscillations in primate auditory cortex. J Neurophysiol *87*, 2715-2725.
32. Brunel, N., and Wang, X.J. (2003). What determines the frequency of fast network oscillations with irregular neural discharges? I. Synaptic dynamics and excitation-inhibition balance. J Neurophysiol *90*, 415-430.

33. Bruno, R.M., and Sakmann, B. (2006). Cortex is driven by weak but synchronously active thalamocortical synapses. Science *312*, 1622-1627.
34. Buhl, D.L., Harris, K.D., Hormuzdi, S.G., Monyer, H., and Buzsaki, G. (2003). Selective impairment of hippocampal gamma oscillations in connexin-36 knock-out mouse in vivo. J Neurosci *23*, 1013-1018.
35. Bullier, J., Hupe, J.M., James, A., and Girard, P. (1996). Functional interactions between areas V1 and V2 in the monkey. J Physiol Paris *90*, 217-220.
36. Burns, S.P., Xing, D., and Shapley, R.M. (2010a). Comparisons of the dynamics of local field potential and multiunit activity signals in macaque visual cortex. J Neurosci *30*, 13739-13749.
37. Burns, S.P., Xing, D., Shelley, M.J., and Shapley, R.M. (2010b). Searching for autocoherence in the cortical network with a time-frequency analysis of the local field potential. J Neurosci *30*, 4033-4047.
38. Buschman, T.J., and Miller, E.K. (2007). Top-down versus bottom-up control of attention in the prefrontal and posterior parietal cortices. Science *315*, 1860-1862.
39. Buxton, R.B., and Frank, L.R. (1997). A model for the coupling between cerebral blood flow and oxygen metabolism during neural stimulation. J Cereb Blood Flow Metab *17*, 64-72.
40. Buzsaki, G. (2006). Rhythms of the brain (New York: Oxford University Press).
41. Buzsaki, G., and Chrobak, J.J. (1995). Temporal structure in spatially organized neuronal ensembles: a role for interneuronal networks. Curr Opin Neurobiol *5*, 504-510.
42. Buzsaki, G., and Draguhn, A. (2004). Neuronal oscillations in cortical networks. Science *304*, 1926-1929.
43. Buzsaki, G., Leung, L.W., and Vanderwolf, C.H. (1983). Cellular bases of hippocampal EEG in the behaving rat. Brain Res *287*, 139-171.
44. Canolty, R.T., Edwards, E., Dalal, S.S., Soltani, M., Nagarajan, S.S., Kirsch, H.E., Berger, M.S., Barbaro, N.M., and Knight, R.T. (2006). High gamma power is phase-locked to theta oscillations in human neocortex. Science *313*, 1626-1628.
45. Cantero, J.L., Atienza, M., and Salas, R.M. (2000). Spectral features of EEG alpha activity in human REM sleep: two variants with different functional roles? Sleep *23*, 746-750.
46. Cantero, J.L., Atienza, M., Salas, R.M., and Gomez, C.M. (1999). Brain spatial microstates of human spontaneous alpha activity in relaxed wakefulness, drowsiness period, and REM sleep. Brain Topogr *11*, 257-263.
47. Cantero, J.L., Atienza, M., Stickgold, R., Kahana, M.J., Madsen, J.R., and Kocsis, B. (2003). Sleep-dependent theta oscillations in the human hippocampus and neocortex. J Neurosci *23*, 10897-10903.
48. Carandini, M., Heeger, D.J., and Movshon, J.A. (1997). Linearity and normalization in simple cells of the macaque primary visual cortex. J Neurosci *17*, 8621-8644.
49. Cardin, J.A., Carlen, M., Meletis, K., Knoblich, U., Zhang, F., Deisseroth, K., Tsai, L.H., and Moore, C.I. (2009). Driving fast-spiking cells induces gamma rhythm and controls sensory responses. Nature *459*, 663-667.

50. Castelo-Branco, M., Neuenschwander, S., and Singer, W. (1998). Synchronization of visual responses between the cortex, lateral geniculate nucleus, and retina in the anesthetized cat. J Neurosci *18*, 6395-6410.
51. Cavanaugh, J.R., Bair, W., and Movshon, J.A. (2002a). Nature and interaction of signals from the receptive field center and surround in macaque V1 neurons. J Neurophysiol *88*, 2530-2546.
52. Cavanaugh, J.R., Bair, W., and Movshon, J.A. (2002b). Selectivity and spatial distribution of signals from the receptive field surround in macaque V1 neurons. J Neurophysiol *88*, 2547-2556.
53. Clement, E.A., Richard, A., Thwaites, M., Ailon, J., Peters, S., and Dickson, C.T. (2008). Cyclic and sleep-like spontaneous alternations of brain state under urethane anaesthesia. PLoS One *3*, e2004.
54. Cohen, M.R., and Kohn, A. (2011). Measuring and interpreting neuronal correlations. Nat Neurosci *14*, 811-819.
55. Cohen, M.R., and Maunsell, J.H. (2009). Attention improves performance primarily by reducing interneuronal correlations. Nat Neurosci *12*, 1594-1600.
56. Colgin, L.L., Denninger, T., Fyhn, M., Hafting, T., Bonnevie, T., Jensen, O., Moser, M.B., and Moser, E.I. (2009). Frequency of gamma oscillations routes flow of information in the hippocampus. Nature *462*, 353-357.
57. Crair, M.C., Ruthazer, E.S., Gillespie, D.C., and Stryker, M.P. (1997). Relationship between the ocular dominance and orientation maps in visual cortex of monocularly deprived cats. Neuron *19*, 307-318.
58. Crespel, A., Velizarova, R., Garrigues, G., and Gelisse, P. (2009). A new case of slow alpha variant during REM sleep. Neurophysiologie clinique = Clinical neurophysiology *39*, 263-265.
59. Csibra, G., Davis, G., Spratling, M.W., and Johnson, M.H. (2000). Gamma oscillations and object processing in the infant brain. Science *290*, 1582-1585.
60. Csicsvari, J., Jamieson, B., Wise, K.D., and Buzsaki, G. (2003). Mechanisms of gamma oscillations in the hippocampus of the behaving rat. Neuron *37*, 311-322.
61. Cunningham, M.O., Davies, C.H., Buhl, E.H., Kopell, N., and Whittington, M.A. (2003). Gamma oscillations induced by kainate receptor activation in the entorhinal cortex in vitro. J Neurosci *23*, 9761-9769.
62. Cunningham, M.O., Halliday, D.M., Davies, C.H., Traub, R.D., Buhl, E.H., and Whittington, M.A. (2004a). Coexistence of gamma and high-frequency oscillations in rat medial entorhinal cortex in vitro. J Physiol *559*, 347-353.
63. Cunningham, M.O., Whittington, M.A., Bibbig, A., Roopun, A., LeBeau, F.E., Vogt, A., Monyer, H., Buhl, E.H., and Traub, R.D. (2004b). A role for fast rhythmic bursting neurons in cortical gamma oscillations in vitro. Proc Natl Acad Sci U S A *101*, 7152-7157.
64. Daniel, P.M., and Whitteridge, D. (1961). The representation of the visual field on the cerebral cortex in monkeys. J Physiol *159*, 203-221.
65. Das, A., and Gilbert, C.D. (1995). Long-range horizontal connections and their role in cortical reorganization revealed by optical recording of cat primary visual cortex. Nature *375*, 780-784.

66. David, S.V., Malaval, N., and Shamma, S.A. (2010). Decoupling action potential bias from cortical local field potentials. Comput Intell Neurosci, 393019.
67. De Baene, W., and Vogels, R. (2010). Effects of adaptation on the stimulus selectivity of macaque inferior temporal spiking activity and local field potentials. Cereb Cortex *20*, 2145-2165.
68. Desimone, R., Albright, T.D., Gross, C.G., and Bruce, C. (1984). Stimulus-selective properties of inferior temporal neurons in the macaque. J Neurosci *4*, 2051-2062.
69. Donoghue, J.P., Sanes, J.N., Hatsopoulos, N.G., and Gaal, G. (1998). Neural discharge and local field potential oscillations in primate motor cortex during voluntary movements. J Neurophysiol *79*, 159-173.
70. Dow, B.M., Vautin, R.G., and Bauer, R. (1985). The mapping of visual space onto foveal striate cortex in the macaque monkey. J Neurosci *5*, 890-902.
71. Dragoi, V., Sharma, J., Miller, E.K., and Sur, M. (2002). Dynamics of neuronal sensitivity in visual cortex and local feature discrimination. Nat Neurosci *5*, 883-891.
72. Dragoi, V., Sharma, J., and Sur, M. (2000). Adaptation-induced plasticity of orientation tuning in adult visual cortex. Neuron *28*, 287-298.
73. Draguhn, A., Traub, R.D., Schmitz, D., and Jefferys, J.G. (1998). Electrical coupling underlies high-frequency oscillations in the hippocampus in vitro. Nature *394*, 189-192.
74. Eckhorn, R. (2000). Neural mechanisms of visual feature grouping. Neurol Neurochir Pol *34*, 27-42.
75. Eckhorn, R., Bauer, R., Jordan, W., Brosch, M., Kruse, W., Munk, M., and Reitboeck, H.J. (1988). Coherent oscillations: a mechanism of feature linking in the visual cortex? Multiple electrode and correlation analyses in the cat. Biol Cybern *60*, 121-130.
76. Edwards, E., Soltani, M., Deouell, L.Y., Berger, M.S., and Knight, R.T. (2005). High gamma activity in response to deviant auditory stimuli recorded directly from human cortex. J Neurophysiol *94*, 4269-4280.
77. Ego-Stengel, V., and Wilson, M.A. (2007). Spatial selectivity and theta phase precession in CA1 interneurons. Hippocampus *17*, 161-174.
78. Engel, A., Konig, P., Kreiter, A., and Singer, W. (1991a). Interhemispheric synchronization of oscillatory neuronal responses in cat visual cortex. Science *252*, 1177-1179.
79. Engel, A.K., Fries, P., Konig, P., Brecht, M., and Singer, W. (1999). Temporal binding, binocular rivalry, and consciousness. Conscious Cogn *8*, 128-151.
80. Engel, A.K., Fries, P., and Singer, W. (2001). Dynamic predictions: oscillations and synchrony in top-down processing. Nat Rev Neurosci *2*, 704-716.
81. Engel, A.K., Kreiter, A.K., Konig, P., and Singer, W. (1991b). Synchronization of oscillatory neuronal responses between striate and extrastriate visual cortical areas of the cat. Proc Natl Acad Sci U S A *88*, 6048-6052.
82. Engel, A.K., Roelfsema, P.R., Fries, P., Brecht, M., and Singer, W. (1997). Role of the temporal domain for response selection and perceptual binding. Cereb Cortex *7*, 571-582.

83. Engel, S.A. (2005). Adaptation of oriented and unoriented color-selective neurons in human visual areas. Neuron *45*, 613-623.
84. Everson, R.M., Prashanth, A.K., Gabbay, M., Knight, B.W., Sirovich, L., and Kaplan, E. (1998). Representation of spatial frequency and orientation in the visual cortex. Proc Natl Acad Sci U S A *95*, 8334-8338.
85. Fang, F., Murray, S.O., Kersten, D., and He, S. (2005). Orientation-tuned FMRI adaptation in human visual cortex. J Neurophysiol *94*, 4188-4195.
86. Felleman, D.J., and Van Essen, D.C. (1991). Distributed hierarchical processing in the primate cerebral cortex. Cereb Cortex *1*, 1-47.
87. Fellous, J.M., and Sejnowski, T.J. (2000). Cholinergic induction of oscillations in the hippocampal slice in the slow (0.5-2 Hz), theta (5-12 Hz), and gamma (35-70 Hz) bands. Hippocampus *10*, 187-197.
88. Felsen, G., Shen, Y.S., Yao, H., Spor, G., Li, C., and Dan, Y. (2002). Dynamic modification of cortical orientation tuning mediated by recurrent connections. Neuron *36*, 945-954.
89. Fenno, L., Yizhar, O., and Deisseroth, K. (2011). The development and application of optogenetics. Annu Rev Neurosci *34*, 389-412.
90. Fisahn, A. (2005). Kainate receptors and rhythmic activity in neuronal networks: hippocampal gamma oscillations as a tool. J Physiol *562*, 65-72.
91. Fisahn, A., Contractor, A., Traub, R.D., Buhl, E.H., Heinemann, S.F., and McBain, C.J. (2004). Distinct roles for the kainate receptor subunits GluR5 and GluR6 in kainate-induced hippocampal gamma oscillations. J Neurosci *24*, 9658-9668.
92. Fisahn, A., Pike, F.G., Buhl, E.H., and Paulsen, O. (1998). Cholinergic induction of network oscillations at 40 Hz in the hippocampus in vitro. Nature *394*, 186-189.
93. Fitzpatrick, D., Lund, J.S., Schmechel, D.E., and Towles, A.C. (1987). Distribution of GABAergic neurons and axon terminals in the macaque striate cortex. J Comp Neurol *264*, 73-91.
94. Foster, D.J., and Wilson, M.A. (2007). Hippocampal theta sequences. Hippocampus *17*, 1093-1099.
95. Foster, K.H., Gaska, J.P., Nagler, M., and Pollen, D.A. (1985). Spatial and temporal frequency selectivity of neurones in visual cortical areas V1 and V2 of the macaque monkey. J Physiol *365*, 331-363.
96. Freeman, J., Brouwer, G.J., Heeger, D.J., and Merriam, E.P. (2011). Orientation decoding depends on maps, not columns. J Neurosci *31*, 4792-4804.
97. Freiwald, W.A., Kreiter, A.K., and Singer, W. (1995). Stimulus dependent intercolumnar synchronization of single unit responses in cat area 17. Neuroreport *6*, 2348-2352.
98. Friedman-Hill, S., Maldonado, P.E., and Gray, C.M. (2000). Dynamics of striate cortical activity in the alert macaque: I. Incidence and stimulus-dependence of gamma-band neuronal oscillations. Cereb Cortex *10*, 1105-1116.
99. Frien, A., and Eckhorn, R. (2000). Functional coupling shows stronger stimulus dependency for fast oscillations than for low-frequency components in striate cortex of awake monkey. Eur J Neurosci *12*, 1466-1478.

100. Frien, A., Eckhorn, R., Bauer, R., Woelbern, T., and Gabriel, A. (2000). Fast oscillations display sharper orientation tuning than slower components of the same recordings in striate cortex of the awake monkey. Eur J Neurosci *12*, 1453-1465.
101. Frien, A., Eckhorn, R., Bauer, R., Woelbern, T., and Kehr, H. (1994). Stimulus-specific fast oscillations at zero phase between visual areas V1 and V2 of awake monkey. Neuroreport *5*, 2273-2277.
102. Fries, P. (2005). A mechanism for cognitive dynamics: neuronal communication through neuronal coherence. Trends Cogn Sci *9*, 474-480.
103. Fries, P. (2009). Neuronal gamma-band synchronization as a fundamental process in cortical computation. Annu Rev Neurosci *32*, 209-224.
104. Fries, P., Nikolic, D., and Singer, W. (2007). The gamma cycle. Trends Neurosci *30*, 309-316.
105. Fries, P., Reynolds, J.H., Rorie, A.E., and Desimone, R. (2001). Modulation of oscillatory neuronal synchronization by selective visual attention. Science *291*, 1560-1563.
106. Fries, P., Roelfsema, P.R., Engel, A.K., Konig, P., and Singer, W. (1997). Synchronization of oscillatory responses in visual cortex correlates with perception in interocular rivalry. Proc Natl Acad Sci U S A *94*, 12699-12704.
107. Fries, P., Schroder, J.H., Roelfsema, P.R., Singer, W., and Engel, A.K. (2002). Oscillatory neuronal synchronization in primary visual cortex as a correlate of stimulus selection. J Neurosci *22*, 3739-3754.
108. Fries, P., Womelsdorf, T., Oostenveld, R., and Desimone, R. (2008). The effects of visual stimulation and selective visual attention on rhythmic neuronal synchronization in macaque area V4. J Neurosci *28*, 4823-4835.
109. Frohlich, F., and McCormick, D.A. (2010). Endogenous electric fields may guide neocortical network activity. Neuron *67*, 129-143.
110. Fukuda, T., and Kosaka, T. (2000). Gap junctions linking the dendritic network of GABAergic interneurons in the hippocampus. J Neurosci *20*, 1519-1528.
111. Fukuda, T., Kosaka, T., Singer, W., and Galuske, R.A. (2006). Gap junctions among dendrites of cortical GABAergic neurons establish a dense and widespread intercolumnar network. J Neurosci *26*, 3434-3443.
112. Gail, A., Brinksmeyer, H.J., and Eckhorn, R. (2000). Contour decouples gamma activity across texture representation in monkey striate cortex. Cereb Cortex *10*, 840-850.
113. Gail, A., Brinksmeyer, H.J., and Eckhorn, R. (2004). Perception-related modulations of local field potential power and coherence in primary visual cortex of awake monkey during binocular rivalry. Cereb Cortex *14*, 300-313.
114. Galindo-Leon, E.E., Lin, F.G., and Liu, R.C. (2009). Inhibitory plasticity in a lateral band improves cortical detection of natural vocalizations. Neuron *62*, 705-716.
115. Galindo-Leon, E.E., and Liu, R.C. (2010). Predicting stimulus-locked single unit spiking from cortical local field potentials. J Comput Neurosci *29*, 581-597.
116. Gelisse, P., and Crespel, A. (2008). Slow alpha variant during REM sleep. Neurophysiologie clinique = Clinical neurophysiology *38*, 3-8.

117. Gentet, L.J., Avermann, M., Matyas, F., Staiger, J.F., and Petersen, C.C. (2010). Membrane potential dynamics of GABAergic neurons in the barrel cortex of behaving mice. Neuron *65*, 422-435.
118. Ghose, G.M., and Freeman, R.D. (1992). Oscillatory discharge in the visual system: does it have a functional role? J Neurophysiol *68*, 1558-1574.
119. Giaschi, D., Douglas, R., Marlin, S., and Cynader, M. (1993). The time course of direction-selective adaptation in simple and complex cells in cat striate cortex. J Neurophysiol *70*, 2024-2034.
120. Gibson, J.R., Beierlein, M., and Connors, B.W. (1999). Two networks of electrically coupled inhibitory neurons in neocortex. Nature *402*, 75-79.
121. Gieselmann, M.A., and Thiele, A. (2008). Comparison of spatial integration and surround suppression characteristics in spiking activity and the local field potential in macaque V1. Eur J Neurosci *28*, 447-459.
122. Gilbert, C.D., and Wiesel, T.N. (1983). Clustered intrinsic connections in cat visual cortex. J Neurosci *3*, 1116-1133.
123. Gilbert, C.D., and Wiesel, T.N. (1989). Columnar specificity of intrinsic horizontal and corticocortical connections in cat visual cortex. J Neurosci *9*, 2432-2442.
124. Gillies, M.J., Traub, R.D., LeBeau, F.E., Davies, C.H., Gloveli, T., Buhl, E.H., and Whittington, M.A. (2002). A model of atropine-resistant theta oscillations in rat hippocampal area CA1. J Physiol *543*, 779-793.
125. Girard, P., and Bullier, J. (1989). Visual activity in area V2 during reversible inactivation of area 17 in the macaque monkey. J Neurophysiol *62*, 1287-1302.
126. Girard, P., Hupe, J.M., and Bullier, J. (2001). Feedforward and feedback connections between areas V1 and V2 of the monkey have similar rapid conduction velocities. J Neurophysiol *85*, 1328-1331.
127. Givre, S.J., Schroeder, C.E., and Arezzo, J.C. (1994). Contribution of extrastriate area V4 to the surface-recorded flash VEP in the awake macaque. Vision Res *34*, 415-428.
128. Goense, J.B., and Logothetis, N.K. (2008). Neurophysiology of the BOLD fMRI signal in awake monkeys. Curr Biol *18*, 631-640.
129. Graham, G. (1989). Visual pattern analyzers. Oxford University Press.
130. Gray, C.M. (1999). The temporal correlation hypothesis of visual feature integration: still alive and well. Neuron *24*, 31-47, 111-125.
131. Gray, C.M., Engel, A.K., Konig, P., and Singer, W. (1990). Stimulus-Dependent Neuronal Oscillations in Cat Visual Cortex: Receptive Field Properties and Feature Dependence. Eur J Neurosci *2*, 607-619.
132. Gray, C.M., Konig, P., Engel, A.K., and Singer, W. (1989). Oscillatory responses in cat visual cortex exhibit inter-columnar synchronization which reflects global stimulus properties. Nature *338*, 334-337.
133. Gray, C.M., and McCormick, D.A. (1996). Chattering cells: superficial pyramidal neurons contributing to the generation of synchronous oscillations in the visual cortex. Science *274*, 109-113.
134. Gray, C.M., and Singer, W. (1989). Stimulus-specific neuronal oscillations in orientation columns of cat visual cortex. Proc Natl Acad Sci U S A *86*, 1698-1702.

135. Gray, C.M., and Viana Di Prisco, G. (1997). Stimulus-dependent neuronal oscillations and local synchronization in striate cortex of the alert cat. J Neurosci *17*, 3239-3253.
136. Gregoriou, G.G., Gotts, S.J., Zhou, H., and Desimone, R. (2009). High-frequency, long-range coupling between prefrontal and visual cortex during attention. Science *324*, 1207-1210.
137. Greicius, M.D., Supekar, K., Menon, V., and Dougherty, R.F. (2009). Resting-state functional connectivity reflects structural connectivity in the default mode network. Cereb Cortex *19*, 72-78.
138. Grice, S.J., Spratling, M.W., Karmiloff-Smith, A., Halit, H., Csibra, G., de Haan, M., and Johnson, M.H. (2001). Disordered visual processing and oscillatory brain activity in autism and Williams syndrome. Neuroreport *12*, 2697-2700.
139. Grill-Spector, K., Henson, R., and Martin, A. (2006). Repetition and the brain: neural models of stimulus-specific effects. Trends Cogn Sci *10*, 14-23.
140. Grill-Spector, K., and Malach, R. (2001). fMR-adaptation: a tool for studying the functional properties of human cortical neurons. Acta Psychol (Amst) *107*, 293-321.
141. Grossberg, S. (2001). Linking the laminar circuits of visual cortex to visual perception: development, grouping, and attention. Neuroscience and biobehavioral reviews *25*, 513-526.
142. Gruber, T., and Muller, M.M. (2002). Effects of picture repetition on induced gamma band responses, evoked potentials, and phase synchrony in the human EEG. Brain Res Cogn Brain Res *13*, 377-392.
143. Guld, C., and Bertulis, A. (1976). Representation of fovea in the striate cortex of vervet monkey, Cercopithecus aethiops pygerythrus. Vision Res *16*, 629-631.
144. Haas, L.F. (2003). Hans Berger (1873-1941), Richard Caton (1842-1926), and electroencephalography. J Neurol Neurosurg Psychiatry *74*, 9.
145. Haberly, L.B., and Shepherd, G.M. (1973). Current-density analysis of summed evoked potentials in opossum prepyriform cortex. J Neurophysiol *36*, 789-802.
146. Haider, B., Krause, M.R., Duque, A., Yu, Y., Touryan, J., Mazer, J.A., and McCormick, D.A. (2010). Synaptic and network mechanisms of sparse and reliable visual cortical activity during nonclassical receptive field stimulation. Neuron *65*, 107-121.
147. Hajos, N., Katona, I., Naiem, S.S., MacKie, K., Ledent, C., Mody, I., and Freund, T.F. (2000). Cannabinoids inhibit hippocampal GABAergic transmission and network oscillations. Eur J Neurosci *12*, 3239-3249.
148. Hammond, P., Mouat, G.S., and Smith, A.T. (1988). Neural correlates of motion after-effects in cat striate cortical neurones: monocular adaptation. Exp Brain Res *72*, 1-20.
149. Hansen, B.J., and Dragoi, V. (2011). Adaptation-induced synchronization in laminar cortical circuits. Proc Natl Acad Sci U S A *108*, 10720-10725.
150. Harris, K.D., Henze, D.A., Hirase, H., Leinekugel, X., Dragoi, G., Czurko, A., and Buzsaki, G. (2002). Spike train dynamics predicts theta-related phase precession in hippocampal pyramidal cells. Nature *417*, 738-741.

151. Harrison, M.T., and Geman, S. (2009). A rate and history-preserving resampling algorithm for neural spike trains. Neural Comput *21*, 1244-1258.
152. Hasenstaub, A., Shu, Y., Haider, B., Kraushaar, U., Duque, A., and McCormick, D.A. (2005). Inhibitory postsynaptic potentials carry synchronized frequency information in active cortical networks. Neuron *47*, 423-435.
153. Hawken, M.J., Shapley, R.M., and Grosof, D.H. (1996). Temporal-frequency selectivity in monkey visual cortex. Vis Neurosci *13*, 477-492.
154. Haynes, J.D., and Rees, G. (2006). Decoding mental states from brain activity in humans. Nat Rev Neurosci *7*, 523-534.
155. Heldman, D.A., Wang, W., Chan, S.S., and Moran, D.W. (2006). Local field potential spectral tuning in motor cortex during reaching. IEEE Trans Neural Syst Rehabil Eng *14*, 180-183.
156. Hendry, S.H., Schwark, H.D., Jones, E.G., and Yan, J. (1987). Numbers and proportions of GABA-immunoreactive neurons in different areas of monkey cerebral cortex. J Neurosci *7*, 1503-1519.
157. Henrie, J.A., and Shapley, R. (2005). LFP power spectra in V1 cortex: the graded effect of stimulus contrast. J Neurophysiol *94*, 479-490.
158. Henze, D.A., Borhegyi, Z., Csicsvari, J., Mamiya, A., Harris, K.D., and Buzsaki, G. (2000). Intracellular features predicted by extracellular recordings in the hippocampus in vivo. J Neurophysiol *84*, 390-400.
159. Herculano-Houzel, S., Munk, M.H., Neuenschwander, S., and Singer, W. (1999). Precisely synchronized oscillatory firing patterns require electroencephalographic activation. J Neurosci *19*, 3992-4010.
160. Hess, R.F., and Dakin, S.C. (1997). Absence of contour linking in peripheral vision. Nature *390*, 602-604.
161. Hobson, J.A., and Pace-Schott, E.F. (2002). The cognitive neuroscience of sleep: neuronal systems, consciousness and learning. Nat Rev Neurosci *3*, 679-693.
162. Hopfield, J.J. (2004). Encoding for computation: recognizing brief dynamical patterns by exploiting effects of weak rhythms on action-potential timing. Proc Natl Acad Sci U S A *101*, 6255-6260.
163. Hormuzdi, S.G., Pais, I., LeBeau, F.E., Towers, S.K., Rozov, A., Buhl, E.H., Whittington, M.A., and Monyer, H. (2001). Impaired electrical signaling disrupts gamma frequency oscillations in connexin 36-deficient mice. Neuron *31*, 487-495.
164. Horton, J.C., and Adams, D.L. (2005). The cortical column: a structure without a function. Philos Trans R Soc Lond B Biol Sci *360*, 837-862.
165. Hubel, D.H., and Wiesel, T.N. (1962). Receptive fields, binocular interaction and functional architecture in the cat's visual cortex. J Physiol *160*, 106-154.
166. Hubel, D.H., and Wiesel, T.N. (1965). Receptive Fields and Functional Architecture in Two Nonstriate Visual Areas (18 and 19) of the Cat. J Neurophysiol *28*, 229-289.
167. Hubel, D.H., and Wiesel, T.N. (1968). Receptive fields and functional architecture of monkey striate cortex. J Physiol *195*, 215-243.

168. Hupe, J.M., James, A.C., Girard, P., and Bullier, J. (2001a). Response modulations by static texture surround in area V1 of the macaque monkey do not depend on feedback connections from V2. J Neurophysiol *85*, 146-163.
169. Hupe, J.M., James, A.C., Girard, P., Lomber, S.G., Payne, B.R., and Bullier, J. (2001b). Feedback connections act on the early part of the responses in monkey visual cortex. J Neurophysiol *85*, 134-145.
170. Hupe, J.M., James, A.C., Payne, B.R., Lomber, S.G., Girard, P., and Bullier, J. (1998). Cortical feedback improves discrimination between figure and background by V1, V2 and V3 neurons. Nature *394*, 784-787.
171. Huxter, J., Burgess, N., and O'Keefe, J. (2003). Independent rate and temporal coding in hippocampal pyramidal cells. Nature *425*, 828-832.
172. Issa, N.P., Trepel, C., and Stryker, M.P. (2000). Spatial frequency maps in cat visual cortex. J Neurosci *20*, 8504-8514.
173. Jensen, O., Kaiser, J., and Lachaux, J.P. (2007). Human gamma-frequency oscillations associated with attention and memory. Trends Neurosci *30*, 317-324.
174. Jia, X., and Kohn, A. (2009). The relationship between LFP gamma power and neural population synchrony in the primary visual cortex of macaque monkey. *Program No.166.14. 2009 Neuroscience Meeting Planner.*, Online.
175. Jia, X., and Kohn, A. (2011). Gamma rhythms in the brain. PLoS Biol *9*, e1001045.
176. Jia, X., Smith, M.A., and Kohn, A. (2011). Stimulus selectivity and spatial coherence of gamma components of the local field potential. J Neurosci *31*, 9390-9403.
177. Jones, H.E., Grieve, K.L., Wang, W., and Sillito, A.M. (2001). Surround suppression in primate V1. J Neurophysiol *86*, 2011-2028.
178. Jones, M.W., and Wilson, M.A. (2005a). Phase precession of medial prefrontal cortical activity relative to the hippocampal theta rhythm. Hippocampus *15*, 867-873.
179. Jones, M.W., and Wilson, M.A. (2005b). Theta rhythms coordinate hippocampal-prefrontal interactions in a spatial memory task. PLoS Biol *3*, e402.
180. Juergens, E., Guettler, A., and Eckhorn, R. (1999). Visual stimulation elicits locked and induced gamma oscillations in monkey intracortical- and EEG-potentials, but not in human EEG. Exp Brain Res *129*, 247-259.
181. Jutras, M.J., Fries, P., and Buffalo, E.A. (2009). Gamma-band synchronization in the macaque hippocampus and memory formation. J Neurosci *29*, 12521-12531.
182. Kajikawa, Y., and Schroeder, C.E. (2011). How Local Is the Local Field Potential? Neuron *72*, 847-858.
183. Kaliukhovich, D.A., and Vogels, R. (2011). Stimulus repetition probability does not affect repetition suppression in macaque inferior temporal cortex. Cereb Cortex *21*, 1547-1558.
184. Kamitani, Y., and Tong, F. (2005). Decoding the visual and subjective contents of the human brain. Nat Neurosci *8*, 679-685.

185. Kang, K., Shelley, M., Henrie, J.A., and Shapley, R. (2009). LFP spectral peaks in V1 cortex: network resonance and cortico-cortical feedback. J Comput Neurosci.
186. Kapadia, M.K., Westheimer, G., and Gilbert, C.D. (1999). Dynamics of spatial summation in primary visual cortex of alert monkeys. Proc Natl Acad Sci U S A *96*, 12073-12078.
187. Kapadia, M.K., Westheimer, G., and Gilbert, C.D. (2000). Spatial distribution of contextual interactions in primary visual cortex and in visual perception. J Neurophysiol *84*, 2048-2062.
188. Katzner, S., Nauhaus, I., Benucci, A., Bonin, V., Ringach, D.L., and Carandini, M. (2009). Local origin of field potentials in visual cortex. Neuron *61*, 35-41.
189. Kayser, C., Kim, M., Ugurbil, K., Kim, D.S., and Konig, P. (2004). A comparison of hemodynamic and neural responses in cat visual cortex using complex stimuli. Cereb Cortex *14*, 881-891.
190. Kayser, C., and Konig, P. (2004). Stimulus locking and feature selectivity prevail in complementary frequency ranges of V1 local field potentials. Eur J Neurosci *19*, 485-489.
191. Kayser, C., Montemurro, M.A., Logothetis, N.K., and Panzeri, S. (2009). Spike-phase coding boosts and stabilizes information carried by spatial and temporal spike patterns. Neuron *61*, 597-608.
192. Keil, A., Muller, M.M., Ray, W.J., Gruber, T., and Elbert, T. (1999). Human gamma band activity and perception of a gestalt. J Neurosci *19*, 7152-7161.
193. Kelly, R.C., Smith, M.A., Samonds, J.M., Kohn, A., Bonds, A.B., Movshon, J.A., and Lee, T.S. (2007). Comparison of recordings from microelectrode arrays and single electrodes in the visual cortex. J Neurosci *27*, 261-264.
194. Knierim, J.J., and van Essen, D.C. (1992). Neuronal responses to static texture patterns in area V1 of the alert macaque monkey. J Neurophysiol *67*, 961-980.
195. Knoblich, U., Siegle, J.H., Pritchett, D.L., and Moore, C.I. (2010). What do we gain from gamma? Local dynamic gain modulation drives enhanced efficacy and efficiency of signal transmission. Front Hum Neurosci *4*, 185.
196. Koffka, K. (1935). Principles of Gestalt Psychology. Harcourt Brace.
197. Kohn, A. (2007). Visual adaptation: physiology, mechanisms, and functional benefits. J Neurophysiol *97*, 3155-3164.
198. Kohn, A., and Movshon, J.A. (2003). Neuronal adaptation to visual motion in area MT of the macaque. Neuron *39*, 681-691.
199. Kohn, A., and Movshon, J.A. (2004). Adaptation changes the direction tuning of macaque MT neurons. Nat Neurosci *7*, 764-772.
200. Kohn, A., and Smith, M.A. (2005). Stimulus dependence of neuronal correlation in primary visual cortex of the macaque. J Neurosci *25*, 3661-3673.
201. Kohn, A., Zandvakili, A., and Smith, M.A. (2009). Correlations and brain states: from electrophysiology to functional imaging. Curr Opin Neurobiol *19*, 434-438.
202. Konig, P., Engel, A.K., and Singer, W. (1995). Relation between oscillatory activity and long-range synchronization in cat visual cortex. Proc Natl Acad Sci U S A *92*, 290-294.

203. Konig, P., Engel, A.K., and Singer, W. (1996). Integrator or coincidence detector? The role of the cortical neuron revisited. Trends Neurosci *19*, 130-137.
204. Kopell, N., Ermentrout, G.B., Whittington, M.A., and Traub, R.D. (2000). Gamma rhythms and beta rhythms have different synchronization properties. Proc Natl Acad Sci U S A *97*, 1867-1872.
205. Koulakov, A.A., and Chklovskii, D.B. (2001). Orientation preference patterns in mammalian visual cortex: a wire length minimization approach. Neuron *29*, 519-527.
206. Kovacs, I., and Julesz, B. (1993). A closed curve is much more than an incomplete one: effect of closure in figure-ground segmentation. Proc Natl Acad Sci U S A *90*, 7495-7497.
207. Kreiman, G., Hung, C.P., Kraskov, A., Quiroga, R.Q., Poggio, T., and DiCarlo, J.J. (2006). Object selectivity of local field potentials and spikes in the macaque inferior temporal cortex. Neuron *49*, 433-445.
208. Krekelberg, B., Boynton, G.M., and van Wezel, R.J. (2006). Adaptation: from single cells to BOLD signals. Trends Neurosci *29*, 250-256.
209. Krishnan, G.P., Vohs, J.L., Hetrick, W.P., Carroll, C.A., Shekhar, A., Bockbrader, M.A., and O'Donnell, B.F. (2005). Steady state visual evoked potential abnormalities in schizophrenia. Clin Neurophysiol *116*, 614-624.
210. Kruse, W., and Eckhorn, R. (1996). Inhibition of sustained gamma oscillations (35-80 Hz) by fast transient responses in cat visual cortex. Proc Natl Acad Sci U S A *93*, 6112-6117.
211. Kuffler, S.W. (1953). Discharge patterns and functional organization of mammalian retina. J Neurophysiol *16*, 37-68.
212. Kwon, J.S., O'Donnell, B.F., Wallenstein, G.V., Greene, R.W., Hirayasu, Y., Nestor, P.G., Hasselmo, M.E., Potts, G.F., Shenton, M.E., and McCarley, R.W. (1999). Gamma frequency-range abnormalities to auditory stimulation in schizophrenia. Arch Gen Psychiatry *56*, 1001-1005.
213. Kwong, K.K., Belliveau, J.W., Chesler, D.A., Goldberg, I.E., Weisskoff, R.M., Poncelet, B.P., Kennedy, D.N., Hoppel, B.E., Cohen, M.S., Turner, R.*, et al.* (1992). Dynamic magnetic resonance imaging of human brain activity during primary sensory stimulation. Proc Natl Acad Sci U S A *89*, 5675-5679.
214. Lamme, V.A. (1995). The neurophysiology of figure-ground segregation in primary visual cortex. J Neurosci *15*, 1605-1615.
215. Lamme, V.A., Rodriguez-Rodriguez, V., and Spekreijse, H. (1999). Separate processing dynamics for texture elements, boundaries and surfaces in primary visual cortex of the macaque monkey. Cereb Cortex *9*, 406-413.
216. Lamme, V.A., and Roelfsema, P.R. (2000). The distinct modes of vision offered by feedforward and recurrent processing. Trends Neurosci *23*, 571-579.
217. Lamme, V.A., Super, H., and Spekreijse, H. (1998a). Feedforward, horizontal, and feedback processing in the visual cortex. Curr Opin Neurobiol *8*, 529-535.
218. Lamme, V.A., van Dijk, B.W., and Spekreijse, H. (1993). Contour from motion processing occurs in primary visual cortex. Nature *363*, 541-543.

219. Lamme, V.A., Zipser, K., and Spekreijse, H. (1998b). Figure-ground activity in primary visual cortex is suppressed by anesthesia. Proc Natl Acad Sci U S A *95*, 3263-3268.
220. Lamme, V.A., Zipser, K., and Spekreijse, H. (2002). Masking interrupts figure-ground signals in V1. J Cogn Neurosci *14*, 1044-1053.
221. Lampl, I., Reichova, I., and Ferster, D. (1999). Synchronous membrane potential fluctuations in neurons of the cat visual cortex. Neuron *22*, 361-374.
222. Landisman, C.E., and Ts'o, D.Y. (2002). Color processing in macaque striate cortex: relationships to ocular dominance, cytochrome oxidase, and orientation. J Neurophysiol *87*, 3126-3137.
223. Lee, T.S., and Nguyen, M. (2001). Dynamics of subjective contour formation in the early visual cortex. Proc Natl Acad Sci U S A *98*, 1907-1911.
224. Legatt, A.D., Arezzo, J., and Vaughan, H.G., Jr. (1980). Averaged multiple unit activity as an estimate of phasic changes in local neuronal activity: effects of volume-conducted potentials. J Neurosci Methods *2*, 203-217.
225. Leopold, D.A., Murayama, Y., and Logothetis, N.K. (2003). Very slow activity fluctuations in monkey visual cortex: implications for functional brain imaging. Cereb Cortex *13*, 422-433.
226. Lepage, K.Q., Kramer, M.A., and Eden, U.T. (2011). The dependence of spike field coherence on expected intensity. Neural Comput *23*, 2209-2241.
227. LeVay, S., Connolly, M., Houde, J., and Van Essen, D.C. (1985). The complete pattern of ocular dominance stripes in the striate cortex and visual field of the macaque monkey. J Neurosci *5*, 486-501.
228. Leventhal, A.G., Thompson, K.G., Liu, D., Zhou, Y., and Ault, S.J. (1995). Concomitant sensitivity to orientation, direction, and color of cells in layers 2, 3, and 4 of monkey striate cortex. J Neurosci *15*, 1808-1818.
229. Levitt, J.B., Kiper, D.C., and Movshon, J.A. (1994). Receptive fields and functional architecture of macaque V2. J Neurophysiol *71*, 2517-2542.
230. Levitt, J.B., and Lund, J.S. (1997). Contrast dependence of contextual effects in primate visual cortex. Nature *387*, 73-76.
231. Li, B., Peterson, M.R., and Freeman, R.D. (2003). Oblique effect: a neural basis in the visual cortex. J Neurophysiol *90*, 204-217.
232. Lima, B., Singer, W., Chen, N.H., and Neuenschwander, S. (2010). Synchronization dynamics in response to plaid stimuli in monkey V1. Cereb Cortex *20*, 1556-1573.
233. Linden, H., Pettersen, K.H., and Einevoll, G.T. (2010). Intrinsic dendritic filtering gives low-pass power spectra of local field potentials. J Comput Neurosci *29*, 423-444.
234. Liu, J., and Newsome, W.T. (2006). Local field potential in cortical area MT: stimulus tuning and behavioral correlations. J Neurosci *26*, 7779-7790.
235. Livingstone, M.S. (1996). Oscillatory firing and interneuronal correlations in squirrel monkey striate cortex. J Neurophysiol *75*, 2467-2485.
236. Livingstone, M.S., and Hubel, D.H. (1984). Anatomy and physiology of a color system in the primate visual cortex. J Neurosci *4*, 309-356.

237. Logothetis, N.K. (2002). The neural basis of the blood-oxygen-level-dependent functional magnetic resonance imaging signal. Philos Trans R Soc Lond B Biol Sci *357*, 1003-1037.
238. Logothetis, N.K. (2003). The underpinnings of the BOLD functional magnetic resonance imaging signal. J Neurosci *23*, 3963-3971.
239. Logothetis, N.K., Kayser, C., and Oeltermann, A. (2007). In vivo measurement of cortical impedance spectrum in monkeys: implications for signal propagation. Neuron *55*, 809-823.
240. Logothetis, N.K., Pauls, J., Augath, M., Trinath, T., and Oeltermann, A. (2001). Neurophysiological investigation of the basis of the fMRI signal. Nature *412*, 150-157.
241. Logothetis, N.K., and Sheinberg, D.L. (1996). Visual object recognition. Annu Rev Neurosci *19*, 577-621.
242. Lubenov, E.V., and Siapas, A.G. (2009). Hippocampal theta oscillations are travelling waves. Nature *459*, 534-539.
243. Lund, J.S. (1988). Anatomical organization of macaque monkey striate visual cortex. Annu Rev Neurosci *11*, 253-288.
244. Lund, J.S., Angelucci, A., and Bressloff, P.C. (2003). Anatomical substrates for functional columns in macaque monkey primary visual cortex. Cereb Cortex *13*, 15-24.
245. Lund, J.S., Henry, G.H., MacQueen, C.L., and Harvey, A.R. (1979). Anatomical organization of the primary visual cortex (area 17) of the cat. A comparison with area 17 of the macaque monkey. J Comp Neurol *184*, 599-618.
246. Lutz, A., Greischar, L.L., Rawlings, N.B., Ricard, M., and Davidson, R.J. (2004). Long-term meditators self-induce high-amplitude gamma synchrony during mental practice. Proc Natl Acad Sci U S A *101*, 16369-16373.
247. Lytton, W.W., and Sejnowski, T.J. (1991). Simulations of cortical pyramidal neurons synchronized by inhibitory interneurons. J Neurophysiol *66*, 1059-1079.
248. Maffei, L., and Fiorentini, A. (1976). The unresponsive regions of visual cortical receptive fields. Vision Res *16*, 1131-1139.
249. Maier, A., Adams, G.K., Aura, C., and Leopold, D.A. (2010). Distinct superficial and deep laminar domains of activity in the visual cortex during rest and stimulation. Front Syst Neurosci *4*.
250. Maier, A., Aura, C.J., and Leopold, D.A. (2011). Infragranular sources of sustained local field potential responses in macaque primary visual cortex. J Neurosci *31*, 1971-1980.
251. Maldonado, P.E., Friedman-Hill, S., and Gray, C.M. (2000). Dynamics of striate cortical activity in the alert macaque: II. Fast time scale synchronization. Cereb Cortex *10*, 1117-1131.
252. Mann, E.O., Radcliffe, C.A., and Paulsen, O. (2005). Hippocampal gamma-frequency oscillations: from interneurones to pyramidal cells, and back. J Physiol *562*, 55-63.
253. Masquelier, T., Hugues, E., Deco, G., and Thorpe, S.J. (2009). Oscillations, phase-of-firing coding, and spike timing-dependent plasticity: an efficient learning scheme. J Neurosci *29*, 13484-13493.

254. Mastronarde, D.N. (1983). Correlated firing of cat retinal ganglion cells. I. Spontaneously active inputs to X- and Y-cells. J Neurophysiol *49*, 303-324.
255. McGinty, D.J., and Drucker-Colin, R.R. (1982). Sleep mechanisms: biology and control of REM sleep. International review of neurobiology *23*, 391-436.
256. Mehta, M.R., Lee, A.K., and Wilson, M.A. (2002). Role of experience and oscillations in transforming a rate code into a temporal code. Nature *417*, 741-746.
257. Merigan, W.H., Nealey, T.A., and Maunsell, J.H. (1993). Visual effects of lesions of cortical area V2 in macaques. J Neurosci *13*, 3180-3191.
258. Middleton, S., Jalics, J., Kispersky, T., Lebeau, F.E., Roopun, A.K., Kopell, N.J., Whittington, M.A., and Cunningham, M.O. (2008). NMDA receptor-dependent switching between different gamma rhythm-generating microcircuits in entorhinal cortex. Proc Natl Acad Sci U S A *105*, 18572-18577.
259. Miles, R., Toth, K., Gulyas, A.I., Hajos, N., and Freund, T.F. (1996). Differences between somatic and dendritic inhibition in the hippocampus. Neuron *16*, 815-823.
260. Mitchell, J.F., Sundberg, K.A., and Reynolds, J.H. (2009). Spatial attention decorrelates intrinsic activity fluctuations in macaque area V4. Neuron *63*, 879-888.
261. Mitra, P.P., and Pesaran, B. (1999). Analysis of dynamic brain imaging data. Biophys J *76*, 691-708.
262. Mitzdorf, U. (1985). Current source-density method and application in cat cerebral cortex: investigation of evoked potentials and EEG phenomena. Physiol Rev *65*, 37-100.
263. Mochizuki, H., Ugawa, Y., Machii, K., Terao, Y., Hanajima, R., Furubayashi, T., Uesugi, H., and Kanazawa, I. (1999). Somatosensory evoked high-frequency oscillation in Parkinson's disease and myoclonus epilepsy. Clin Neurophysiol *110*, 185-191.
264. Montemurro, M.A., Rasch, M.J., Murayama, Y., Logothetis, N.K., and Panzeri, S. (2008). Phase-of-firing coding of natural visual stimuli in primary visual cortex. Curr Biol *18*, 375-380.
265. Montgomery, S.M., and Buzsaki, G. (2007). Gamma oscillations dynamically couple hippocampal CA3 and CA1 regions during memory task performance. Proc Natl Acad Sci U S A *104*, 14495-14500.
266. Mountcastle, V.B., Davies, P.W., and Berman, A.L. (1957). Response properties of neurons of cat's somatic sensory cortex to peripheral stimuli. J Neurophysiol *20*, 374-407.
267. Movshon, J.A., Kiorpes, L., Hawken, M.J., and Cavanaugh, J.R. (2005). Functional maturation of the macaque's lateral geniculate nucleus. J Neurosci *25*, 2712-2722.
268. Movshon, J.A., and Lennie, P. (1979). Pattern-selective adaptation in visual cortical neurones. Nature *278*, 850-852.
269. Movshon, J.A., and Newsome, W.T. (1996). Visual response properties of striate cortical neurons projecting to area MT in macaque monkeys. J Neurosci *16*, 7733-7741.

270. Movshon, J.A., Thompson, I.D., and Tolhurst, D.J. (1978). Spatial and temporal contrast sensitivity of neurones in areas 17 and 18 of the cat's visual cortex. J Physiol *283*, 101-120.
271. Muller, J.R., Metha, A.B., Krauskopf, J., and Lennie, P. (1999). Rapid adaptation in visual cortex to the structure of images. Science *285*, 1405-1408.
272. Muller, M.M., Bosch, J., Elbert, T., Kreiter, A., Sosa, M.V., Sosa, P.V., and Rockstroh, B. (1996). Visually induced gamma-band responses in human electroencephalographic activity--a link to animal studies. Exp Brain Res *112*, 96-102.
273. Murthy, V.N., and Fetz, E.E. (1992). Coherent 25- to 35-Hz oscillations in the sensorimotor cortex of awake behaving monkeys. Proc Natl Acad Sci U S A *89*, 5670-5674.
274. Nagasaki, H., Nakamura, R., and Taniguchi, R. (1978). Disturbances of rhythm formation in patients with Parkinson's disease: part II. a forced oscillation model. Percept Mot Skills *46*, 79-87.
275. Nase, G., Singer, W., Monyer, H., and Engel, A.K. (2003). Features of neuronal synchrony in mouse visual cortex. J Neurophysiol *90*, 1115-1123.
276. Nassi, J.J., and Callaway, E.M. (2009). Parallel processing strategies of the primate visual system. Nat Rev Neurosci *10*, 360-372.
277. Nauhaus, I., Busse, L., Carandini, M., and Ringach, D.L. (2009). Stimulus contrast modulates functional connectivity in visual cortex. Nat Neurosci *12*, 70-76.
278. Nelson, J.I., and Frost, B.J. (1985). Intracortical facilitation among co-oriented, co-axially aligned simple cells in cat striate cortex. Exp Brain Res *61*, 54-61.
279. Nelson, M.J., Pouget, P., Nilsen, E.A., Patten, C.D., and Schall, J.D. (2008). Review of signal distortion through metal microelectrode recording circuits and filters. J Neurosci Methods *169*, 141-157.
280. Neuenschwander, S., and Singer, W. (1996). Long-range synchronization of oscillatory light responses in the cat retina and lateral geniculate nucleus. Nature *379*, 728-732.
281. Nikolic, D. (2007). Non-parametric detection of temporal order across pairwise measurements of time delays. J Comput Neurosci *22*, 5-19.
282. Nir, Y., Fisch, L., Mukamel, R., Gelbard-Sagiv, H., Arieli, A., Fried, I., and Malach, R. (2007). Coupling between neuronal firing rate, gamma LFP, and BOLD fMRI is related to interneuronal correlations. Curr Biol *17*, 1275-1285.
283. O'Keefe, L.P., Levitt, J.B., Kiper, D.C., Shapley, R.M., and Movshon, J.A. (1998). Functional organization of owl monkey lateral geniculate nucleus and visual cortex. J Neurophysiol *80*, 594-609.
284. Ogawa, S., and Lee, T.M. (1990). Magnetic resonance imaging of blood vessels at high fields: in vivo and in vitro measurements and image simulation. Magn Reson Med *16*, 9-18.
285. Ogawa, S., Lee, T.M., Kay, A.R., and Tank, D.W. (1990a). Brain magnetic resonance imaging with contrast dependent on blood oxygenation. Proc Natl Acad Sci U S A *87*, 9868-9872.

286. Ogawa, S., Lee, T.M., Nayak, A.S., and Glynn, P. (1990b). Oxygenation-sensitive contrast in magnetic resonance image of rodent brain at high magnetic fields. Magn Reson Med *14*, 68-78.
287. Ogawa, S., Menon, R.S., Kim, S.G., and Ugurbil, K. (1998). On the characteristics of functional magnetic resonance imaging of the brain. Annual review of biophysics and biomolecular structure *27*, 447-474.
288. Ogawa, S., Tank, D.W., Menon, R., Ellermann, J.M., Kim, S.G., Merkle, H., and Ugurbil, K. (1992). Intrinsic signal changes accompanying sensory stimulation: functional brain mapping with magnetic resonance imaging. Proc Natl Acad Sci U S A *89*, 5951-5955.
289. Okun, M., Naim, A., and Lampl, I. (2010). The subthreshold relation between cortical local field potential and neuronal firing unveiled by intracellular recordings in awake rats. J Neurosci *30*, 4440-4448.
290. Ozeki, H., Sadakane, O., Akasaki, T., Naito, T., Shimegi, S., and Sato, H. (2004). Relationship between excitation and inhibition underlying size tuning and contextual response modulation in the cat primary visual cortex. J Neurosci *24*, 1428-1438.
291. Paik, S.B., and Ringach, D.L. (2011). Retinal origin of orientation maps in visual cortex. Nat Neurosci *14*, 919-925.
292. Pang, X.D., and Bonds, A.B. (1991). Visual evoked potential responses of the anesthetized cat to contrast modulation of grating patterns. Vision Res *31*, 1509-1516.
293. Pellerin, J.P., and Lamarre, Y. (1997). Local field potential oscillations in primate cerebellar cortex during voluntary movement. J Neurophysiol *78*, 3502-3507.
294. Penttonen, M., Kamondi, A., Acsady, L., and Buzsaki, G. (1998). Gamma frequency oscillation in the hippocampus of the rat: intracellular analysis in vivo. Eur J Neurosci *10*, 718-728.
295. Pesaran, B., Pezaris, J.S., Sahani, M., Mitra, P.P., and Andersen, R.A. (2002). Temporal structure in neuronal activity during working memory in macaque parietal cortex. Nat Neurosci *5*, 805-811.
296. Petermann, T., Thiagarajan, T.C., Lebedev, M.A., Nicolelis, M.A., Chialvo, D.R., and Plenz, D. (2009). Spontaneous cortical activity in awake monkeys composed of neuronal avalanches. Proc Natl Acad Sci U S A *106*, 15921-15926.
297. Peters, A., Rockland, K.S., Kaas, J.H., and Casagrande, V.A. (1994). Primary Visual Cortex in Primates. Cereb Cortex *10*.
298. Poe, G.R., Walsh, C.M., and Bjorness, T.E. (2010). Cognitive neuroscience of sleep. Prog Brain Res *185*, 1-19.
299. Poenaru, L., Akli, S., Rocchiccioli, F., Eydoux, P., and Zamet, P. (1992). Human beta-mannosidosis: a 3-year-old boy with speech impairment and emotional instability. Clin Genet *41*, 331-334.
300. Popescu, A.T., Popa, D., and Pare, D. (2009). Coherent gamma oscillations couple the amygdala and striatum during learning. Nat Neurosci *12*, 801-807.
301. Pouget, A., Dayan, P., and Zemel, R. (2000). Information processing with population codes. Nat Rev Neurosci *1*, 125-132.

302. Poulet, J.F., and Petersen, C.C. (2008). Internal brain state regulates membrane potential synchrony in barrel cortex of behaving mice. Nature *454*, 881-885.
303. Powell, T.P., and Hendrickson, A.E. (1981). Similarity in number of neurons through the depth of the cortex in the binocular and monocular parts of area 17 of the monkey. Brain Res *216*, 409-413.
304. Priebe, N.J., and Lisberger, S.G. (2002). Constraints on the source of short-term motion adaptation in macaque area MT. II. tuning of neural circuit mechanisms. J Neurophysiol *88*, 370-382.
305. Qiu, F.T., and von der Heydt, R. (2007). Neural representation of transparent overlay. Nat Neurosci *10*, 283-284.
306. Rajkai, C., Lakatos, P., Chen, C.M., Pincze, Z., Karmos, G., and Schroeder, C.E. (2008). Transient cortical excitation at the onset of visual fixation. Cereb Cortex *18*, 200-209.
307. Rampp, S., and Stefan, H. (2006). Fast activity as a surrogate marker of epileptic network function? Clin Neurophysiol *117*, 2111-2117.
308. Ranck, J.B., Jr. (1963). Specific impedance of rabbit cerebral cortex. Exp Neurol *7*, 144-152.
309. Rasch, M., Logothetis, N.K., and Kreiman, G. (2009). From neurons to circuits: linear estimation of local field potentials. J Neurosci *29*, 13785-13796.
310. Rasch, M.J., Gretton, A., Murayama, Y., Maass, W., and Logothetis, N.K. (2008). Inferring spike trains from local field potentials. J Neurophysiol *99*, 1461-1476.
311. Ray, S., and Maunsell, J.H. (2010). Differences in gamma frequencies across visual cortex restrict their possible use in computation. Neuron *67*, 885-896.
312. Ray, S., and Maunsell, J.H. (2011a). Different origins of gamma rhythm and high-gamma activity in macaque visual cortex. PLoS Biol *9*, e1000610.
313. Ray, S., and Maunsell, J.H. (2011b). Network Rhythms Influence the Relationship between Spike-Triggered Local Field Potential and Functional Connectivity. J Neurosci *31*, 12674-12682.
314. Rees, G., Friston, K., and Koch, C. (2000). A direct quantitative relationship between the functional properties of human and macaque V5. Nat Neurosci *3*, 716-723.
315. Reimer, A., Hubka, P., Engel, A.K., and Kral, A. (2011). Fast propagating waves within the rodent auditory cortex. Cereb Cortex *21*, 166-177.
316. Reyes, A.D. (2003). Synchrony-dependent propagation of firing rate in iteratively constructed networks in vitro. Nat Neurosci *6*, 593-599.
317. Rickert, J., Oliveira, S.C., Vaadia, E., Aertsen, A., Rotter, S., and Mehring, C. (2005). Encoding of movement direction in different frequency ranges of motor cortical local field potentials. J Neurosci *25*, 8815-8824.
318. Rockland, K.S. (1992). Laminar distribution of neurons projecting from area V1 to V2 in macaque and squirrel monkeys. Cereb Cortex *2*, 38-47.
319. Rockland, K.S., and Pandya, D.N. (1979). Laminar origins and terminations of cortical connections of the occipital lobe in the rhesus monkey. Brain Res *179*, 3-20.
320. Roelfsema, P.R. (2006). Cortical algorithms for perceptual grouping. Annu Rev Neurosci *29*, 203-227.

321. Roy, A., Steinmetz, P.N., Hsiao, S.S., Johnson, K.O., and Niebur, E. (2007). Synchrony: a neural correlate of somatosensory attention. J Neurophysiol *98*, 1645-1661.
322. Rubino, D., Robbins, K.A., and Hatsopoulos, N.G. (2006). Propagating waves mediate information transfer in the motor cortex. Nat Neurosci *9*, 1549-1557.
323. Salinas, E., and Sejnowski, T.J. (2000). Impact of correlated synaptic input on output firing rate and variability in simple neuronal models. J Neurosci *20*, 6193-6209.
324. Salinas, E., and Sejnowski, T.J. (2001). Correlated neuronal activity and the flow of neural information. Nat Rev Neurosci *2*, 539-550.
325. Samonds, J.M., and Bonds, A.B. (2005). Gamma oscillation maintains stimulus structure-dependent synchronization in cat visual cortex. J Neurophysiol *93*, 223-236.
326. Sandell, J.H., and Schiller, P.H. (1982). Effect of cooling area 18 on striate cortex cells in the squirrel monkey. J Neurophysiol *48*, 38-48.
327. Sasaki, Y., Rajimehr, R., Kim, B.W., Ekstrom, L.B., Vanduffel, W., and Tootell, R.B. (2006). The radial bias: a different slant on visual orientation sensitivity in human and nonhuman primates. Neuron *51*, 661-670.
328. Sceniak, M.P., Hawken, M.J., and Shapley, R. (2002). Contrast-dependent changes in spatial frequency tuning of macaque V1 neurons: effects of a changing receptive field size. J Neurophysiol *88*, 1363-1373.
329. Sceniak, M.P., Ringach, D.L., Hawken, M.J., and Shapley, R. (1999). Contrast's effect on spatial summation by macaque V1 neurons. Nat Neurosci *2*, 733-739.
330. Scherberger, H., Jarvis, M.R., and Andersen, R.A. (2005). Cortical local field potential encodes movement intentions in the posterior parietal cortex. Neuron *46*, 347-354.
331. Schiller, P.H., and Malpeli, J.G. (1977). The effect of striate cortex cooling on area 18 cells in the monkey. Brain Res *126*, 366-369.
332. Schmidt, K.E., Goebel, R., Lowel, S., and Singer, W. (1997). The perceptual grouping criterion of colinearity is reflected by anisotropies of connections in the primary visual cortex. Eur J Neurosci *9*, 1083-1089.
333. Schneidman, E., Berry, M.J., 2nd, Segev, R., and Bialek, W. (2006). Weak pairwise correlations imply strongly correlated network states in a neural population. Nature *440*, 1007-1012.
334. Schoffelen, J.M., Oostenveld, R., and Fries, P. (2005a). Neuronal coherence as a mechanism of effective corticospinal interaction. Science *308*, 111-113.
335. Schoffelen, J.M., Oostenveld, R., and Fries, P. (2005b). Neuronal coherence as a mechanism of effective corticospinal interaction. Science *308*, 111-113.
336. Schroeder, C.E., and Lakatos, P. (2009). The gamma oscillation: master or slave? Brain Topogr *22*, 24-26.
337. Schroeder, C.E., Tenke, C.E., and Givre, S.J. (1992). Subcortical contributions to the surface-recorded flash-VEP in the awake macaque. Electroencephalogr Clin Neurophysiol *84*, 219-231.
338. Schroeder, C.E., Tenke, C.E., Givre, S.J., Arezzo, J.C., and Vaughan, H.G., Jr. (1991). Striate cortical contribution to the surface-recorded pattern-reversal VEP in the alert monkey. Vision Res *31*, 1143-1157.

339. Schwabe, L., Obermayer, K., Angelucci, A., and Bressloff, P.C. (2006). The role of feedback in shaping the extra-classical receptive field of cortical neurons: a recurrent network model. J Neurosci *26*, 9117-9129.
340. Shao, Z., and Burkhalter, A. (1996). Different balance of excitation and inhibition in forward and feedback circuits of rat visual cortex. J Neurosci *16*, 7353-7365.
341. Shlens, J., Field, G.D., Gauthier, J.L., Grivich, M.I., Petrusca, D., Sher, A., Litke, A.M., and Chichilnisky, E.J. (2006). The structure of multi-neuron firing patterns in primate retina. J Neurosci *26*, 8254-8266.
342. Shmuel, A., Korman, M., Sterkin, A., Harel, M., Ullman, S., Malach, R., and Grinvald, A. (2005). Retinotopic axis specificity and selective clustering of feedback projections from V2 to V1 in the owl monkey. J Neurosci *25*, 2117-2131.
343. Siapas, A.G., Lubenov, E.V., and Wilson, M.A. (2005). Prefrontal phase locking to hippocampal theta oscillations. Neuron *46*, 141-151.
344. Siegel, M., and Konig, P. (2003). A functional gamma-band defined by stimulus-dependent synchronization in area 18 of awake behaving cats. J Neurosci *23*, 4251-4260.
345. Singer, W. (1999). Neuronal synchrony: a versatile code for the definition of relations? Neuron *24*, 49-65, 111-125.
346. Singer, W., and Gray, C.M. (1995). Visual feature integration and the temporal correlation hypothesis. Annu Rev Neurosci *18*, 555-586.
347. Singer, W., Kreiter, A.K., Engel, A.K., Fries, P., Roelfsema, P.R., and Volgushev, M. (1996). Precise timing of neuronal discharges within and across cortical areas: implications for synaptic transmission. J Physiol Paris *90*, 221-222.
348. Smith, M.A., Bair, W., and Movshon, J.A. (2006). Dynamics of suppression in macaque primary visual cortex. J Neurosci *26*, 4826-4834.
349. Smith, M.A., Kelly, R.C., and Lee, T.S. (2007). Dynamics of response to perceptual pop-out stimuli in macaque V1. J Neurophysiol *98*, 3436-3449.
350. Smith, M.A., and Kohn, A. (2008). Spatial and temporal scales of neuronal correlation in primary visual cortex. J Neurosci *28*, 12591-12603.
351. Sohal, V.S., Zhang, F., Yizhar, O., and Deisseroth, K. (2009). Parvalbumin neurons and gamma rhythms enhance cortical circuit performance. Nature *459*, 698-702.
352. Steriade, M., Timofeev, I., Durmuller, N., and Grenier, F. (1998). Dynamic properties of corticothalamic neurons and local cortical interneurons generating fast rhythmic (30-40 Hz) spike bursts. J Neurophysiol *79*, 483-490.
353. Stettler, D.D., Das, A., Bennett, J., and Gilbert, C.D. (2002). Lateral connectivity and contextual interactions in macaque primary visual cortex. Neuron *36*, 739-750.
354. Stopfer, M., Bhagavan, S., Smith, B.H., and Laurent, G. (1997). Impaired odour discrimination on desynchronization of odour-encoding neural assemblies. Nature *390*, 70-74.
355. Takahashi, K., Saleh, M., Penn, R.D., and Hatsopoulos, N.G. (2011). Propagating waves in human motor cortex. Front Hum Neurosci *5*, 40.

356. Tallon-Baudry, C. (2003). Oscillatory synchrony and human visual cognition. J Physiol Paris *97*, 355-363.
357. Tallon-Baudry, C. (2009). The roles of gamma-band oscillatory synchrony in human visual cognition. Front Biosci *14*, 321-332.
358. Tallon-Baudry, C., and Bertrand, O. (1999). Oscillatory gamma activity in humans and its role in object representation. Trends Cogn Sci *3*, 151-162.
359. Tallon-Baudry, C., Bertrand, O., Delpuech, C., and Pernier, J. (1996). Stimulus specificity of phase-locked and non-phase-locked 40 Hz visual responses in human. J Neurosci *16*, 4240-4249.
360. Tallon-Baudry, C., Kreiter, A., and Bertrand, O. (1999). Sustained and transient oscillatory responses in the gamma and beta bands in a visual short-term memory task in humans. Vis Neurosci *16*, 449-459.
361. Tanaka, K. (1996). Inferotemporal cortex and object vision. Annu Rev Neurosci *19*, 109-139.
362. Tiesinga, P., Fellous, J.M., and Sejnowski, T.J. (2008). Regulation of spike timing in visual cortical circuits. Nat Rev Neurosci *9*, 97-107.
363. Tiesinga, P., and Sejnowski, T.J. (2009). Cortical enlightenment: are attentional gamma oscillations driven by ING or PING? Neuron *63*, 727-732.
364. Tiesinga, P.H., and Sejnowski, T.J. (2010). Mechanisms for Phase Shifting in Cortical Networks and their Role in Communication through Coherence. Front Hum Neurosci *4*, 196.
365. Tolhurst, D.J., and Movshon, J.A. (1975). Spatial and temporal contrast sensitivity of striate cortical neurones. Nature *257*, 674-675.
366. Tootell, R.B., Hadjikhani, N.K., Vanduffel, W., Liu, A.K., Mendola, J.D., Sereno, M.I., and Dale, A.M. (1998). Functional analysis of primary visual cortex (V1) in humans. Proc Natl Acad Sci U S A *95*, 811-817.
367. Tootell, R.B., Switkes, E., Silverman, M.S., and Hamilton, S.L. (1988). Functional anatomy of macaque striate cortex. II. Retinotopic organization. J Neurosci *8*, 1531-1568.
368. Touboul, J., and Destexhe, A. (2010). Can power-law scaling and neuronal avalanches arise from stochastic dynamics? PLoS One *5*, e8982.
369. Tovee, M.J., and Rolls, E.T. (1992). Oscillatory activity is not evident in the primate temporal visual cortex with static stimuli. Neuroreport *3*, 369-372.
370. Traub, R.D., Bibbig, A., LeBeau, F.E., Buhl, E.H., and Whittington, M.A. (2004). Cellular mechanisms of neuronal population oscillations in the hippocampus in vitro. Annu Rev Neurosci *27*, 247-278.
371. Traub, R.D., Cunningham, M.O., Gloveli, T., LeBeau, F.E., Bibbig, A., Buhl, E.H., and Whittington, M.A. (2003). GABA-enhanced collective behavior in neuronal axons underlies persistent gamma-frequency oscillations. Proc Natl Acad Sci U S A *100*, 11047-11052.
372. Traub, R.D., Jefferys, J.G., and Whittington, M.A. (1997). Simulation of gamma rhythms in networks of interneurons and pyramidal cells. J Comput Neurosci *4*, 141-150.
373. Traub, R.D., Kopell, N., Bibbig, A., Buhl, E.H., LeBeau, F.E., and Whittington, M.A. (2001). Gap junctions between interneuron dendrites can enhance

synchrony of gamma oscillations in distributed networks. J Neurosci *21*, 9478-9486.
374. Traub, R.D., Whittington, M.A., Colling, S.B., Buzsaki, G., and Jefferys, J.G. (1996a). Analysis of gamma rhythms in the rat hippocampus in vitro and in vivo. J Physiol *493 (Pt 2)*, 471-484.
375. Traub, R.D., Whittington, M.A., Stanford, I.M., and Jefferys, J.G. (1996b). A mechanism for generation of long-range synchronous fast oscillations in the cortex. Nature *383*, 621-624.
376. Treisman, A. (1996). The binding problem. Curr Opin Neurobiol *6*, 171-178.
377. Ts'o, D.Y., Gilbert, C.D., and Wiesel, T.N. (1986). Relationships between horizontal interactions and functional architecture in cat striate cortex as revealed by cross-correlation analysis. J Neurosci *6*, 1160-1170.
378. Turner, R., Le Bihan, D., Moonen, C.T., Despres, D., and Frank, J. (1991). Echo-planar time course MRI of cat brain oxygenation changes. Magn Reson Med *22*, 159-166.
379. Uhlhaas, P.J., Linden, D.E., Singer, W., Haenschel, C., Lindner, M., Maurer, K., and Rodriguez, E. (2006). Dysfunctional long-range coordination of neural activity during Gestalt perception in schizophrenia. J Neurosci *26*, 8168-8175.
380. Uhlhaas, P.J., Pipa, G., Lima, B., Melloni, L., Neuenschwander, S., Nikolic, D., and Singer, W. (2009). Neural synchrony in cortical networks: history, concept and current status. Front Integr Neurosci *3*, 17.
381. Uhlhaas, P.J., and Singer, W. (2006). Neural synchrony in brain disorders: relevance for cognitive dysfunctions and pathophysiology. Neuron *52*, 155-168.
382. Usrey, W.M., Reppas, J.B., and Reid, R.C. (1998). Paired-spike interactions and synaptic efficacy of retinal inputs to the thalamus. Nature *395*, 384-387.
383. Van Essen, D.C., Anderson, C.H., and Felleman, D.J. (1992). Information processing in the primate visual system: an integrated systems perspective. Science *255*, 419-423.
384. Van Essen, D.C., Newsome, W.T., and Maunsell, J.H. (1984). The visual field representation in striate cortex of the macaque monkey: asymmetries, anisotropies, and individual variability. Vision Res *24*, 429-448.
385. Van Essen, D.C., Newsome, W.T., Maunsell, J.H., and Bixby, J.L. (1986). The projections from striate cortex (V1) to areas V2 and V3 in the macaque monkey: asymmetries, areal boundaries, and patchy connections. J Comp Neurol *244*, 451-480.
386. Vida, I., Bartos, M., and Jonas, P. (2006). Shunting inhibition improves robustness of gamma oscillations in hippocampal interneuron networks by homogenizing firing rates. Neuron *49*, 107-117.
387. Vinck, M., Lima, B., Womelsdorf, T., Oostenveld, R., Singer, W., Neuenschwander, S., and Fries, P. (2010). Gamma-phase shifting in awake monkey visual cortex. J Neurosci *30*, 1250-1257.
388. von der Heydt, R., Macuda, T., and Qiu, F.T. (2005). Border-ownership-dependent tilt aftereffect. J Opt Soc Am A Opt Image Sci Vis *22*, 2222-2229.
389. Wang, X.J., and Buzsaki, G. (1996). Gamma oscillation by synaptic inhibition in a hippocampal interneuronal network model. J Neurosci *16*, 6402-6413.

390. Webb, B.S., Dhruv, N.T., Solomon, S.G., Tailby, C., and Lennie, P. (2005). Early and late mechanisms of surround suppression in striate cortex of macaque. J Neurosci *25*, 11666-11675.
391. Whittington, M.A., Cunningham, M.O., Lebeau, F.E., Racca, C., and Traub, R.D. (2010). Multiple origins of the cortical gamma rhythm. Dev Neurobiol.
392. Whittington, M.A., Cunningham, M.O., LeBeau, F.E., Racca, C., and Traub, R.D. (2011). Multiple origins of the cortical gamma rhythm. Dev Neurobiol *71*, 92-106.
393. Whittington, M.A., Doheny, H.C., Traub, R.D., LeBeau, F.E., and Buhl, E.H. (2001). Differential expression of synaptic and nonsynaptic mechanisms underlying stimulus-induced gamma oscillations in vitro. J Neurosci *21*, 1727-1738.
394. Whittington, M.A., Traub, R.D., Faulkner, H.J., Stanford, I.M., and Jefferys, J.G. (1997). Recurrent excitatory postsynaptic potentials induced by synchronized fast cortical oscillations. Proc Natl Acad Sci U S A *94*, 12198-12203.
395. Whittington, M.A., Traub, R.D., and Jefferys, J.G. (1995). Synchronized oscillations in interneuron networks driven by metabotropic glutamate receptor activation. Nature *373*, 612-615.
396. Wiesel, T.N., and Hubel, D.H. (1974). Ordered arrangement of orientation columns in monkeys lacking visual experience. J Comp Neurol *158*, 307-318.
397. Wiesel, T.N., Hubel, D.H., and Lam, D.M. (1974). Autoradiographic demonstration of ocular-dominance columns in the monkey striate cortex by means of transneuronal transport. Brain Res *79*, 273-279.
398. Wilke, M., Logothetis, N.K., and Leopold, D.A. (2006). Local field potential reflects perceptual suppression in monkey visual cortex. Proc Natl Acad Sci U S A *103*, 17507-17512.
399. Wolfe, J.M., and Cave, K.R. (1999). The psychophysical evidence for a binding problem in human vision. Neuron *24*, 11-17, 111-125.
400. Womelsdorf, T., and Fries, P. (2006). Neuronal coherence during selective attentional processing and sensory-motor integration. J Physiol Paris *100*, 182-193.
401. Womelsdorf, T., and Fries, P. (2007). The role of neuronal synchronization in selective attention. Curr Opin Neurobiol *17*, 154-160.
402. Womelsdorf, T., Fries, P., Mitra, P.P., and Desimone, R. (2006). Gamma-band synchronization in visual cortex predicts speed of change detection. Nature *439*, 733-736.
403. Womelsdorf, T., Schoffelen, J.M., Oostenveld, R., Singer, W., Desimone, R., Engel, A.K., and Fries, P. (2007). Modulation of neuronal interactions through neuronal synchronization. Science *316*, 1609-1612.
404. Wu, W., Wheeler, D.W., Staedtler, E.S., Munk, M.H., and Pipa, G. (2008). Behavioral performance modulates spike field coherence in monkey prefrontal cortex. Neuroreport *19*, 235-238.
405. Wulff, P., Ponomarenko, A.A., Bartos, M., Korotkova, T.M., Fuchs, E.C., Bahner, F., Both, M., Tort, A.B., Kopell, N.J., Wisden, W*., et al.* (2009). Hippocampal theta rhythm and its coupling with gamma oscillations require fast

inhibition onto parvalbumin-positive interneurons. Proc Natl Acad Sci U S A *106*, 3561-3566.
406. Xiao, Y., Wang, Y., and Felleman, D.J. (2003). A spatially organized representation of colour in macaque cortical area V2. Nature *421*, 535-539.
407. Xing, D., Shapley, R.M., Hawken, M.J., and Ringach, D.L. (2005). Effect of stimulus size on the dynamics of orientation selectivity in Macaque V1. J Neurophysiol *94*, 799-812.
408. Xing, D., Yeh, C.I., and Shapley, R.M. (2009). Spatial spread of the local field potential and its laminar variation in visual cortex. J Neurosci *29*, 11540-11549.
409. Young, M.P., Tanaka, K., and Yamane, S. (1992). On oscillating neuronal responses in the visual cortex of the monkey. J Neurophysiol *67*, 1464-1474.
410. Yu, C., Klein, S.A., and Levi, D.M. (2003). Cross- and iso- oriented surrounds modulate the contrast response function: the effect of surround contrast. J Vis *3*, 527-540.
411. Zanos, T.P., Mineault, P.J., and Pack, C.C. (2011). Removal of spurious correlations between spikes and local field potentials. J Neurophysiol *105*, 474-486.
412. Zhou, H., Friedman, H.S., and von der Heydt, R. (2000). Coding of border ownership in monkey visual cortex. J Neurosci *20*, 6594-6611.
413. Zhou, Z., Bernard, M.R., and Bonds, A.B. (2008). Deconstruction of spatial integrity in visual stimulus detected by modulation of synchronized activity in cat visual cortex. J Neurosci *28*, 3759-3768.
414. Zipser, K., Lamme, V.A., and Schiller, P.H. (1996). Contextual modulation in primary visual cortex. J Neurosci *16*, 7376-7389.
415. Zohary, E., Shadlen, M.N., and Newsome, W.T. (1994). Correlated neuronal discharge rate and its implications for psychophysical performance. Nature *370*, 140-143.